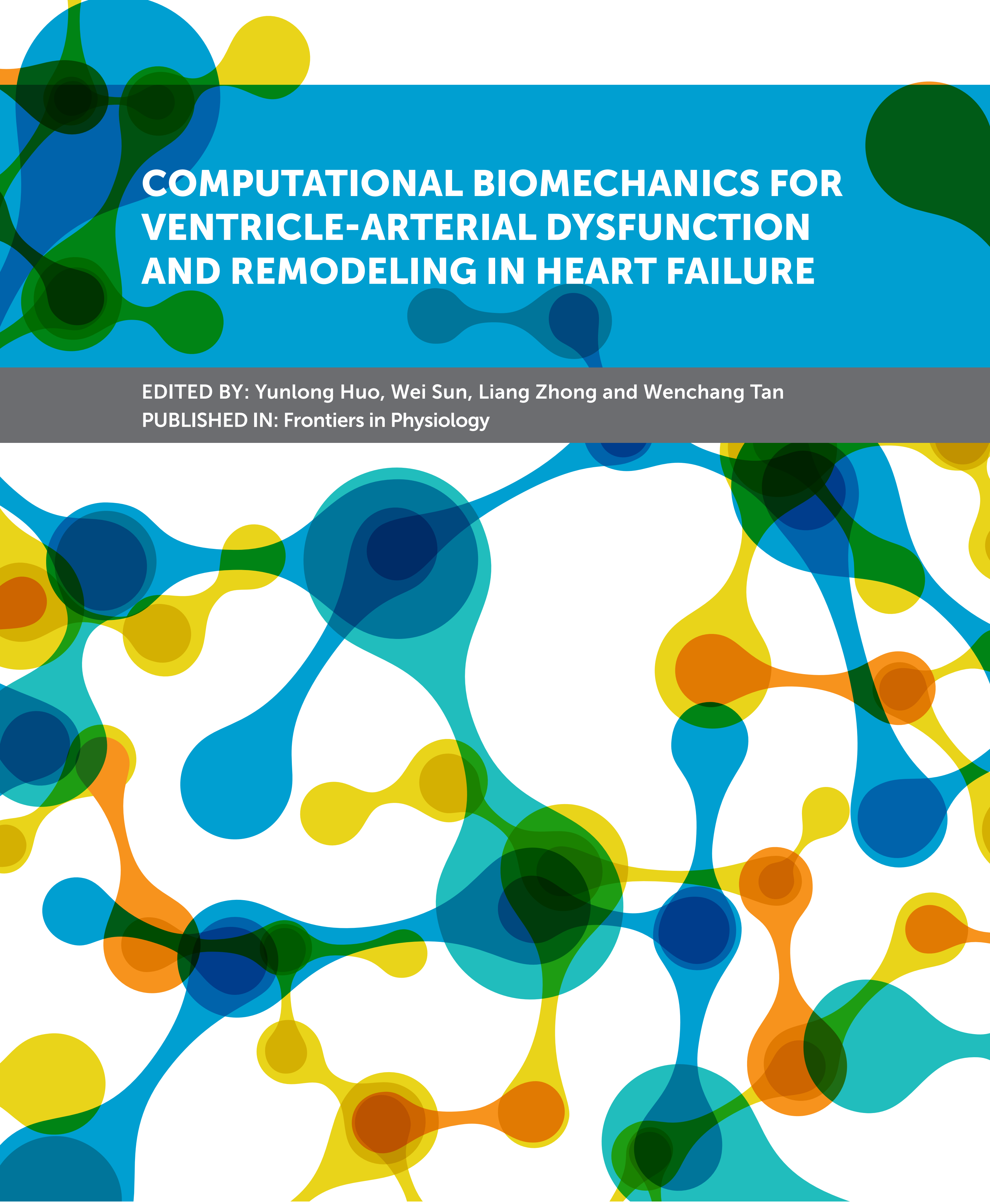

COMPUTATIONAL BIOMECHANICS FOR VENTRICLE-ARTERIAL DYSFUNCTION AND REMODELING IN HEART FAILURE

EDITED BY: Yunlong Huo, Wei Sun, Liang Zhong and Wenchang Tan
PUBLISHED IN: Frontiers in Physiology

frontiers Research Topics

ISSN 1664-8714
ISBN 978-2-88971-210-6
DOI 10.3389/978-2-88971-210-6

About Frontiers

Frontiers is more than just an open-access publisher of scholarly articles: it is a pioneering approach to the world of academia, radically improving the way scholarly research is managed. The grand vision of Frontiers is a world where all people have an equal opportunity to seek, share and generate knowledge. Frontiers provides immediate and permanent online open access to all its publications, but this alone is not enough to realize our grand goals.

Frontiers Journal Series

The Frontiers Journal Series is a multi-tier and interdisciplinary set of open-access, online journals, promising a paradigm shift from the current review, selection and dissemination processes in academic publishing. All Frontiers journals are driven by researchers for researchers; therefore, they constitute a service to the scholarly community. At the same time, the Frontiers Journal Series operates on a revolutionary invention, the tiered publishing system, initially addressing specific communities of scholars, and gradually climbing up to broader public understanding, thus serving the interests of the lay society, too.

Dedication to Quality

Each Frontiers article is a landmark of the highest quality, thanks to genuinely collaborative interactions between authors and review editors, who include some of the world's best academicians. Research must be certified by peers before entering a stream of knowledge that may eventually reach the public - and shape society; therefore, Frontiers only applies the most rigorous and unbiased reviews.
Frontiers revolutionizes research publishing by freely delivering the most outstanding research, evaluated with no bias from both the academic and social point of view. By applying the most advanced information technologies, Frontiers is catapulting scholarly publishing into a new generation.

What are Frontiers Research Topics?

Frontiers Research Topics are very popular trademarks of the Frontiers Journals Series: they are collections of at least ten articles, all centered on a particular subject. With their unique mix of varied contributions from Original Research to Review Articles, Frontiers Research Topics unify the most influential researchers, the latest key findings and historical advances in a hot research area! Find out more on how to host your own Frontiers Research Topic or contribute to one as an author by contacting the Frontiers Editorial Office: frontiersin.org/about/contact

COMPUTATIONAL BIOMECHANICS FOR VENTRICLE-ARTERIAL DYSFUNCTION AND REMODELING IN HEART FAILURE

Topic Editors:
Yunlong Huo, Shanghai Jiao Tong University, China
Wei Sun, Georgia Institute of Technology, United States
Liang Zhong, National Heart Centre Singapore, Singapore
Wenchang Tan, Peking University, China

Citation: Huo, Y., Sun, W., Zhong, L., Tan, W., eds. (2021). Computational Biomechanics for Ventricle-arterial Dysfunction and Remodeling in Heart Failure. Lausanne: Frontiers Media SA. doi: 10.3389/978-2-88971-210-6

Table of Contents

ORIGINAL RESEARCH
published: 31 January 2020
doi: 10.3389/fphys.2020.00002

Multiscale Modeling Framework of Ventricular-Arterial Bi-directional Interactions in the Cardiopulmonary Circulation

Sheikh Mohammad Shavik[1,2], Christopher Tossas-Betancourt[3], C. Alberto Figueroa[3,4], Seungik Baek[1] and Lik Chuan Lee[1]*

[1] Department of Mechanical Engineering, Michigan State University, East Lansing, MI, United States, [2] Department of Mechanical Engineering, Bangladesh University of Engineering and Technology, Dhaka, Bangladesh, [3] Department of Biomedical Engineering, University of Michigan, Ann Arbor, MI, United States, [4] Department of Surgery, University of Michigan, Ann Arbor, MI, United States

Edited by:
Yunlong Huo,
Peking University, China

Reviewed by:
Haiyang Tang,
University of Arizona, United States
Junmei Zhang,
National Heart Centre
Singapore, Singapore

***Correspondence:**
Lik Chuan Lee
lclee@egr.msu.edu

Specialty section:
This article was submitted to
Computational Physiology and
Medicine,
a section of the journal
Frontiers in Physiology

Received: 22 October 2019
Accepted: 03 January 2020
Published: 31 January 2020

Citation:
Shavik SM, Tossas-Betancourt C,
Figueroa CA, Baek S and Lee LC
(2020) Multiscale Modeling
Framework of Ventricular-Arterial
Bi-directional Interactions in the
Cardiopulmonary Circulation.
Front. Physiol. 11:2.
doi: 10.3389/fphys.2020.00002

Ventricular-arterial coupling plays a key role in the physiologic function of the cardiovascular system. We have previously described a hybrid lumped-finite element (FE) modeling framework of the systemic circulation that couples idealized FE models of the aorta and the left ventricle (LV). Here, we describe an extension of the lumped-FE modeling framework that couples patient-specific FE models of the left and right ventricles, aorta and the large pulmonary arteries in both the systemic and pulmonary circulations. Geometries of the FE models were reconstructed from magnetic resonance (MR) images acquired in a pediatric patient diagnosed with pulmonary arterial hypertension (PAH). The modeling framework was calibrated with pressure waveforms acquired in the heart and arteries by catheterization as well as ventricular volume and arterial diameter waveforms measured from MR images. The calibrated model hemodynamic results match well with the clinically-measured waveforms (volume and pressure) in the LV and right ventricle (RV) as well as with the clinically-measured waveforms (pressure and diameter) in the aorta and main pulmonary artery. The calibrated framework was then used to simulate three cases, namely, (1) an increase in collagen in the large pulmonary arteries, (2) a decrease in RV contractility, and (3) an increase in the total pulmonary arterial resistance, all characteristics of progressive PAH. The key finding from these simulations is that hemodynamics of the pulmonary vasculature and RV wall stress are more sensitive to vasoconstriction with a 10% of reduction in the lumen diameter of the distal vessels than a 67% increase in the proximal vessel's collagen mass.

Keywords: pulmonary arterial hypertension (PAH), cardiac mechanics, vascular mechanics, image-based modeling, ventricular-arterial coupling

INTRODUCTION

Ventricular-arterial coupling plays a vital role in the physiologic function of the cardiopulmonary circulation as well as in the evolution of cardiovascular diseases, such as pulmonary arterial hypertension (PAH) (Borlaug and Kass, 2011; Ky et al., 2013). In physiologic conditions, the arterial compliance (endowed by arterial wall tissue constituents) and the ventricular dynamic stiffness (inherent from the contraction of myocytes) confine the dynamic pressure variation to a physiological range to prevent end organ damage, while providing sufficient blood flow to meet oxygen demand of the body under varying workload (Borlaug and Kass, 2011). In pathological conditions, such as PAH, malfunction of one compartment (e.g., microcirculation) in the cardiopulmonary circulation may affect other compartments (e.g., ventricle) through a positive feedback loop that is driven by the tight coupling of ventricular and arterial systems, ultimately leading to end-stage heart failure. A modeling framework that captures the complex ventricular-arterial coupling would help elucidate the mechanisms governing the progression of PAH.

Existing mathematical modeling frameworks describing ventricular-arterial coupling in the cardiopulmonary circulation can be broadly classified as either a lumped parameter or a multi-scale finite element (FE) modeling framework. In a lumped parameter modeling framework, the ventricular-arterial coupling is described by an electrical analog representation of the cardiovascular system (Ursino, 1998; Smith et al., 2004). While such modeling framework is computationally inexpensive, it cannot directly take into account detailed geometrical and microstructural features associated with pathological conditions in the ventricles and arteries. In a hybrid lumped-FE modeling framework, a FE model describing either ventricular mechanics (Kerckhoffs et al., 2007; Shavik et al., 2017, 2019) or arterial hemodynamics (Lau and Figueroa, 2015; Zambrano et al., 2018) is coupled to lumped-parameter representation of the other compartments to provide a detailed description of the cardiovascular system. To overcome limitations associated with simplified representations of cardiovascular components, we previously introduced a hybrid lumped-FE modeling framework that bidirectionally couples FE models of the aorta and left ventricle (LV) mechanics in a closed-loop circulatory system (Shavik et al., 2018). Based on an idealized geometry of the LV and aorta, the modeling framework is able to reproduce pressure, arterial diameter, and LV volume waveforms found in a healthy individual. The modeling framework, however, considers only the systemic circulation and does not take into account the pulmonary circulation.

Here, we describe the extension of our earlier framework (Shavik et al., 2018) in which image-based FE models of the large pulmonary arteries, aorta, and heart (including both ventricles) are coupled bidirectionally in a closed-loop multi-scale FE modeling framework of the cardiopulmonary circulation. The multi-scale framework was calibrated using *in vivo* clinical measurements of the anatomy, deformation, and hemodynamics from a PAH pediatric patient. Using the calibrated model, we further investigate how changes associated with the mechanical behavior and microstructure of the microcirculation, large pulmonary arteries, and right ventricle (RV), consequent of PAH progression, affect each other.

METHODS

This study was approved by the University of Michigan Board of Review (HUM00117706), and informed consent was obtained from the parents/guardians of the patient.

Patient History

Clinical data was prospectively acquired in a 11-year-old female patient who was diagnosed with PAH. The patient had an elevated mean pulmonary arterial pressure (mPAP) of 59 mmHg with normal pulmonary capillary wedge pressure (PCWP) of 6 mmHg and elevated pulmonary vascular resistance (PVR) of 13.5 WU, falling within the clinical classification of PAH (mPAP $\geq$ 20 mmHg, PCWP $\leq$ 15 mmHg, and PVR $\geq$ 3 WU) (Simonneau et al., 2019). She has family history of chronic obstructive pulmonary disease and PAH.

Data Acquisition

Anatomical and hemodynamic data were obtained using magnetic resonance (MR) imaging and arterial catheterization. Cine MR images of the short- and long-axis views of the ventricles were acquired at 30 time points in the cardiac cycle. Using the cine MR images, left and right ventricular endocardial surfaces were segmented with the medical image analysis software MeVisLab (www.mevislab.de) to acquire ventricular volume waveforms. Cardiac-gated gradient echo MR images of the vascular anatomy were acquired in the diastolic phase. Luminal area waveforms were also acquired with phase-contrast MR images (PC-MRI) at the ascending aorta and main pulmonary artery. Arterial catheterization was performed to acquire pressure waveforms in the LV, RV, main pulmonary artery (MPA), and aorta. The ventricular volume and pressure waveforms were synchronized to reconstruct pressure-volume (PV) loops (Xi et al., 2016; Shavik et al., 2019). Hemodynamic and cardiovascular function metrics of the PAH patient are listed in **Table 1**.

Biventricular and Vascular Geometries

Anatomical models of the LV, RV, aorta, and pulmonary arteries (PA) (consisting of the main, left, and right pulmonary arteries) were reconstructed from the acquired MR images. The biventricular model was reconstructed from images that correspond to the point in the cardiac cycle where ventricular pressures were lowest during filling (Geuzaine and Remacle, 2009). Furthermore, anatomical models of the aorta and large pulmonary arteries were reconstructed using the blood

---

Abbreviations: AO, Aorta; EDPVR, End-diastolic Pressure Volume Relationship; EF, Ejection Fraction; ESPVR, End-systolic Pressure Volume Relationship; FE, Finite Element; HR, Heart Rate; LA, Left Atrium; LPA, Left Pulmonary Artery; LV, Left Ventricle; LVEDV, Left Ventricular End-diastolic Volume; LVEF, Left Ventricular Ejection Fraction; LVESV, Left Ventricular End-systolic Volume; LVFW, Left Ventricular Free Wall; MAP, Mean Aortic Pressure; MPA, Main Pulmonary Artery; mPAP, Mean Pulmonary Arterial Pressure; MR, Magnetic Resonance; PA, Pulmonary Artery; PAH, Pulmonary Arterial Hypertension; PC-MRI, Phase-Contrast Magnetic Resonance Image; PCWP, Pulmonary Capillary Wedge Pressure; PV, Pressure-Volume; pv, Pulmonary Veins; PVR, Pulmonary Vascular Resistance; RA, Right Atrium; RPA, Right Pulmonary Artery; RV, Right Ventricle; RVEDV, Right Ventricular End-diastolic Volume; RVEF, Right Ventricular Ejection Fraction; RVESV, Right Ventricular End-systolic Volume; RVFW, Right Ventricular Free Wall; sa, Systemic Arteries; SMC, Smooth Muscle Cells; sv, Systemic Veins; WU, Wood Unit.

TABLE 1 | Hemodynamic measurements of PAH patient.

Quantities	Values
HR, bpm	75
LVEDV, ml	72
LVESV, ml	25
LVEF, %	65
MAP, mmHg	68
RVEDV, ml	77
RVESV, ml	30
RVEF, %	61
RVEDV/LVEDV	1.07
mPAP, mmHg	59
PCWP, mmHg	6

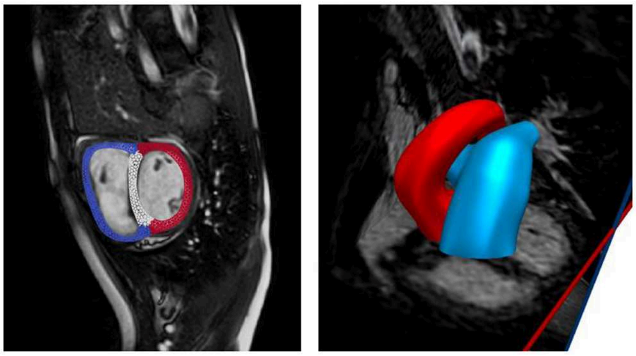

FIGURE 1 | Reconstruction of biventricular model **(left)** and large proximal arteries **(right)** from cine MR images.

flow modeling software CRIMSON (www.crimson.software) (**Figure 1**).

Closed Loop Circulatory System

The biventricular, aorta and pulmonary artery FE models were coupled through a closed loop lumped-parameter circulatory model that describes both systemic and pulmonary circulations (**Figure 2**). The modeling framework consists of eight compartments with four cardiovascular components (ventricle, atrium, artery, and vein) each in the systemic and pulmonary circulations. Conservation of total blood mass in the circulatory model requires the net change of inflow and outflow rates of each compartment to be related to the rate of change of the volume by the following relations

$$\frac{dV_{LV}(t)}{dt} = q_{mv}(t) - q_{av}(t), \tag{1a}$$

$$\frac{dV_{sa}(t)}{dt} = q_{av}(t) - q_{sa}(t), \tag{1b}$$

$$\frac{dV_{sv}(t)}{dt} = q_{sa}(t) - q_{sv}(t), \tag{1c}$$

$$\frac{dV_{RA}(t)}{dt} = q_{sv}(t) - q_{tv}(t), \tag{1d}$$

$$\frac{dV_{RV}(t)}{dt} = q_{tv}(t) - q_{pvv}(t), \tag{1e}$$

$$\frac{dV_{pa}(t)}{dt} = q_{pvv}(t) - q_{pa}(t) \tag{1f}$$

$$\frac{dV_{pv}(t)}{dt} = q_{pa}(t) - q_{pv}(t), \tag{1g}$$

$$\frac{dV_{LA}(t)}{dt} = q_{pv}(t) - q_{mv}(t). \tag{1h}$$

In Equation (1), V_{LV}, V_{sa}, V_{sv}, V_{RA}, V_{RV}, V_{pa}, V_{pv}, and V_{LA} are the volumes of the eight compartments with the subscripts denoting the LV, systemic arteries (sa), systemic veins (sv), right atrium (RA), RV, pulmonary arteries (pa), pulmonary veins (pv), and left atrium (LA), respectively. Flow rates at different segments of the circulatory model are denoted by q_{mv}, q_{av}, q_{sa}, q_{sv}, q_{tv}, q_{pvv}, q_{pa}, and q_{pv}.

Systemic and pulmonary arteries and veins were modeled using their electrical analogs based on Ohm's law. At each segment, the flow rate depends on the pressure gradient and resistance to the flow as described in the following equation

$$q_{mv}(t) = \begin{cases} \frac{P_{LA}(t) - P_{LV}(t)}{R_{mv}} & when,\ P_{LA}(t) \geq P_{LV}(t) \\ 0 & when,\ P_{LA}(t) < P_{LV}(t) \end{cases} \tag{2a}$$

$$q_{av}(t) = \begin{cases} \frac{P_{LV}(t) - P_{sa}(t)}{R_{av}} & when,\ P_{LV}(t) \geq P_{sa}(t) \\ 0 & when,\ P_{LV}(t) < P_{sa}(t) \end{cases}, \tag{2b}$$

$$q_{sa}(t) = \frac{P_{sa}(t) - P_{sv}(t)}{R_{sa}}, \tag{2c}$$

$$q_{sv}(t) = \frac{P_{sv}(t) - P_{RA}(t)}{R_{sv}}, \tag{2d}$$

$$q_{tv}(t) = \begin{cases} \frac{P_{RA}(t) - P_{RV}(t)}{R_{tv}} & when,\ P_{RA}(t) \geq P_{RV}(t) \\ 0 & when,\ P_{RA}(t) < P_{RV}(t) \end{cases}, \tag{2e}$$

$$q_{pvv}(t) = \begin{cases} \frac{P_{RV}(t) - P_{pa}(t)}{R_{pvv}} & when,\ P_{RV}(t) \geq P_{pa}(t) \\ 0 & when,\ P_{RV}(t) < P_{pa}(t) \end{cases}, \tag{2f}$$

$$q_{pa}(t) = \frac{P_{pa}(t) - P_{pv}(t)}{R_{pa}}, \tag{2g}$$

$$q_{pv}(t) = \frac{P_{pv}(t) - P_{LA}(t)}{R_{pv}}. \tag{2h}$$

In Equation (2), R_{mv}, R_{av}, R_{tv}, and R_{pvv} are the resistances associated with the mitral, aortic, tricuspid, and pulmonary valves, respectively. The valves are each represented by a diode that only permits one-way flow as in previous studies (Punnoose et al., 2012; Shavik et al., 2019). The vessel resistances are denoted by R_{sa}, R_{sv}, R_{pa}, and R_{pv}, respectively. To describe the compliance of the systemic and pulmonary vessels, we used the following PV relationships

$$P_{sv}(t) = \frac{V_{sv}(t) - V_{sv,0}}{C_{sv}}, \tag{3a}$$

$$P_{pv}(t) = \frac{V_{pv}(t) - V_{pv,0}}{C_{pv}}, \tag{3b}$$

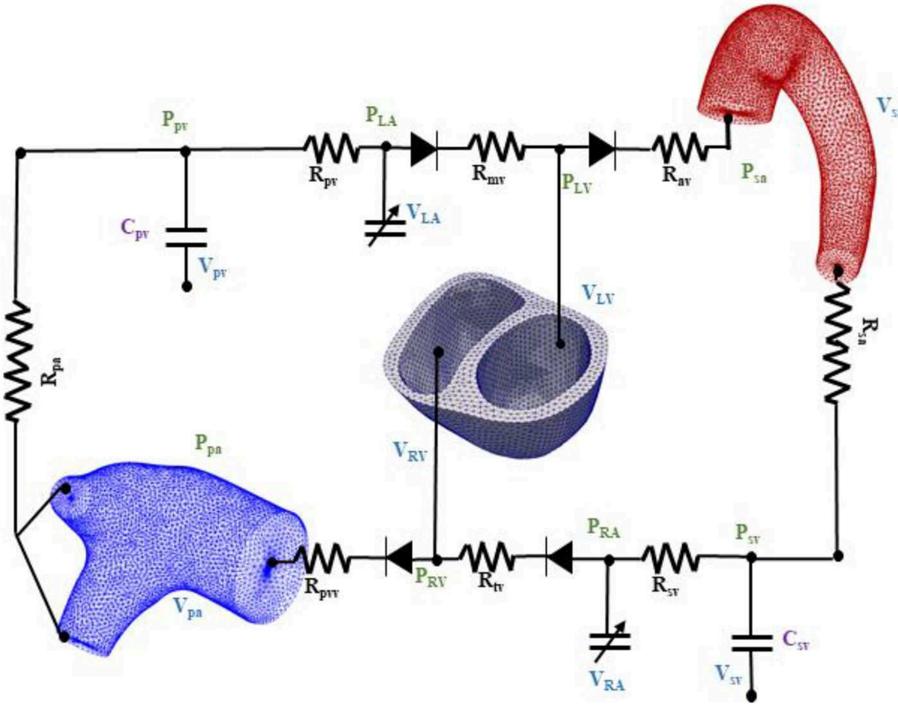

FIGURE 2 | Schematic of the finite element ventricular-vascular coupling closed loop circulatory modeling framework.

where $V_{sv,0}$ and $V_{pv,0}$ are the resting volumes and C_{sv} and C_{pv} are the total compliance of the systemic and pulmonary veins, respectively.

Contraction of the LA and RA was modeled using a time varying elastance function that is given by the following PV relations

$$P_k(t) = e(t)P_{es,k}(V_k(t)) + (1 - e(t))\, P_{ed,k}(V_k(t)), \tag{4a}$$

where,

$$P_{es,k}(V_k(t)) = E_{es,k}(V_k(t) - V_{0,k}), \tag{4b}$$

$$P_{ed,k}(V_k(t)) = A_k\,(e^{B_k(V_k(t) - V_{0,k})} - 1). \tag{4c}$$

In Equation (4), the subscript k denotes either LA or RA. The volume, end-systolic elastance, and volume-intercept of the end-systolic pressure-volume relationship (ESPVR) of the corresponding atrium are denoted by V_k, $E_{es,k}$, and $V_{0,k}$, respectively. The parameters A_k and B_k define the atrium curvilinear end-diastolic pressure volume relationship (EDPVR) and the driving function is defined as

$$e\,(t) = \begin{cases} \frac{1}{2}\left(\sin\left[\left(\frac{\pi}{t_{max}}\right)t \, - \frac{\pi}{2}\right] + 1\right); & 0 < \, t \, \leq \, 3t_{max}/2 \\ \frac{1}{2}\, e^{\frac{-(t - \frac{3t_{max}}{2})}{\tau}}; & t > 3t_{max}/2, \end{cases}, \tag{5}$$

where t_{max} is the point of maximal chamber elastance and τ is the time constant of relaxation. The time-varying elastance model has been shown to be able to describe atrium contraction well (Hoit et al., 1994).

The relationships between pressures and volumes in the biventricular unit (i.e., LV and RV), pulmonary artery and aorta were computed from their corresponding FE models. These relationships can be expressed as non-closed form functions.

$$P_{RV}\,(t)\,, P_{LV}(t) = f^{BV}(V_{LV}\,(t)\,,\, V_{RV}(t)), \tag{6a}$$

$$P_{pa}\,(t) = f^{PA}(V_{pa}(t)), \tag{6b}$$

$$P_{sa}\,(t) = f^{AO}\,(V_{sa}\,(t))\,. \tag{6c}$$

Finite Element Formulation of the Biventricular Unit

The weak form associated with the biventricular FE model was derived based on minimization of the following Lagrangian functional

$$\begin{aligned} &\mathcal{L}_{BV}\left(\boldsymbol{u}_{BV}, p_{BV}, P_{LV}, P_{RV}, \boldsymbol{c}_{1,BV}, \boldsymbol{c}_{2,BV}\right) \\ &= \int_{\Omega_{0,BV}} W_{BV}\left(\boldsymbol{u}_{BV}\right) dV - \int_{\Omega_{0,BV}} p_{BV}\left(J_{BV} - 1\right) dV \\ &- P_{LV}\left(V_{LV,\text{cav}}\left(\boldsymbol{u}_{BV}\right) - V_{LV}\right) + P_{RV}\left(V_{RV,\text{cav}}\left(\boldsymbol{u}_{BV}\right) - V_{RV}\right) \\ &- \boldsymbol{c}_{1,BV}\cdot \int_{\Omega_{0,BV}} \boldsymbol{u}_{BV}\, dV - \boldsymbol{c}_{2,BV}\cdot \int_{\Omega_{0,BV}} \boldsymbol{X}_{BV} \times \boldsymbol{u}_{BV}\, dV, \end{aligned} \tag{7}$$

where $\Omega_{0,BV}$ is the reference configuration of the biventricular unit, $\boldsymbol{u}_{BV}$ is the displacement field, P_{LV} and P_{RV} are, respectively, the Lagrange multipliers that constrain the LV cavity volume

$V_{LV,cav}(\boldsymbol{u}_{BV})$ to a prescribed value V_{LV} and the RV cavity volume $V_{RV,cav}(\boldsymbol{u}_{BV})$ to a prescribed value V_{RV} (Pezzuto and Ambrosi, 2014). We note that V_{LV} and V_{RV} are prescribed from the closed-loop circulatory model in Equation (6). The Lagrange multiplier p_{BV} was used to enforce incompressibility of the tissue (i.e., Jacobian of the deformation gradient tensor $J = 1$). The vectors $\boldsymbol{c}_{1,BV}$ and $\boldsymbol{c}_{2,BV}$ are Lagrange multipliers applied to constrain, respectively, the rigid body translation (i.e., zero mean translation) and rotation (i.e., zero mean rotation) (Pezzuto et al., 2014). In Equation (7), $\boldsymbol{X}_{BV}$ denotes a material point in $\Omega_{0,BV}$ and W_{BV} is the strain energy function of the myocardial tissue. The cavity volume of the LV and RV were obtained from the displacement field by using the following functional relationship ($k = LV$ or RV)

$$V_{k,cav}(\boldsymbol{u}_{BV}) = \int_{\Omega_{inner,k}} dv_k = -\frac{1}{3}\int_{\Gamma_{inner,k}} \boldsymbol{x}_{BV}.\boldsymbol{n}\, da_k\,, \tag{8}$$

where $\Omega_{inner,k}$ is the volume enclosed by the inner surface $\Gamma_{inner,k}$ of the LV or RV, and $\boldsymbol{n}$ denotes the outward unit normal vector of those surfaces. Taking the first variation of the Lagrangian functional given in Equation (7) leads to

$$\begin{aligned}\delta\mathcal{L}_{BV} = &\int_{\Omega_{0,\,BV}} (\boldsymbol{P}_{BV} - p_{BV}\boldsymbol{F}_{BV}{}^{-\mathbf{T}}) : \nabla\delta\boldsymbol{u}_{BV}\, dV \\ &- \int_{\Omega_{0,\,BV}} \delta p_{BV}\,(J-1)\, dV - (P_{LV} \\ &+ P_{RV})\int_{\Omega_{0,\,BV}} cof\,(\boldsymbol{F}_{BV}) : \nabla\delta\boldsymbol{u}_{BV}\, dV \; - \delta P_{LV}\left(V_{LV,\,\mathrm{cav}}(\boldsymbol{u}_{BV})\right. \\ &\left.- V_{LV}\right) - \delta P_{RV}\left(V_{RV,\,\mathrm{cav}}(\boldsymbol{u}_{BV}) - V_{RV}\right) \\ &- \delta\boldsymbol{c}_{1,\,BV}\cdot\int_{\Omega_{0,\,BV}} \boldsymbol{u}_{BV}\, dV - \delta\boldsymbol{c}_{2,\,BV}\cdot\int_{\Omega_{0,\,BV}} \mathbf{X}_{BV}\times\boldsymbol{u}_{BV}\, dV \\ &- \boldsymbol{c}_{1,\,BV}\cdot\int_{\Omega_{0,\,BV}} \delta\boldsymbol{u}_{BV}\, dV - \boldsymbol{c}_{2,\,BV}\cdot\int_{\Omega_{0,\,BV}} \boldsymbol{X}_{BV}\times\delta\boldsymbol{u}_{BV}\, dV.\end{aligned} \tag{9}$$

In Equation (9), $\boldsymbol{P}_{BV}$ is the first Piola Kirchhoff stress tensor and $\boldsymbol{F}_{BV}$ is the deformation gradient tensor. The variations of the displacement field, Lagrange multiplier for enforcing incompressibility and volume constraint, zero mean translation, and rotation are denoted by $\delta\boldsymbol{u}_{BV}$, δp_{BV}, $\delta P_{LV,\,\mathrm{cav}}$, $\delta P_{RV,\mathrm{cav}}$, $\delta\boldsymbol{c}_{1,BV}$, and $\delta\boldsymbol{c}_{2,BV}$, respectively. Together with the constraint that the basal deformation at $z = 0$ is in-plane in the biventricular unit, the solution of the Euler-Lagrange problem was obtained by finding $\boldsymbol{u}_{BV}\in H^1(\Omega_0)$, $p_{BV}\in L^2(\Omega_0)$, $P_{LV,\,\mathrm{cav}}\in\mathbb{R}$, $P_{RV,\,\mathrm{cav}}\in\mathbb{R}$, $\boldsymbol{c}_{1,BV}\in\mathbb{R}^{\mathbf{3}}$, $\boldsymbol{c}_{2,BV}\in\mathbb{R}^{\mathbf{3}}$ that satisfies

$$\delta\mathcal{L}_{BV} = 0, \tag{10a}$$

$$\boldsymbol{u}_{BV}\left(x, y, 0\right).\boldsymbol{n}\big|_{base} = 0, \tag{10b}$$

for all $\delta\boldsymbol{u}_{BV}\in H^1(\Omega_0)$, $\delta p_{BV}\in L^2(\Omega_0)$, $\delta P_{LV,\,\mathrm{cav}}\in\mathbb{R}$, $\delta P_{RV,\,\mathrm{cav}}\in\mathbb{R}$, $\delta\boldsymbol{c}_{1,\,BV}\in\mathbb{R}^{\mathbf{3}}$, $\delta\boldsymbol{c}_{2,\,BV}\in\mathbb{R}^{\mathbf{3}}$. The solution of Equation (10) gives the relationship between $P_{RV}, P_{LV}, V_{RV}, V_{LV}$ in Equation (6).

Mechanical Behavior of the Cardiac Tissue

Mechanical behavior of the myocardial tissue was described by an active stress formulation in which the first Piola-Kirchhoff stress tensor $\boldsymbol{P}_{BV}$ in Equation (9) was additively decomposed into a passive and an active component, i.e.,

$$\boldsymbol{P}_{BV} = \boldsymbol{P}_{BV,\,p} + P_{BV,\,a}\,\boldsymbol{e_f}\otimes\boldsymbol{e_{f_0}}. \tag{11}$$

In Equation (11), $\boldsymbol{P}_{BV,\,p}$ is the passive stress tensor, $P_{BV,\,a}$ is the magnitude of the active stress, whereas $\boldsymbol{e_f}$ and $\boldsymbol{e_{f_0}}$ are the local basis vectors that define the cardiac muscle fiber directions in the current and reference configuration, respectively. The passive stress tensor $\boldsymbol{P}_{BV,\,p}$ is related to the strain energy function $W_{BV,p}$ and deformation gradient tensor $\boldsymbol{F}_{BV}$ by

$$\boldsymbol{P}_{BV,\,p} = \frac{dW_{BV,p}}{d\boldsymbol{F}_{BV}}\,. \tag{12}$$

A Fung-type transversely-isotropic hyperelastic strain energy function (Guccione et al., 1991)

$$W_{BV,\,p} \;=\; \frac{1}{2}C_{BV}\left(e^{Q} - 1\right), \tag{13a}$$

with

$$\begin{aligned}Q \;=\; & b_{ff}E_{ff}^2 + b_{xx}\left(E_{ss}^2 + E_{nn}^2 + E_{sn}^2 + E_{ns}^2\right) \\ & +\; b_{fx}\left(E_{fn}^2 + E_{nf}^2 + E_{fs}^2 + E_{sf}^2\right)\end{aligned} \tag{13b}$$

was prescribed. In Equation (13b), E_{ij} with $(i,\, j)\,\epsilon\,(f,\, s,\, n)$ denote the components of the Green-Lagrange strain tensor $\boldsymbol{E} = \frac{1}{2}(\boldsymbol{F}_{BV}{}^{\boldsymbol{T}}\boldsymbol{F}_{BV} - \boldsymbol{I})$ with f, s, n denoting the myofiber, sheet and sheet normal directions, respectively. Material parameters of the Fung-type constitutive model are C_{BV}, b_{ff}, b_{xx}, and b_{fx}.

To describe the active stress behavior, a previously developed active contraction model (Kerckhoffs et al., 2003) was used. The magnitude of the active stress $P_{BV,\,a}$ was described by

$$P_{BV,\,a} \;=\; \frac{l_s}{l_{s0}} f^{iso}\left(l_c\right) f^{twitch}\left(t, l_s\right)\left(l_s - l_c\right) E_a, \tag{14}$$

where l_s is the sarcomere length, l_c is the length of the contractile element, l_{s0} is the sarcomere length in a prescribed reference state (relaxed sarcomere length), and E_a is the stiffness of the serial elastic element. The function $f^{iso}\left(l_c\right)$ denotes the dependency of the isometrically developed active stress on l_c and is given by

$$f^{iso}\left(l_c\right) = \begin{cases} T_0\tanh^2[\mathrm{a}_6(\mathrm{l_c} - \mathrm{a}_7)] & when,\ l_c < a_7 \\ 0 & when,\ l_c > a_7 \end{cases}, \tag{15}$$

where T_0 is a model parameter that scales the active tension. Both a_6 and a_7 are model parameters. The time course of the active tension development is controlled by

$$f^{twitch}\left(t, l_s\right) \;=\; \begin{cases} 0 & when,\ \ t < 0 \\ \tanh^2\left(\frac{t}{t_r}\right)\tanh^2\left(\frac{t_{max}-t}{t_d}\right) & when,\ \ 0 < t < t_{max} \\ 0 & when,\ \ t > 0\,, \end{cases} \tag{16a}$$

$$t_{max} \;=\; b(l_s - l_d). \tag{16b}$$

In Equation (16), t_r is the activation rise time constant, t_d is the activation decay time constant, b relates activation duration t_{max} to the sarcomere length l_s, and l_d is the sarcomere length at the start of the activation time, i.e., when $t_{max} = 0$. The time course of the contractile element l_c was expressed by an ordinary differential equation

$$\frac{\partial l_c}{\partial t} = \left[E_a\left(l_s - l_c\right) - 1\right] v_0, \tag{17}$$

where v_0 is the unloaded shortening velocity. The sarcomere length l_s was calculated from the myofiber stretch λ and the relaxed sarcomere length l_{s0} by

$$\lambda = \sqrt{\boldsymbol{e}_{f0}\cdot\boldsymbol{F}_{BV}{}^{\boldsymbol{T}}\boldsymbol{F}_{BV}\boldsymbol{e}_{f0}}\,, \tag{18a}$$

$$l_s = \lambda l_{s0}. \tag{18b}$$

Finite Element Formulation of the Arteries

The pulmonary artery and aorta were modeled as 3D membranes. In the formulation that follows, the subscript $k = AO$ denotes the aorta and $k = PA$ denotes the pulmonary artery. Similar to that of the biventricular unit, the finite element formulation of these two arteries can be generalized from the minimization of the following Lagrangian functional, described in the following equation

$$\begin{aligned}&\mathcal{L}_k\left(\boldsymbol{u}_k, P_{k,\text{cav}}, \boldsymbol{c}_{1,k}, \boldsymbol{c}_{2,k}\right)\\ &= \int_{\Omega_{0,k}} W_k\left(\boldsymbol{u}_k\right) dV - P_{k,\text{cav}}\left(V_{k,\text{cav}}\left(\boldsymbol{u}_k\right) - V_k\right)\\ &-\boldsymbol{c}_{1,k}\cdot\int_{\Omega_{0,k}} \boldsymbol{u}_k\, dV - \boldsymbol{c}_{2,k}\cdot\int_{\Omega_{0,k}} \boldsymbol{X}_k \times \boldsymbol{u}_k\, dV,\end{aligned} \tag{19}$$

where $\Omega_{0,k}$ is the reference configuration of the arteries, $\boldsymbol{u}_k$ is the displacement field and $P_{k,\text{cav}}$ is the Lagrange multiplier that constrains the arterial cavity volume $V_{k,\text{cav}}\left(\boldsymbol{u}_k\right)$ to a prescribed value V_k. The vectors $\boldsymbol{c}_{1,k}$ and $\boldsymbol{c}_{2,k}$ are Lagrange multipliers applied to constrain rigid body motions. The inlet and outlets of the arteries were constrained to move only in-plane. Therefore, the solution of the Euler-Lagrange problem was obtained by finding $\boldsymbol{u}_k \in H^1\left(\Omega_0\right),\ P_{k,\text{cav}} \in \mathbb{R}, \boldsymbol{c}_{1,k} \in \mathbb{R}^{\mathbf{3}}, \boldsymbol{c}_{2,k} \in \mathbb{R}^{\mathbf{3}}$ that satisfies

$$\delta\mathcal{L}_k = 0, \tag{20a}$$

$$\boldsymbol{u}_k\left(x, y, 0\right)\boldsymbol{.n}\big|_{inlet,\ outlets} = 0, \tag{20b}$$

for all $\delta\boldsymbol{u}_k \in H^1\left(\Omega_0\right),\ \delta P_{k,\text{cav}} \in \mathbb{R}, \delta\boldsymbol{c}_{1,k} \in \mathbb{R}^{\mathbf{3}}, \delta\boldsymbol{c}_{2,k} \in \mathbb{R}^{\mathbf{3}}$. The solution above gives the relationships between P_{pa}, V_{pa}, and P_{sa}, V_{sa} in Equations (6b) and (6c), respectively.

Mechanical Behavior of the Vascular Tissue

The mechanical behavior of the arteries were described by the strain energy function W_k in Equation (21), which is given as the sum of the key tissue constituents, namely, elastin-dominated matrix $W_{k,e}$, collagen fiber families $W_{k,c,i}$ and vascular smooth muscle cells (SMC) $W_{k,m}$ (Baek et al., 2007; Zeinali-Davarani et al., 2011), i.e.,

$$W_k = W_{k,e} + \sum_{i=1}^{4} W_{k,c,i} + W_{k,m}. \tag{21}$$

Strain energy function of the elastin-dominated amorphous matrix in the arteries is given by

$$W_{k,e} = M_{k,e}\left(\frac{C_{k,1}}{2}\right)\left(\text{tr}\left(\boldsymbol{C}_k\right) - 3\right), \tag{22}$$

where $M_{k,e}$ is the mass per unit volume of the elastin in the tissue, $C_{k,1}$ is a stiffness parameter and, $\mathbf{C}_k = \mathbf{F}_k^{\mathbf{T}}\mathbf{F}_k$ is the right Cauchy-Green deformation tensor associated with the arteries.

In the membrane models, four collagen fiber families were considered. The first and second families of collagen fibers ($i = 1$ and 2) were oriented in the longitudinal and circumferential directions, whereas the third and fourth families of collagen fibers ($i = 3$ and 4) were oriented, respectively, at an angle $\alpha = 45^\circ$ and -45° with respect to the longitudinal axis based on a previous study (Zeinali-Davarani et al., 2011). We assumed that the same strain energy function for all the families of collagen fibers is given by

$$W_{k,c,i} = M_{k,i}\frac{c_{k,2}}{4c_{k,3}}\left\{\exp\left[c_{k,3}\left(\lambda_{k,i}{}^2 - 1\right)^2\right] - 1\right\}. \tag{23}$$

In Equation (23), $M_{k,i}$ is the mass per unit volume of ith family of collagen fibers, $\lambda_{k,i}$ is the corresponding stretch of those fibers, and both $c_{k,2}$ and $c_{k,3}$ are the material parameters that govern the collagen stiffness. The stretch in the ith family of collagen fibers was defined by $\lambda_{k,i} = \sqrt{\boldsymbol{e}_{k,i0}\cdot\boldsymbol{C}_k\boldsymbol{e}_{k,i0}}$ where $\boldsymbol{e}_{k,i0}$ is the local unit vector that defines the corresponding fiber orientation.

Strain energy function of the SMC $W_{k,m}$ is given by

$$W_{k,m} = M_{k,m}\frac{c_{k,4}}{4c_{k,5}}\left\{\exp\left[c_{k,5}\left(\lambda_{k,m}{}^2 - 1\right)^2\right] - 1\right\}. \tag{24}$$

Here, $M_{k,m}$ is the mass per unit volume of the SMC in the tissue, $\lambda_{k,m}$ is the stretch of the SMC, whereas $c_{k,4}$ and $c_{k,5}$ are the stiffness parameters. The SMC was assumed to be aligned in the circumferential direction. Mass per unit volume for the different constituents were calculated using following relations

$$M_{k,e} = \phi_{k,e}\rho, \tag{25a}$$

$$M_{k,m} = \phi_{k,m}\rho, \tag{25b}$$

$$M_{k,i} = \phi_{k,i}\left(1 - \phi_{k,e} - \phi_{k,m}\right)\rho, \tag{25c}$$

where $\phi_{k,e}$, $\phi_{k,m}$, $\phi_{k,i}$ denote the mass fraction for elastin, SMC and ith family of collagen fibers, respectively. Twenty percent of the total collagen mass is assumed to be equally distributed in the longitudinal and circumferential fiber families and the remaining 80% was distributed equally to $\alpha = 45^\circ$ and -45° fiber directions. Constitutive parameters, mass fraction of each constituent and other parameters of the pulmonary artery and aorta membrane models are listed in **Table 2**.

TABLE 2 | Model parameters for FE models for the baseline case.

Biventricular FE model	
Passive material model	$C_{LV} = 280\,\text{Pa}$, $C_{RV} = 170\,\text{Pa}$
Active contraction model	$T_{0,LV} = 2000\,\text{kPa}$, $T_{0,RV} = 1800\,\text{kPa}$, $t_r = 280\,\text{ms}$, $t_d = 80\,\text{ms}$, $b = 0.17\,\text{ms}.\mu\text{m}^{-1}$
Circulatory model	$C_{sv} = 0.02\,\text{Pa}\bullet\text{ml}$, $C_{pv} = 0.09\,\text{Pa}\bullet\text{ml}$, $R_{sa} = 125\,\text{kPa}\bullet\text{ms}\bullet\text{ml}^{-1}$, $R_{pa} = 75\,\text{kPa}\bullet\text{ms}\bullet\text{ml}^{-1}$, $R_{sv} = R_{pv} = 2\,\text{kPa}\bullet\text{ms}\bullet\text{ml}^{-1}$, $R_{av} = 3.2\,\text{kPa}\bullet\text{ms}\bullet\text{ml}^{-1}$, $R_{mv} = 0.9\,\text{kPa}\bullet\text{ms}\bullet\text{ml}^{-1}$, $R_{tv} = 0.4\,\text{kPa}\bullet\text{ms}\bullet\text{ml}^{-1}$, $R_{pvv} = 2\,\text{kPa}\bullet\text{ms}\bullet\text{ml}^{-1}$, $V_{sv,0} = 3570\,\text{ml}$, $V_{pv,0} = 485\,\text{ml}$
Time varying elastance model of LA and RA	$E_{es} = 60\,\text{Pa/ml}$, $V_0 = 10\,\text{ml}$, $t_{max} = 135\,\text{ms}$, $\tau = 50\,\text{ms}$, $A = 58.67\,\text{Pa}$, $B = 0.049\,\text{ml}^{-1}$
Aorta FE model	
Elastin	$c_{AO,1} = 120\,\text{kPa}$, $\phi_{AO,e} = 0.35$
Collagen families	$c_{AO,2} = 0.2\,\text{kPa}$, $c_{AO,3} = 8.0$, $\phi_{AO,c} = 0.20$ ($\phi_{AO,1} = 0.1\phi_{AO,c}$, $\phi_{AO,2} = 0.1\phi_{AO,c}$, $\phi_{AO,3} = 0.4\phi_{AO,c}$, $\phi_{AO,4} = 0.4\phi_{AO,c}$)
SMC	$c_{AO,4} = 0.08\,\text{kPa}$, $c_{AO,5} = 3.5$, $\phi_{AO,m} = 0.45$
Pulmonary artery FE model	
Elastin	$c_{PA,1} = 45\,\text{kPa}$, $\phi_{PA,e} = 0.35$
Collagen families	$c_{PA,2} = 100.0\,\text{kPa}$, $c_{PA,3} = 3.0$, $\phi_{PA,c} = 0.42$ ($\phi_{PA,1} = 0.1\phi_{PA,c}$, $\phi_{PA,2} = 0.1\phi_{PA,c}$, $\phi_{PA,3} = 0.4\phi_{PA,c}$, $\phi_{PA,4} = 0.4\phi_{PA,c}$)
SMC	$c_{PA,4} = 5\,\text{kPa}$, $c_{PA,5} = 3.5$, $\phi_{PA,m} = 0.23$

Solution Algorithm

An explicit time integration scheme was used to solve the ODEs in Equation (1). Specifically, compartment volumes (V_{LV}, V_{sa}, V_{sv}, V_{RA}, V_{RV}, V_{pa}, V_{pv}, V_{LA}) at each time t_i were determined from their respective values and the segmental flow rates (q_{mv}, q_{av}, q_{sa}, q_{sv}, q_{tv}, q_{pvv}, q_{pa}, q_{pv}) at previous time t_{i-1} in Equation (2). The computed compartment volumes at t_i were used to update the corresponding pressures (P_{LA}, P_{RA}, P_{LV}, P_{RV}, P_{sa}, P_{pa}, P_{sv}, P_{pv}). Pressures in the atrium (P_{LA}, P_{RA}) and veins (P_{sv}, P_{pv}) were computed from Equations (4) and (3), respectively. On the other hand, pressures in the LV (P_{LV}), RV (P_{RV}), were computed from the FE solutions of Equation (10) for the biventricular unit with the volumes (V_{LV}, V_{RV}) at time t_i as input. Similarly, pressures in the aorta (P_{sa}) and pulmonary artery (P_{pa}) were computed from the FE solutions of Equation (20) with their corresponding volumes (V_{sa}, V_{pa}) at time t_i. We note here that (P_{LV}, P_{RV}, P_{sa}, P_{pa}) are scalar Lagrange multipliers in the FE formulation for constraining the cavity volumes to the prescribed values (V_{LV}, V_{RV}, V_{sa}, V_{pa}). The computed pressures at time t_i were then used to update the segmental flow rates in Equation (2) that will be used to compute the compartment volumes at time t_{i+1} in the next iteration.

Model Parameterization and Simulation

The biventricular FE model was divided into three material regions, namely the LV free wall (LVFW), the septum, and the RV free wall (RVFW). Similar to a previous study (Finsberg et al., 2018), passive stiffness C and contractility T_0 were prescribed to be the same values in the LVFW and septum (denoted as C_{LV} and $T_{0,LV}$) and had different values in the RVFW (denoted as C_{RV} and $T_{0,RV}$). In the baseline case, model parameters were adjusted to fit the clinically measured LV and RV PV loops, volume and pressure waveforms throughout the cardiac cycle. Specifically, the LV and RV end diastolic pressures were matched by adjusting the passive stiffness parameters C_{LV} and C_{RV}. Stroke volume (SV) of the LV and RV were matched by adjusting the regional contractility parameters (i.e., $T_{0,LV}$, $T_{0,RV}$). While other model parameters can also affect the SV (e.g., peripheral resistances R_{sa} *and* R_{pa} of the systemic and pulmonary circulations as well as preload), the parameters $T_{0,LV}$ and $T_{0,RV}$, which scale the active stress generated by the myofiber, have a larger effect on the LV and RV SV, respectively. On the other hand, the contraction model parameters t_r, t_d and b were adjusted to match the time course of the volume and pressure waveforms measured in the LV and RV. Parameters t_r and t_d were adjusted to match the time to peak tension and b was adjusted to achieve the desirable relaxation of the myofibers. Circulatory model parameters (resistances and compliances) were also adjusted to match the systolic pressure (afterload), preload and systemic and pulmonary vein pressures. Aortic and PA peripheral resistances (R_{sa}, R_{pa}) were calibrated to match the systolic pressures of LV and RV. The parameters related to LA and RA time-varying elastance models were prescribed based on a previous study (Shavik et al., 2019). Parameters related to the aorta and PA constitutive models (that alter the vessel's compliance) were adjusted to match the measured pressure waveforms, and the diameters estimated from the PC-MRI. All the model parameters for the biventricular, aorta and PA FE models are listed in **Table 2**.

The multiscale modeling framework was implemented using FEniCS (Alnæs et al., 2015). The biventricular unit was meshed with ∼7,700 tetrahedral elements based on a previous study (Finsberg et al., 2018) showing that local fiber stress and global features related to cardiac contraction are not sensitive to mesh resolution beyond ∼4,000 elements. Furthermore, the aorta and pulmonary arteries FE models contain ∼8,000 triangular elements based on previous study (Zeinali-Davarani et al., 2011) that used ∼1,500 elements. Steady state PV loop was established by running the simulation over several cardiac cycles until cycle-to-cycle periodicity was achieved. The prescribed cardiac cycle time (690 ms) was derived from the heart rate (87 bpm) measured during the PC-MRI acquisition.

Since it is known that key features of the progression of PAH include stiffening of main PA, reduced RV contraction, and increased distal resistance of PA (Fan et al., 1997; Shimoda and Laurie, 2013), we used our calibrated model to investigate how these changes affect the cardiopulmonary circulation. Specifically, a sensitivity analysis on the parameters associated with PAH progression was performed by simulating the following cases: (1) a 67% increase in PA collagen mass fraction $\phi_{PA,c}$, (2) a 50% decrease in RV contractility $T_{0,RV}$, and (3) a 50% increase in the pulmonary arterial resistance R_{pa}.

RESULTS

Comparison Between Simulated Results and Clinical Measurements

Model predictions of the LV and RV PV loops, volume waveforms, and pressure waveforms in the baseline case matched reasonably well with the clinically measured PAH patient data described in Section Data Acquisition (**Figure 3**). Good overall fitting was obtained for the volume and pressure in both the LV and RV with the coefficients of determination R^2 value of 0.901 and 0.903, respectively (**Figure 4**). Pressure waveforms in the pulmonary and systemic circulations predicted by the model also agree, in general, reasonably well with the measurements, except for the diastolic pressure. The model predicted smaller diastolic pressure in the aorta (by ∼17 mmHg) and PA (by ∼15 mmHg) when compared to the measurements (**Figure 3B**). The simulated ascending AO and PA diameter waveforms compared well with the clinical measurements of the dynamic cross-sectional area from the PC-MRI (**Figure 3C**). Specifically, the simulated and clinically measured diameter waveforms in the ascending AO are in good agreement (max. abs difference ∼10%) while the model predicted a larger change of the diameter compared to the measurements for the MPA (max. abs difference ∼28%).

Effects of the Changes in Vascular Microstructure on Cardiac Function

Changing the mass fractions of the constituents in the PA wall led to changes in its function, which in turn affects the RV function. Specifically, increasing the mass fraction $\phi_{PA,c}$ of the collagen of PA wall by 67% (from 0.42 to 0.70) with a corresponding decrease in the mass fraction of the elastin (from 0.35 to 0.15) and SMC (from 0.23 to 0.15) produced an increase in the PA pressure of 10% (from 71 to 78 mmHg). The RV systolic pressure also increased by 11% (from 68 to 76 mmHg) correspondingly (**Figure 5A**). Because of the more exponential mechanical response of the PA with higher collagen fraction, the PA pressure also decayed more rapidly during the diastolic phase resulting in an increased pulse pressure (from 45 mmHg baseline to 55 mmHg) (**Figure 5C**). The LV and RV SV and EF remained relatively unchanged (**Figures 5A,B**). In the aorta, systolic, diastolic, and pulse pressures did not change significantly from the baseline case (**Figure 5D**). The change in PA diameter was slightly reduced when compared to baseline (**Figure 5F**) as the vessel becomes stiffer with higher collagen mass fraction. Spatially averaged RV fiber stress did not change when compared to the baseline case. Maximum arterial wall stress located at the bifurcation increased (∼7.4%) but the spatially averaged wall stress did not change significantly from baseline (**Figure 6**).

Effects of the Change in RV Contractility on Vasculature

Decreasing the RV contractility $T_{0,RV}$ by 50% (from 1,800 kPa baseline to 900 kPa) reduced the RV EF by 5% (from 58 to 53%) (**Figure 5A**). Due to less contractile force being generated by the RV, both RV and PA peak systolic pressure decreased by about 9% (RV: 71 to 65 mmHg; PA: 68 to 62 mmHg) (**Figure 5C**). In addition, the LV EF as well as peak systolic pressure in both the LV and aorta were slightly decreased compared to the baseline (**Figures 5B,D,E**). Because of the reduced pressure, PA diameter was slightly reduced during systole when compared to baseline (**Figure 5F**). Average RV fiber stress also decreased by 37% (from 195 to 124 kPa) compared to baseline. Both maximum arterial and spatially averaged RV wall stress were reduced by about 9% (**Figure 6**).

Effects of the Change in PA Resistance

Increasing the pulmonary arterial resistance R_{pa} by 50% led to an increase in PA pulse pressure by 36% (from 45 to 61 mmHg), which was also accompanied by an increase in PA systolic and diastolic pressure (**Figure 5C**). The RV peak systolic pressure increased by 34% (from 71 to 95 mmHg) and the RV EF decreased by 2% (from 58 to 56%) (**Figure 5A**). Due to the higher pressure, the PA diameter waveform shifted upwards and became higher than the baseline throughout the cardiac cycle. Similar to the case with reduced RV contractility, LV EF as well as peak systolic pressure in both the LV and aorta were slightly decreased compared to the baseline (**Figures 5B,D,E**). A 7% (195 to 208 kPa) increase in average RV fiber stress as well as a 41% increase in maximum arterial wall stress were also found in the PA (**Figure 6**).

DISCUSSION

In order to characterize the intricate progression of PAH, we developed the first closed-loop multiscale modeling framework (consisting of image-based FE models of the left and right ventricles, large pulmonary arteries, and aorta) that captures detailed bi-directional ventricular-arterial interactions. We have shown that our proposed model describes the cardiopulmonary circulation reasonably well by reproducing patient-specific measurements of (1) LV and RV PV loops, (2) LV and RV volume and pressure waveforms, and (3) aorta and PA pressure and diameter waveforms of a PAH patient.

This framework extends our previously developed hybrid lumped-FE model of the systemic circulation (Shavik et al., 2018) by including the RV, large pulmonary arteries and the pulmonary micro-circulation (represented with a lumped model). Previous modeling frameworks have coupled a FE biventricular model with a lumped representation of the pulmonary circulation (Kerckhoffs et al., 2007; Xi et al., 2016) but not with FE model of the large pulmonary arteries. The ability to couple a FE model of the large arteries and both ventricles in this framework enables us

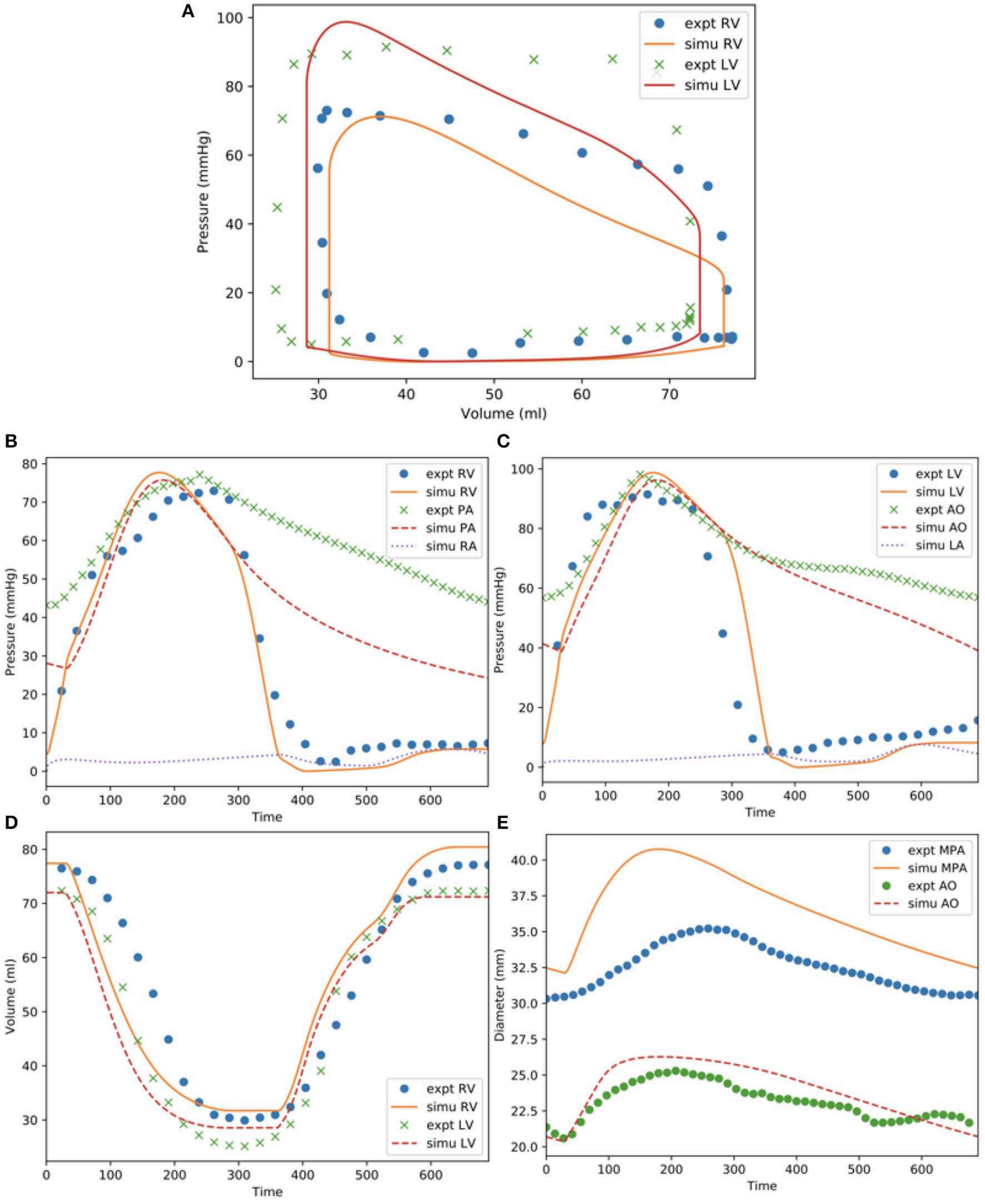

FIGURE 3 | Measurements and model predictions for the baseline case. **(A)** LV and RV PV loops; **(B)** pressure waveforms of pulmonary circulation; **(C)** pressure waveforms of systemic circulations; **(D)** LV and RV volume waveforms; **(E)** MPA and AO diameter waveforms.

to investigate PAH progression reflected in the large pulmonary arteries and the RV. Specifically, the framework allows us to alter the microstructural, geometrical and mechanical behaviors of the pulmonary arteries and characterize how these changes affect the RV, and vice versa. Implementing 3D FE models of the arteries in the framework also allow us to capture non-homogeneous stress distribution in the vessels (e.g., high stress concentration at the bifurcation of the pulmonary artery in **Figure 6**) which would not be possible using lumped-parameter models. Using the calibrated framework, we have created three cases to simulate progressive pathological changes associated with PAH in the (1) large pulmonary arteries (increase in collagen mass and degradation of elastin) (Wang et al., 2013), (2) RV (decrease in contractility due to right ventricular failure) (Naeije

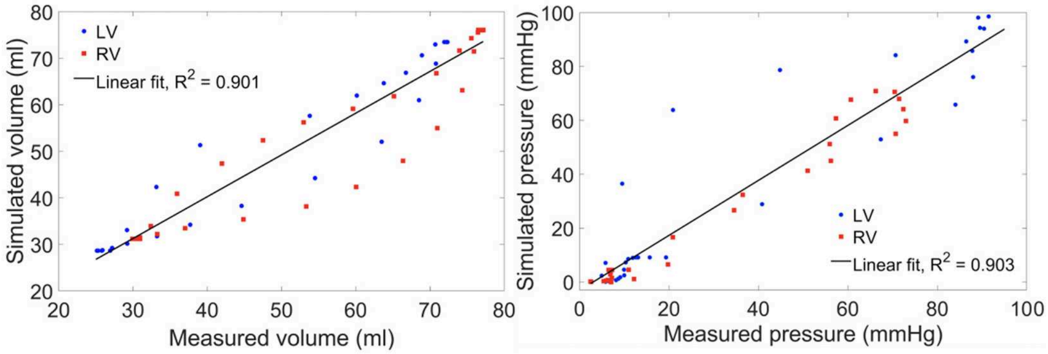

FIGURE 4 | Scatter plot of the simulated vs. measured volume **(left)** and pressure **(right)** at all cardiac time points of the baseline case with a linear fit showing the zero-error reference.

and Manes, 2014), and (3) pulmonary microcirculation (increase in resistance due to remodeling) (Kobs et al., 2005).

Increasing the collagen mass in the elastic proximal pulmonary arteries increased PA pulse pressure from baseline. This behavior is due to the stiffening of the PA, which results from a more exponential stress-strain behavior associated with the higher concentration of collagen fibers. This result is consistent with animal experiments where an increase in PA pulse pressure has been associated with an increase in collagen mass in PAH (Wang et al., 2017). Furthermore, the connection between pulse pressure and changes in collagen can also be found in the aorta during aging, where a loss of elastin (which results in a more collagen-dominated extracellular matrix) produces an increase in systemic pulse pressure (Safar et al., 2003). A decrease in PA compliance that is caused by an increase in collagen mass produced an increase in RV afterload as reflected by an increase in RV systolic pressure in our model, consistent with previous studies (Mahapatra et al., 2006; Gan et al., 2007). Consistent with our previous study (Shavik et al., 2018), the more pulsatile PA waveform can also be observed in the ejection phase of the RV PV loop, where the pressure-volume curve became steeper toward end-of-systole (**Figure 5A**). Our model did not predict a significant reduction in the SV, which could be attributed to a high RV end-systolic elastance in the model. We note that a high RV end-systolic elastance has also been associated with PAH (Vélez-Rendón et al., 2018), especially during the compensatory phase.

Decreasing RV contractility (by 50%) in the model, which reflects the transition to decompensated heart failure, produced an expected decrease in EF and peak systolic pressure that results in a substantial decrease in myofiber stress in the RV. Reducing the RV contractility also reduces the PA peak and pulse pressures, only decreasing the arterial wall stress in the PA slightly. Based on consensus that arterial wall stress is the driver for vascular remodeling (Humphrey, 2008), this result suggests that remodeling in the large pulmonary arteries may attenuate the transition to the decompensated phase. This result also suggests that negative inotropic agent targeted at the RV may help attenuate remodeling in the PA vasculature.

Lastly, increasing the distal pulmonary arterial resistance, which reflects remodeling of the distal vessels, increased pressures in the proximal PA and RV. A 50% increase in the distal pulmonary arterial resistance (equivalent to a ∼10% reduction of the vascular lumen diameter based on Poiseuille's law) causes ejection to start at a higher pressure and the EF to be slightly reduced in the RV. These results are broadly consistent with the effects on the RV measured in patients under acute hypoxia (Akgül et al., 2007), which shows an increase in both end-systolic and end-diastolic volume and a slight (but not significant) decrease in EF. The same increase in resistance also produced a significantly higher increase in the systolic PA pressure than the simulation with a 67% increase in collagen mass in the proximal pulmonary arteries. These results suggest that remodeling in the microcirculation contributes more to changes in the pulmonary pressure than remodeling in the proximal pulmonary arteries, suggesting that PAH is primarily driven by distal arterial remodeling. In summary, we have shown that isolated changes in both the arteries and ventricles as predicted by our modeling framework lead to expected effects in the cardiopulmonary circulation. This confirms that the modeling framework can capture bi-directional ventricular-arterial interactions, which can be used to further our understanding of PAH progression.

MODEL LIMITATIONS

Though our modeling framework is able to predict behaviors that are consistent with the measurements there are, however, some limitations associated with it. First, the local myofiber orientation was varied transmurally from 60° in the endocardium to −60° at the epicardium using a "rule based" method. Thus, we did not take into account any changes in myofiber orientation during RV remodeling (Hill et al., 2014) that may occur in PAH. Second, we have assumed a uniform wall thickness and homogeneous material properties for both aorta and PA in our model. We believe that this assumption contributes to the mismatch in the MPA diameter waveforms. Third, we have assumed that FE models of the pulmonary arteries and aorta account for the compliance of the entire pulmonary and systemic arterial system, respectively. This is a limitation because the FE models are associated with only a segment of their corresponding arterial systems. We show in a preliminary study (see **Appendix**) that the addition of a lumped-parameter compliance to the modeling framework can be used to provide a better match

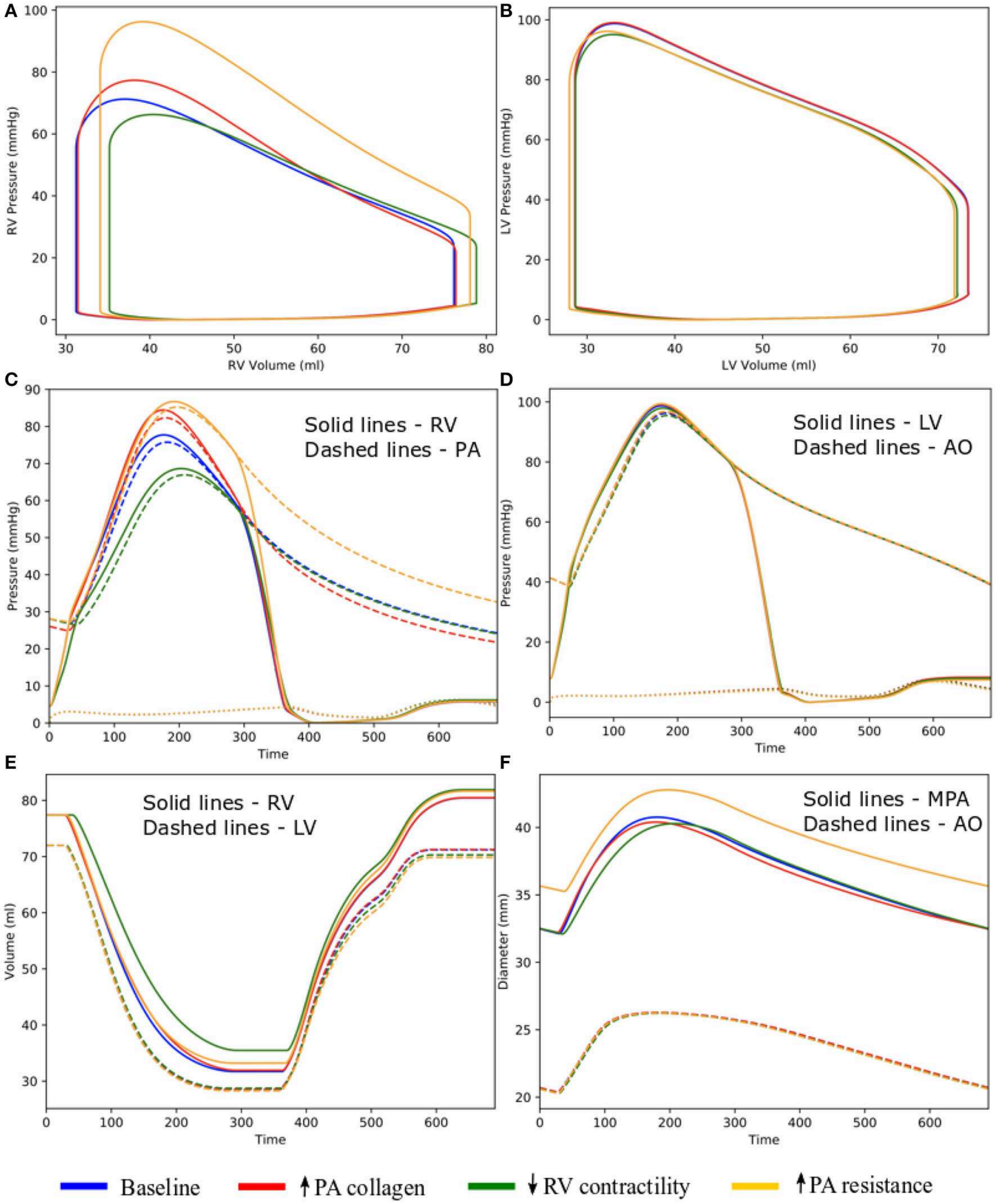

FIGURE 5 | Hemodynamic comparison between the different simulations. **(A)** RV and **(B)** LV PV loops; **(C)** Pulmonary and **(D)** systemic circulation pressure waveforms; **(E)** LV and RV volume waveforms; and **(F)** MPA and AO diameter waveforms.

of pulmonary artery pressure and diameter waveforms, as well as the pressure-volume loops. Fourth, we have neglected the dynamic behavior of the fluid and its interaction with the vessel walls and the spatial variation of pressure waveform along the aortic and pulmonary tree and shear stress on the luminal surface of the vessels. We note, however, that the computed shear stress (∼Pa) is several order of magnitude smaller than the normal traction force (pressure) on the surface of the vessel (∼kPa) and variation of peak pressure within the vessel is <10%. For these reasons, the omission of shear traction should not affect the computed arterial stresses. Last, the modeling framework was calibrated using data acquired from one PAH patient. Caution must be exercised in extrapolating results to the general population of pediatric PAH patients.

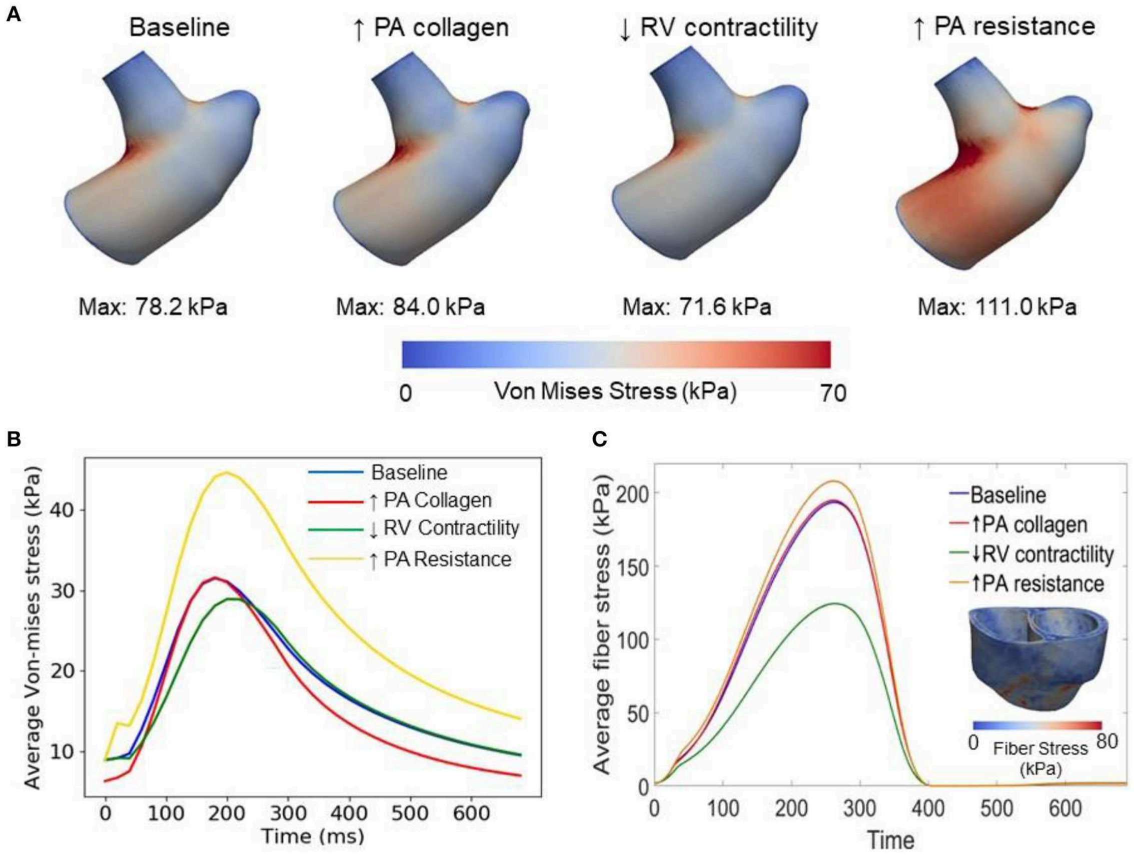

FIGURE 6 | Comparison of wall stresses in the different simulations. **(A)** Von-mises stress map of the pulmonary artery FE model. **(B)** Average von-mises wall stress waveforms in the pulmonary artery FE model. **(C)** Average fiber stress waveforms in the biventricular FE model and fiber stress map of baseline model.

DATA AVAILABILITY STATEMENT

The datasets generated for this study are available on request to the corresponding author.

ETHICS STATEMENT

This study was approved by the University of Michigan Board of Review (HUM00117706). Written informed consent to participate in this study was provided by the participants' legal guardian/next of kin.

AUTHOR CONTRIBUTIONS

SS, SB, and LL developed the theoretical formulation and computational framework of the model. SS and CT-B carried out the simulations for different cases and prepared the results. CT-B and CF acquired the clinical data. LL, SB, and CF planned and supervised the work. All authors helped in interpretation of the results and contributed to the final manuscript.

FUNDING

This work was supported by American Heart Association (AHA) 17SDG33370110, NIH R01HL134841, and NIH U01HL135842 grants.

SUPPLEMENTARY MATERIAL

The Supplementary Material for this article can be found online at: https://www.frontiersin.org/articles/10.3389/fphys.2020.00002/full#supplementary-material

REFERENCES

Akgül, F., Batyraliev, T., Karben, Z., and Pershukov, I. (2007). Effects of acute hypoxia on left and right ventricular contractility in chronic obstructive pulmonary disease. *Int. J. Chron. Obstruct. Pulmon. Dis.* 2:77. doi: 10.2147/copd.2007.2.1.77

Alnæs, M., Blechta, J., Hake, J., Johansson, A., Kehlet, B., Logg, A., et al. (2015). The FEniCS project version 1.5. *Arch. Numer. Softw.* 3, 9–23. doi: 10.11588/ans.2015.100.20553

Baek, S., Valentín, A., and Humphrey, J. D. (2007). Biochemomechanics of cerebral vasospasm and its resolution: II. Constitutive relations and model simulations. *Ann. Biomed. Eng.* 35, 1498–1509. doi: 10.1007/s10439-007-9322-x

Borlaug, B. A., and Kass, D. A. (2011). Ventricular-vascular interaction in heart failure. *Cardiol. Clin.* 29, 447–459. doi: 10.1016/j.ccl.2011.06.004

Fan, D., Wannenburg, T., and De Tombe, P. P. (1997). Decreased myocyte tension development and calcium responsiveness in rat right ventricular pressure overload. *Circulation* 95, 2312–2317. doi: 10.1161/01.CIR.95.9.2312

Finsberg, H., Xi, C., Tan, J. L., Zhong, L., Genet, M., Sundnes, J., et al. (2018). Efficient estimation of personalized biventricular mechanical function employing gradient-based optimization. *Int. J. Numer. Method. Biomed. Eng.* 34:e2982. doi: 10.1002/cnm.2982

Gan, C. T. J., Lankhaar, J. W., Westerhof, N., Marcus, J. T., Becker, A., Twisk, J. W. R., et al. (2007). Noninvasively assessed pulmonary artery stiffness predicts mortality in pulmonary arterial hypertension. *Chest*. 132, 1906–1912. doi: 10.1378/chest.07-1246

Geuzaine, C., and Remacle, J. F. (2009). Gmsh: A 3-D finite element mesh generator with built-in pre- and post-processing facilities. *Int. J. Numer. Methods Eng.* 79, 1309–1331. doi: 10.1002/nme.2579

Guccione, J. M., McCulloch, A. D., and Waldman, L. K. (1991). Passive material properties of intact ventricular myocardium determined from a cylindrical model. *J. Biomech. Eng.* 113, 42–55. doi: 10.1115/1.2894084

Hill, M. R., Simon, M. A., Valdez-Jasso, D., Zhang, W., Champion, H. C., and Sacks, M. S. (2014). Structural and mechanical adaptations of right ventricle free wall myocardium to pressure overload. *Ann. Biomed. Eng.* 42, 2451–2465. doi: 10.1007/s10439-014-1096-3

Hoit, B. D., Shao, Y., Gabel, M., and Walsh, R. A. (1994). *In vivo* assessment of left atrial contractile performance in normal and pathological conditions using a time-varying elastance model. *Circulation*. 89, 1829–1838. doi: 10.1161/01.CIR.89.4.1829

Humphrey, J. D. (2008). Mechanisms of arterial remodeling in hypertension coupled roles of wall shear and intramural stress. *Hypertension*. 52, 195–200. doi: 10.1161/HYPERTENSIONAHA.107.103440

Kerckhoffs, R. C. P., Bovendeerd, P. H. M., Kotte, J. C. S., Prinzen, F. W., Smits, K., and Arts, T. (2003). Homogeneity of cardiac contraction despite physiological asynchrony of depolarization: a model study. *Ann. Biomed. Eng.* 31, 536–547. doi: 10.1114/1.1566447

Kerckhoffs, R. C. P., Neal, M. L., Gu, Q., Bassingthwaighte, J. B., Omens, J. H., and McCulloch, A. D. (2007). Coupling of a 3D finite element model of cardiac ventricular mechanics to lumped systems models of the systemic and pulmonic circulation. *Ann. Biomed. Eng.* 35, 1–18. doi: 10.1007/s10439-006-9212-7

Kobs, R. W., Muvarak, N. E., Eickhoff, J. C., and Chesler, N. C. (2005). Linked mechanical and biological aspects of remodeling in mouse pulmonary arteries with hypoxia-induced hypertension. *Am. J. Physiol. Heart Circ. Physiol.* 288, 1209–1217. doi: 10.1152/ajpheart.01129.2003

Ky, B., French, B., May Khan, A., Plappert, T., Wang, A., Chirinos, J. A., et al. (2013). Ventricular-arterial coupling, remodeling, and prognosis in chronic heart failure. *J. Am. Coll. Cardiol.* 62, 1165–1172. doi: 10.1016/j.jacc.2013.03.085

Lau, K. D., and Figueroa, C. A. (2015). Simulation of short-term pressure regulation during the tilt test in a coupled 3D−0D closed-loop model of the circulation. *Biomech. Model. Mechanobiol.* 14, 915–929. doi: 10.1007/s10237-014-0645-x

Mahapatra, S., Nishimura, R. A., Sorajja, P., Cha, S., and McGoon, M. D. (2006). Relationship of pulmonary arterial capacitance and mortality in idiopathic pulmonary arterial hypertension. *J. Am. Coll. Cardiol.* 48, 850–851. doi: 10.1016/j.jacc.2005.09.054

Naeije, R., and Manes, A. (2014). The right ventricle in pulmonary arterial hypertension. *Eur. Respir. Rev.* 23, 476–487. doi: 10.1183/09059180.00007414

Pezzuto, S., and Ambrosi, D. (2014). Active contraction of the cardiac ventricle and distortion of the microstructural architecture. *Int. J. Numer. Method. Biomed. Eng.* 30, 1578–1596. doi: 10.1002/cnm.2690

Pezzuto, S., Ambrosi, D., and Quarteroni, A. (2014). An orthotropic active-strain model for the myocardium mechanics and its numerical approximation. *Eur. J. Mech. A/Solids*. 48, 83–96. doi: 10.1016/j.euromechsol.2014.03.006

Punnoose, L., Burkhoff, D., Rich, S., and Horn, E. M. (2012). Right ventricular assist device in end-stage pulmonary arterial hypertension: insights from a computational model of the cardiovascular system. *Prog. Cardiovasc. Dis.* 55, 234–243.e2. doi: 10.1016/j.pcad.2012.07.008

Safar, M. E., Levy, B. I., and Struijker-Boudier, H. (2003). Current perspectives on arterial stiffness and pulse pressure in hypertension and cardiovascular diseases. *Circulation*. 107, 2864–2869. doi: 10.1161/01.CIR.0000069826.36125.B4

Shavik, S. M., Jiang, Z., Baek, S., and Lee, L. C. (2018). High spatial resolution multi-organ finite element modeling of ventricular-arterial coupling. *Front. Physiol*. 9:119. doi: 10.3389/fphys.2018.00119

Shavik, S. M., Wall, S. T., Sundnes, J., Burkhoff, D., and Lee, L. C. (2017). Organ-level validation of a cross-bridge cycling descriptor in a left ventricular finite element model: effects of ventricular loading on myocardial strains. *Physiol. Rep*. 5:e13392. doi: 10.14814/phy2.13392

Shavik, S. M., Zhong, L., Zhao, X., and Lee, L. C. (2019). *In-silico* assessment of the effects of right ventricular assist device on pulmonary arterial hypertension using an image based biventricular modeling framework. *Mech. Res. Commun.* 97, 101–111. doi: 10.1016/j.mechrescom.2019.04.008

Shimoda, L. A., and Laurie, S. S. (2013). Vascular remodeling in pulmonary hypertension. *J. Mol. Med.* 91, 297–309. doi: 10.1007/s00109-013-0998-0

Simonneau, G., Montani, D., Celermajer, D. S., Denton, C. P., Gatzoulis, M. A., Krowka, M., et al. (2019). Haemodynamic definitions and updated clinical classification of pulmonary hypertension. *Eur. Respir. J*. 53:1801913. doi: 10.1183/13993003.01913-2018

Smith, B. W., Chase, J. G., Nokes, R. I., Shaw, G. M., and Wake, G. (2004). Minimal haemodynamic system model including ventricular interaction and valve dynamics. *Med. Eng. Phys*. 26, 131–139. doi: 10.1016/j.medengphy.2003.10.001

Ursino, M. (1998). Interaction between carotid baroregulation and the pulsating heart: a mathematical model. *Am. J. Physiol*. 275(5 Pt 2), H1733–H1747. doi: 10.1152/ajpheart.1998.275.5.H1733

Vélez-Rendón, D., Zhang, X., Gerringer, J., and Valdez-Jasso, D. (2018). Compensated right ventricular function of the onset of pulmonary hypertension in a rat model depends on chamber remodeling and contractile augmentation. *Pulm. Circ.* 8:2045894018800439. doi: 10.1177/2045894018800439

Wang, Z., Lakes, R. S., Eickhoff, J. C., and Chesler, N. C. (2013). Effects of collagen deposition on passive and active mechanical properties of large pulmonary arteries in hypoxic pulmonary hypertension. *Biomech. Model. Mechanobiol*. 12, 1115–1125. doi: 10.1007/s10237-012-0467-7

Wang, Z., Schreier, D. A., Abid, H., Hacker, T. A., and Chesler, N. C. (2017). Pulmonary vascular collagen content, not cross-linking, contributes to right ventricular pulsatile afterload and overload in early pulmonary hypertension. *J. Appl. Physiol.* 122, 253–263. doi: 10.1152/japplphysiol.00325.2016

Xi, C., Latnie, C., Zhao, X., Tan, J. L., Wall, S. T., Genet, M., et al. (2016). Patient-specific computational analysis of ventricular mechanics in pulmonary arterial hypertension. *J. Biomech. Eng*. 138:111001. doi: 10.1115/1.4034559

Zambrano, B. A., McLean, N. A., Zhao, X., Tan, J.-L., Zhong, L., Figueroa, C. A., et al. (2018). Image-based computational assessment of vascular wall mechanics and hemodynamics in pulmonary arterial hypertension patients. *J. Biomech*. 68, 84–92. doi: 10.1016/j.jbiomech.2017.12.022

Zeinali-Davarani, S., Sheidaei, A., and Baek, S. (2011). A finite element model of stress-mediated vascular adaptation: application to abdominal aortic aneurysms. *Comput. Methods Biomech. Biomed. Eng*. 14, 803–817. doi: 10.1080/10255842.2010.495344

Conflict of Interest: The authors declare that the research was conducted in the absence of any commercial or financial relationships that could be construed as a potential conflict of interest.

frontiers in Physiology

ORIGINAL RESEARCH
published: 21 February 2020
doi: 10.3389/fphys.2020.00133

Numerical Simulation of the Influence of Geometric Configurations on Pressure Difference in the Intraventricular Tunnel

Yao Yang[1†], *Junjie Wang*[2†], *Aike Qiao*[2] *and Xiangming Fan*[1*]

[1] Beijing Anzhen Hospital, Capital Medical University, Beijing, China, [2] College of Life Sciences and Bioengineering, Beijing University of Technology, Beijing, China

OPEN ACCESS

Edited by:
Yunlong Huo,
Shanghai Jiao Tong University, China

Reviewed by:
Junmei Zhang,
National Heart Centre Singapore,
Singapore
Niu Pei,
Hebei University, China

Correspondence:
Xiangming Fan
fanxiangming@126.com

† These authors share first authorship

Specialty section:
This article was submitted to
Computational Physiology
and Medicine,
a section of the journal
Frontiers in Physiology

Received: *21 October 2019*
Accepted: *07 February 2020*
Published: *21 February 2020*

Citation:
Yang Y, Wang J, Qiao A and Fan X
(2020) Numerical Simulation of the
Influence of Geometric Configurations
on Pressure Difference
in the Intraventricular Tunnel.
Front. Physiol. 11:133.
doi: 10.3389/fphys.2020.00133

Objective: The geometric configuration of the intraventricular tunnel is related to the re-intervention of left ventricular outflow tract stenosis after double outlet right ventricle (DORV) correction. Hemodynamic simulation was performed in order to study the influence of the geometric configuration of the IVT on the pressure difference.

Methods: CT images of DORV were processed to reconstruct 3D models of left and right ventricular flow chambers and aortic valve orifice, and then the size and relative position of the aortic valve orifice and ventricular septal defect were determined. Twenty five groups of the idealized models were established according to orthogonal test design and computational fluid dynamics method was applied to simulate hemodynamics. Three factors of geometric configuration were considered for the study of their influences on the pressure difference. The first factor is the distance between the ventricular septal defect and the plane of the aortic valve (D_{SA}), the second factor is the ejection angle of blood from left ventricle flowing into the IVT (A_{LT}), and the third factor is the turning radius of the IVT (R_{TT}). SPSS software was employed to perform the orthogonal analysis. Additionally, twelve models with different turning radii were established for hemodynamic analysis, with the turning radii increasing from 0 mm with an interval of 1 mm, so as to study the influence of turning radius on pressure difference of IVT.

Results: The analysis of variance showed that only the change of R_{TT} had a significant effect on the pressure difference ($P = 0 < 0.05$), while the change of D_{SA} and A_{LT} had no significant effect on the pressure difference ($P = 0.459 > 0.05$, $P = 0.263 > 0.05$). The pressure difference decreases with the increase of R_{TT}. When R_{TT} reaches 6 mm, the pressure difference gradually remains unchanged with the increase of R_{TT}, and the rate of change is less than 5%.

Conclusion: R_{TT} in the IVT is the main factor affecting the pressure difference. A small R_{TT} will lead to a large pressure difference in the IVT. When R_{TT} increases to 6 mm, the pressure difference in the IVT remains nearly unchanged. When performing the right ventricular double outlet correction; the turning radius of the IVT should be about 6 mm to ensure relatively small pressure difference.

Keywords: double outlet right ventricle, intraventricular tunnel, hemodynamics, numerical simulation, surgical planning

INTRODUCTION

Double outlet right ventricle (DORV) has been a contentious topic in congenital heart pathology and surgery. In 2000, the International Association of Thoracic Surgeons and the European Association for Cardio-Thoracic Surgery adopted a new naming rule for DORV, namely the "50%" rule: one aorta and more than 50% of the other originate in the right ventricle and the only outlet of the left ventricle is the ventricular septal defect (VSD) (Lacour-Gayet et al., 2002). VSD is one of the most common cardiovascular malformation, referring to disrupt the integrity of tissue between left and right ventricle and result in existing abnormal channel between the ventricles.

Congenital (VSD), which accounts for about 12 to 20% of the congenital cardiovascular malformation, is caused by the development of fetal original ventricular septal dysplasia. It can exist as a single malformation or as part of other complex cardiac malformations, such as tetralogy of fallot, complete atrioventricular malformation, transposition of the great arteries, tricuspid atresia, and double outlet of the right ventricle. The location, size and shape of aortic valve orifice and VSD are the key to preoperative preparation (Villemain et al., 2016).

By combining cardiac CT angiography with 3D printing technology, scholars can accurately determine the pathological classification of DORV before surgery. Pathological heart model analysis and simulated surgery can significantly reduce the intraoperative exploration time of DORV with VSD far from the two main arteries (Lefort et al., 2001; Meduri et al., 2007; Garekar et al., 2016; Pang et al., 2017; Wang et al., 2017; Mostefa-Kara et al., 2018).

Double outlet right ventricle is primarily treated with a surgical treatment, which establishes intraventricular tunnel (IVT) connecting the VSD to the aortic valve orifice to restore normal cardiac function. The 10-year survival rate was 87% and the re-intervention rate was 24% (Lefort et al., 2001). The main post-operative diagnosis is echocardiography, and the pressure difference (ΔP) is the main criterion for evaluating IVT stenosis. Left ventricular outflow tract obstruction occurs when ΔP exceeds 10 mmHg (Ware and Matthay, 2000; Hashirnoto et al., 2004). The most significant re-intervention factors were related to IVT, such as post-operative residual fistula and left ventricular outflow tract obstructions (Marshall et al., 2000; Shoda et al., 2007). IVT stenosis is the most common complication and indication of reintervention (Iwai et al., 2007; Pang et al., 2015; Egbe et al., 2016; Cui et al., 2019).

However, the state-of-the-art studies mainly focus on the anatomical morphology and preoperative diagnosis of DORV, without pointing out the effect of IVT morphology on the left ventricular outflow tract or the suggestions on how to improve IVT morphology from the view point of biomechanics.

The main purpose of this study is to investigate the effect of geometric configuration of IVT on ΔP, and to provide reasonable suggestions and theoretical basis for surgeons to establish IVT.

MATERIALS AND METHODS

In order to simplify the calculation, all the models established in this study are idealized models. The size of the idealized model was established according to the 3D reconstruction model of the patient's ventricle. The diameter of VSD is not equal to the diameter of aortic valve orifice. During the operation, VSD will be cut to make the diameter of VSD equal to that of aortic valve orifice. Therefore, the diameter of the aortic valve in the ideal model established in this study is equal to that of the VSD. Orthogonal test design was used to arrange the experiment and the significance of the experimental results was analyzed. A single factor test was carried out for the factors that had significant influence on the results.

Model Reconstruction

Orthogonal experimental design is a method to study multiple factors and levels. According to the orthogonality, some representative points are selected from the overall test to carry out the test. These representative points have the characteristics of "uniform dispersion and uniform comparison." Orthogonal test design is the main method of fractional factorial design, which is an efficient, fast and economical test design method. Therefore, this paper adopts the orthogonal experiment design to arrange experiments, which can not only reduce the number of experiments but also obtain the specific influence factor *P* value of each factor on the results.

The orthogonal test method was used to arrange the experiment and analyze the results in SPSS. The main factors were the distance (D_{SA}), the ejection angle (A_{LT}) and the turning radius of the IVT (R_{TT}). D_{SA} was the distance between the VSD and the plane of the aortic valve, A_{LT} was the ejection angle of blood from left ventricle flowing into the IVT, and R_{TT} was the turning radius of the IVT (**Figure 1**). Each factor takes five values. Twenty five groups of the idealized models were established according to the orthogonal test design and computational fluid dynamics (CFD) method was applied to simulate hemodynamics (**Table 1**).

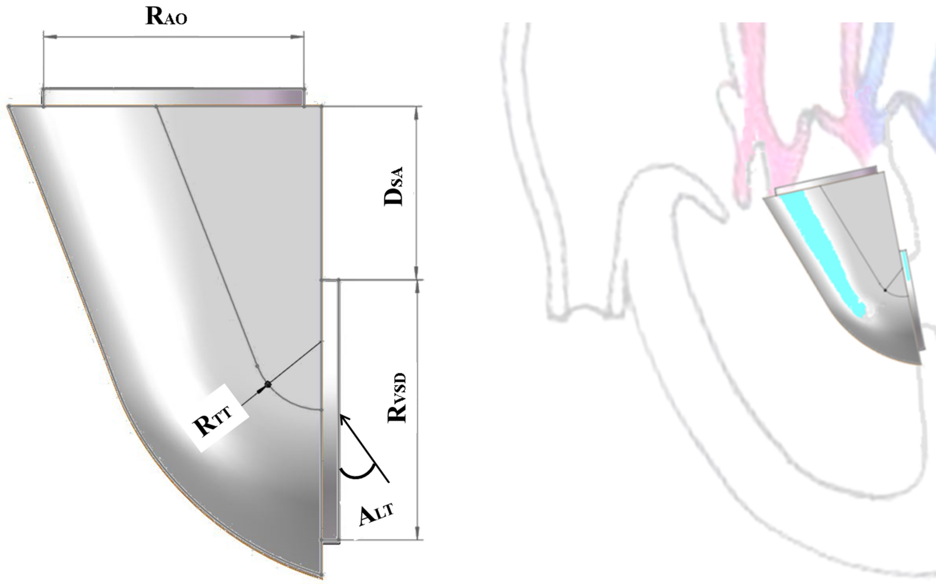

FIGURE 1 | (A) Idealized IVT geometry; **(B)**. IVT assembly diagram.

The small steps at the aortic valve and VSD conform to the physiological structure, and there is thickness of the ventricular septum and space below the aortic valve. Therefore, the models established in this paper retain the small steps, which not only simplify the mesh division, but also facilitate the application of boundary conditions.

TABLE 1 | Orthogonal test design table and results.

Model	D_{SA} (mm)	A_{LT} (°)	R_{TT} (mm)	△P (mmHg)
1	10	20	5	3.27
2	10	10	2.5	5.36
3	15	20	0	6.79
4	20	0	2.5	8.23
5	25	20	2.5	5.6
6	20	40	0	2.88
7	20	20	7.5	3.47
8	25	30	5	2.75
9	30	30	0	8.34
10	15	30	2.5	2.77
11	20	30	10	2.19
12	25	0	10	4.56
13	30	10	7.5	4.43
14	30	20	10	3.25
15	15	40	5	1.49
16	30	40	2.5	1.75
17	10	30	7.5	1.77
18	10	40	10	1.1
19	10	0	0	8.26
20	25	40	7.5	1.23
21	30	0	5	6.6
22	15	10	10	3.89
23	20	10	5	5.13
24	25	10	0	12.91
25	15	0	7.5	5.11

The results of orthogonal experiment were analyzed with the analysis of variance in SPSS. $P < 0.05$ was considered statistically significant. In this study, only the P value of R_{TT} was less than 0.05, so the influence of R_{TT} on ΔP was studied in detail. The R_{TT} was chosen to increase from 0 mm with an interval 1 mm, and 12 groups of models were established. The other sizes of the idealized IVT remained the same.

Mesh Generation

The idealized models were meshed using Ansys ICEM CFD (Ansys, Inc). Combination of tetrahedral and prism elements were used, with five layers of prism elements along the walls. After grid dependency analysis, the final mesh elements count of IVT was about 150000. CFD analyses of the idealized IVT were conducted using Ansys-CFX.

Finite Element Analysis

The meshed fluid model was imported into the pretreatment of the finite element analysis software ANSYS-Workbench to set the boundary conditions and blood parameters. The VSD was set as the blood flow inlet, and the aortic root was set as the pressure outlet.

Boundary conditions: Steady-state simulation of ventricular systolic conditions was carried out in this study to mimic the peak flow condition in a cardiac cycle. Although DORV is a congenital heart disease, there was a wide age gap among patients receiving surgical treatment, including infants and adults. Therefore, the selection of boundary conditions in this study was based on the physiological status of normal adults. So the boundary condition of the inlet is set as the flow velocity, 1 m/s, and the boundary condition of the outlet is set as the pressure, 110 mmHg.

Blood parameters: In all numerical simulations of the steady flow of aorta, blood was considered as Newtonian, homogeneous, and incompressible. The fluid satisfies no slip condition on the wall. The fluid viscosity was set to 0.0035 Pa·s and the density to 1050 kg/m^3 [17]. Since the maximum Reynolds number is about 4000, the turbulent models were applied for the hemodynamic simulation.

RESULTS

According to the variance analysis of the orthogonal experiment results, the influence of the value of each factor on the ΔP could be found: only the change of curvature of the center line has a significant effect on convection resistance ($P = 0 < 0.05$) (**Table 2**). The distance and the angle have no significant influence on ΔP ($P = 0.459 > 0.05$, $P = 0.263 > 0.05$). Through multiple comparisons of R_{TT}, it was found that the increase of R_{TT} would have a significant impact on the results when R_{TT} was small. However, the change of R_{TT} had no significant effect on the result when R_{TT} was larger. For example, it was significantly different from other values when $R_{TT} = 0$ mm. However, there was no significant difference with $R_{TT} = 5$ mm and $R_{TT} = 10$ mm when $R_{TT} = 7.5$ mm (**Table 3**).

Analysis of the orthogonal test results showed that R_{TT} changes had a significant impact on ΔP, so R_{TT} was further studied and ΔP—R_{TT} and ΔP rate of change - relation chart were drawn in **Figure 2**. The results showed that the ΔP decreases with the decrease of curvature. When the curvature diameter reached 12 mm, the ΔP gradually remained stable with the increase of diameter, and the change rate of ΔP decreased to less than 5%. The IVT internal velocity and wall pressure also decreased with the increase of R_{TT} (**Figure 3**).

TABLE 2 | Anova analysis of orthogonal test.

	Type III sums of squares	The square of average	*F*	Statistical significance (*P*)
D_{SA}	0.004	0.001	1.374	0.459
A_{LT}	0.002	0.001	0.63	0.263
R_{TT}	64.981	16.245	20477.055	0.000

TABLE 3 | Multiple comparison single factor.

R_{TT} (mm)		Statistical significance *(P)*	R_{TT} (mm)		Statistical significance (*P*)
0	2.5	0.004	7.5	0	0
	5	0.001		2.5	0.107
	7.5	0		5	0.379
	10	0		10	0.822
2.5	0	0.004	10	0	0
	5	0.332		2.5	0.072
	7.5	0.107		5	0.356
	10	0.072		7.5	0.822
5	0	0.001			
	2.5	0.032			
	7.5	0.379			
	10	0.356			

DISCUSSION

Some studies have demonstrated the effect of IVT morphology on the surgical outcome, however no study to our knowledge has ever included hemodynamic analysis of IVT morphology to investigate the effect of IVT morphology on the ΔP.

The main reason why we adopted the CFD analysis was that computational modeling enabled a quantitative analysis of fluid-dynamic parameters, such as velocity streamlines and pressure, which were impossible to measure non-invasively in clinics with sufficient accuracy. In fact, although transthoracic (TTE) and transoesophageal echocardiography (TEE) are available in the clinic to measure the blood flow velocity in IVT, both techniques can only provide average information on the velocity magnitude and direction in the sampling volume, without being able to give detailed spatial 3D information on the local flow conditions (Fukuda et al., 2003; Dentamaro et al., 2017). Therefore, it is impossible to accurately evaluate the hemodynamics of IVT morphology. Because the inlet velocity and the VSD diameter is constant, the flow rate at the inlet of each model is constant. According to Poiseuille's law, the mean pressure difference (ΔP) is proportional to the flow resistance when the flow rate is constant. Therefore, the ΔP between the aortic valve and the VSD was used as the evaluation criterion of flow resistance. So the CFD analysis was used to study the influence of IVT morphology on the ΔP.

According to the CFD analysis results of the idealized IVT models, it could be observed that the maximum pressure was concentrated on the IVT wall near the inlet. The high pressure on the IVT was caused by the impact of blood flow on the wall. Under the same model, the position of high pressure area was mainly affected by A_{LT}: with the increase of A_{LT}, the high pressure area was shifted upward.

According to the conservation of mechanical energy, the increased kinetic energy of fluid is mainly due to the decrease of potential energy. So the increase of the flow rate led to the increase of ΔP. So the increase of velocity in IVT leaded to a sharp increase of ΔP. By comparing CFD results of different R_{TT} models, the increase of R_{TT} could effectively reduce the flow velocity within IVT, and the ΔP also decreased. Anova of orthogonal test results also proved that the change of R_{TT} had a significant impact on the ΔP ($P < 0.05$). Therefore, we could ensure the left ventricular outflow tract unimpeded by changing R_{TT} to make the IVT flow velocity less than 1.2 m/s or ΔP less than 10 mmHg.

As R_{TT} increased, ΔP gradually decreases. When R_{TT} was equal to 6 mm as R_{TT} increased, ΔP largely remained unchanged. An increase in R_{TT} would result in an increase in IVT volume. Since the IVT was established in the right ventricle, the IVT encroached on the volume of the right ventricle. Excessive IVT volume could lead to increased right ventricular pressure,

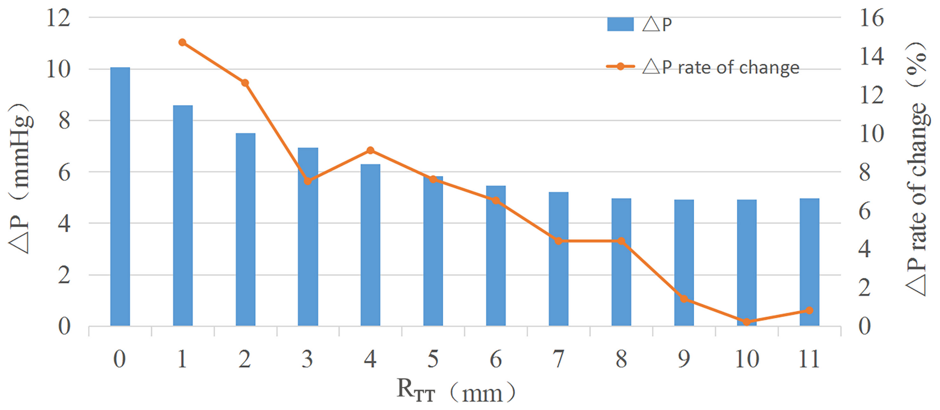

FIGURE 2 | ΔP-R_{TT} and ΔP rate of change-R_{TT}.

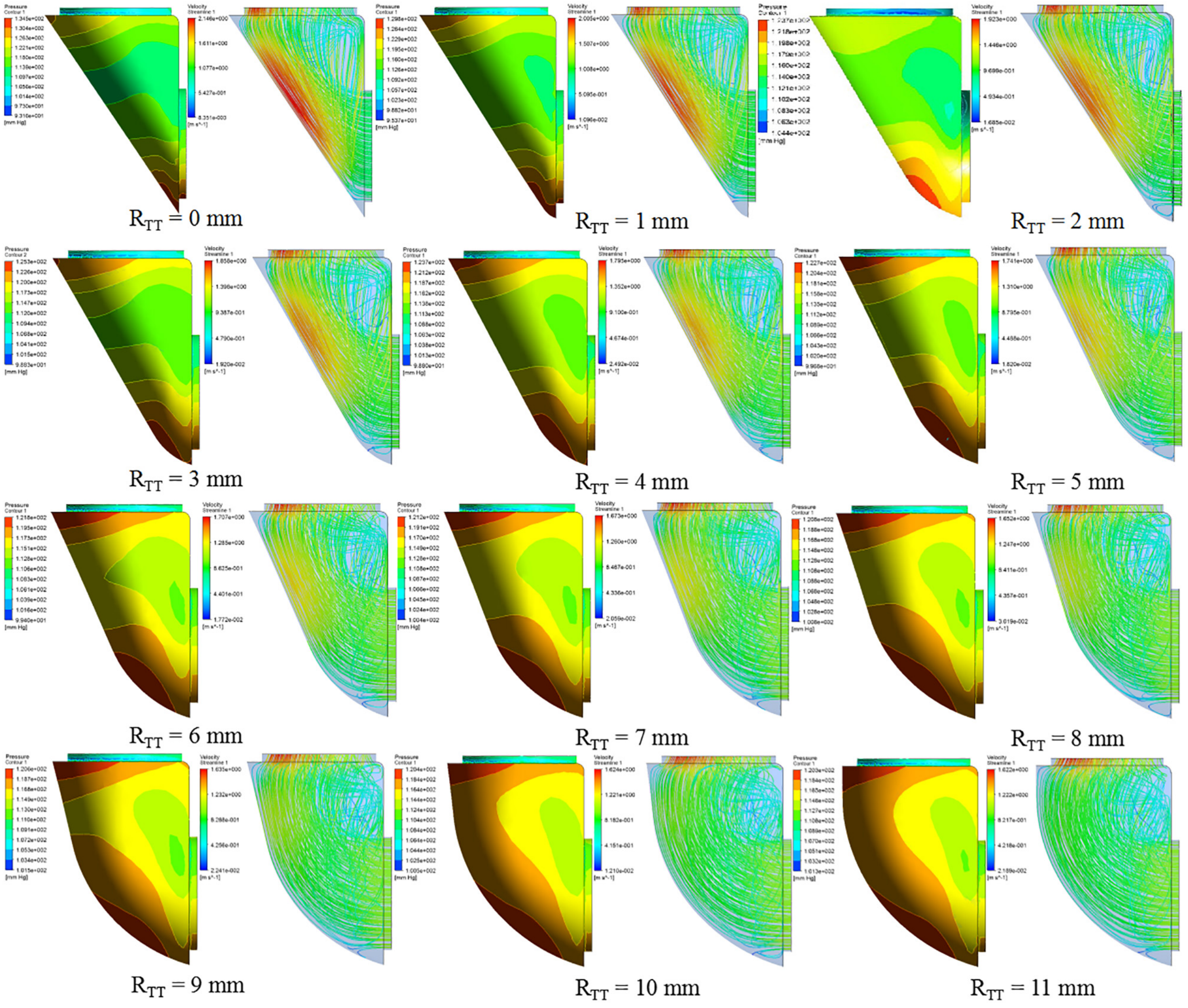

FIGURE 3 | The distribution of pressure and streamline of 12 groups of different R_{TT} models.

decreased ejection, and ultimately right ventricular dysfunction. The R_{TT} should be 6 mm when constructing the IVT, and the ΔP and volume of the IVT should reach the minimum value.

LIMITATIONS

The main limitations of this study were as follows: (1) The idealized model was adopted for simulation without considering the complex structure of the heart chamber; (2) Only 3paramenters of IVT were selected for research based on experience; (3) CFD applications did not consider fluid-solid interaction (FSI), valves or moving walls, which made it impossible for us to compare any measurements with cardiac functions. However, as mentioned earlier, this study only explored the effect of the IVT geometry sizes on hemodynamics.

Due to the randomness of the geometric size and relative position of aortic valve orifice and VSD in DORV, we selected three factors that may have a greater impact on hemodynamics to establish idealized models for simulation. Therefore, the small sample size of this study limited the generality and statistical significance of the results.

When the blood flow enters the IVT, there was an impact and interaction between the IVT and the blood flow. The blood flow out of the IVT also interacted with the valve. These two interactions would have certain impact on the results, limiting the generality of the results (Töger et al., 2012; Kouchoukos et al., 2013; Vedula et al., 2016), but it was impossible to capture in this study.

All in all, future work will include increasing the geometry sizes of IVT for research, establishing IVT models in real ventricular models and using FSI for simulation. This allows us to compare our findings with *in vivo* measurements.

CONCLUSION

The turning radius of the IVT, R_{TT} is the main factor affecting the ΔP. A small R_{TT} will lead to a large ΔP in the IVT. When R_{TT} increases to 6 mm, the ΔP in the IVT remains nearly unchanged. When performing the DORV correction, the turning radius of the IVT should be about 6 mm to ensure relatively low ΔP and small volume.

The CFD model mentioned in this study highlighted the significant influence of IVT shape on ΔP. This computational study supported the hypothesis that IVT shape was the primary cause of DORV surgical complications. Although the method used needs further improvement and large-scale verification, it could quantitatively analyze the parameters that couldn't be measured in clinical practice and provide theoretical basis for clinical surgery.

DATA AVAILABILITY STATEMENT

All of the data produced and analyzed in the present study are involved in the manuscript as tables or figures. The corresponding author will respond to the requests concerning the raw data and reasonable accommodations will be provided.

AUTHOR CONTRIBUTIONS

JW designed and simulated the IVT of virtual surgery and performed the data analysis. YY and XF provided support of clinical knowledge. The initial manuscript draft was prepared by JW and subsequently revised by AQ. All authors approved the final submitted version of the manuscript.

FUNDING

This work was supported by the National Natural Science Foundation of China (11772015) to AQ and the Beijing Municipal Administration of Hospitals Clinical Medicine Development of Special Funding Support (XMLX201845) to XF.

REFERENCES

Cui, H., Schaff, H., Abel, M., Helder, M., Frye, R., Ommen, S., et al. (2019). Left ventricular ejection hemodynamics before and after relief of outflow tract obstruction in patients with hypertrophic obstructive cardiomyopathy and valvular aortic stenosis. *J. Thorac. Cardiovasc. Surg.* S0022-5223, 30749–30744. doi: 10.1016/j.jtcvs.2019.03.071

Dentamaro, I., Vestito, D., Michelotto, E., Santis, D., Ostuni, V., Cadeddu, C., et al. (2017). Evaluation of left atrial appendage function and thrombi in patients with atrial fibrillation: from transthoracic to real time 3D transesophageal echocardiography. *Int. J. Cardiovasc. Imaging* 33, 491–498. doi: 10.1007/s10554-016-1026-6

Egbe, A. C., Connolly, H. M., Qureshi, M. Y., and Schaff, H. V. (2016). Surgically constructed double-outlet right ventricle. *Circulation* 8, 765–767. doi: 10.1161/circulationaha.115.019312

Fukuda, N., Shinohara, H., Sakabe, K., Onose, Y., Nada, T., and Tamura, Y. (2003). Transthoracic doppler echocardiographic measurement of left atrial appendage blood flow velocity: comparison with transoesophageal measurement. *Eur. J. Echocardiogr.* 3, 191–195. doi: 10.1016/s1525-2167(02)00166-x

Garekar, S., Bharati, A., Chokhandre, M., Mali, S., Trivedi, B., Changela, V., et al. (2016). Clinical application and multidisciplinary assessment of three dimensional printing in double outlet right ventricle with remote ventricular septal defect. *World J. Pediatr. Congeni. Heart Surg.* 7, 344–350. doi: 10.1177/2150135116645604

Hashirnoto, N., Kawabe, T., Imaizumi, K., Hara, T., Okamoto, M., Kojima, K., et al. (2004). CD40 plays a crucial role in lipopolysaccharide-induced acute lung injury. *Am. J. Respir. Cell Mol. Biol.* 6, 808–815. doi: 10.1165/rcmb.2003-0197oc

Iwai, S., Ichikawa, H., Fukushima, N., and Sawa, Y. (2007). Left ventricular outflow tract after kawashima intraventricular rerouting. *Asian Cardiovasc. Thorac. Ann.* 5, 367–370. doi: 10.1177/021849230701500502

Kouchoukos, N., Blackstone, E., and Hanley, F. (2013). Kirklin/barratt-boyes cardiac surgery. *Curr. Surg.* 5, 1932–1957.

Lacour-Gayet, F., Haun, C., Ntalakoura, K., Belli, E., Houyel, L., Marcsek, P., et al. (2002). Biventricular repair of double outlet right ventricle with non-committed ventricular septal defect (VSD) by VSD rerouting to the pulmonary artery and arterial switch. *Eur. J. Cardiothorac. Surg.* 6, 1042–1048. doi: 10.1016/s1010-7940(02)00105-7

Lefort, J., Mortreff, L., and Vargaftig, B. (2001). Airway administration of *Escherichia coli* endotoxin to mice induces glucocorticoid-resist ant bronchoconstriction and vasopermeation. *Am. J. Respir. Cell Mol. Biol.* 3, 345–351. doi: 10.1165/ajrcmb.24.3.4289

Marshall, R. P., Bellingan, G., Webb, S., Puddicombe, A., Goldsack, N., McAnulty, R. J., et al. (2000). Fibroproliferation occurs early in the acute respiratory distress syndrome and impacts on outcome. *Am. J. Respir. Crit. Care Med.* 5, 1783–1788. doi: 10.1164/ajrccm.162.5.2001061

Meduri, G. U., Golden, E., Freire, A. X., Taylor, E., Zaman, M., Carson, S. J., et al. (2007). Methylprednisolone infusion in early severe ARDS: results of a randomized controlled trial. *Chest* 4, 954–963. doi: 10.1378/chest.06-2100

Mostefa-Kara, M., Houyel, L., and Bonnet, D. (2018). Anatomy of the ventricular septal defect in congenital heart defects: a random association? *Orphanet J. Rare Dis.* 1, 118–126.

Pang, K., Meng, H., Wang, H., Hu, S. S., Hua, Z. D., Pan, X. B., et al. (2015). Value of a novel categorization of congenital double-outlet right ventricle on guiding the choice of surgical approaches. *Chin. J. Cardiovasc. Dis.* 11, 969–974.

Pang, K. J., Meng, H., Hu, S. S., Wang, H., His, D., Hua, Z. D., et al. (2017). Echocardiographic Classification and Surgical Approaches to Double-Outlet Right Ventricle for Great Arteries Arising Almost Exclusively from the Right Ventricle. *Texas Heart Inst,. J.* 4, 245–251. doi: 10.14503/THIJ-16-5759

Shoda, H., Yokoyama, A., Nishino, R., Nakashima, T., Ishikawa, N., Haruta, Y., et al. (2007). Overproduction of collagen and diminished SOCS1 expression are causally linked in fibroblasts from idiopathic pulmonary fibrosis. *Biochem. Biophys. Res. Commun.* 4, 1004–1010. doi: 10.1016/j.bbrc.2006.12.128

Töger, J., Kanski, M., Carlsson, M., Kovács, S. J., Söderlind, G., Arheden, H., et al. (2012). Vortex ring formation in the left ventricle of the heart: analysis by 4D flow MRI and lagrangian coherent structures. *Ann. Biomed. Eng.* 40, 2652–2662. doi: 10.1007/s10439-012-0615-3

Vedula, V., Seo, J. H., Lardo, A. C., and Mittal, R. (2016). Effect of trabeculae and papillary muscles on the hemodynamics of the left ventricle. *Theor. Comput. Fluid Dyn.* 2, 3–21. doi: 10.1007/s00162-015-0349-6

Villemain, O., Belli, E., Ladouceur, M., Houyel, L., Jalal, Z., Lambert, V., et al. (2016). Impact of anatomic characteristics and initial biventricular surgical strategy on out-comes in various forms of double-outlet right ventricle. *J. Thorac. Cardiovasc. Surg.* 3, 698–706.

Wang, C. J., Chen, S. B., Zhang, H. B., Liu, J. F., Xu, Z. W., Zheng, J. H., et al. (2017). Anatomical classifications of the coronary arteries in complete transposition of the great arteries and double outlet right ventricle with subpulmonary ventricular septal defect. *Thorac. Cardiovas. Surg.* 1, 26–30.

Ware, L. B., and Matthay, M. A. (2000). The acute respiratory distress syndrome. *N. Eng. J. Med.* 18, 1334–1349.

Conflict of Interest: The authors declare that the research was conducted in the absence of any commercial or financial relationships that could be construed as a potential conflict of interest.

frontiers
in Physiology

ORIGINAL RESEARCH
published: 10 March 2020
doi: 10.3389/fphys.2020.00206

Numerical Simulation of Hemodynamics in Two Models for Total Anomalous Pulmonary Venous Connection Surgery

Yeyang Cheng[1], *Aike Qiao*[1], *Yao Yang*[2] *and Xiangming Fan*[2]*

[1] *College of Life Science and Bioengineering, Beijing University of Technology, Beijing, China,* [2] *Beijing Anzhen Hospital, Capital Medical University, Beijing, China*

Objective: To numerically compare the prospective hemodynamic outcomes between a new window surgery and a traditional surgery in the treatment of supracardiac total anomalous pulmonary venous connection (S-TAPVC).

Methods: A 3D geometry model, composed of pulmonary vein (PV) and left atrium (LA), was reconstructed based on summarized data with S-TAPVC. Two surgery models were established based on this model. One is the traditional surgery model, where an elliptical anastomosis was created by incising and stitching the LA and the common vein (CV) along the axis of the CV. The other is the new window surgery model, where the CV was incised with an H-shaped orifice, and LA was incised with a transposed H-shaped orifice, and then the orifice edges were stitched like a window. Two models with a relative cross sectional area (RCSA) of 300 mm^2/m^2 and 500 mm^2/m^2 were established, which correspond to traditional surgery and window surgery. Numerical simulation of hemodynamics was carried out. The velocity, left atrium and pulmonary vein pressure, the pressure difference of anastomosis and the energy conversion efficiency were analyzed to evaluate the prospective hemodynamic outcomes of these two operations.

Results: Window surgery presented a lower blood flow velocity, pressure difference, and the WSS at the anastomosis, compared to traditional surgery. In terms of energy loss, the power conversion efficiency of window surgery was significantly higher than that of traditional surgery, with 66.8% and 53.5%, respectively.

Conclusion: The new window surgery demonstrates a lower pressure difference of anastomosis and higher energy conversion efficiency, which may be a better choice compared with the traditional surgery for S-TAPVC patient.

Keywords: TAPVC, surgical planning, hemodynamics, numerical simulation, congenital heart disease

Edited by:
Yunlong Huo,
Shanghai Jiao Tong University, China

Reviewed by:
Junmei Zhang,
National Heart Centre Singapore,
Singapore
Yundi Feng,
Peking University, China

Correspondence:
Xiangming Fan
fanxiangming@126.com

Specialty section:
This article was submitted to
Computational Physiology
and Medicine,
a section of the journal
Frontiers in Physiology

Received: *23 October 2019*
Accepted: *21 February 2020*
Published: *10 March 2020*

Citation:
Cheng Y, Qiao A, Yang Y and
Fan X (2020) Numerical Simulation
of Hemodynamics in Two Models
for Total Anomalous Pulmonary
Venous Connection Surgery.
Front. Physiol. 11:206.
doi: 10.3389/fphys.2020.00206

INTRODUCTION

Total anomalous pulmonary venous connection (TAPVC) is a rare but serious congenital heart disease (CHD) in which all pulmonary veins (PV) connect to the right atrium (RA) rather than the left atrium (LA) (Hassan et al., 2010; Ho et al., 2018; **Figure 1**). Its incidence is about 1.5%∼3.6% of CHD (Seale et al., 2010; Zhang et al., 2017; Wu et al., 2019).

Surgical treatment is usually required for this disease, in which anastomosis of the pulmonary vein and left atrium is a key step. The common vein (CV) and LA will be divided parallel along

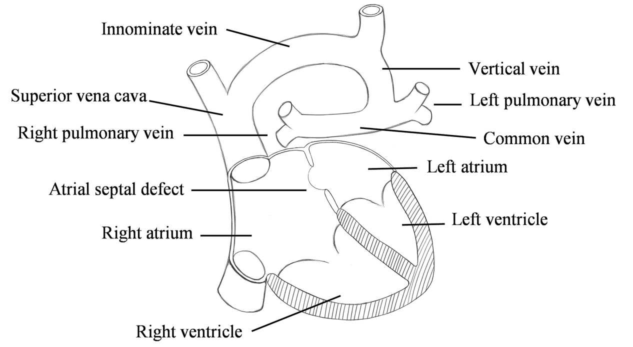

FIGURE 1 | Schematic diagram of the supracardiac total anomalous pulmonary venous connection (S-TAPVC).

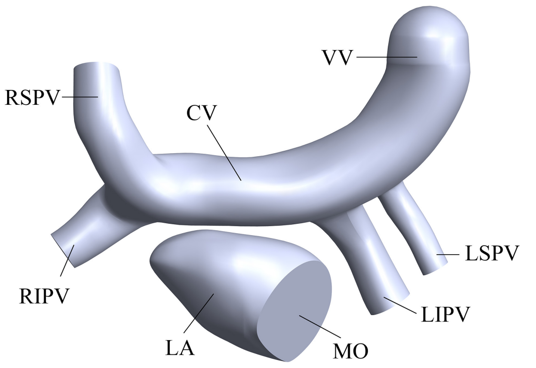

FIGURE 2 | Three-dimensional of the LA and PVs. "LA" means left atrium, "MO" means mitral orifice, "RSPV" means right superior pulmonary vein, "RIPV" means right inferior pulmonary vein, "LSPV" means left superior pulmonary vein, "LIPV" means left inferior pulmonary vein, "CV" means common vein and "VV" means vertical vein.

the axis of the former and anastomosed in traditional surgery. However, the therapeutic effect of this operation is poor in physiology and hemodynamics. In addition, pulmonary vein obstruction (PVO) is one of the most frequently stated problems with postoperative death (Seale et al., 2013; Hoashi et al., 2015; Shi et al., 2017).

Recent evidence suggests that the larger anastomotic area of pulmonary vein and left atrium is the key factor to improve the therapeutic effect of TAPVC (Ricci et al., 2003). On the other hand, new surgical procedures have been studied. In the 1990s, sutureless technique to relieve PVO after TAPVC repair, and the early treatment effect was good (Najm et al., 1998; Lacour-Gayet et al., 1999). However, the long-term outcomes of this technique are still unclear (Azakie et al., 2011; Yoshimura et al., 2017; Wu et al., 2019). What's worse, the surgical procedures cannot completely avoid the occurrence of anastomotic stenosis. In addition, the current research mostly focuses on mathematical statistical analysis of the postoperative mortality and postoperative complications of the disease, and few numerical simulations on the hemodynamics of the disease have been performed. Harada et al. (2018) used the Cox proportional hazard model to study the patient variables that may be associated with time to death. Wu et al. (2019) performed a meta-analysis using the Cochrane *Q* test and the I^2 statistic to assess heterogeneity to compare the treatment effects of sutureless technique and conventional surgery for primary repair. White et al. (2019) used univariable and multivariable Cox proportional hazard regression methods to identify factors associated with the primary outcome.

Therefore, a new window surgery was proposed in this study, and computational fluid dynamics (CFD) was used to evaluate the prospective hemodynamic effects of the new window surgery.

MATERIALS AND METHODS

Three-Dimensional Model Construction

The simplified three-dimensional (3D) model of supracardiac total anomalous pulmonary venous connection (S-TAPVC) was constructed based on summarized data in the references and the recommendations of the surgeons (Kim et al., 2005; Cronin et al., 2007), including the PV, LA, CV, and part of the vertical vein (**Figure 2**). It was constructed in the Computer Aided Design (CAD) software of SolidWorks.

Surgery and Geometry Processing

In order to evaluate the therapeutic effect of TAPVC, two surgical models were established for comparison. One is the traditional surgery model, where an elliptical anastomosis was created by incising and stitching the LA and the CV along the axis of the CV (**Figures 3A,B**). The other is the new window surgery model, where the CV was incised with an H-shaped orifice, and LA was incised with a transposed H-shaped orifice, and then the orifice edges were stitched like a window (**Figures 3D,E**). The cross-sections of the anastomosis of the two models were shown in **Figures 3C,F**.

The relative cross sectional area (RCSA), which is defined as the ratio of actual anastomotic area to body surface area, is a critical geometric factor with regards to the surgical outcomes. RCSAs for the traditional surgery model and the window surgery model were about 300 mm^2/m^2 and 500 mm^2/m^2, respectively. RCSAs in the two models have been designed as large as possible.

The computational fluid models were reconstructed in the software of Solidworks for the two surgeries (**Figure 4**). The mesh was generated by the software of Hypermesh. The mesh density was increased in the region of interest. By performing mesh independency analysis, the feasible mesh size was adopted. The element size on the wall was in the range of $0.2 \sim 0.8$ mm. In addition, the mesh in the boundary layer was created. The parameters of the boundary layer are as follows: the thickness of the first layer is 0.07 mm, the growth ratio is 1.1, and the number of mesh layers is five (**Figure 5**).

Materials and Boundary Conductions

The walls of the left atrium and blood vessels were assumed to be rigid and no-slip. The blood was assumed to be an incompressible, Newtonian fluid with density of 1050 kg/m^3 and

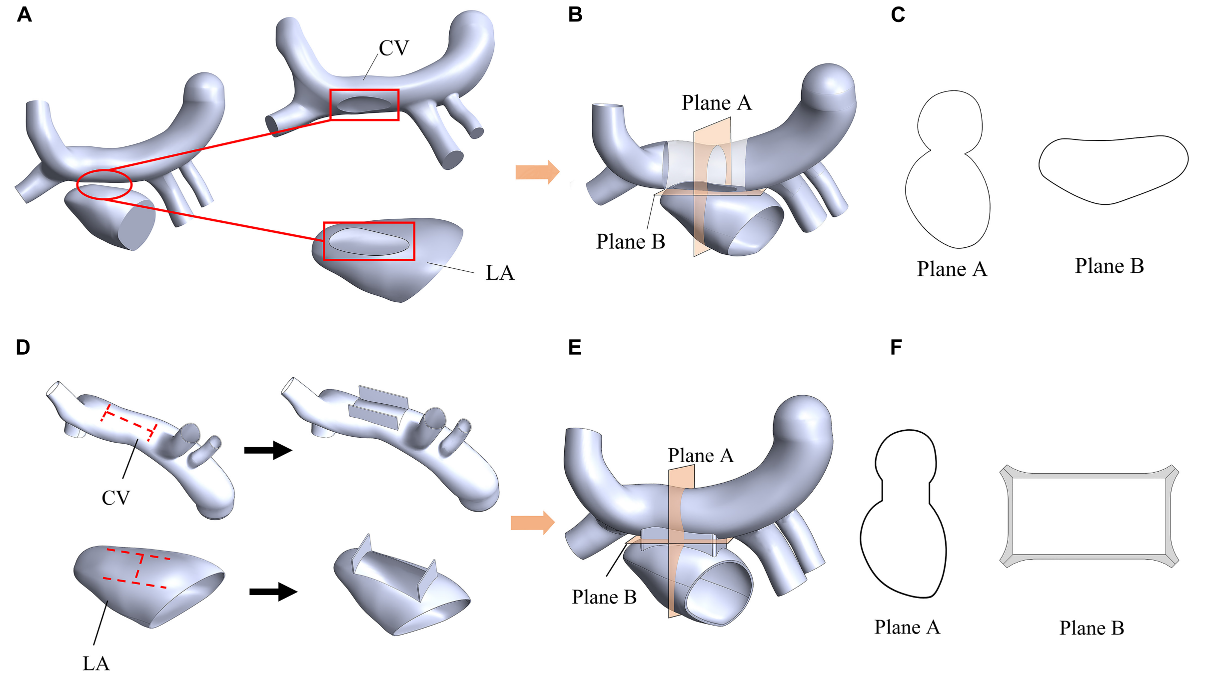

FIGURE 3 | Schematic diagram of a traditional surgery **(A,B,C)** and the window surgery **(D,E,F)**. **(A)** The elliptical anastomoses were created on the CV and LA; **(B)** Two orifice edges were sutured using traditional methods; **(C)** Plane A and Plane B were two sections of the model of the traditional surgery; **(D)** CV and LA were incised with an H-shaped orifice and a transposed H-shaped orifice, respectively; **(E)** These orifice edges faced outward and were sutured; **(F)** Plane A and Plane B were two sections of the model of the window surgery. Plane A was defined as the plane passing through the center of the CV and perpendicular to the CV axis; Plane B was defined as a plane near the anastomosis and perpendicular to Plane A.

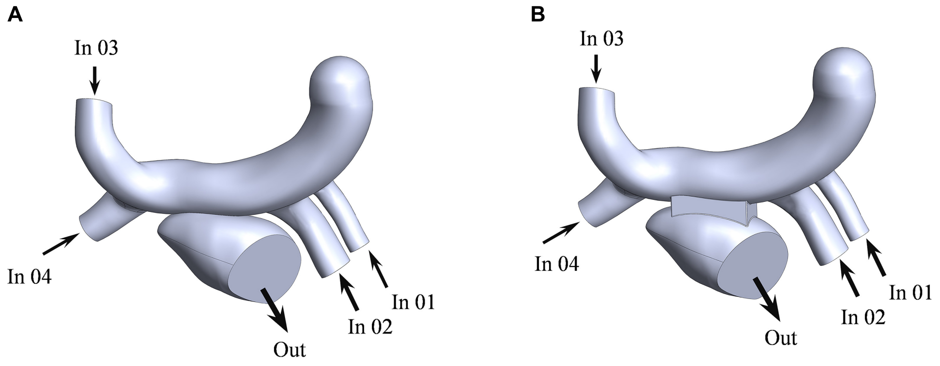

FIGURE 4 | The fluid models of the traditional surgery **(A)** and the window surgery **(B)**. LSPV, LIPV, RSPV, and RIPV were defined as the inlet for numerical simulation, corresponding to In 01, In 02, In 03, and In 04 in the figure, respectively; mitral orifice was defined as the outlet, out corresponding to the figure.

viscosity of 0.0035 Pa·s (Soulis et al., 2008; Ding et al., 2013; Lantz et al., 2016).

The left atrium is the passage of blood from the pulmonary veins to the left ventricle. The purpose of this study was to explain the effect of window surgery on the function of the left atrium. Therefore, this function can be simulated using steady-state flow. The mass flow of the pulmonary vein was defined as the boundary condition at the inlet (**Figure 4**). The average flow rate in a cardiac cycle was distributed to four pulmonary veins in proportion to the area of the pulmonary veins (Lantz et al., 2019). In addition, mitral orifice was defined as the outlet boundary condition of computational fluid model with average left atrial pressure (Migliavacca et al., 2003), as shown in **Table 1**. In clinical surgery, the vertical vein is usually ligated. Therefore, it was neither the inlet nor the outlet in the computational fluid model.

Numerical Computation

Based on the abovementioned models and boundary conditions, the flow field was computed by using CFX 14.5 (Ansys, United States) on a computer with Intel Core i5-4590 processors at 3.30 GHz and 8 GB RAM. Analysis type was set to steady state. In solver control panel, advection scheme was set to high

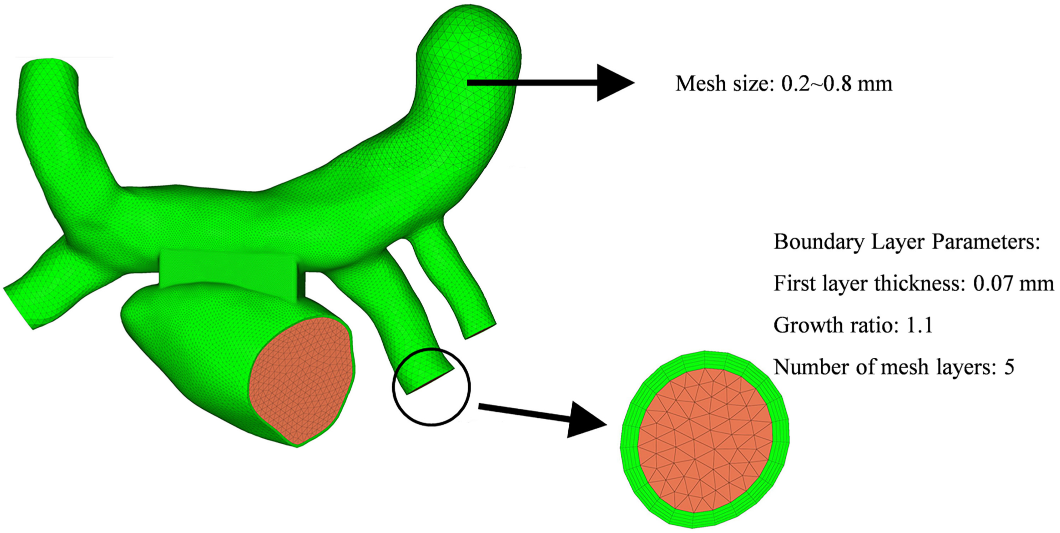

FIGURE 5 | Schematic diagram of the mesh details in a cross section of the vessel.

resolution, and the maximum iteration steps were set to 200. Furthermore, the residual tolerance was set to 1.0e-4 in order to make the calculated result within an acceptable range.

The Reynolds number (Re) was defined as

$$\mathrm{Re} = \frac{\rho v d}{\mu} \tag{1}$$

where the ρ, v, d, μ are the density, velocity, the hydraulic diameter and the dynamic viscosity of blood, respectively (**Table 2**).

Considering that the maximum Reynolds number (Re) was approximately 1063, the blood flow was assumed laminar.

Energy Loss

Energy loss is an important indicator for evaluating hemodynamic performance. This study evaluated the energy loss by the power loss and the power conversion efficiency (Guadagni et al., 2001; Migliavacca et al., 2003).

The power loss was defined as

$$W = Q\left(P + \frac{1}{2}\rho v^2\right) \tag{2}$$

$$W_l = \sum W_{in} - \sum W_{out} \tag{3}$$

where the W, Q, P, ρ, v are the power, mass flow, static pressure, the blood density and the blood velocity, respectively. The W_l means the power loss, and $\sum W_{in} \sum W_{out}$ are the total power of inlet and outlet, respectively. What's more, the power conversion efficiency (e) was defined as:

$$e = 1 - \frac{W_l}{\sum W_{in}} \tag{4}$$

TABLE 1 | The setting of the boundary conditions.

	Inlet flow rate (kg/s)				Outlet pressure (mmHg)
Location	In 01	In 02	In 03	In 04	Out
Parameter	0.0075	0.0189	0.0214	0.0159	4.0

TABLE 2 | The velocity, diameter, and Reynolds number of blood in the four pulmonary veins.

	LSPV	LIPV	RSPV	RIPV
Velocity (m/s)	0.476	0.474	0.485	0.473
Diameter (m)	0.0044	0.0069	0.0073	0.0064
Density (kg/m^3)	1050	1050	1050	1050
Dynamic viscosity (Pa·s)	0.0035	0.0035	0.0035	0.0035
Reynolds number	629	981	1063	909

RESULTS

Flow Patterns

The streamline reflects the magnitude and direction of the flow velocity at each point in the fluid domain. The streamlines of the two models could be observed clearly in the **Figure 6**, and the region with high blood flow velocity was located near the PV-LA anastomosis in both of the models. The blood flow velocity of traditional surgery was significantly higher than that of the window surgery with 1.0 m/s and 0.8 m/s, respectively.

On the other hand, blood in the pulmonary veins flowed into the left atrium smoothly in the window surgery model. A complex vortex extended from the anastomosis to the bottom of the left atrium along the left atrial wall in the traditional surgery model, which seemed not obvious in the window surgery model. There were low-velocity blood flows in the vertical vein

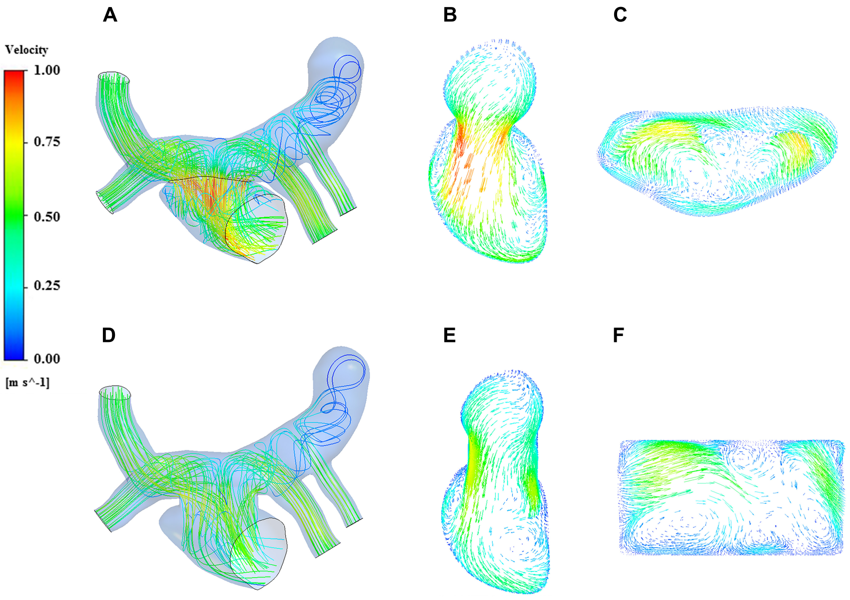

FIGURE 6 | Streamline and velocity vector diagrams of the two models. **(A)** streamline of traditional surgery; **(B)** velocity vector on the Plane A of traditional surgery; **(C)** velocity vector on the Plane B of traditional surgery; **(D)** streamline of window surgery; **(E)** velocity vector on the Plane A of window surgery; **(F)** velocity vector on the Plane B of window surgery.

on both models, and the vortices produced by traditional surgery were more obvious.

Pressure Distribution

The pressure distribution contour of the two models obtained from the analysis of CFD was showed in **Figure 7**. On the whole, the pressure of traditional surgery on the wall was higher than that of window surgery. The high-pressure region of traditional surgery focused on the CV and pulmonary veins, with the value up to 9.42 mmHg, while in window surgery, the pressure distribution was relatively uniform. In terms of pressure at the PV-LA anastomosis, the pressure difference was defined as the difference between the average pressure in the CV region and the average pressure in the left atrium region on the plane A, which was a section of the models. The pressure difference of conventional surgery was greater than that of window surgery, with approximately 3 mmHg and 1 mmHg, respectively.

Wall Shear Stress

Wall shear stress (WSS) is an important parameter in hemodynamic analysis, and many studies have shown that WSS was associated with remodeling of blood vessels (Farmakis et al., 2004; Fukumoto et al., 2008; Pekkan et al., 2009). The WSS distribution was extracted and shown in **Figure 8**. The highest WSS in both models were located near the anastomosis, and that of the traditional surgery was larger than that of the window surgery, with 47.01 Pa and 29.47 Pa, respectively.

Power Loss

Power loss can visually reflect the work of blood flow, and has a positive effect on evaluating the expected therapeutic effects of different surgical procedures on TAPVC. The results of the power loss and the power conversion efficiency of two models can be calculated and compared in **Table 3**. There is a significant reduction in power loss from 32.8 mW in the traditional surgery to 17.7 mW in window surgery. In terms of the power conversion efficiency, the window surgery has increased from 53.5 to 66.8% compared with the traditional surgery.

DISCUSSION

The left atrium is the channel through which blood in the pulmonary veins flows back to the left ventricle. A smooth blood flow state from the pulmonary vein to the left atrium is an important condition for ensuring left ventricular function. Local disturbed flow may cause anastomotic stenosis (Honjo et al., 2010; Azakie et al., 2011; Yoshimura et al., 2017). In clinic, it is generally considered that anastomotic stenosis and PVO are prone to occur when the blood flow velocity at the PV-LA anastomosis is greater than 1.2 m/s. From the results of numerical simulation, the blood flow velocity at the anastomosis of the two surgical procedures was less than 1.2 m/s, and the window surgery demonstrates lower velocity than the traditional surgery. We believe this is the result of the window surgery which increased the PV-LA anastomotic area.

In clinical treatment, high pressures in the pulmonary vein and the left atrium aren't what the surgeon expects. In the present study, the maximum pressure region of the two models was located on the opposite side of the junction of LIPV and

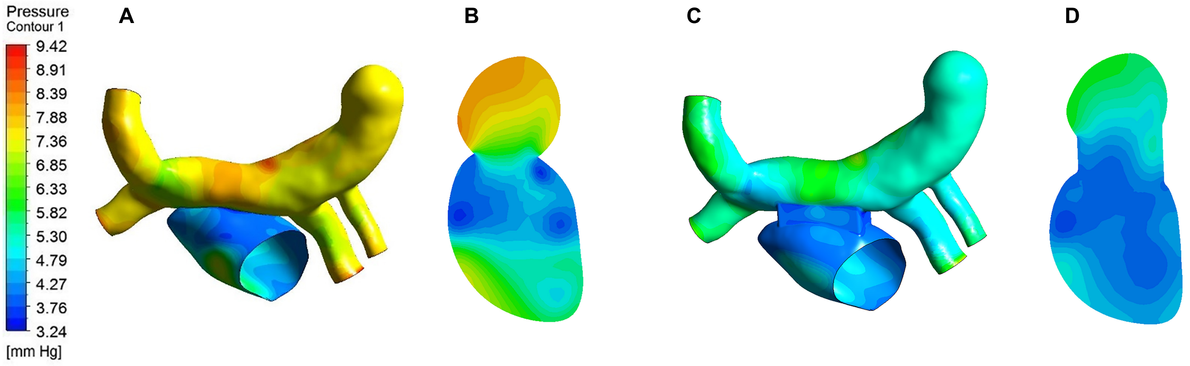

FIGURE 7 | Pressure distribution of the two models. **(A)** Pressure distribution on the wall of traditional surgery; **(B)** Pressure distribution of Plane A in traditional surgery; **(C)** Pressure distribution on the wall of window surgery; **(D)** Pressure distribution of Plane A in window surgery.

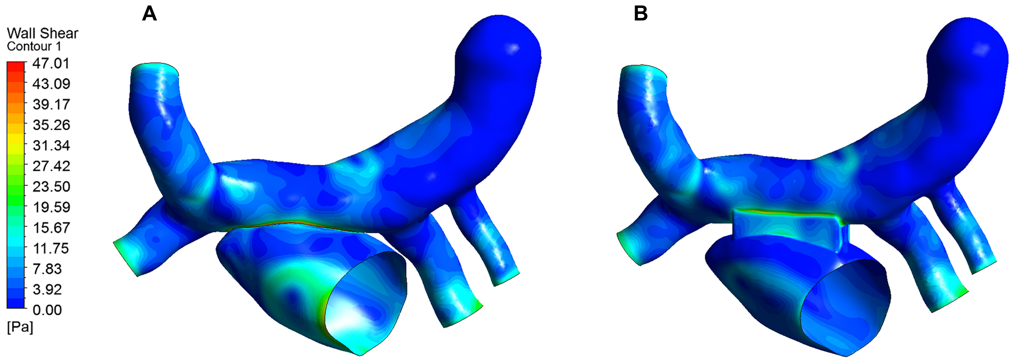

FIGURE 8 | WSS distribution of the two models. **(A)** WSS for the traditional surgery; **(B)** WSS for the window surgery.

the CV due to the impact of blood flow from the LIPV on the CV. On the other hand, it is interesting to note that the pressure and the pressure differences between the pulmonary veins and the left atrium of window surgery were lower than those of the traditional surgery. This is because the former is able to provide a larger area of the PV-LA anastomosis, which is beneficial to the reduction of the resistance of the lungs to the left heart system.

The heart pumps blood all the time to ensure the normal life of the body. If the heart has too much ineffective work, it will not only affect the normal physiological function of the human body, but also increase the load on the heart, which is unfavorable to the health of the patient from the perspective of long-term outcomes. In order to analyze long-term efficacy, power loss was calculated. In the window surgery, the structural transition from the pulmonary vein to the left atrium is more gradual, avoiding the structure of sudden expansion and contraction in traditional surgery, and blood in the pulmonary vein flows more smoothly into the left atrium and energy loss can be reduced. The results of numerical simulation confirmed that the window surgery has a positive effect of on the treatment of TAPVC in terms of reducing power loss and increasing power conversion efficiency.

Previous studies have noted that WSS is closely related to the function and structure of endothelial cells, and suggested that when WSS $>$ 35 Pa or WSS $<$ 0.2 Pa, intimal hyperplasia has the possibility of proliferation (Fry, 1968; Meyerson et al., 2001; Cunnane et al., 2017; de Villiers et al., 2018). The WSS of this study were all greater than 0.2 Pa, and WSS in the window surgery was less than 35 Pa, and WSS in the traditional surgery was greater than 35 Pa. It may be related to the structure of the anastomosis in the traditional surgery and the complex changes in blood flow velocity at this location. So we speculate that traditional surgery may increase the possibility of intimal hyperplasia. But this view needs further verification.

TABLE 3 | Power loss and power conversion efficiency.

	Traditional surgery	Window surgery
Power loss (mW)	32.8	17.7
Power conversion efficiency (%)	53.5	66.8

LIMITATIONS

The reconstructed CFD model and boundary conditions were simplified. In the future work, more patient-specific models should be established and their boundary conditions should be obtained to ensure the accuracy and validity of the numerical simulation results. In addition, the pulmonary veins and the left atrium were assumed to be rigid walls, and the interaction between blood flow and the wall was not considered, which may have an impact on the calculated results. Fluid-solid coupling methods should be considered to simulate the treatment of TAPVC in different surgical procedures in future work. Finally, it would be better to confirm the conclusion in animal experiments.

CONCLUSION

This preliminary study demonstrates that the proposed window surgery has some advantages over the traditional surgery in the treatment of TAPVC. The window surgery presented a good hemodynamic performance, which allowed smoother flow of blood from the pulmonary veins into the left atrium, reduced the pressure difference between the pulmonary veins and left atrium, and increased the power conversion efficiency. In summary, the window surgery may provide a new surgical alteration for the treatment of TAPVC and provide a reference for clinicians to develop new surgical planning.

DATA AVAILABILITY STATEMENT

All of the data produced and analyzed in the present study are involved in the manuscript as tables or figures. The corresponding author will respond to the requests concerning the raw data and reasonable accommodations will be provided.

AUTHOR CONTRIBUTIONS

YC performed numerical simulation of computational fluid dynamics and performed the data analysis under the instruction of AQ. YY and XF provided the support of medical knowledge. The initial manuscript draft was prepared by YC and subsequently revised by AQ. All authors approved the final submitted version.

FUNDING

This work was supported by the National Natural Science Foundation of China to AQ (11772015) and the Beijing Municipal Administration of Hospitals Clinical Medicine Development of Special Funding Support of China to XF (XMLX201845).

REFERENCES

Azakie, A., Lavrsen, M. J., Johnson, N. C., and Sapru, A. (2011). Early outcomes of primary sutureless repair of the pulmonary veins. *Ann. Thor. Surg.* 92, 666–672. doi: 10.1016/j.athoracsur.2011.04.024

Cronin, P., Kelly, A. M., Desjardins, B., Patel, S., Gross, B. H., Kazerooni, E. A., et al. (2007). Normative analysis of pulmonary vein drainage patterns on multidetector CT with measurements of pulmonary vein ostial diameter and distance to first bifurcation. *Acad. Radiol.* 14, 178–188. doi: 10.1016/j.acra.2006.11.004

Cunnane, C. V., Cunnane, E. M., and Walsh, M. T. (2017). A review of the hemodynamic factors believed to contribute to vascular access dysfunction. *Cardiovasc. Eng. Technol.* 8, 280–294. doi: 10.1007/s13239-017-0307-0

de Villiers, AM, McBride, A. T., Reddy, B. D., Franz, T., and Spottiswoode, B. S. (2018). A validated patient-specific FSI model for vascular access in haemodialysis. *Biomech. Model. Mechanobiol.* 17, 479–497. doi: 10.1007/s10237-017-0973-8

Ding, J., Liu, Y., and Wang, F. (2013). Influence of bypass angles on extracardiac Fontan connections: a numerical study. *Int. J. Numer. Methods Biomed. Eng.* 29, 351–362. doi: 10.1002/cnm.2508

Farmakis, T. M., Soulis, J. V., Giannoglou, G. D., Zioupos, G. J., and Louridas, G. E. (2004). Wall shear stress gradient topography in the normal left coronary arterial tree: possible implications for atherogenesis. *Curr. Med. Res. Opin.* 20, 587–596. doi: 10.1185/030079904125003340

Fry, D. L. (1968). Acute vascular endothelial changes associated with increased blood velocity gradients. *Circ. Res.* 22, 165–197. doi: 10.1161/01.res.22.2.165

Fukumoto, Y., Hiro, T., Fujii, T., Hashimoto, G., Fujimura, T., Yamada, J., et al. (2008). Localized elevation of shear stress is related to coronary plaque rupture: a 3-dimensional intravascular ultrasound study with in-vivo color mapping of shear stress distribution. *J. Am. Coll. Cardiol.* 51, 645–650. doi: 10.1016/j.jacc.2007.10.030

Guadagni, G., Bove, E. L., Migliavacca, F., and Dubini, G. (2001). Effects of pulmonary afterload on the hemodynamics after the hemi-Fontan procedure. *Med. Eng. Phys.* 23, 293–298. doi: 10.1016/s1350-4533(01)00035-2

Harada, T., Nakano, T., Oda, S., and Kado, H. (2018). Surgical results of total anomalous pulmonary venous connection repair in 256 patients. *Interact. Cardiovasc. Thorac. Surg.* 28, 421–426. doi: 10.1093/icvts/ivy267

Hassan, M. K., Hasan, K. A., Ahmed, F., Rahim, A., Quader, S. A., Ullah, M., et al. (2010). Total anomalous pulmonary venous connection (TAPVC) (Supra cardiac type)-a case study. *Cardiovasc. J.* 3, 104–106. doi: 10.1111/j.1540-8191.2012.01438.x

Ho, D. Y., White, B. R., Glatz, A. C., Mascio, C. E., Stephens, P. Jr., and Cohen, M. (2018). Postoperative obstruction of the pulmonary veins in mixed total anomalous pulmonary venous connection. *Pediatr. Cardiol.* 39, 1489–1495. doi: 10.1007/s00246-018-1921-9

Hoashi, T., Kagisaki, K., Kurosaki, K., Kitano, M., Shiraishi, I., and Ichikawa, H. (2015). Intrinsic obstruction in pulmonary venous drainage pathway is associated with poor surgical outcomes in patients with total anomalous pulmonary venous connection. *Pediatr. Cardiol.* 36, 432–437. doi: 10.1007/s00246-014-1031-2

Honjo, O., Atlin, C. R., Hamilton, B. C. S., Al-Radi, O., Viola, N., Cloes, J. G., et al. (2010). Primary sutureless repair for infants with mixed total anomalous pulmonary venous drainage. *Ann. Thorac. Surg.* 90, 862–868. doi: 10.1016/j.athoracsur.2010.05.007

Kim, Y. H., Marom, E. M., Herndon, J. E., and McAdams, H. P. (2005). Pulmonary vein diameter, cross-sectional area, and shape: CT analysis. *Radiology* 235, 43–49. doi: 10.1148/radiol.2351032106

Lacour-Gayet, F., Zoghbi, J., Serraf, A. E., Belli, E., Piot, D., Rey, C., et al. (1999). Surgical management of progressive pulmonary venous obstruction after repair of total anomalous pulmonary venous connection. *J. Thorac. Cardiovasc. Surg.* 117, 679–687. doi: 10.1016/s0022-5223(99)70287-4

Lantz, J., Gupta, V., Henriksson, L., Karlsson, M., Persson, A., Carlhall, C. J., et al. (2019). Impact of pulmonary venous inflow on cardiac flow simulations: comparison with *in vivo* 4D flow MRI. *Ann. Biomed. Eng.* 47, 413–424. doi: 10.1007/s10439-018-02153-5

Lantz, J., Henriksson, L., Persson, A., Karlsson, M., and Ebbers, T. (2016). Patient-specific simulation of cardiac blood flow from high-resolution computed tomography. *J. Biomech. Eng.* 138:121004.

Meyerson, S. L., Skelly, C. L., Curi, M. A., Shakur, U. M., Vosicky, J. E., Glagov, S., et al. (2001). The effects of extremely low shear stress on cellular proliferation and neointimal thickening in the failing bypass graft. *J. Vasc. Surg.* 34, 90–97. doi: 10.1067/mva.2001.114819

Migliavacca, F., Dubini, G., Bove, E. L., and de Leval, M. R. (2003). Computational fluid dynamics simulations in realistic 3-D geometries of the total cavopulmonary anastomosis: the influence of the inferior caval anastomosis. *J. Biomech. Eng.* 125, 805–813. doi: 10.1115/1.1632523

Najm, H. K., Caldarone, C. A., Smallhorn, J., Smallhorn, J., and Coles, J. G. (1998). A sutureless technique for the relief of pulmonary vein stenosis with the use of in situ pericardium. *J. Thorac. Cardiovasc. Surg.* 115, 468–470. doi: 10.1016/s0022-5223(98)70294-6

Pekkan, K., Dasi, L. P., de Zélicourt, D., Sundareswaran, K. S., Fogel, M. A., Kanter, K. R., et al. (2009). Hemodynamic performance of stage-2 univentricular reconstruction: glenn vs. hemi-Fontan templates. *Ann. Biomed. Eng.* 37, 50–63. doi: 10.1007/s10439-008-9591-z

Ricci, M., Elliott, M., Cohen, G. A., Catalan, G., Stark, J., de Leval, M. R., et al. (2003). Management of pulmonary venous obstruction after correction of TAPVC: risk factors for adverse outcome. *Eur. J. Cardio Thorac. Surg.* 24, 28–36. doi: 10.1016/s1010-7940(03)00180-5

Seale, A. N., Uemura, H., Webber, S. A., Partridge, J., Roughton, M., Ho, S. Y., et al. (2010). Total anomalous pulmonary venous connection: morphology and outcome from an international population-based study. *Circulation* 122, 2718–2726. doi: 10.1161/CIRCULATIONAHA.110.940825

Seale, A. N., Uemura, H., Webber, S. A., Partridge, J., Roughton, M., Ho, S. Y., et al. (2013). Total anomalous pulmonary venous connection: outcome of postoperative pulmonary venous obstruction. *J. Thorac. Cardiovasc. Surg.* 145, 1255–1262. doi: 10.1016/j.jtcvs.2012.06.031

Shi, G., Zhu, Z., Chen, J., Ou, Y., Hong, H., Nie, Z., et al. (2017). Total anomalous pulmonary venous connection: the current management strategies in a pediatric cohort of 768 patients. *Circulation* 135, 48–58. doi: 10.1161/circulationaha.116.023889

Soulis, J. V., Giannoglou, G. D., Chatzizisis, Y. S., Seralidou, K. V., Parcharidis, G. E., and Louridas, G. E. (2008). Non-Newtonian models for molecular viscosity and wall shear stress in a 3D reconstructed human left coronary artery. *Med. Eng. Phys.* 30, 9–19. doi: 10.1016/j.medengphy.2007.02.001

White, B. R., Ho, D. Y., Faerber, J. A., Katcoff, H., Glatz, A. C., Mascio, C. E., et al. (2019). Repair of total anomalous pulmonary venous connection: risk factors for postoperative obstruction. *Ann. Thorac. Surg.* 108, 122–129. doi: 10.1016/j.athoracsur.2019.02.017

Wu, Y., Xin, L., Zhou, Y., Kuang, H., Jin, X., Li, Y., et al. (2019). Is sutureless technique beneficial in the primary repair of total anomalous pulmonary venous connection? A systematic review and meta-analysis. *Pediatr. Cardiol.* 40, 881–891. doi: 10.1007/s00246-018-1948-y

Yoshimura, N., Fukahara, K., Yamashita, A., Doi, T., Takeuchi, K., Yamashita, S., et al. (2017). Surgery for total anomalous pulmonary venous connection: primary sutureless repair vs. conventional repair. *Gen. Thorac. Cardiovasc. Surg.* 65, 245–251. doi: 10.1007/s11748-017-0769-x

Zhang, Y., Shao, Q., Sun, L., Ge, S., and He, Y. (2017). Prenatal diagnosis of total anomalous pulmonary venous connection by 2D and 3D fetal echocardiography. *Echocardiography* 34, 1852–1857. doi: 10.1111/echo.13698

Conflict of Interest: The authors declare that the research was conducted in the absence of any commercial or financial relationships that could be construed as a potential conflict of interest.

frontiers in Physiology

ORIGINAL RESEARCH
published: 13 March 2020
doi: 10.3389/fphys.2020.00158

A Novel MRI-Based Finite Element Modeling Method for Calculation of Myocardial Ischemia Effect in Patients With Functional Mitral Regurgitation

Yue Zhang[1,2,3], Vicky Y. Wang[1,2,3], Ashley E. Morgan[2], Jiwon Kim[4], Liang Ge[1,2,3], Julius M. Guccione[1,2,3], Jonathan W. Weinsaft[4] and Mark B. Ratcliffe[1,2,3]*

[1] San Francisco Veterans Affairs Medical Center, San Francisco, CA, United States, [2] Department of Surgery, University of California, San Francisco, San Francisco, CA, United States, [3] Department of Bioengineering, University of California, San Francisco, San Francisco, CA, United States, [4] Department of Medicine, Weill Cornell Medicine, New York, NY, United States

Edited by:
Wei Sun,
Georgia Institute of Technology,
United States

Reviewed by:
Vijay Rajagopal,
The University of Melbourne, Australia
Junmei Zhang,
National Heart Centre Singapore,
Singapore

Correspondence:
Mark B. Ratcliffe
mark.ratcliffe@va.gov;
mark.ratcliffe@ucsf.edu

Specialty section:
This article was submitted to Computational Physiology and Medicine, a section of the journal Frontiers in Physiology

Received: *23 September 2019*
Accepted: *12 February 2020*
Published: *13 March 2020*

Citation:
Zhang Y, Wang VY, Morgan AE, Kim J, Ge L, Guccione JM, Weinsaft JW and Ratcliffe MB (2020) A Novel MRI-Based Finite Element Modeling Method for Calculation of Myocardial Ischemia Effect in Patients With Functional Mitral Regurgitation. Front. Physiol. 11:158. doi: 10.3389/fphys.2020.00158

Background: Functional Mitral Regurgitation (FMR) associated with coronary artery disease affects nearly 3 million patients in the United States. Both myocardial infarction (MI) and ischemia contribute to FMR development but uncertainty as to which patients will respond to revascularization (REVASC) of ischemia alone prevents rational decision making about FMR therapy. The aim of this study was to create patient-specific cardiac MRI (CMR) informed finite element (FE) models of the left ventricle (LV), calculate regional LV systolic contractility and then use optimized systolic material properties to simulate the effect of revascularization (virtual REVASC).

Methods: We describe a novel FE method able to predict the effect of myocardial ischemia on regional LV function. CMR was obtained in five patients with multi-vessel coronary disease and FMR before and 3 months after percutaneous REVASC and a single healthy volunteer. Patient-specific FE models were created and divided into 17 sectors where the systolic contractility parameter, *Tmax* of each sector was a function of regional stress perfusion (SP-CMR) and myocardial infarction (LGE-CMR) scores. Sector-specific circumferential and longitudinal end-systolic strain and LV volume from CSPAMM were used in a formal optimization to determine the sector based myocardial contractility, *Tmax* and ischemia effect, α. Virtual REVASC was simulated by setting α to zero.

Results: The FE optimization successfully converged with good agreement between calculated and experimental end-systolic strain and LV volumes. Specifically, the optimized T_{max} for the healthy myocardium for five patients and the volunteer was 495.1, 336.8, 173.5, 227.9, 401.4, and 218.9 kPa. The optimized α was found to be 1.0, 0.44, and 0.08 for Patients 1, 2, and 3, and 0 for Patients 4 and 5. The calculated average of radial strain for Patients 1, 2, and 3 at baseline and after virtual REVASC was 0.23 and 0.25, respectively.

Conclusion: We developed a novel computational method able to predict the effect of myocardial ischemia in patients with FMR. This method can be used to predict the effect of ischemia on the regional myocardium and promises to facilitate better understanding of FMR response to REVASC.

Keywords: myocardial ischemia, myocardial infarction, coronary artery disease, coronary artery bypass, mitral valve insufficiency, inverse finite element analysis, computer simulation

INTRODUCTION

Functional mitral regurgitation (FMR) associated with coronary artery disease (CAD) is a leading cause of valvular heart disease. FMR occurs in 1.2 to 2.1 million patients with CAD (Gorman et al., 2003) in whom it doubles the risk of heart failure and death (Aronson et al., 2006).

Both myocardial infarction (MI) and ischemia contribute to FMR development. Specifically, creation of inferior MI in large animals leads to left ventricular (LV) remodeling, papillary muscle displacement, restriction of mitral leaflets and subsequent development of FMR (Gorman et al., 1995; Liel-Cohen et al., 2000). Conversely, the evidence for ischemia comes from clinical studies where in approximately half of patients, FMR improves with coronary revascularization (REVASC), whereas in the remainder FMR persists or worsens (Aklog et al., 2001; Penicka et al., 2009; Kang et al., 2011). Uncertainty as to which patients will respond to REVASC impedes rational decision-making regarding FMR management.

Cardiac magnetic resonance imaging (CMR) allows LV remodeling, tissue characteristics including MI and non-ischemic fibrosis, ischemia and regional contractile function to be assessed with high precision. Cine-CMR has been employed as a reference standard for measuring LV size and function (Codella et al., 2008, 2012; Janik et al., 2008). Stress perfusion CMR (SP-CMR) has been shown to provide high diagnostic accuracy for ischemia as can occur with obstructive CAD (Klem et al., 2006). Late gadolinium enhancement CMR (LGE-CMR) provides near exact agreement with histopathology evidenced MI (Kim et al., 1999, 2000) and CMR with non-invasive tags CSPAMM-CMR has been widely used to measure systolic myocardial deformation and strain (Ryf et al., 2002).

The relationship between MI fibrosis, ischemia and function and recovery of function after REVASC in chronically ischemic hibernating myocardium in which myocardial metabolism and contractile function are down-regulated (Wijns et al., 1998) is complex (Canty and Suzuki, 2012). In that regard, we recently measured MI fibrosis, stress perfusion and regional strain with CMR in patients with FMR associated with CAD (Morgan et al., 2018). Briefly, CSPAMM-CMR measured circumferential and longitudinal strain were modestly reduced in sectors without MI or ischemia when compared to volunteers and then decreased in an approximately linearly fashion as the amount of MI fibrosis and ischemia increased (Morgan et al., 2018). In addition, chronically ischemic hibernating myocardium can partially recover function after surgical or percutaneous REVASC (Kim et al., 2000; Hocum Stone et al., 2017). However, fewer than 10% of dysfunctional segments with LGE hyperenhancement greater than 50% recover function (Kim et al., 2000).

Finite element (FE) modeling has the unique potential to (1) determine the effect of ischemia in FMR associated with CAD and to then (2) simulate the effect of REVASC. Prior FE modeling studies by our group (Walker et al., 2005; Wenk et al., 2011) and others (Bogen et al., 1980; Genet et al., 2015) have focused on the impact of MI but without incorporation of ischemia effect. Most previous FE modeling studies of the LV with ischemia have focused on arrhythmogenesis (Wang et al., 2013; Mendonca Costa et al., 2018) without incorporation of ischemia effect on LV function. There have been FE modeling studies of ischemia effect on regional LV function in which models were based on an idealized LV shape (Bovendeerd et al., 1996), cardiac imaging (XCAT) phantom (Veress et al., 2015) and physical measurements in an excised large animal heart (Mazhari et al., 2000). However, in those studies, regions of ischemia were assumed to have little (Mazhari et al., 2000) or no (Bovendeerd et al., 1996; Veress et al., 2015) regional contractile function. To date, FE models that incorporate CMR-based tissue characteristics to determine regional contractility have not been described.

This study describes a novel FE method able to predict the effect of myocardial ischemia on regional LV function. The method leverages CMR imaging data obtained from patients with multivessel CAD and FMR before and after percutaneous REVASC. It includes patient-specific FE models in which the regional systolic contractility parameter is a function of regional CMR-based tissue characteristics including stress perfusion and MI. The aim of the study is to calculate systolic material properties of ischemic myocardium and then use optimized systolic material properties to simulate the effect of REVASC (virtual REVASC).

MATERIALS AND METHODS

Five patients were selected from a larger group of patients prospectively enrolled in a protocol entitled "CMR Myocardial Tissue Based Prediction of Ischemic MR Revascularization Response" at Weill Cornell Medical College (New York, NY, United States) examining REVASC effect in patients with FMR associated with CAD. The protocol included CMR and transthoracic echocardiography before and 3 months after percutaneous revascularization (PCI). One healthy volunteer without cardiovascular risk factors was also studied. The Cornell Institutional Review Board approved this study, and written informed consent was obtained at time of enrollment.

Computational Modeling Pipeline

The proposed method is summarized in **Figure 1**. The CMR images were used to create LV and right ventricular (RV) surfaces (see section "Image Analysis"), to calculate 3D regional strains (see section "Constitutive Laws"), and to configure LV mechanical parameters (see section "Sector-Based Myocardial Material Parameters"). LV mechanics models were constructed using the patient-specific LV and RV surfaces, LV and RV pressures, rule-based fiber angles, diastolic and systolic myocardial constitutive relationships and LV myocardial material parameters. A formal parameter optimization framework was then constructed based on the LV mechanics models and the *in vivo* sector-specific circumferential and longitudinal end-systolic strain and LV volume.

Image Acquisition

CMR was performed with a 3.0 Tesla MRI scanner (General Electric, Waukesha, WI, United States) (Morgan et al., 2018) both before and 3 months after PCI. CMR included 4 pulse sequences. Specifically, Cine-CMR was performed with a steady-state free precession pulse sequence. Images were acquired in contiguous LV short axis and standard (2-, 3- and 4-chamber) long axis orientations (**Figure 2A**). SP-CMR was assessed in accordance with established methods previously validated by members of our group (Klem et al., 2006; Heitner et al., 2019). In brief, pharmacologic stress was induced with regadenoson (0.4 mg), during which gadolinium was infused (0.1 mmol/kg) and LV short axis images (4–5, evenly distributed from base-apex) were acquired using a gradient echo pulse sequence (**Figure 2B**). Perfusion CMR was repeated 5-min thereafter under baseline (non-stress) conditions. Myocardial infarction (LGE-CMR) was assessed using an inversion recovery pulse sequence, which was acquired 10–30 min post-gadolinium (0.2 mmol/kg) infusion and acquired in spatial orientations matched to Cine-CMR (**Figure 2C**). CSPAMM in contiguous LV short and long axis slices (8 mm tag spacing, 10 mm slice thickness, no gap) was performed to measure myocardial deformation and strain (**Figure 2D**).

Image Analysis

LV and RV Segmentation

Left ventricular short and long axis and RV short axis Cine-CMR images were contoured at LV early diastolic filling (EDF; MeVisLab, version 2.7.1, Bremen, DE) where the EDF phase was defined as the time step immediately prior to opening of the mitral valve. The LV and RV contours included the papillary muscle bases but excluded the trabeculae (**Figure 2A**).

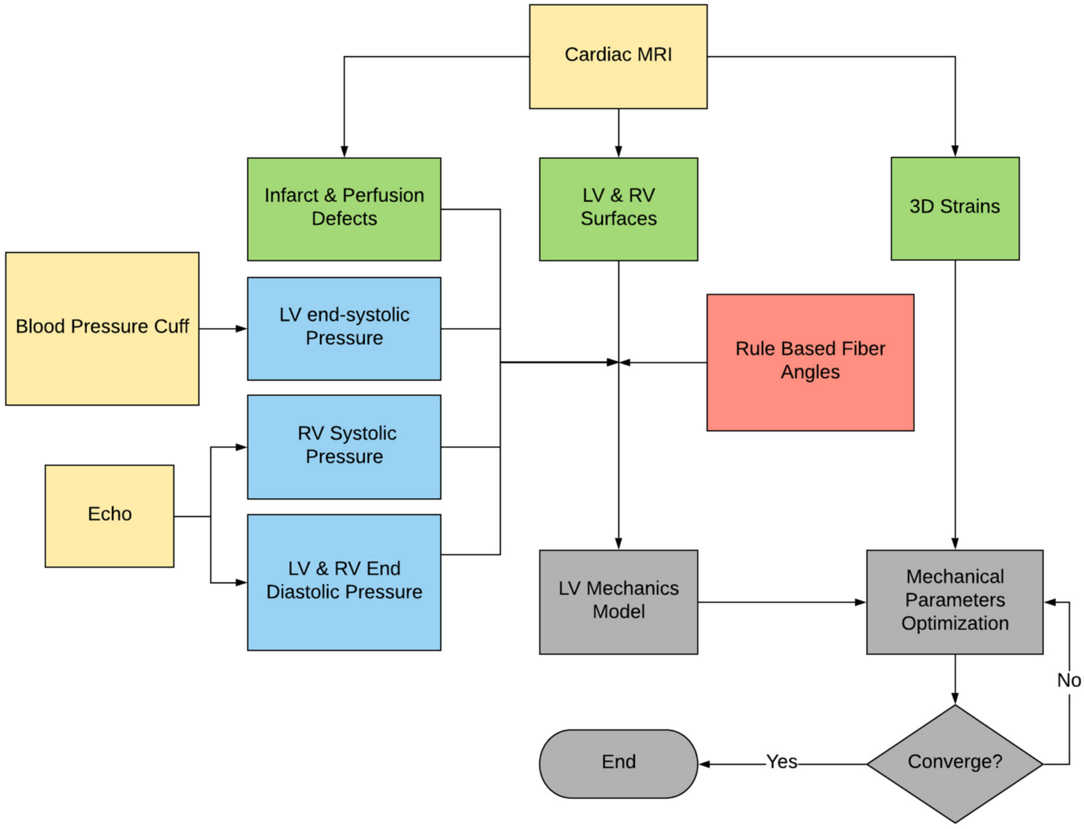

FIGURE 1 | Flowchart of the proposed method. Note that the raw data are in yellow, the derived pressure in blue, the CMR-derived geometry and strains in green, and the FE modeling process in gray.

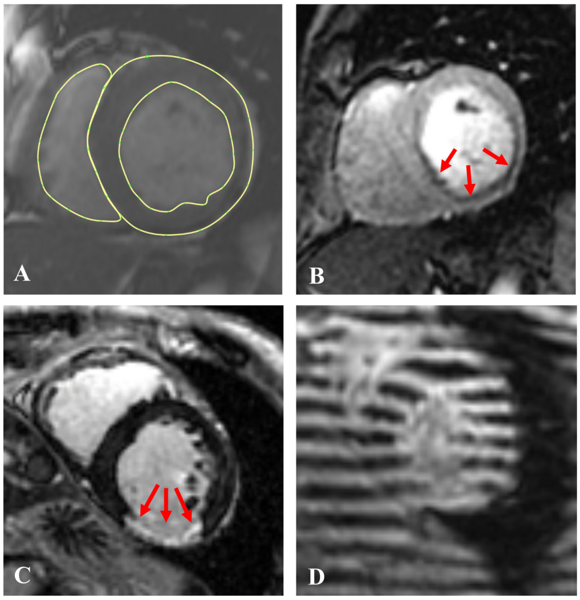

FIGURE 2 | (A) Short axis Cine-CMR with LV epicardial and endocardial and RV endocardial contours; **(B)** A stress perfusion image with arrows indicating the ischemic region; **(C)** A late gadolinium enhancement (LGE-CMR) image with red arrows indicating the infarcted region, and **(D)** A short axis tagged (CSPAMM) image.

To eliminate short axis image alignment breathing artifacts, an LV surface was created based on the three epicardial long axis contours. LV short axis contours were moved in plane so that the contour centroid was over the centroid of the corresponding plane from the long axis surface. After alignment, LV epicardial and endocardial and RV endocardial surfaces were created using the aligned short axis contours.

Scoring of Cine-, SP- and LGE-CMR Images

Left ventricular function, MI scar and stress perfusion were localized using the AHA/ACC 17 segment model (Cerqueira et al., 2002). LV wall thickening was measured on Cine-CMR using a 5-point scale (0 = normal (at least 50% wall thickening), 1 = mild hypokinesis, 2 = moderate hypokinesis, 3 = akinesis (no wall thickening), 4 = dyskinesis).

Myocardial infarction was identified on LGE-CMR, for which transmural extent was graded using a 5-point segmental scale (0 = no hyperenhancement; 1 = 1–25%; 2 = 26–50%; 3 = 51–75%; 4 = 76–100%) (Sievers et al., 2007). LGE in non-coronary arterial patterns (mid-wall or epicardial) was not included in MI analyses.

Ischemia was assessed semi-quantitatively on SP-CMR based on peak myocardial signal intensity during first-pass gadolinium infusion. Perfusion deficits were defined as persistent hypo-enhancement on ≥ 4 consecutive heart beats (Klem et al., 2006) and the severity of stress perfusion defects was graded semi-quantitatively using an established 4-point scale (0 = absent, 1 = mild, 2 = moderate, 3 = severe) based on the magnitude of hypo-enhancement (Kim et al., 2019).

CMR-Measured Strains

Regional 3D circumferential (E_{cc}) and longitudinal (E_{ll}) strain for each sector were calculated from CSPAMM images. The HARmonic Phase (HARP) method developed by Osman et al. (2000) was implemented. Implementation in MeVisLab has been previously reported (Morgan et al., 2018). Please note that all the strain presented in this study is LV end-systolic strain.

LV FE Model Generation

Using LV epicardial and endocardial surfaces as input, TruGrid (XYZ Scientific Applications, Inc., Pleasant Hill, CA, United States) was used to create patient-specific meshes of the LV composed of hexahedral elements as shown in **Figure 3**. Meshes with different density were created and optimal mesh density was determined as a function of parameter calculation accuracy and calculation time.

Each element was assigned a material direction with a rule-based fiber angle method (Bayer et al., 2012) where the myofiber helix angle varying transmurally from 60° at the endocardium to −60° at the epicardium.

Custom software (C#, Visual Studio 2017, Microsoft, Redmond, WA, United States) that included a ray casting method (Möller and Trumbore, 1997) to locate the interventricular septum (**Figure 3A**) was used to break the mesh into 17 AHA sectors (Cerqueira et al., 2002; **Figure 3B**)[1].

Loading and Boundary Condition

LV pressure (LVP) at end systole was obtained from a blood pressure cuff and LVP at end-diastole (ED) and RV end-diastolic and systolic pressures were estimated from concomitant transthoracic echocardiography data (Ommen et al., 2000; **Table 1**). Patient-specific LV pressure was applied to the LV endocardial surface and RV pressure was applied to the LV septal epicardial surface.

Note that these models contract from the apex to the base. Specifically, nodes at the LV base (top surface) were fixed in the valve plane (Z direction movement = 0) but able to slide in the *X* and *Y* directions during passive filling and systolic contraction.

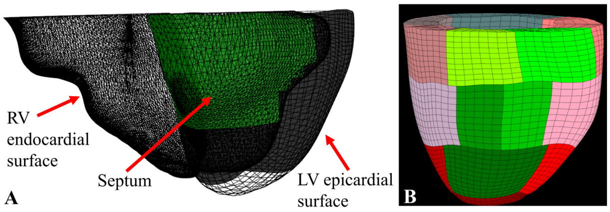

FIGURE 3 | (A) RV endocardial surface (triangle mesh), LV epicardial surface (hexahedral mesh), and the septum (in green) determined using a ray-casting method; **(B)** the final 17 sector FE model with the septal sectors in green.

---

[1] https://github.com/mratcliffe/ElementSearch/, available on request

TABLE 1 | Patient-specific LV and RV pressures and LV ejection fraction (EF).

	Patient 1	Patient 2	Patient 3	Patient 4	Patient 5	Volunteer
LV EDP [mmHg]	20	20	20	20	10	10
LV ESP [mmHg]	121	140	100	134	140	120
RV EDP [mmHg]	3	8	8	3	8	8
RV ESP [mmHg]	23	28	23	20	40	25
Ejection fraction (%)	36	31	15	43	45	58

Constitutive Laws

Passive and active myocardial constitutive laws described by Guccione et al. (1991, 1993) were used in this study. Specifically, the passive myocardium is modeled by a strain energy function, W, that is anisotropic relative to the local fiber direction:

$$W = 0.5C\left(e^{Q} - 1\right) \tag{1}$$

where

$$Q = \left[b_f E_{11}^2 + b_t\left(E_{22}^2 + E_{33}^2 + E_{23}^2 + E_{32}^2\right) + b_{fs}\left(E_{12}^2 + E_{21}^2 + E_{13}^2 + E_{31}^2\right)\right] \tag{2}$$

E_{11} is fiber strain, E_{22} is cross-fiber in-plane strain, E_{33} is radial strain, E_{23} is shear strain in the transverse plane, and E_{12} and E_{13} are shear strain in the fiber-cross fiber and fiber-radial planes, respectively, and where $b_f = 49.25$, $b_t = 19.25$ and $b_{fs} = 17.44$ (Walker et al., 2005).

A time-varying elastance model is used to simulate the active contraction of cardiac muscles (Guccione et al., 2001). The time-varying elastance model has the following form:

$$T_0 = T_{max}\frac{Ca_0^2}{Ca_0^2 + ECa_{50}^2}C_t \tag{3}$$

where T_{max} is the maximum isometric tension achieved at the longest sarcomere length and maximum peak intracellular calcium concentration $(Ca_0)_{max}$. Ca_0 is the intracellular calcium concentration and ECa_{50} is length-dependent calcium sensitivity. C_t is a time-varying variable defined as follows:

$$C_t = \frac{1}{2}\left[1 - cos\left(\varpi\right)\right] \tag{4}$$

where ϖ is a time and sarcomere length dependent variable that increases from 0 at the start of contraction to π during peak contraction and then decreases to 0 during diastole.

Material laws were implemented with a user-defined material subroutine in the explicit FE solver, LS-DYNA (Livermore Software Technology Corporation, Livermore, CA, United States).

Sector-Based Myocardial Material Parameters

The LGE score was an integer from 0 to 4 and the SP score was an integer ranging from 0 to 3. In each case, a score of 0 represented the absence of disease. Further LGE and SP scoring details are described above (see section "Scoring of Cine-, SP- and LGE-CMR Images"). Passive stiffness, C, was determined using the following:

$$C_n = C_H + 9 \cdot C_H \cdot \frac{LGE_n}{4} \tag{5}$$

where C_n represents the passive stiffness for each sector and C_H the stiffness of a "healthy" sector with LGE = 0. Note that when LGE = 4 (transmural MI), $C_n = 10\ C_H$ which is consistent with our prior work (Wenk et al., 2011).

On the other hand, both LGE and SP were assumed to effect regional contractility, $Tmax$ according to the following linear relationship:

$$Tmax_n = Tmax_H \cdot \left(1 - \frac{LGE_n}{4}\right) \cdot \left(1 - \alpha \cdot \frac{SP_n}{3}\right) \tag{6}$$

where $Tmax_n$ represents the contractility for each sector, $Tmax_H$ the contractility for healthy sector with LGE and SP = 0, α the ischemia effect and LGE_n and SP_n the LGE and SP scores for each sector. It's known that $Tmax_n \geq 0$ and LGE_n is $\ni[0,\ 4]$ and SP_n is $\ni[0,\ 3]$ then it can be determined $\alpha\ni[0,\ 1]$. Since we assumed that the LGE and SP scores were 0 for the healthy volunteer, C_n and $Tmax_n$ for the volunteer were equal to C_H and $Tmax_H$, respectively.

Model Optimization

A formal optimization of C_H, $Tmax_H$ and α were performed where the objective function for the optimization was taken to be the mean-squared errors (MSE) (Guccione et al., 2001). C_H was determined such that the FE model predicted LV ED volume matched the patient-specific *in vivo* measured volume. $Tmax_H$ was estimated by minimizing the MSE between FE model-predicted and *in vivo* MRI-measured end-systolic longitudinal and circumferential strains and the LV end-systolic volume. The goal of the optimization is to minimize the MSE as follows:

$$\begin{aligned} &\textit{Objective function} \\ &= \frac{1}{2N}\left(\sum_{n=1}^{N}\left(\left(E_{cc,\,n} - \bar{E}_{cc,n}\right)^2 + \left(E_{ll,\,n} - \bar{E}_{ll,n}\right)^2\right)\right) \\ &\quad + W\left(\frac{V_{ES} - \bar{V}_{ES}}{\bar{V}_{ES}}\right)^2, \end{aligned} \tag{7}$$

where n is the *in vivo* average strain at each sector (note the apex sector was excluded so $n = 16$), $E_{cc,n}$ the calculated FE circumferential strain, $E_{ll,n}$ the calculated longitudinal strain, V_{ES} the LV end-systolic volume and W is the weight applied to the volume term. The overbar represents the experimental *in vivo* measurements.

$W = 10$ was applied to the volume term to make the strain and volume effects more balanced. For each case, the $Tmax_H$ was initially = 350 kPa. α was initially = 0.5 in the FMR patient models and = 0 in the healthy volunteer model. No constraints were applied to either $Tmax_H$ or V_{ES}.

Mesh Convergence Study

A mesh convergence study was performed on models of patients 2 and 5 to find the minimum number of elements needed to obtain stable calculations of C_H, $Tmax_H$, and α within the fastest computation time. Four sets of meshes with different density were created with the transmural elements from 3 to 4, circumferential elements from 40 to 64, and longitudinal elements from 22 to 38.

Testing With Synthetic Data

Method accuracy was determined using idealized input data. Briefly, multiple simulations of diastolic inflation and systolic contraction for Patients 2 and 5 were firstly conducted by setting α to be 0 and 1, respectively (note that C_H and $Tmax_H$ were set as the optimized values as presented in section "Testing With Synthetic Data" under "Results"). For each case, the simulated strain and LV end-systolic volume (ESV) were used as input in our optimization framework as "experimental data." In addition, for Patient 2, the optimization was initiated with α set at 0, 0.5, and 1 while the $Tmax_H$ was set at 100 kPa, 350 kPa, and 600 kPa to test whether the current optimization scheme is sensitive to the initial guess of the parameters.

TABLE 2 | Patient-specific LGE and SP scores at baseline (BL), and wall motion (WM) scores at BL and follow up (FU) studies.

Subjects	Segments	1	2	3	4	5	6	7	8	9	10	11	12	13	14	15	16	17
Patient 1	LGE score (BL)	0	0	0	3	1	1	0	0	0	3	4	2	0	0	0	0	0
	SP score (BL)	2	1	0	2	2	2	1	0	0	2	2	2	0	3	3	0	3
	WM score (BL)	1	1	1	3	4	3	1	1	1	3	4	0	0	0	0	0	0
	WM score (FU)	0	0	2	2	3	1	0	0	1	3	4	1	0	0	0	1	0
Patient 2	LGE score (BL)	0	0	0	0	3	0	1	0	0	1	3	1	1	0	0	0	0
	SP score (BL)	0	0	2	3	3	1	2	1	1	2	2	1	3	1	2	0	0
	WM score (BL)	0	0	1	3	4	1	3	0	0	3	3	1	3	0	3	1	3
	WM score (FU)	0	0	1	2	2	1	1	0	0	2	1	1	2	0	1	1	2
Patient 3	LGE score (BL)	0	0	0	0	0	0	0	0	0	1	1	0	0	0	0	0	0
	SP score (BL)	0	0	1	2	2	2	1	0	0	2	2	0	0	0	2	0	0
	WM score (BL)	3	3	3	4	3	3	3	3	3	4	3	3	3	3	4	3	3
	WM score (FU)	2	2	2	3	3	2	2	2	2	3	2	2	2	2	2	2	2
Patient 4	LGE score (BL)	0	0	0	0	0	0	1	1	0	0	0	0	2	1	0	0	3
	SP score (BL)	0	1	0	0	0	0	3	3	0	0	0	0	3	3	2	0	3
	WM score (BL)	0	0	0	0	0	0	1	0	0	0	0	0	3	3	1	0	4
	WM score (FU)	0	0	0	0	0	0	1	1	0	0	0	0	2	2	1	0	4
Patient 5	LGE score (BL)	0	0	0	0	4	0	0	0	0	1	4	0	1	0	0	3	0
	SP score (BL)	0	0	0	1	1	0	2	0	0	0	0	0	1	0	0	0	0
	WM score (BL)	0	0	0	0	2	0	0	0	0	1	3	1	0	0	1	3	0
	WM score (FU)	0	0	0	0	2	0	0	0	0	1	3	1	0	0	1	3	0

TABLE 3 | Mesh convergence study.

	Number of elements	C_H (kPa)	$Tmax_H$ (kPa)	α	Calculation time (hrs × cpu)
Patient 1	7952	0.099	523.3	1.0	137.3
Patient 2	2700	0.207	322.7	0.32	48.0
	4176	0.207	338.9	0.4	77.5
	7952	0.192	336.8	0.44	175.0
	10752	0.192	330.7	0.44	250.0
Patient 3	7952	1.7	173.5	0.08	599.4
Patient 4	7952	0.019	227.9	0	462.3
Patient 5	2700	0.0095	405.3	0.0	77.5
	4176	0.0095	414.8	0.0	125.0
	7952	0.0094	401.4	0.0	400.0
	10752	0.0090	408.6	0.0	560.0
Volunteer	7952	0.00011	259.4	N/A	1741.5

Virtual REVASC

Virtual REVASC was performed on patient-specific models that had an ischemia effect ($\alpha > 0$) by setting $\alpha = 0$. As seen in Eq. 6, by setting $\alpha = 0$, $Tmax_n$ becomes a function of LGE only and SP has no effect.

Virtual REVASC was validated by comparing sector specific radial strain, E_{rr} calculated from baseline models and after virtual REVASC with a Cine-CMR wall motion based estimation of revascularization effect. Briefly, the following relationship was developed:

$$E_{rr}\_WM = E_{rr}\_BL \cdot (1 + \Delta WM \cdot 50\%) , \tag{8}$$

where E_{rr}_BL is E_{rr} calculated from baseline models, ΔWM the difference between Cine-CMR wall motion scores at baseline and after revascularization and E_{rr}_WM is an estimated E_{rr} after revascularization based on the change in wall motion score. Eq. 8 is consistent with a wall motion score of 0 having a wall thickening of at least 50%. For instance, if $E_{rr}\_BL = 0.2$ and wall motion improved by 2 points, E_{rr}_WM would be 0.4.

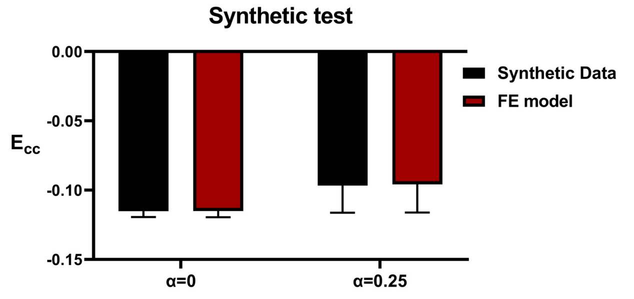

FIGURE 4 | Comparison of synthetic E_{cc} with FE model predicted strain in patients 2 and 5.

RESULTS

Patient-specific LV and RV pressures and LV ejection fraction (EF) are shown in **Table 1**. Patient-specific LGE and SP scores at baseline and wall motion scores at baseline and follow-up studies are shown in **Table 2**. Four of the 5 patients had perfusion defects in sectors without MI/fibrosis (have over 3 sectors with SP score – LGE score $\geq$2). One of the patients had MI but no significant ischemia. Note that the wall motion scores were normal and LGE and SP scores were assumed = 0 for the healthy volunteer.

Mesh Convergence Study

The mesh convergence study determined that 7952 elements (**Table 3**) are required and further mesh refinement only results in an average of 2% change in C, $<$ 2% change in $Tmax_H$ and no change in α. Note that only the optimization results for using 7952 elements will be presented in the following sections.

Testing With Synthetic Data

Figure 4 shows excellent agreement between the synthetically generated "experimental strain" and the strain after optimization. The target and optimized parameters are summarized in **Table 4** with a maximal difference of 1.4%, which shows the proposed method has great capability of predicting Tmax_H and α accurately. The synthetic test also demonstrated that the current

TABLE 4 | Results of testing with synthetic data.

ID	Input				Optimized	
	$Tmax_H$ kPa)	α	Initial guess $Tmax_H$ kPa)	Initial guess α	$Tmax_H$ kPa)	α
Patient 2	336.8	0.0	100.0	0.0	336.7	0.0
			350.0	0.5	337.6	0.0
			600.0	1.0	336.7	0.0
Patient 2	336.8	1.0	100.0	0.0	332.3	1.0
			350.0	0.5	332.2	1.0
			600.0	1.0	332.6	1.0
Patient 5	401.4	0.0	350.0	0.5	401.5	0.0
Patient 5	401.4	1.0	350.0	0.5	401.0	1.0

TABLE 5 | CMR-based *in vivo* volumes and the FE-predicted volumes after optimization.

ID	CMR-based		FE-predicted	
	EDV (ml)	ESV (ml)	EDV (ml)	ESV (ml)
Patient 1	245.4	157.0	245.4	158.3
Patient 2	160.9	111.0	160.9	108.3
Patient 3	300.0	255.5	300.0	249.2
Patient 4	170.0	97.4	170.0	96.5
Patient 5	94.9	52.2	94.9	51.3
Volunteer	118.7	49.7	118.7	48.6

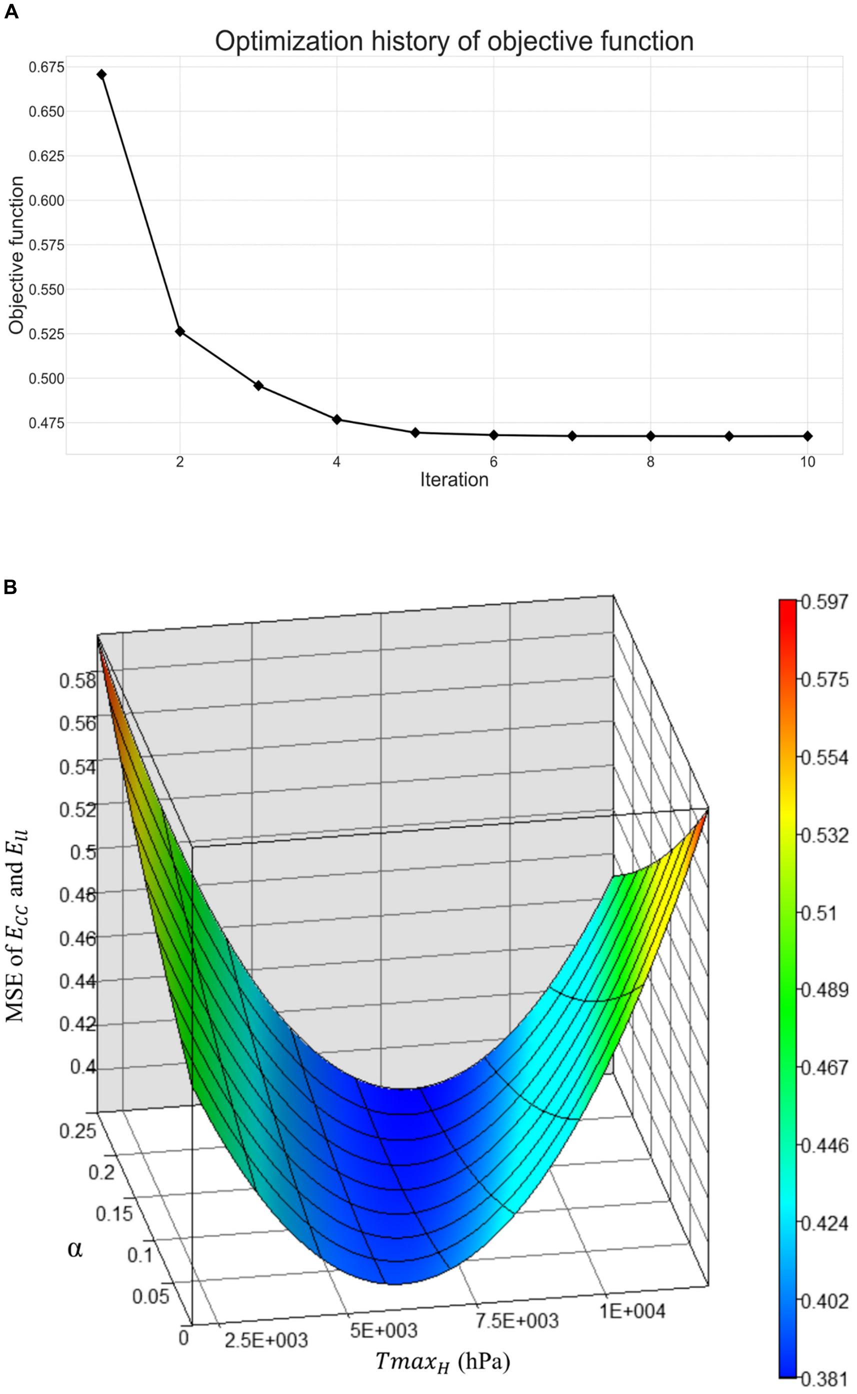

FIGURE 5 | (A) Optimization history of the overall objective function, and **(B)** surface plot of mean-squared-error of strain with respect to $Tmax_H$ and α.

optimization scheme is insensitive to the selection of the initial guess of the parameters.

Prediction of C_H, $Tmax_H$ and α

C_H was determined such that the FE model predicted LV EDV matched the patient-specific *in vivo* measured EDV (**Table 5**).

Figure 5A shows excellent convergence of the objective function (OF) during a representative model optimization. **Figure 5B** shows a surface plot of MSE of the strain with respect to $Tmax_H$ and α, where the valley of the surface indicates lowest MSE value relating to the best match between the experimental and FE model-predicted strain. The optimized $Tmax_H$ and α are summarized in **Table 3**. The optimized $Tmax_H$ and α displayed good convergence as shown in **Figure 6**. The final OF value of 0.297 (an average calculated using all six subjects) was obtained indicating generally good agreement between the FE model-predicted systolic strain and the patient-specific *in vivo* measured strain. The LV EDV and ESV were summarized in **Table 5**, where the results showed that the difference between the predicted LV ESV and volume measured with CMR was on average less than 2%.

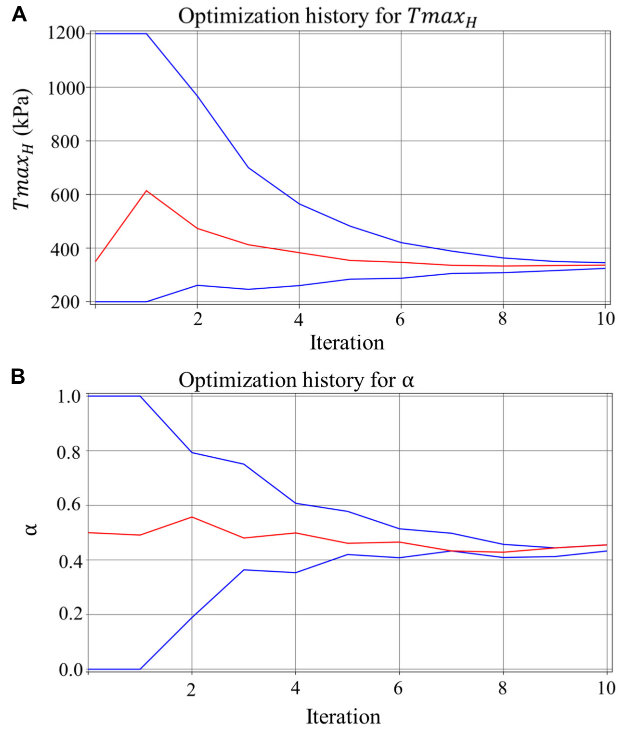

FIGURE 6 | The convergence of the parameter (lines in blue represent the upper and lower bounds) for **(A)** $Tmax_H$ for healthy myocardium, and **(B)** ischemia effect, α, on the LV myocardial contractility, with each parameter resulted in a precise final converged optimum.

The average of E_{cc} along with its standard error of the mean for all sectors with LGE score <3 from overall subjects derived from the experimental data and calculated with the FE model are -0.135 ± 0.044 and -0.127 ± 0.042. **Figure 7** shows the regional comparisons of E_{cc} calculated from CSPAMM and FEM simulations. It can be seen that the model-predicted E_{cc} generally has good agreement with the E_{cc} derived from CSPAMM.

Virtual REVASC

Figure 8 shows the E_{rr}_BL, E_{rr}_VR and E_{rr}_WM for all 3 patients that were determined with positive α. In all studies, virtual REVASC underestimated the actual E_{rr} effect. In patients 1 and 2 the difference was mild. However, patient 3 had a small predicted alpha (0.08) and minimal improvement in E_{rr} with virtual REVASC in spite of the fact that at baseline there was significant ischemia and the improvement in actual wall motion after revascularization was significant.

DISCUSSION

In this study, we demonstrated a novel method to estimate the effect of ischemia on regional LV myocardial contractility. The proposed method takes the advantage of multiple CMR sequences and the FE modeling to formally optimize the LV mechanics parameters. To the best of our knowledge, this study is the first study that incorporated 17-segment-based patient-specific perfusion and LGE scores into constitutive model, which allowed regional mechanical properties to be estimated with better physiological constraints. A linear relationship was proposed to describe the effect of LV infarct and ischemia on LV active contraction. Our approach was tested with CMR data from five patients with multi-vessel CAD and moderate FMR and a healthy volunteer. Good agreement between the FE model-predicted systolic strains and the patient-specific

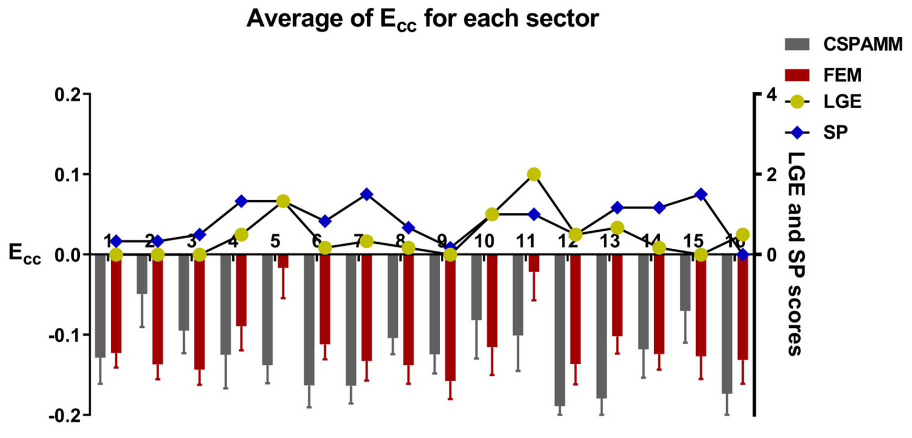

FIGURE 7 | Comparison of sector-specific CSPAMM and FE model predicted E_{cc} across all 6 subjects. E_{cc} derived from CSPAMM and calculated from FE simulations are in gray and red bars, respectively. The average sector specific MI/fibrosis (LGE) and stress perfusion (SP) scores are in yellow circle and blue diamond, respectively.

in vivo measured strains were observed, which suggests that the optimized model was faithful to the experimental data.

Ischemia Effect

The effect of ischemia, α, on LV contractility was found to be >0 for Patients 1, 2, and 3, but = 0 for Patients 4 and 5. This is consistent with the patient-specific wall motion scores seen in **Table 2** where the cumulative wall motion score in patients 1, 2 and 3 decreased (improved) after PCI but remained unchanged or increased (worsened) in patients 4 and 5.

It should be noted that stress induced perfusion defects are associated with either normal or depressed regional myocardial function and in the latter case the myocardium would be described as hibernating (Wijns et al., 1998). First, by definition, our method identifies only hibernating myocardium and simple demand ischemia without dysfunction is not considered. As a corollary, if a patient with multi-vessel CAD had a large amount of demand ischemia without LV dysfunction, our method would not identify an ischemia effect. Specifically, if the SP defect is showing simple demand ischemia without underlying contractility deficit, then α would likely be 0. If the SP defect is associated with hibernating myocardium where contractility is reduced, then α will likely be >0.

MI Stiffness

Our assumption that infarct stiffness is ten times that of normal myocardium is consistent with our prior studies (Walker et al., 2005; Wenk et al., 2011) and others (Genet et al., 2015). However, there is reason to believe that better measurement of infarct stiffness is necessary in patients with multi-vessel coronary disease and FMR. First, model accuracy was much better when sectors with transmural infarction were excluded. Second, the optimized $Tmax_H$ was higher in Patients 1, 2, and 5 (523.3, 336.8, and 401.4 kPa respectively) than the healthy volunteer (259.4 kPa). The reason for this discrepancy is unclear but might be explained if Eq. 6 is overestimating the effect of infarct and ischemia on LV contractility. It is anticipated that future studies that measure infarct stiffness in patients with MI but without ischemia will help to better determine the relationship between infarct and myocardial contractility.

Diastolic Stiffness in Patients With Multi-Vessel CAD

As seen in **Table 3**, there is a large variance in optimized C_H between the healthy volunteer and patients with multi-vessel CAD and FMR. We suspect this is likely a function of myocardial fibrosis (LGE scores >0) and, consistent with this, prior clinical studies have shown the extent of LGE to correspond to impaired LV relaxation (Moreo et al., 2009). However, the cumulative LGE scores of patients 1 and 2 are similar and further studies are therefore necessary to establish our hypothesis. On the other hand, the lack of diastolic strain in this study limits our ability to better optimize passive LV material parameters.

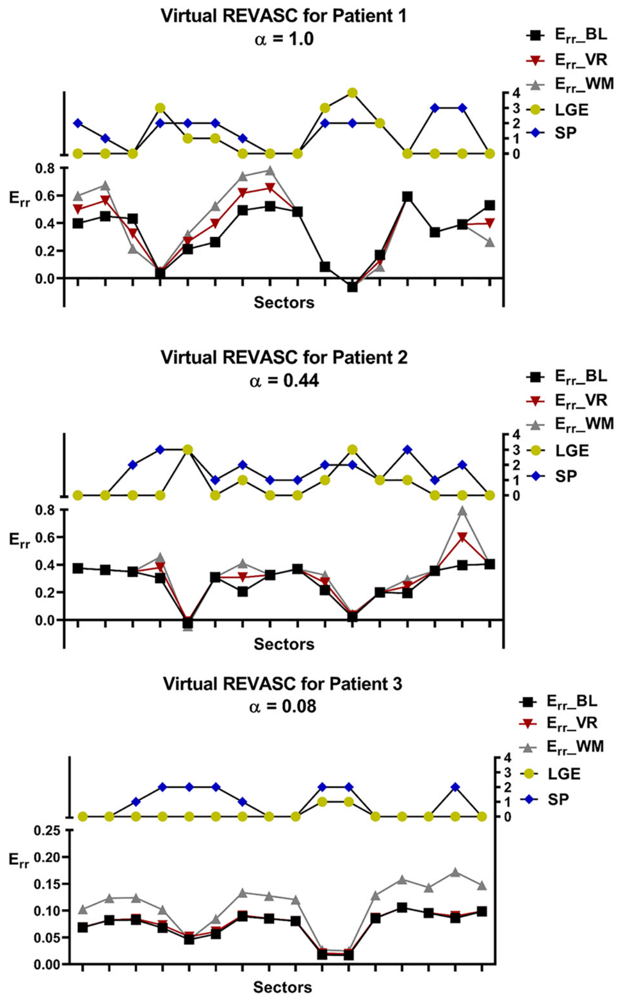

FIGURE 8 | Comparison of the sector specific E_{rr} before and after virtual REVASC for the 3 patients with positive ischemia effect, α. Sector specific MI/fibrosis (LGE) and stress perfusion (SP) scores are plotted for reference. E_{rr} BL represents E_{rr} calculated using the FE simulations at baseline, E_{rr} VR is the E_{rr} obtained from the FE simulations after virtual REVASC, and E_{rr} WM is an "actual" E_{rr} effect estimated using the qualitative wall thickening scores.

It is interesting to note that in **Figure 7** in the sectors with large LGE scores (i.e., sectors 5 and 11), the model-predicted E_{cc} is much smaller than that derived from CSPAMM, while this is not seen in the sectors with large SP scores (i.e., sectors 4 and 7). This may be due to the effect of MI fibrosis/LGE on either regional diastolic stiffness or systolic contractility or interaction between the two. In the current study we assumed that systolic contractility was affected by both LGE and SP scores but that diastolic stiffness was only affected by the LGE scores. Those assumptions about the form and amount of LGE effect on diastolic stiffness and systolic contractility may be overestimated. Furthermore, it should be noted that fibrosis (LGE) -based effect on diastolic stiffness will affect systolic E_{cc} through its effect on strain at ED and sarcomere stretch. The mismatch between the model-predicted E_{cc} and E_{cc} derived from CSPAMM in the regions with large LGE scores shows that a better understanding of the effect of LGE scores on the diastolic stiffness is important.

Model Accuracy

Results of a mesh sensitivity study suggest that the optimized LV material parameters are relatively insensitive to the mesh density, although slight differences were observed between FE models with different mesh density. **Table 2** indicates that a mesh with 7952 elements may be the optimal choice for the current study because of the balanced calculation time and parameter optimization accuracy. Furthermore, synthetic test results suggest that the proposed method is capable of precisely determining the LV passive and active material properties and the ischemia effect on LV active contractility.

Virtual REVASC

Validation of virtual REVASC using Cine-CMR wall thickening shows that the magnitude of ischemia effect is underestimated. This could be due to an incorrect T_{max} and LGE relationship. For example, we assumed a sector with LGE = 2 had the T_{max} as 50% of the T_{max} for a healthy sector and this may be over-estimating the effect of infarct on the myocardial contractility. As a result, according to Eq. 6, the model-predicted ischemia effect might be smaller than reality to compensate the over-estimated LGE effect on myocardial contractility. A non-linear relationship between T_{max} and LGE and a scaling factor in front of LGE score is under development.

Figure 8 shows that patient 3 had a small predicted alpha (0.08) and minimal improvement in E_{rr} with virtual REVASC in spite of the fact that at baseline there was significant ischemia and the improvement in actual wall motion after revascularization was significant. The reason for this is unclear but possibilities include that measured CSPAMM strain was inaccurate. In addition, patient 3 had a dilated LV and the subsequent decrease in systolic strain magnitude might make it hard to discriminate the ischemia (SP) effect. Regardless, this points out the need for accurate strain measurement with good spatial resolution as simulation input.

Limitations

First, only systolic strains were calculated since the CSPAMM data were acquired during the systolic phase, which resulted in a fact that only systolic myocardial material parameters can be optimized. Because of the lack of diastolic strains, the main diastolic material parameter, C_H was calibrated to match the measured LV end-diastolic volume. Second, the border zone effect was not taken into consideration in the current study. Third, only a linear relationship between the infarct and ischemia and the LV contractility were employed in this study. Fourth, boundary conditions near the valve plane of the LV may affect longitudinal strain calculations in that local area. However, longitudinal strain in the body of the LV is realistic. Last, the path from end-diastole to end-systole is not specified, and our models cannot therefore provide accurate simulation of isovolumic contraction and ejection. However, simulation of diastolic filling and end-systole are accurate.

CONCLUSION

This study proposed a novel FE method to predict the effect of ischemia on the LV contractility in patients with multi-vessel coronary disease and FMR. The proposed method has good agreement with patient-specific *in vivo* measured strains and is able to predict REVASC effect.

Future studies will explore the stress perfusion and contractility relationship to determine if non-linear relationships allow greater model accuracy. Flow structure models will be implemented so that mitral regurgitation effect can be directly simulated. Last, a study with larger numbers of patient-specific models will better establish the utility of our FE method.

DATA AVAILABILITY STATEMENT

All datasets generated for this study are included in the article/supplementary material.

ETHICS STATEMENT

The Cornell Institutional Review Board approved this study, and written informed consent was obtained at the time of enrollment.

AUTHOR CONTRIBUTIONS

YZ, JW, and MR designed the study. YZ conducted simulations, analyzed results, and wrote the initial draft of the manuscript. MR created the FE models. VW, AM, and JK did data analysis. LG contributed to development of methodology. JW collected the clinical data. LG, JW, and MR supervised the study. YZ, VW, JG, JW, and MR contributed to manuscript writing/review.

REFERENCES

Aklog, L., Filsoufi, F., Flores, K. Q., Chen, R. H., Cohn, L. H., Nathan, N. S., et al. (2001). Does coronary artery bypass grafting alone correct moderate ischemic mitral regurgitation? *Circulation* 104(12 Suppl. 1), I68–I75.

Aronson, D., Goldsher, N., Zukermann, ., Kapeliovich, M., Lessick, J., Mutlak, D., et al. (2006). Ischemic mitral regurgitation and risk of heart failure after myocardial infarction. *Arch. Intern. Med.* 166, 2362–2368. doi: 10.1001/archinte.166.21.2362

Bayer, J. D., Blake, R. C., Plank, G., and Trayanova, N. A. (2012). A novel rule-based algorithm for assigning myocardial fiber orientation to computational heart models. *Ann. Biomed. Eng.* 40, 2243–2254. doi: 10.1007/s10439-012-0593-5

Bogen, D. K., Rabinowitz, S. A., Needleman, A., McMahon, T. A., and Abelmann, W. H. (1980). An analysis of the mechanical disadvantage of myocardial infarction in the canine left ventricle. *Circ. Res.* 47, 728–741. doi: 10.1161/01.res.47.5.728

Bovendeerd, P. H., Arts, T., Delhaas, T., Huyghe, J. M., van Campen, D. H., and Reneman, R. S. (1996). Regional wall mechanics in the ischemic left ventricle: numerical modeling and dog experiments. *Am. J. Physiol.* 270(1 Pt 2), H398–H410. doi: 10.1152/ajpheart.1996.270.1.H398

Canty, J. M. Jr., and Suzuki, G. (2012). Myocardial perfusion and contraction in acute ischemia and chronic ischemic heart disease. *J. Mol. Cell Cardiol.* 52, 822–831. doi: 10.1016/j.yjmcc.2011.08.019

Cerqueira, M. D., Weissman, N. J., Dilsizian, V., Jacobs, A. K., Kaul, S., Laskey, W. K., et al. (2002). Standardized myocardial segmentation and nomenclature for tomographic imaging of the heart. A statement for healthcare professionals from the cardiac imaging committee of the council on clinical cardiology of the American Heart Association. *Circulation* 105, 539–542. doi: 10.1161/hc0402.102975

Codella, N. C., Lee, H. Y., Fieno, D. S., Chen, D. W., Hurtado-Rua, S., Kochar, M., et al. (2012). Improved left ventricular mass quantification with partial voxel interpolation: in vivo and necropsy validation of a novel cardiac MRI segmentation algorithm. *Circ. Cardiovasc. Imaging* 5, 137–146. doi: 10.1161/CIRCIMAGING.111.966754

Codella, N. C., Weinsaft, J. W., Cham, M. D., Janik, M., Prince, M. R., and Wang, Y. (2008). Left ventricle: automated segmentation by using myocardial effusion threshold reduction and intravoxel computation at MR imaging. *Radiology* 248, 1004–1012. doi: 10.1148/radiol.2482072016

Genet, M., Chuan Lee, L., Ge, L., Acevedo-Bolton, G., Jeung, N., Martin, A., et al. (2015). A novel method for quantifying smooth regional variations in myocardial contractility within an infarcted human left ventricle based on delay-enhanced magnetic resonance imaging. *J. Biomech. Eng.* 137:081009. doi: 10.1115/1.4030667

Gorman, R. C., Gorman, J. H. III, and Edmunds, L. H. Jr. (2003). "Ischemic mitral regurgitation," in *Cardiac Surgery in the Adult*, eds L. H. Cohn, and L. H. Edmunds, Jr. (New York: McGraw-Hill), 1751–1770.

Gorman, R. C., McCaughan, J. S., Ratcliffe, M. B., Gupta, K. B., Streicher, J. T., Ferrari, V. A., et al. (1995). Pathogenesis of acute ischemic mitral regurgitation in three dimensions. *J. Thorac. Cardiovasc. Surg.* 109, 684–693. doi: 10.1016/s0022-5223(95)70349-7

Guccione, J. M., McCulloch, A. D., and Waldman, L. K. (1991). Passive material properties of intact ventricular myocardium determined from a cylindrical model. *J. Biomech. Eng.* 113, 42–55. doi: 10.1115/1.2894084

Guccione, J. M., Moonly, S. M., Moustakidis, P., Costa, K. D., Moulton, M. J., Ratcliffe, M. B., et al. (2001). Mechanism underlying mechanical dysfunction in the border zone of left ventricular aneurysm: a finite element model study. *Ann. Thorac. Surg.* 71, 654–662. doi: 10.1016/s0003-4975(00)02338-9

Guccione, J. M., Waldman, L. K., and McCulloch, A. D. (1993). Mechanics of active contraction in cardiac muscle: part II–Cylindrical models of the systolic left ventricle. *J. Biomech. Eng.* 115, 82–90. doi: 10.1115/1.2895474

Heitner, J. F., Kim, R. J., Kim, H. W., Klem, I., Shah, D. J., Debs, D., et al. (2019). Prognostic value of vasodilator stress cardiac magnetic resonance imaging: a multicenter study with 48000 patient-years of follow-up. *JAMA Cardiol.* 4, 256–264. doi: 10.1001/jamacardio.2019.0035

Hocum Stone, L. L., Swingen, C., Holley, C., Wright, C., Chappuis, E., Ward, H. B., et al. (2017). Magnetic resonance imaging assessment of cardiac function in a swine model of hibernating myocardium 3 months following bypass surgery. *J. Thorac. Cardiovasc. Surg.* 153, 582–590. doi: 10.1016/j.jtcvs.2016.10.089

Janik, M., Cham, M. D., Ross, M. I., Wang, Y., Codella, N., Min, J. K., et al. (2008). Effects of papillary muscles and trabeculae on left ventricular quantification: increased impact of methodological variability in patients with left ventricular hypertrophy. *J. Hypertens.* 26, 1677–1685. doi: 10.1097/HJH.0b013e328302ca14

Kang, D. H., Sun, B. J., Kim, D. H., Yun, S. C., Song, J. M., Choo, S. J., et al. (2011). Percutaneous versus surgical revascularization in patients with ischemic mitral regurgitation. *Circulation* 124(11 Suppl.), S156–S162. doi: 10.1161/CIRCULATIONAHA.110.011254

Kim, J., Alakbarli, J., Yum, B., Tehrani, N. H., Pollie, M. P., Abouzeid, C., et al. (2019). Tissue-based markers of right ventricular dysfunction in ischemic mitral regurgitation assessed via stress cardiac magnetic resonance and three-dimensional echocardiography. *Int. J. Cardiovasc. Imaging* 35, 683–693. doi: 10.1007/s10554-018-1500-4

Kim, R. J., Fieno, D. S., Parrish, T. B., Harris, K., Chen, E. L., Simonetti, O., et al. (1999). Relationship of MRI delayed contrast enhancement to irreversible injury, infarct age, and contractile function. *Circulation* 100, 1992–2002. doi: 10.1161/01.cir.100.19.1992

Kim, R. J., Wu, E., Rafael, A., Chen, E. L., Parker, M. A., Simonetti, O., et al. (2000). The use of contrast-enhanced magnetic resonance imaging to identify reversible myocardial dysfunction. *N. Engl. J. Med.* 343, 1445–1453. doi: 10.1056/NEJM200011163432003

Klem, I., Heitner, J. F., Shah, D. J., Sketch, MH Jr, Behar, V., Weinsaft, J., et al. (2006). Improved detection of coronary artery disease by stress perfusion cardiovascular magnetic resonance with the use of delayed enhancement infarction imaging. *J. Am. Coll. Cardiol.* 47, 1630–1638. doi: 10.1016/j.jacc.2005.10.074

Liel-Cohen, N., Guerrero, J. L., Otsuji, Y., Handschumacher, M. D., Rudski, L. G., Hunziker, P. R., et al. (2000). Design of a new surgical approach for ventricular remodeling to relieve ischemic mitral regurgitation: insights from 3-dimensional echocardiography. *Circulation* 101, 2756–2763. doi: 10.1161/01.cir.101.23.2756

Mazhari, R., Omens, J. H., Covell, J. W., and McCulloch, A. D. (2000). Structural basis of regional dysfunction in acutely ischemic myocardium. *Cardiovasc. Res.* 47, 284–293. doi: 10.1016/s0008-6363(00)00089-4

Mendonca Costa, C., Plank, G., Rinaldi, C. A., Niederer, S. A., and Bishop, M. J. (2018). Modeling the electrophysiological properties of the infarct border zone. *Front. Physiol.* 9:356. doi: 10.3389/fphys.2018.00356

Möller, T., and Trumbore, B. (1997). Fast, minimum storage ray-triangle intersection. *J. Graphics Tools* 2, 21–28. doi: 10.1080/10867651.1997.10487468

Moreo, A., Ambrosio, G., De Chiara, B., Pu, M., Tran, T., Mauri, F., et al. (2009). Influence of myocardial fibrosis on left ventricular diastolic function: noninvasive assessment by cardiac magnetic resonance and echo. *Circ. Cardiovasc. Imaging* 2, 437–443. doi: 10.1161/CIRCIMAGING.108.838367

Morgan, A. E., Zhang, Y., Tartibi, M., Goldburg, S., Kim, J. J., Nguyen, T. D., et al. (2018). Ischemic mitral regurgitation: abnormal strain overestimates nonviable myocardium. *Ann. Thorac. Surg.* 105, 1754–1761. doi: 10.1016/j.athoracsur.2018.01.005

Ommen, S. R., Nishimura, R. A., Appleton, C. P., Miller, F. A., Oh, J. K., Redfield, M. M., et al. (2000). Clinical utility of doppler echocardiography and tissue doppler imaging in the estimation of left ventricular filling pressures: a comparative simultaneous doppler-catheterization study. *Circulation* 102, 1788–1794. doi: 10.1161/01.cir.102.15.1788

Osman, N. F., McVeigh, E. R., and Prince, J. L. (2000). Imaging heart motion using harmonic phase MRI. *IEEE Trans. Med. Imaging* 19, 186–202. doi: 10.1109/42.845177

Penicka, M., Linkova, H., Lang, O., Fojt, R., Kocka, V., Vanderheyden, M., et al. (2009). Predictors of improvement of unrepaired moderate ischemic mitral regurgitation in patients undergoing elective isolated coronary artery bypass graft surgery. *Circulation* 120, 1474–1481. doi: 10.1161/CIRCULATIONAHA.108.842104

Ryf, S., Spiegel, M. A., Gerber, M., and Boesiger, P. (2002). Myocardial tagging with 3D-CSPAMM. *J. Magn. Reson. Imaging* 16, 320–325. doi: 10.1002/jmri.10145

Sievers, B., Elliott, M. D., Hurwitz, L. M., Albert, T. S., Klem, I., Rehwald, W. G., et al. (2007). Rapid detection of myocardial infarction by subsecond, free-breathing delayed contrast-enhancement cardiovascular magnetic resonance. *Circulation* 115, 236–244. doi: 10.1161/CIRCULATIONAHA.106.635409

Veress, A. I., Fung, G. S., Lee, T. S., Tsui, B. M., Kicska, G. A., Paul Segars, W., et al. (2015). The direct incorporation of perfusion defect information to define ischemia and infarction in a finite element model of the left ventricle. *J. Biomech. Eng.* 137:051004. doi: 10.1115/1.4028989

Walker, J. C., Ratcliffe, M. B., Zhang, P., Wallace, A. W., Fata, B., Hsu, E. W., et al. (2005). MRI-based finite-element analysis of left ventricular aneurysm. *Am. J. Physiol. Heart Circ. Physiol.* 289, H692–H700. doi: 10.1152/ajpheart.01226.2004

Wang, D., Kirby, R. M., Macleod, R. S., and Johnson, C. R. (2013). Inverse electrocardiographic source localization of ischemia: an optimization framework and finite element solution. *J. Comput. Phys.* 250, 403–424. doi: 10.1016/j.jcp.2013.05.027

Wenk, J. F., Sun, K., Zhang, Z., Soleimani, M., Ge, L., Saloner, D., et al. (2011). Regional left ventricular myocardial contractility and stress in a finite element model of posterobasal myocardial infarction. *J. Biomech. Eng.* 133:044501. doi: 10.1115/1.4003438

Wijns, W., Vatner, S. F., and Camici, P. G. (1998). Hibernating myocardium. *N. Engl. J. Med.* 339, 173–181. doi: 10.1056/NEJM199807163390307

Conflict of Interest: The authors declare that the research was conducted in the absence of any commercial or financial relationships that could be construed as a potential conflict of interest.

frontiers in Physiology

ORIGINAL RESEARCH
published: 17 March 2020
doi: 10.3389/fphys.2020.00207

Numerical Simulation of the Effect of Pulmonary Vascular Resistance on the Hemodynamics of Reoperation After Failure of One and a Half Ventricle Repair

*Yan Fu[1], Aike Qiao[1], Yao Yang[2] and Xiangming Fan[2]**

[1] College of Life Science and Bioengineering, Beijing University of Technology, Beijing, China, [2] Beijing Anzhen Hospital, Capital Medical University, Beijing, China

Edited by:
Yunlong Huo,
Shanghai Jiao Tong University, China

Reviewed by:
Fuyu Lyan,
First Moscow State Medical University, Russia
Shengzhang Wang,
Fudan University, China

***Correspondence:**
Xiangming Fan
fanxiangming@126.com

Specialty section:
This article was submitted to Computational Physiology and Medicine, a section of the journal Frontiers in Physiology

Received: *21 October 2019*
Accepted: *21 February 2020*
Published: *17 March 2020*

Citation:
Fu Y, Qiao A, Yang Y and Fan X (2020) Numerical Simulation of the Effect of Pulmonary Vascular Resistance on the Hemodynamics of Reoperation After Failure of One and a Half Ventricle Repair. Front. Physiol. 11:207. doi: 10.3389/fphys.2020.00207

Objective: The one and a half ventricle repair (1.5VR) is a common clinical choice for patients with right heart dysfunction. Considering the influence of blood circulation failure and reoperation in urgent need, this essay aims to explore the hemodynamic effects of different pulmonary vascular resistance (PVR) values on reoperation after 1.5VR failure.

Methods: The lumped parameter model (LPM) was used to simulate the reoperation, including the return biventricular repair (2VR), ligation of azygos vein (1.5VR′) and return single ventricular repair (1.0VR). Firstly, the debugging parameters were used to simulate the hemodynamics of 2VR. Secondly, the value of PVR was changed from one to four times while the other parameters remained unchanged. Finally, 15 cardiac cycles were simulated and the 15th result was obtained. In this work, the left and right ventricular stroke work and their sum (Plv, Prv, Ptotal), the left and right ventricular ejection fraction (LVEF, RVEF), the mean Cardiac Output (mCO) and the mean pressure and flow-rate ratio of superior and inferior vena cava (mPsvc\mPivc and mQsvc\mQivc), respectively, were used to describe the hemodynamics of reoperation.

Results: With the change of PVR from one to four times, the values of Plv, Prv, Ptotal, LVEF, and RVEF gradually decreased. The change rate of Plv, Ptotal and LVEF of 1.0VR were the largest in the three kinds of reoperation. The change rate of Prv of 1.5VR′ was larger than that of 2VR, but it was the opposite for their EF change rate. The mCO of 2VR, 1.5VR′, and 1.0VR decreased by 18.53%, 37.58%, and 48.07%, respectively. The mPsvc\mPivc of 1.5VR′ increased from 3.76 to 6.77 and the mQsvc\mQivc decreased from 0.55 to 0.36, while the mPsvc\mPivc and mQsvc\mQivc of 2VR and 1.0VR remained 1 and 0.67, respectively. The peak value of the tricuspid flow-rate (Qti) waveform of 2VR and 1.5VR′ changed from “E peak” to “A peak.”

Conclusion: The numerical results demonstrate the highly reoperation-dependent hemodynamic consequences and their responses to variations in PVR. Comprehensive analysis of EF, mCO and ventricular stroke work indicates that PVR has a greater impact on 1.5VR′ and 1.0VR. Therefore, we suggest that the selection strategy of reoperation should focus on PVR.

Keywords: one and a half ventricle repair, pulmonary vascular resistance, lumped parameter model, hemodynamics, numerical simulation

INTRODUCTION

The one and a half ventricle repair (1.5VR) is widely applied in the treatment of congenital heart disease with abnormal structure and function of the right ventricle like the Pulmonary Atresia with Intact Ventricular Septum (PA with IVS) (Talwar et al., 2018; Wright et al., 2019), Tetralogy of Fallot (ToF) (Talwar et al., 2018) and Ebstein's Anomaly (EA) (Malhotra et al., 2018; Talwar et al., 2018; Akkaya et al., 2019). The operation consists of the bidirectional cavopulmonary shunt (BCPS) and the correction of the intracardiac malformation, and aims to make the right ventricle bear only blood flow of the lower body; thus, the sum of the left and right ventricle stroke work (Ptotal) won't change while the right ventricular volume load is reduced (Barron, 2018). This operation maintains a low right atrial pressure, pulsating pulmonary blood flow and adequate blood oxygen during the short/medium term (Bhattarai et al., 2017; Talwar et al., 2018), which reduces the occurrence of poor prognosis such as the biventricular repair induced right heart failure (Talwar et al., 2018) and the single ventricular repair induced circulatory failure (Sharma et al., 2012; Talwar et al., 2018).

However, in patients with pulmonary vascular dysplasia or left ventricular dysfunction, complications such as the superior vena cava hypertension and Cardiac Output (CO) reduction are very likely to happen (Liu et al., 2011). When the superior vena cava pressure (Psvc) is higher than the normal value (4–6 mmHg), an adaptive growth of the azygos vein may occur. In the literature, the internal diameter of the azygos vein was positively correlated with Psvc (Preger et al., 1969; Contou et al., 2014), which would lead to a vascular steal phenomenon in the azygos vein, namely the rate of the blood flow from the superior vena cava to the pulmonary artery will decrease, while the blood flow from the azygos vein back to the right ventricle will increase, as shown in **Figure 1**. This phenomenon causes an increase in the right ventricular preload after 1.5VR. If the Pulmonary Vascular Resistance (PVR) is further increased, irreversible changes will occur in the pulmonary vascular remodeling (Peng et al., 2016), leading to an increase in the right ventricle afterload. Finally, the circulation function after the 1.5VR surgery will deteriorate.

Fortunately, the occurrence of such adverse events can be avoided with reoperation. The clinical reoperation measures include the return biventricular repair (2VR), the ligation of the azygos vein (1.5VR′), the return single ventricular repair (1.0VR), the artificial tonic solution and many others. The selection of the reoperation in clinical practice generally takes into account the morphological parameters and physiological functions of the left and right ventricles (Shimizu et al., 2010). However, there is still a lack of research on the effect of pulmonary vascular development on the hemodynamics after reoperation. Due to the limited number of patients, different conditions of patients and their right ventricles, the effects of pulmonary vascular development on 2VR, 1.5VR′, and 1.0VR cannot be tested through clinical research. For patients with different pulmonary vascular development, it is difficult to design experiments to reproduce the hemodynamics before and after reoperation.

In order to study various hemodynamic problems associated with congenital heart disease (CHD), a wide range of computational models have been established in the literature [i.e., the lumped parameter models (LPM)]. Zhang et al. (2019) developed a zero-dimensional (0D) open-loop model to analyze the hemodynamics in aneurysms. Smith et al. (2004) constructed the smallest human cardiovascular system (OD model) to successfully capture the physiological changes. Ma et al. (2014)

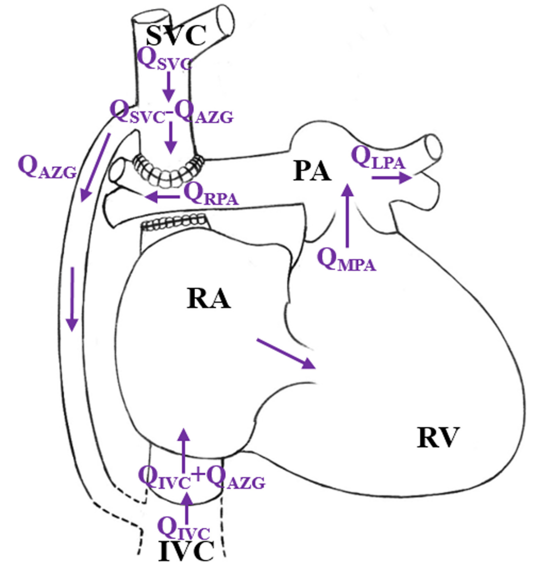

FIGURE 1 | Schematic diagram of "stolen blood" phenomenon of azygos vein. (RA, right atrium; RV, right ventricle; SVC, superior vena cava; IVC, Inferior vena cava; PA, pulmonary artery; Q_{AZG}, flow-rate of azygos vein; Q_{MPA}, flow-rate of main pulmonary artery; Q_{LPA}, flow-rate of left pulmonary artery; Q_{RPA}, flow-rate of right pulmonary artery; Q_{SVC}, flow-rate of superior vena cava; Q_{IVC}, flow-rate of Inferior vena cava).

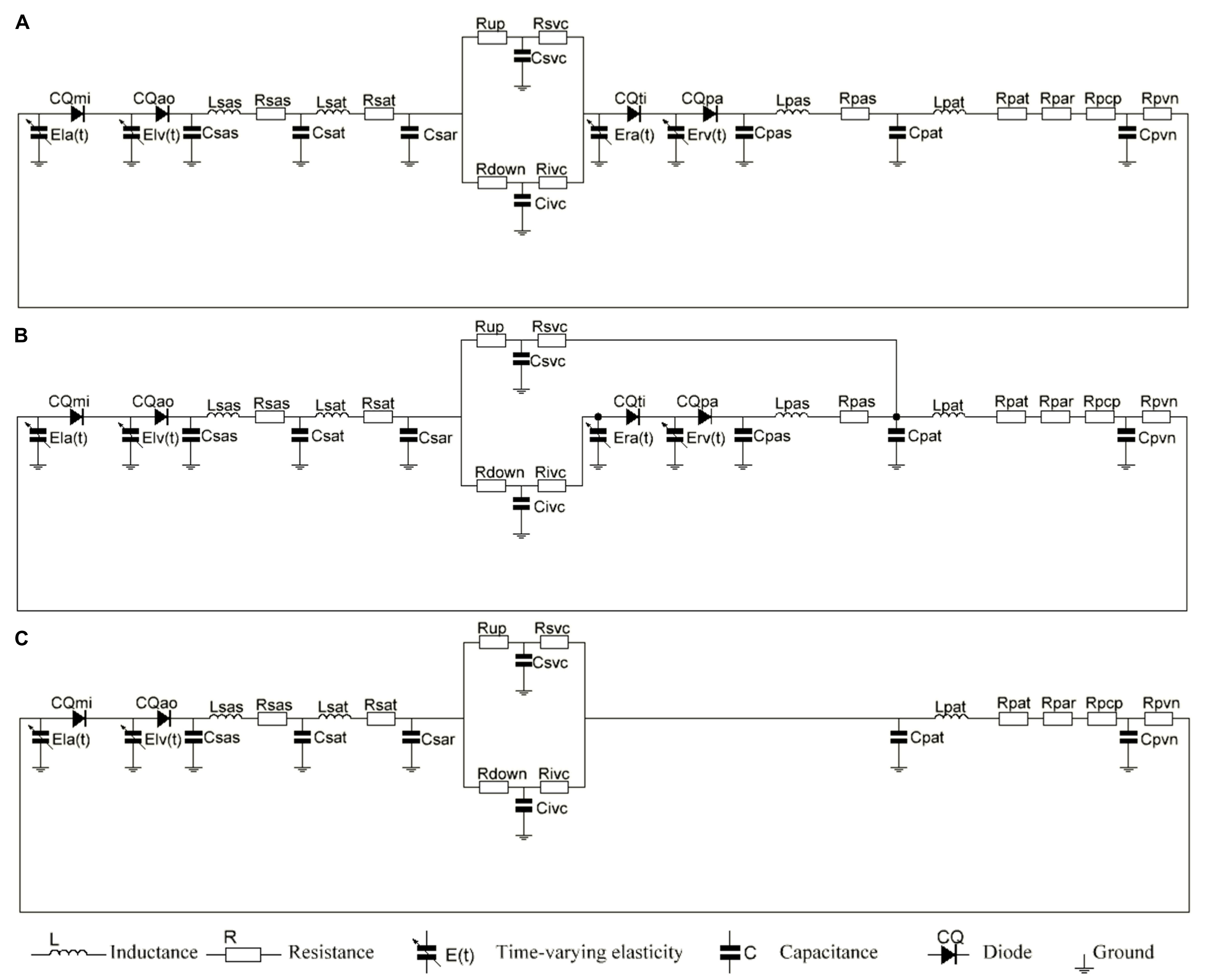

FIGURE 2 | (A) The electric equivalent circuit of biventricular repair (2VR). **(B)** The electric equivalent circuit of ligation of azygos vein (1.5VR′). **(C)** The electric equivalent circuit of single ventricular repair (1.0VR). Nomenclature (R, resistance; C, compliance; CQ, flow coefficient; E, elastance; L, inertance). Subscripts (ao, aortic valve; la, left atrium; lv, left ventricle; mi, mitral value; pa, pulmonary aortic valve; par, pulmonary arterioles; pas, pulmonary artery sinus; pat, pulmonary artery; pcp, pulmonary capillary; pvn, pulmonary vein; ra, right atrium; rv, right ventricle; sar, systemic arterioles; sas, systemic aortic sinus; sat, systemic artery; up, upper of body, down lower of body; svc, systemic vena cava; ivc, interior vena cava; ti, tricuspid valve).

constructed an LPM for the blood circulation system of single ventricular patients to observe the recovery of different stenosis degrees of the pulmonary artery after the Gleen surgery. Zhao et al. (2015) used the 0D/3D (three-dimensional) coupling model to study the hemodynamic effects of the anastomoses in modified Blalock-Taussig shunt. Corsini et al. (2018) focused on coronary perfusion and aortic arch hemodynamics using computational multi-domain modeling.

This work aims to develop a simple and effective LPM closed model, which only includes systemic and pulmonary circulation. According to the 1.5VR surgery characteristics, the systemic circulation is divided into upper and lower body blood circulation. Therefore, this work builds on the modeling experience of the former report. We attempted to use the lumped parameter model (LPM) based on the lumped parameter state-variable equation (Di Molfetta et al., 2015; Duanmu et al., 2018) to quantitatively analyze the hemodynamic differences between three reoperation procedures of a given PVR and their sensitivity to PVR. The results will provide guidance to select the strategy for reoperation procedures after 1.5VR failure.

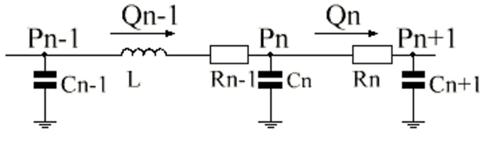

FIGURE 3 | Single-compartment circuit representation. P, pressure; R, resistance; C, compliance; L, inertance; Q, flow-rate, n–1, n and n+1, compartment indexes.

MATERIALS AND METHODS

The equivalent circuit model that was used to simulate the cardiovascular system is shown in **Figure 2**. We coupled the Time-varying Elastic Cardiac Cavity Model with the three-element Windkessel vascular model (Korakianitis and Shi, 2006a) to construct a mathematical model of the cardiovascular system after reoperation. The mathematical model consists of three main parts: the heart, the systemic circulation and the pulmonary circulation.

The Heart

The heart is modeled as a four-chamber pump with a variable elasticity and four heart valves that control the direction of the blood flow.

Ventricle

The pressure-volume relationship is used to describe the basic characteristics of the ventricle. Suga et al. (Suga et al., 1973; Suga and Sagawa, 1974) established the idea of a cardiac pump model to simulate the systolic and diastolic functions of the ventricle based on the Frank Starling theory. The ventricular pressure of

TABLE 1 | Parameters used in model.

Heart rate (HR), beats/min			75			
Duration of cardiac cycle (tc), s			0.8			
Beginning of P wave in ECG (Tpwb), s			0.92*tc			
Duration of P wave in ECG (Tpww), s			0.08*tc			
			LV	**RV**	**LA**	**RA**
End-systolic elastance (Ees), mmHg/mL			2.5	1.15	0.2	0.25
End-diastolic elastance (Eed), mmHg/mL			0.05	0.07	0.15	0.15
Unstressed volume (V0), mL			5	10	0	0
			Mitral	**Aortic**	**Tricuspid**	**Pulmonary aortic**
Valve flow coefficient (CQ), ml/(s·mmHg$^{0.5}$)			400	350	400	350
	Resistance (R), mmHg·s/mL		**Compliance (C), mL/mmHg**		**Inertance (L), mmHg·s^2/mL**	
Systemic circulation	Rsas	0.003	Csas	0.08	Lsas	1.86E-05
	Rsat	0.05	Csat	0.7	Lsat	0.0017
	Rup	2.325	Csar	0.5		
	Rsvc	0.0375	Csvc	8.2		
	Rivc	0.025	Civc	12.3		
	Rdown	1.55				
Pulmonary circulation	Rpas	0.002	Cpas	0.18	Lpas	1.56E-05
	Rpat	0.01	Cpat	4.75	Lpat	0.0017
	Rpar	0.08	Cpvn	20.5		
	Rpcp	0.045				
	Rpvn	0.015				

TABLE 2 | Simulation results and normal physiological range data.

Parameter	**Simulation results**	**Physiological range**
Left ventricular end-systolic pressure (Plves), mmHg	116.1	90–140
Left ventricular end-diastolic pressure (Plved), mmHg	4.206	0–10
Left atrium end-systolic pressure (Plaes), mmHg	7.979	5–10
Left atrium end-diastolic pressure (Plaed), mmHg	4.681	–2–5
Systemic aortic sinus end-systolic pressure (Psas_es), mmHg	116	90–140
Systemic aortic sinus end-diastolic pressure (Psas_ed), mmHg	74.19	60–90
Right ventricular end-systolic pressure (Prves), mmHg	31.98	18–35
Right ventricular end-diastolic pressure (Prved), mmHg	4.195	0–10
Right atrium end-systolic pressure (Praes), mmHg	7.727	5–10
Right atrium end-diastolic pressure (Praed), mmHg	4.649	–2–5
Pulmonary artery sinus end-systolic pressure (Ppas_es), mmHg	31.7	18–35
Pulmonary artery sinus end-diastolic pressure (Ppas_ed), mmHg	9.617	6–15
Stroke volume (SV), mL	72.8	60–80
Mean cardiac output (mCO), L/min	5.46	3.5–5.5

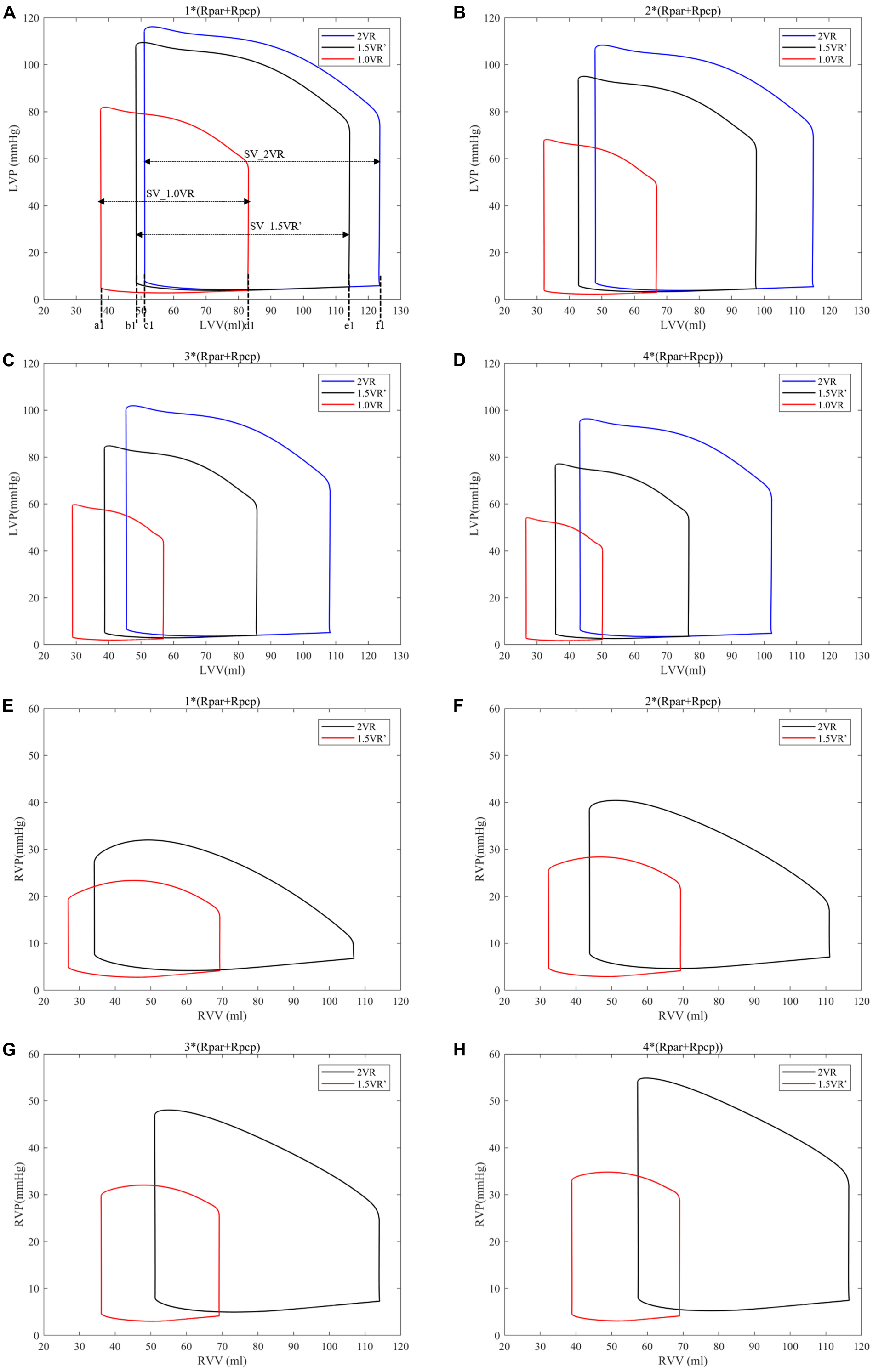

FIGURE 4 | (A) Left ventricular P-V curve for three procedures when PVR is 1*(Rpar + Rpcp). **(B)** Left ventricular P-V curve for three procedures when PVR is 2*(Rpar + Rpcp). **(C)** Left ventricular P-V curve for three procedures when PVR is 3*(Rpar + Rpcp). **(D)** Left ventricular P-V curve for three procedures when PVR is 4*(Rpar + Rpcp). **(E)** Right ventricular P-V curve for three procedures when PVR is 1*(Rpar + Rpcp). **(F)** Right ventricular P-V curve for three procedures when PVR is 2*(Rpar + Rpcp). **(G)** Right ventricular P-V curve for three procedures when PVR is 3*(Rpar + Rpcp). **(H)** right ventricular P-V curve for three procedures when PVR is 4*(Rpar + Rpcp). a1, b1, and c1, left ventricular end-systolic volume as indicated. d1, e1, and f1, left ventricular end-diastole volume as indicated. SV, stroke volume. (Rpar, resistance of pulmonary arterioles; Rpcp, resistance of pulmonary capillary; LVP, left ventricular pressure; LVV, left ventricular volume; RVP, right ventricular pressure; RVV, right ventricular volume; P-V, pressure-volume).

this model is described as a linear function of the chamber volume and elasticity, and can be mathematically expressed as follows:

$$E(t) = \frac{P(t)}{V(t) - V0} \tag{1}$$

where E(t) represents the time-varying elasticity, P(t) and V(t) represent the instantaneous ventricular pressure and volume, respectively, and V0 represents the corresponding ventricular volume when the ventricular pressure is 0. The ventricular model in this paper refers to that of Li et al. (2019) and is expressed by equations (2) and (3).

$$E(t) = (Emax - Emin) \cdot En(tn) + Emin \tag{2}$$

$$En(tn) = 1.55 \cdot \left(\frac{\left(\frac{tn}{0.7}\right)^{1.9}}{1 + \left(\frac{tn}{0.7}\right)^{1.9}} \right) \cdot \left(\frac{1}{1 + \left(\frac{tn}{1.17}\right)^{21.9}} \right) \tag{3}$$

where En(tn) is the normalized elasticity, also known as the "double hill" function, $t_n = t/t_{max} t_{max} = 0.15t_c + 0.2$, tc = 60/HR, and refers to a typical cardiac cycle, HR is the heart rate and Emax and Emin are the end-systolic and end-diastolic elasticity of ventricles, respectively. Although the model of the right ventricle is similar to that of the left one, the coefficients of the elastic chamber are different.

Atrium

With the generation of the P wave in the electrocardiogram (ECG), the atrial contraction leads to a rapid increase in the ventricular volume and pressure during diastole. This effect is sometimes referred to as the "atrial pulsation," which accounts for 20–30% of the ventricular filling and reflects the function of the "booster pump" of the atrium (Korakianitis and Shi, 2006a). The modeling process of the atrium is similar to that of the ventricle. According to the reference (Korakianitis and Shi, 2006b), this essay describes the dynamic changes of the atrium with the parameter values and activation function. Taking the left atrium as an example, the equations of the elastic time-varying function and activation function are shown in Eq. 4 and Eq. 5, respectively.

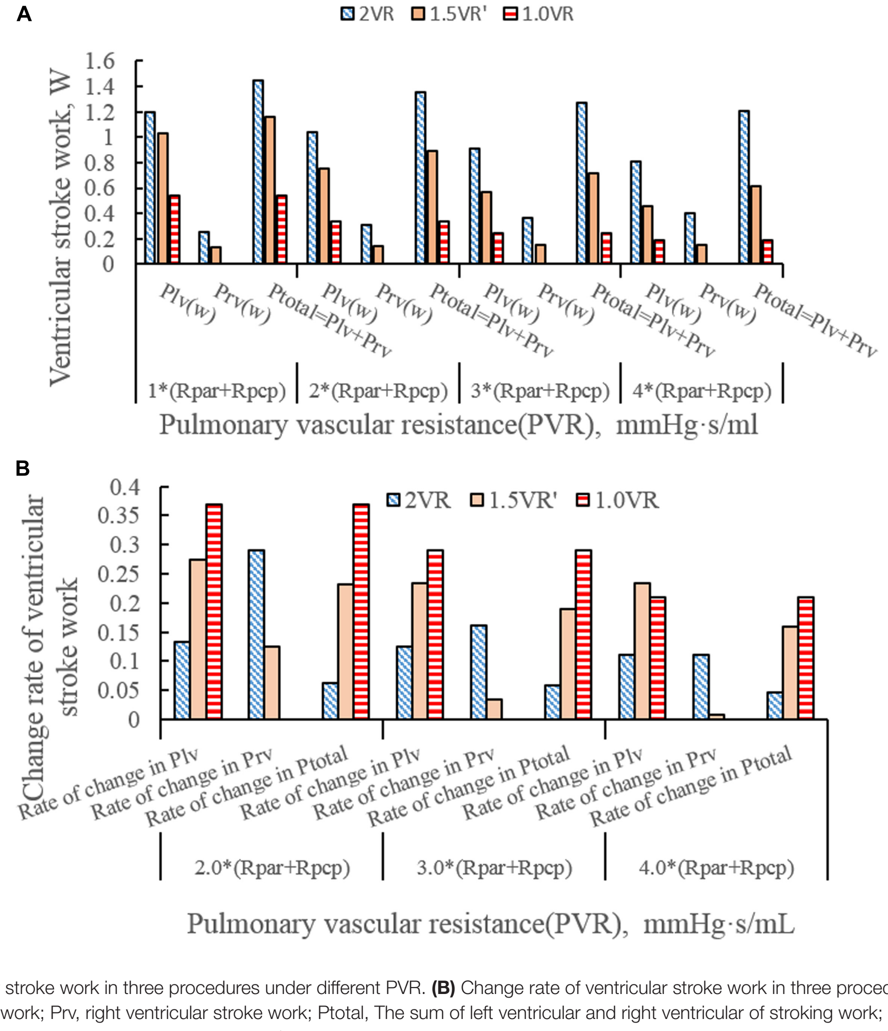

FIGURE 5 | (A) Ventricular stroke work in three procedures under different PVR. **(B)** Change rate of ventricular stroke work in three procedures under different PVR. (Plv, left ventricular stroke work; Prv, right ventricular stroke work; Ptotal, The sum of left ventricular and right ventricular of stroking work; Rpar, resistance of pulmonary arterioles; Rpcp, resistance of pulmonary capillary).

$$\mathrm{Ela} = \left(\mathrm{Elamax} - \mathrm{Elamin}\right) \cdot \mathrm{Enla} + \mathrm{Elamin} \tag{4}$$

$$\mathrm{Enla} = \begin{cases} 0 & 0 \le t < Tpwb \\ 1 - \cos\left(\frac{\mathrm{t-Tpwb}}{\mathrm{Tpww}} \cdot 2\pi\right) & \mathrm{Tpwb} \le t < Tpwb + Tpww \\ 0 & Tpwb + Tpww \le t < tc \end{cases} \tag{5}$$

where Tpwb = 0.92*tc is the start time of the P wave in ECG, Tpww = 0.08*tc represents its duration time and Elamax and Elamin show the elasticity of the end-systolic and end-diastolic of the left atrium, respectively. The modeling equation of the right atrium is the same as that of the left atrium, but the parameter values are different.

Valve

A diode is used to control the one-way flow of blood in the LPM. The basic pressure-flow relationship of the valve is described using the "hole" model in fluid mechanics (Korakianitis and Shi, 2006a). Taking the mitral valve as an example, its mathematical expression is shown in Eq. 6 and Eq. 7.

$$\mathrm{Qmi} = \begin{cases} CQmi \cdot ARmi \cdot \sqrt{\mathrm{Pla - Plv}}\, Pla > Plv \\ CQmi \cdot ARmi \cdot \sqrt{\mathrm{Plv - Pla}}\, Plv > Pla \end{cases} \tag{6}$$

$$\mathrm{ARmi} = \begin{cases} 1, & Pla > Plv \\ 0, & Plv > Pla \end{cases} \tag{7}$$

ARmi is the ratio of the valve open area to the maximum area. In this work, the movement process of the valve was ignored, and the movement of the valve was simplified into two states of being fully opened (1) and completely closed (0). Whether the valve is open or not depends on the pressure at both ends of the valve. Finally, CQmi is the valve flow coefficient, which is related to the orifice area when the valve opens.

Blood Circulation Circuit

The systemic circulation was divided into systemic aortic sinus, systemic artery, systemic arterioles and systemic vein. In order

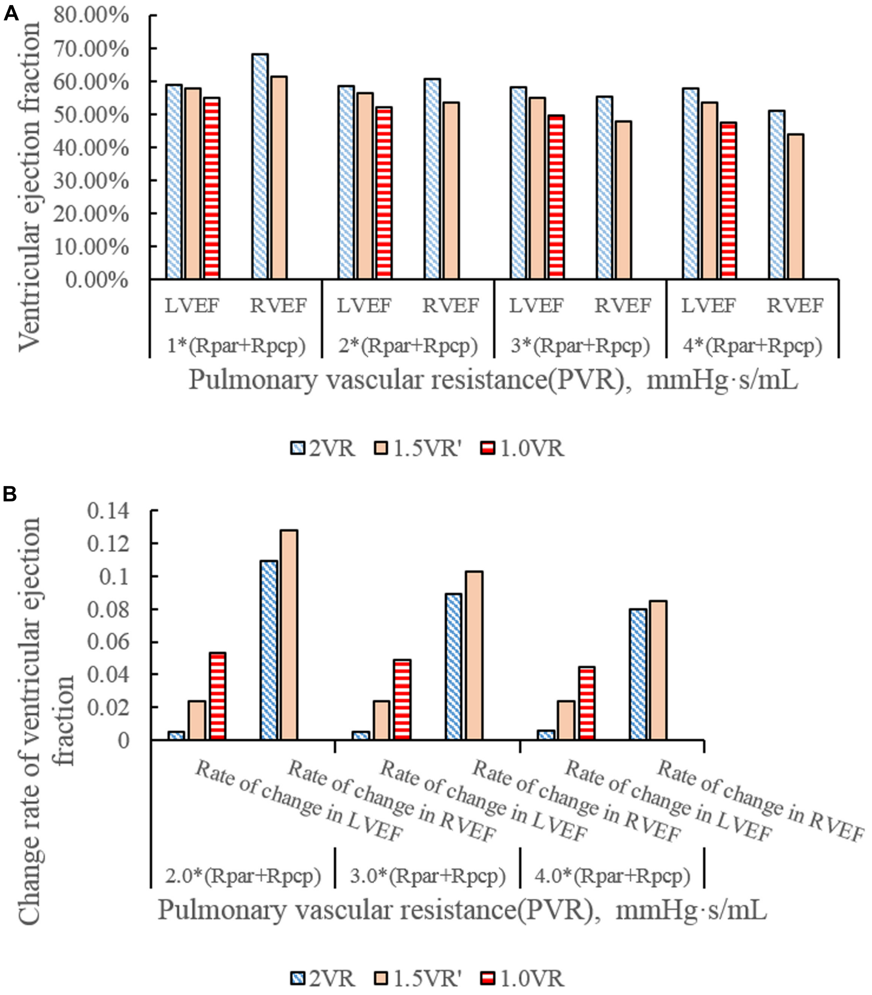

FIGURE 6 | (A)ventricular ejection fraction in three procedures under different PVR. **(B)** Change rate of ventricular ejection fraction in three procedures under different PVR.

to simulate the hemodynamics of the reoperation after 1.5VR failure, systemic arterioles and systemic vein were each divided into two parts: the upper loop and the lower loop (Shimizu et al., 2010). The pulmonary circulation was mainly composed of pulmonary artery sinus, pulmonary artery, pulmonary arterioles, pulmonary capillary and pulmonary vein. Constructing the LPM of the vessel segment needs to focus on the local flow condition (Corsini et al., 2014, 2018). Based on the electrical-fluid parameters, the circuit model of the resistance (R), capacitance (C) and inductance (L) corresponding to the viscosity, elastic coefficient and inertia of the fluid model were applied to mimic the blood flow impedance, blood flow compliance and blood inertia, respectively. Among them, the aortic sinus and artery have better elasticity, and their blood flow is pulsatile. Therefore, the effects of R, C, and L should be considered when modeling these vascular segments. Additionally, the blood flow in the arterioles was relatively smooth, and only the effects of C and R were considered. Moreover, only the R effect needs to be considered for pulmonary capillaries. Otherwise, the main function of the veins is to collect and store blood, so the effects of C and R were considered in venous modeling. The final circuit model is shown in **Figure 2**. The pressure on each C (Pcc) is defined in Eq. 8.

$$\frac{\mathrm{dPcc}}{\mathrm{dt}} = \frac{\sum \mathrm{Qin(t)} - \sum \mathrm{Qout(t)}}{\mathrm{C}} \tag{8}$$

If the effect of L is to be considered, then the flow rate of each part is defined as Eq. 9. Otherwise, it is defined as Eq. 10.

$$\frac{\mathrm{dQin(t)}}{\mathrm{dt}} = \frac{\mathrm{Pin(t)} - \mathrm{Pout(t)} - \mathrm{Qin(t)}*\mathrm{R}}{\mathrm{L}} \tag{9}$$

$$\mathrm{Qin(t)} = \frac{\mathrm{Pin(t)} - \mathrm{Pout(t)}}{\mathrm{R}} \tag{10}$$

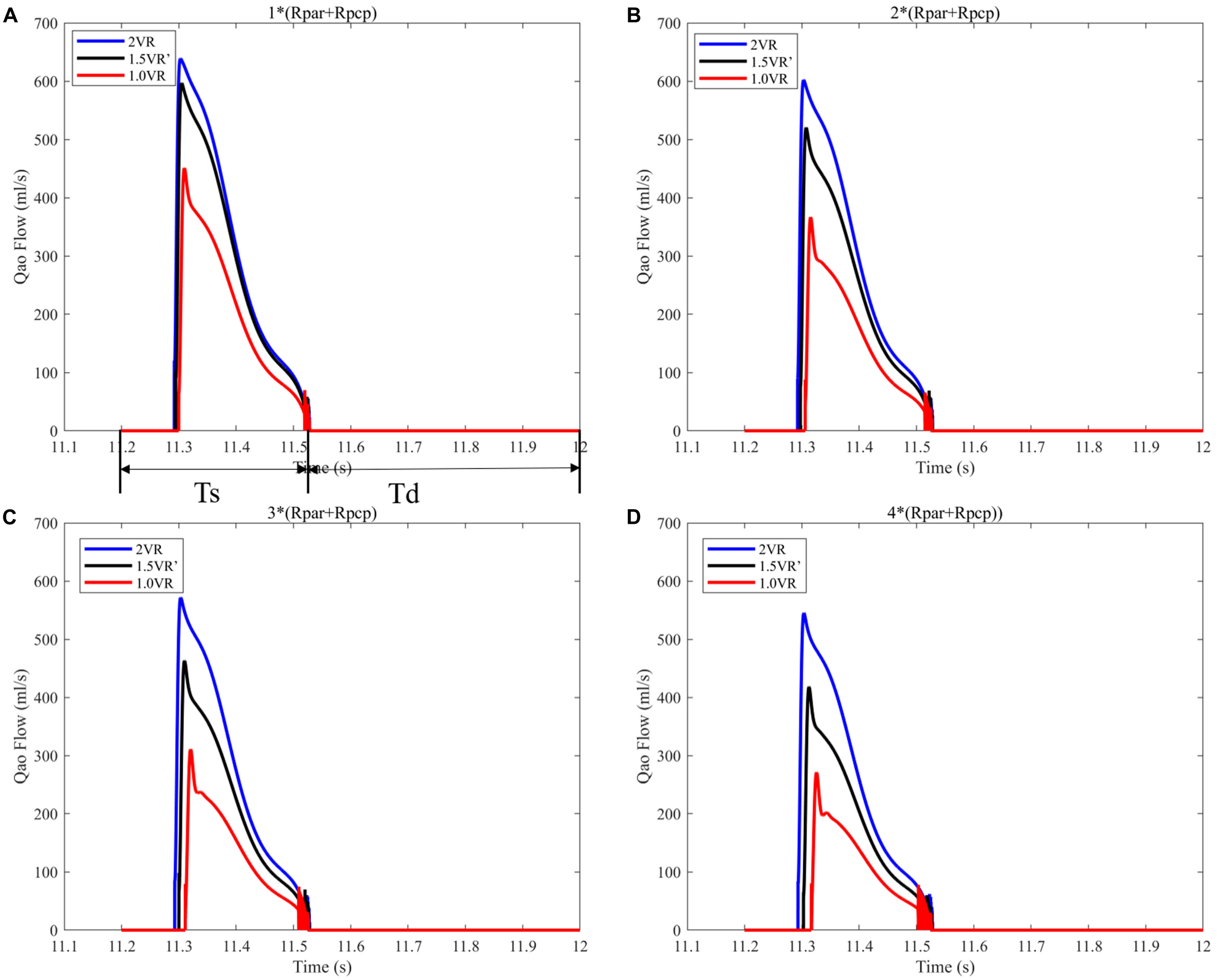

FIGURE 7 | (A) When the PVR is 1*(Rpar + Rpcp), the cardiac output of the three procedures. **(B)** When the PVR is 2*(Rpar + Rpcp), the cardiac output of the three procedures. **(C)** When the PVR is 3*(Rpar + Rpcp), the cardiac output of the three procedures. **(D)** When the PVR is 4*(Rpar + Rpcp), the cardiac output of the three procedures. Ts is the duration of systolic time of left ventricle in a typical cardiac cycle. Td is the duration of diastole time of left ventricle in a typical cardiac cycle. (Qao, cardiac output; PVR, pulmonary vascular resistance; Rpar, resistance of pulmonary arterioles; Rpcp, resistance of pulmonary capillary).

See **Figure 3** illustrates the definition of subscripts in these equations.

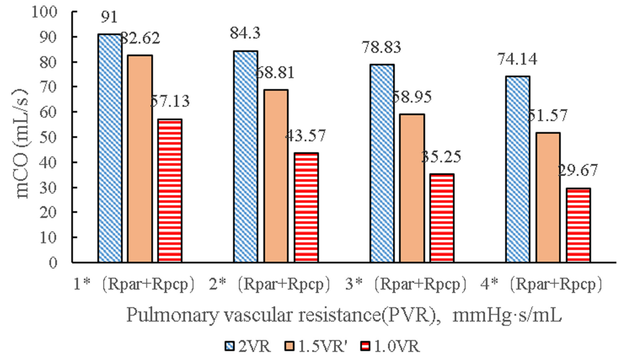

FIGURE 8 | mCO in three procedures under different PVR. (mCO, mean cardiac output; Rpar, resistance of pulmonary arterioles; Rpcp, resistance of pulmonary capillary).

Determining the LPM Parameters

The values of the physiological parameters are generally difficult to measure and vary among individuals. The parameter values in the LPM of reoperation constructed in this work are widely referenced from the literature to select appropriate values. However, in order to simulate different physiological realities, the parameters usually need to be adjusted. It is well known from the literature that the blood flow rate of the descending aorta accounts for 63.8% of CO, and the compliance of the inferior vena cava accounts for 66.6% of the total compliance (Shimizu et al., 2010). Therefore, in this essay, the compliance of the inferior vena cava was set as 0.6 times of the total compliance, and the ratio of the circulating flow of upper body to that of the lower body was 2/3 by adjusting the values of Rup, Rsvc, Rdown, and Rivc. Based on references (Burkhoff and Tyberg, 1993; Heldt et al., 2002), the parameters were adjusted to make the simulation results of 2VR conform to the clinically measured physiological data. The model parameters in this paper are shown in **Table 1**. MATLAB was used to simulate the effect of PVR on the hemodynamics of the reoperation after 1.5VR failure,

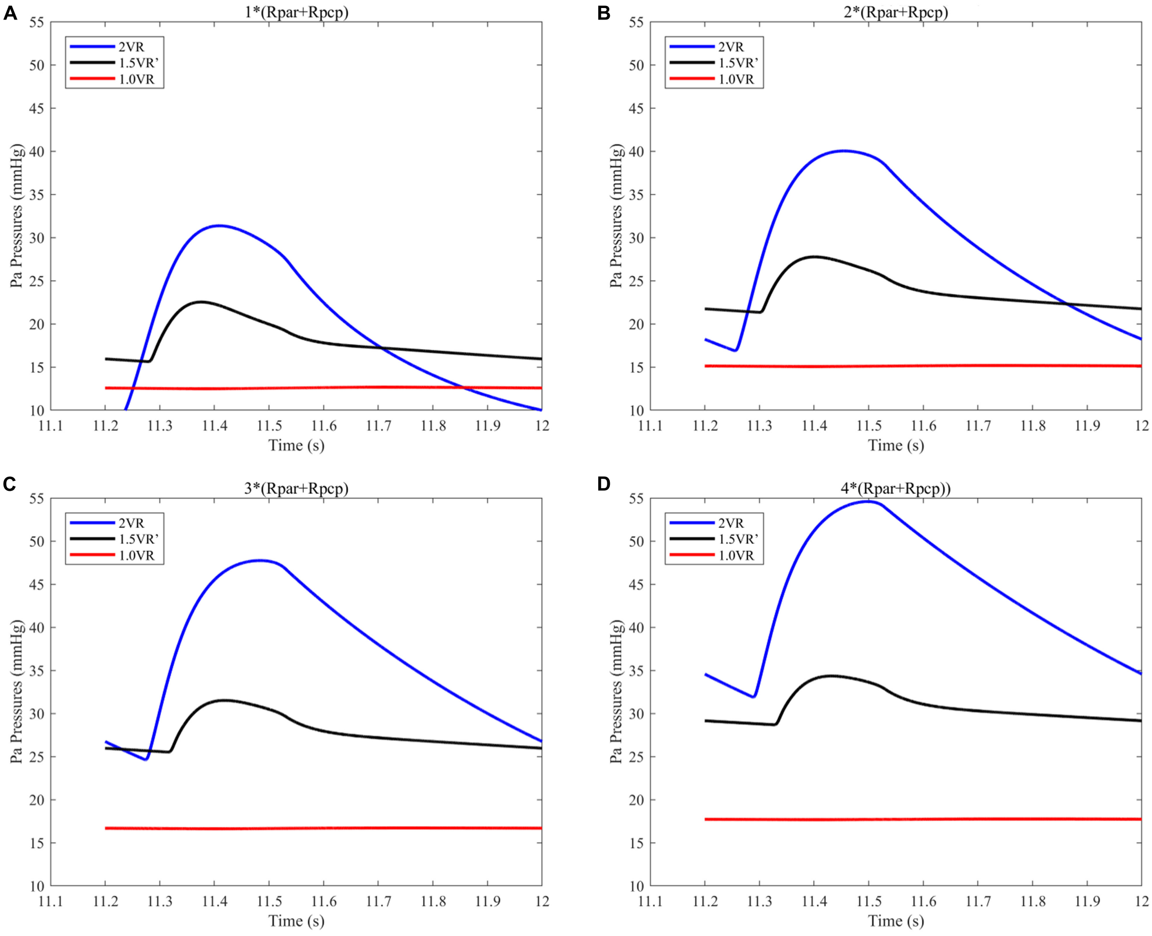

FIGURE 9 | (A) When the PVR is 1*(Rpar + Rpcp), Pa pressure of the three procedures. **(B)** When the PVR is 2*(Rpar + Rpcp), Pa pressure of the three procedures. **(C)** When the PVR is 3*(Rpar + Rpcp), Pa pressure of the three procedures. **(D)** When the PVR is 4*(Rpar + Rpcp), Pa pressure of the three procedures. (Pa, pulmonary artery; Rpar, resistance of pulmonary arterioles; Rpcp, resistance of pulmonary capillary).

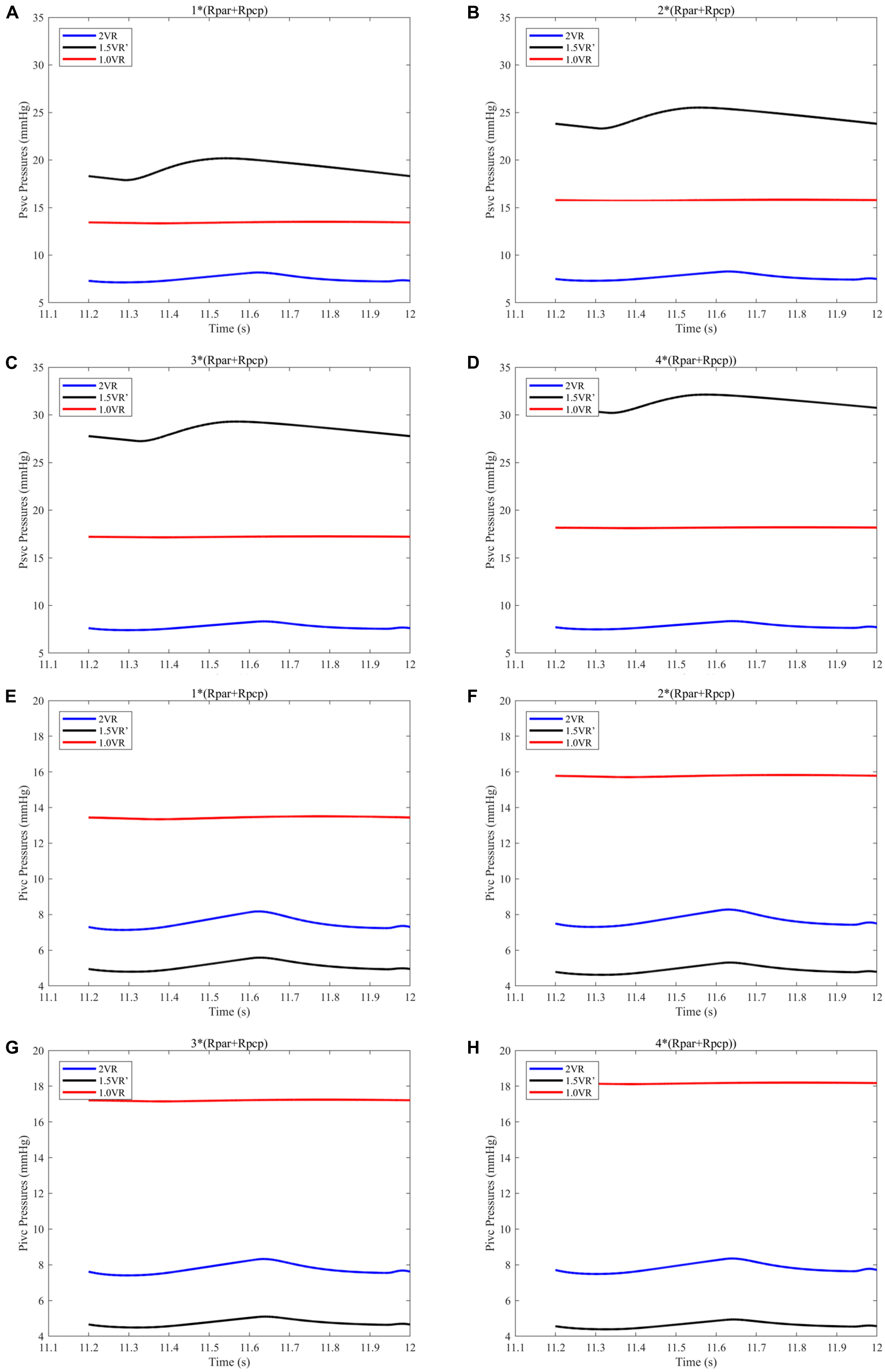

FIGURE 10 | (A) When the PVR is 1*(Rpar + Rpcp), Psvc of the three procedures. **(B)** When the PVR is 2*(Rpar + Rpcp), Psvc of the three procedures. **(C)** When the PVR is 3*(Rpar + Rpcp), Psvc of the three procedures. **(D)** When the PVR is 4*(Rpar + Rpcp), Psvc of the three procedures. **(E)** When the PVR is 1*(Rpar + Rpcp), Pivc of the three procedures. **(F)** When the PVR is 2*(Rpar + Rpcp), Pivc of the three procedures. **(G)** When the PVR is 3*(Rpar + Rpcp), Pivc of the three procedures. **(H)** When the PVR is 4*(Rpar + Rpcp), Pivc of the three procedures. (Psvc, superior vena cava pressure; Pivc, inferior vena cava pressure; Rpar, resistance of pulmonary arterioles; Rpcp, resistance of pulmonary capillary).

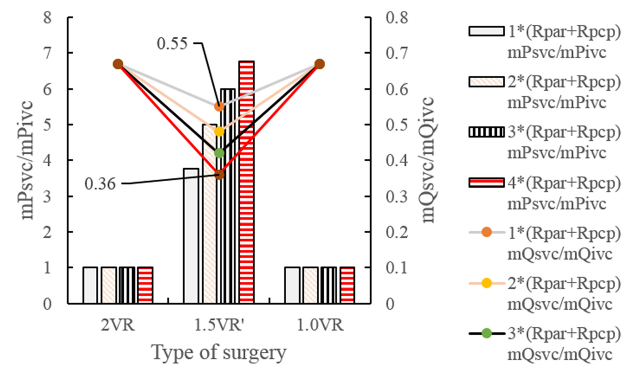

FIGURE 11 | mPsvc/mPivc and mQsvc/mQivc in three procedures under different PVR. (mPsvc mean superior vena cava pressure, mPivc mean inferior vena cava pressure, mQsvc mean flow-rate superior vena cava, mQivc mean flow-rate of inferior vena cava pressure, Rpar resistance of pulmonary arterioles, Rpcp resistance of pulmonary capillary).

in which the value of PVR, defined as the sum of Rpar and Rpcp, was successively increased by 1, 2, 3, and 4 times, while other parameters remained unchanged.

Hemodynamic Parameters of Reoperation

The parameters of Plv, Prv, Ptotal, LVEF, RVEF, mPsvc\mPivc, and mQsvc\mQivc were used to describe the hemodynamics after reoperation in this essay. The ventricular work is calculated using MATLAB to integrate the area surrounding the ventricular P − V curve. EF can be calculated by dividing the ventricular stroke volume (SV) by the ventricular end-diastolic volume (Ved), while SV is equal to Ved and the ventricular end-systolic volume (Ves). The influence of PVR on the ventricular work and the ventricular EF is represented by the change rate of the ventricular work and ventricular EF, respectively. The changing rates of LVEF, RVEF, and mCO are comprehensively analyzed and can reflect the degree of impact of PVR impact on the reoperation.

RESULTS

It can be seen from **Table 2** that the hemodynamic parameters of 2VR at each position simulated under the system parameters listed in **Table 1** are consistent with the clinically measured physiological ranges.

Figures 4A–H show the impact of PVR on the stroke work of the left ventricle and right ventricle after each reoperation procedure; the equivalent quantitative results are shown in **Figure 5A**. Within the range from 1 time to 4 times of PVR, in 2VR, Plv decreased from 1.2 W to 0.81 W, Prv increased from 0.25 W to 0.4 W and Ptotal decreased from 1.45 W to 1.21 W. In 1.5VR′, Plv decreased from 1.03 W to 0.46 W, Prv increased from 0.13 W to 0.15 W and Ptotal decreased from 1.16 W to 0.61 W. In 1.0VR, Plv and Ptotal both decreased from 0.54 W to 0.19 W. Within the range from 1 to 4 times of PVR, the rate of change of Plv and Ptotal of 1.0VR was obviously greater than that of other reoperation producers, while the rate of change of Prv of 2VR was apparently greater than that of 1.5VR′ (**Figure 5B**). The ventricular EF is closely related to SV, end systolic volume (Vlves) and end diastolic volume (Vlved). **Figure 6A** shows that with the increase of PVR, LVEF decreased from 58.80% to 57.86% and RVEF decreased from 68.09% to 50.87% in 2VR. In 1.5VR′, LVEF decreased from 57.73% to 53.66%, and RVEF decreased from 61.31% to 43.86%. In 1.0VR, LVEF decreased from 54.93% to 47.28%. As the PVR increased from 1 to 4 times, the changing rate of LVEF in 1.0VR was obviously greater than that of other reoperation producers, while the changing rate of RVEF in 1.5VR′ was apparently greater than that of 2VR. Detailed data can be obtained from **Figure 6B**.

It can be seen from **Figures 7A–D** that the CO difference among the three kinds of surgical operations was obvious, and the CO of each kind gradually decreased with the increase of PVR. During the systolic time of the left ventricle (Ts), when PVR gradually increased, mCO of 2VR, 1.5VR′, and 1.0VR decreased by 18.53%, 37.58%, and 48.07%, respectively (**Figure 8**).

The results for Pa, Psvc and Pivc are shown in **Figures 9A–D** and **Figures 10A–H**, respectively. In 1.0VR, their wave was without pulsation when PVR increased. Regardless of the condition of PVR, Psvc was always greater than Pivc, and Pa was equal to Psvc in 1.5VR′ in a cardiac cycle. The influence of PVR on mPsvc/mPivc is shown in **Figure 11**. The ratio mPsvc\mPivc of 2VR and 1.0VR was 1, but it increased from 3.76 to 6.76 when PVR increased in 1.5VR′.

Figures 12A–H and **Figures 13A–D** show the impact of PVR on Qsvc, Qivc and Qti, respectively. Qsvc of 1.5VR′ have a negative value in the period of 11.2 s ∼ 11.5 s (Ts), while Qsvc of 2VR have a negative value in the period of 11.9 s ∼ 12.0 s (Td). In 1.0VR, the wave of Qsvc and Qivc was without pulsation when PVR increased. With the increase of PVR, the peak of waveform of Qti changed from "E peak" to "A peak" in 2VR and 1.5VR′. The change in the pressure is the cause of the flow-rate redistribution. Therefore, as PVR increased from 1 to 4 times, mQsvc\mQivc of 1.5VR′ decreased from 0.55 to 0.36, while it was 0.67 in both 2VR and 1.0VR (**Figure 11**).

DISCUSSION

1.5VR has been employed as a useful surgery in patients with CHD. The postoperative results of the surgery are highly patient-specific. In this paper, we have established three general LPM models, representing reoperation procedures after the failure of 1.5VR. They are closed-loop models that only consider the systemic and pulmonary circulation, with the exclusion of the local fine renal and liver circulation. The purpose of developing general LPM models is to mimic the postoperative hemodynamics of reoperation on specific PVR. These models are simple and effective. In addition, based on the models of this paper, we can adjust the lumped parameters of each vascular segment such as R, C, L, and others, so that clinical phenomena such as the azygos vein growth and the results of surgical procedures can be reproduced. The study parameters include Plv, Prv, Ptotal, CO, Qti, Pa, Psvc, Pivc, Qsvc, and Qivc.

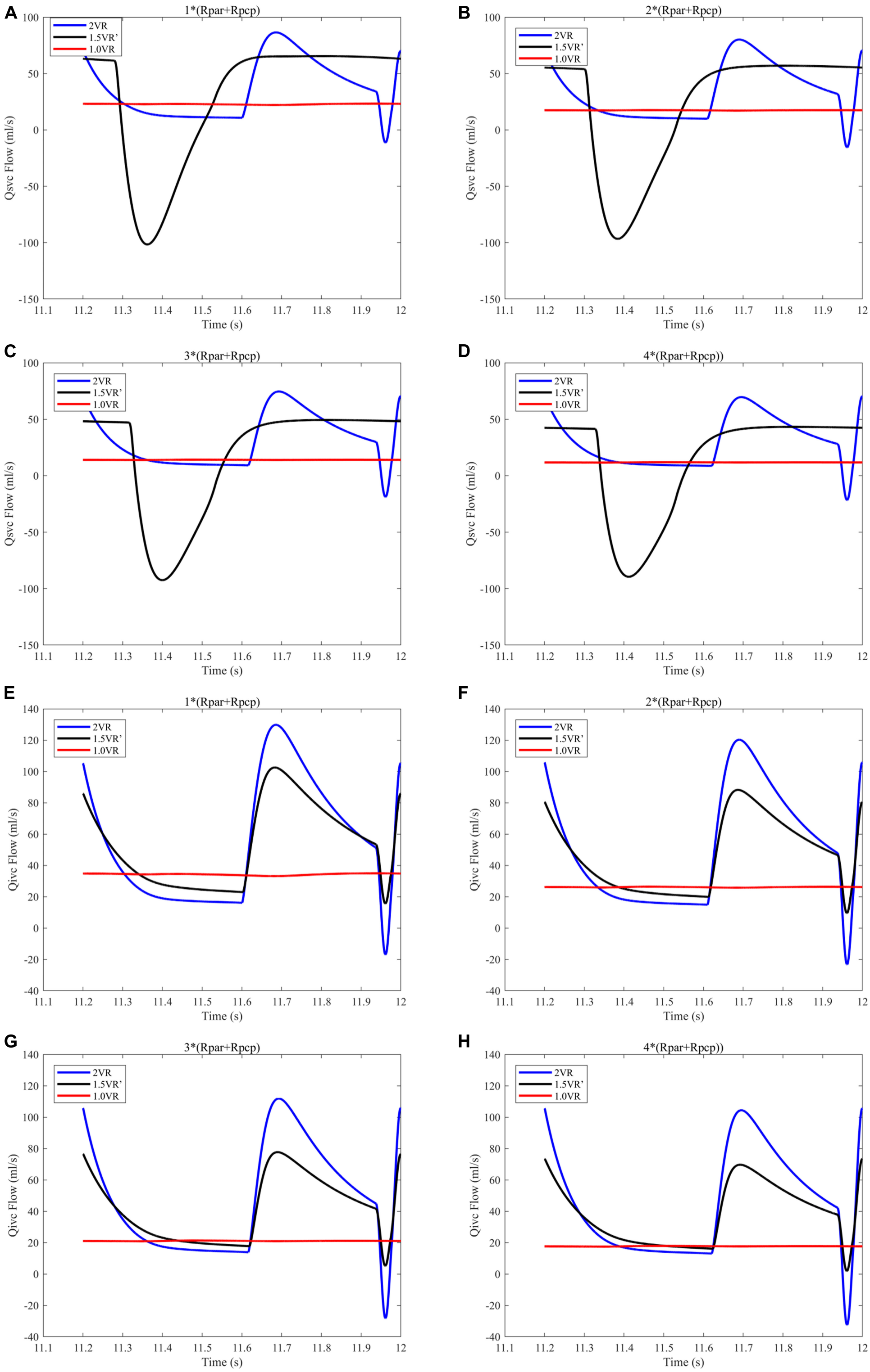

FIGURE 12 | (A) When the PVR is 1*(Rpar + Rpcp), Qsvc of the three procedures. **(B)** When the PVR is 2*(Rpar + Rpcp), Qsvc of the three procedures. **(C)** When the PVR is 3*(Rpar + Rpcp), Qsvc of the three procedures. **(D)** When the PVR is 4*(Rpar + Rpcp), Qsvc of the three procedures. **(E)** When the PVR is 1*(Rpar + Rpcp), Qivc of the three procedures. **(F)** When the PVR is 2*(Rpar + Rpcp), Qivc of the three procedures. **(G)** When the PVR is 3*(Rpar + Rpcp), Qivc of the three procedures. **(H)** When the PVR is 4*(Rpar + Rpcp), Qivc of the three procedures. (Qsvc, flow-rate superior vena cava; Qivc, flow-rate of inferior vena cava; Rpar, resistance of pulmonary arterioles; Rpcp, resistance of pulmonary capillary).

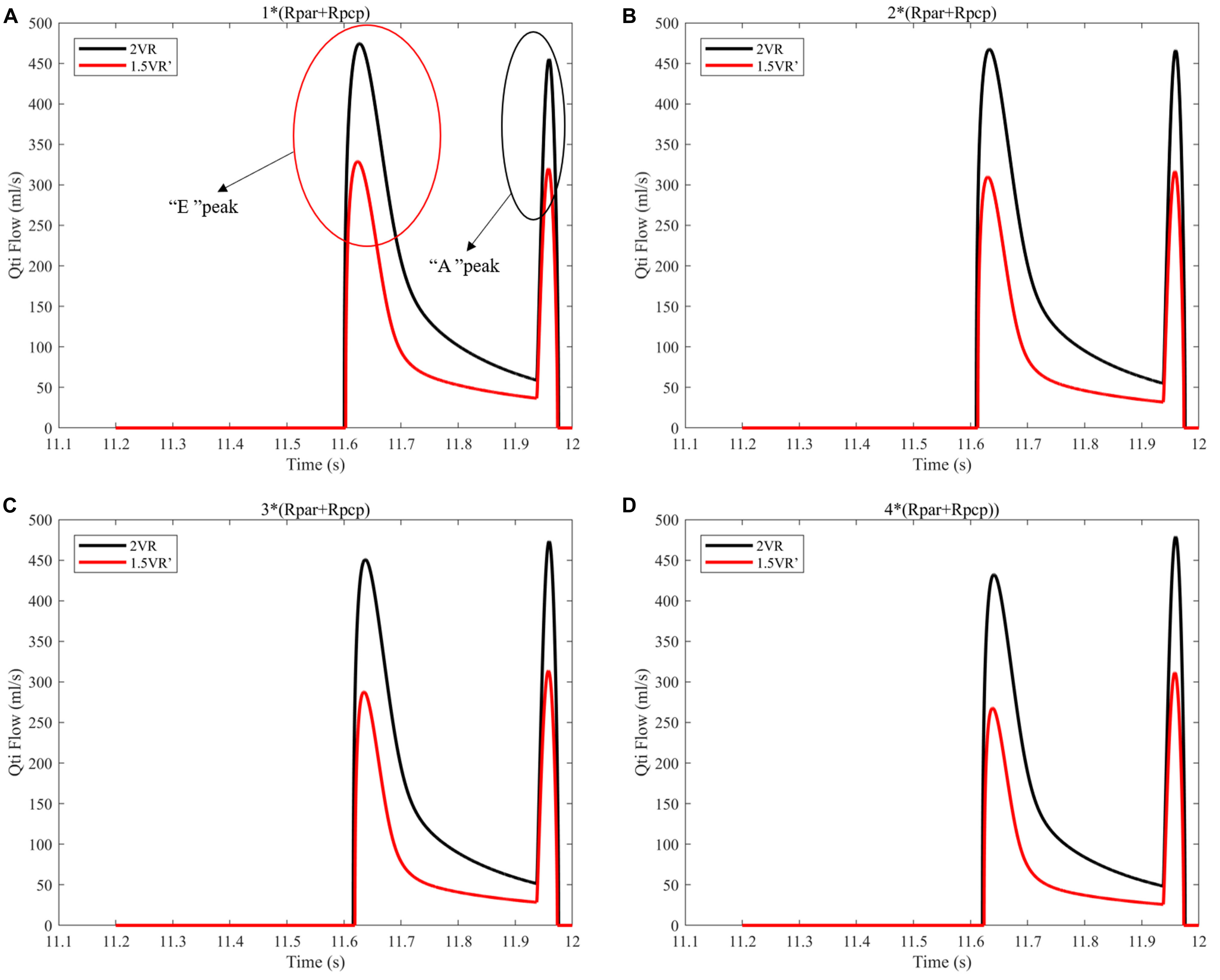

FIGURE 13 | (A) When the PVR is 1*(Rpar + Rpcp), Qti of different procedures. **(B)** When the PVR is 2*(Rpar + Rpcp), Qti of different procedures. **(C)** When the PVR is 3*(Rpar + Rpcp), Qti of different procedures. **(D)** When the PVR is 4*(Rpar + Rpcp), Qti of different procedures. (Qti, flow-rate of right atrium; Rpar, resistance of pulmonary arterioles; Rpcp, resistance of pulmonary capillary).

The ventricular stroke work can directly reflect the function of the ventricle. With the increase of PVR, The value of Prv of 2VR and 1.5VR′ gradually increased. This phenomenon is in accordance with the qualitative results inferred from general cardiovascular physiology. Furthermore, the Plv/Prv of 1.5VR′ exceeded that of 2VR, which is consistent with the purpose of the 1.5VR surgery (Talwar et al., 2018). Considering the changing rates in the ventricular stroke work of the three surgical procedures, Plv and Ptotal of 1.0VR are more sensitive to variations in PVR, while Prv of 2VR is more sensitive to changes in PVR. The ventricular EF also has a higher correlation with the ventricular function. Under different PVR conditions, the LVEF and RVEF of the three surgeries in this paper were all about 50%. This result indicates a better ventricular function under the given PVR (Surkova et al., 2019). As PVR increases, the afterload of the right ventricle increases and EF decreases. The results shown in **Figure 6** are consistent with trends that are qualitatively inferred from general cardiovascular physiology. As seen from the factor of the changing rate of LVEF and RVEF, RVEF is more sensitive to the change of PVR in 2VR and 1.5VR′.

Under different PVR conditions, LVEF and RVEF of the three surgeries stay around 50% in this work, while the mCO values of 1.5VR′ and 1.0VR are obviously decreased. In other words, the filling of the left ventricle decreases (Verhoeff and Mitchell, 2017), which is consistent with the clinical practice. In the clinical situation, the patient with chronic thromboembolic pulmonary hypertension will have an increase in PVR, and the function of the right heart is particularly important (Ruigrok et al., 2019); thus, maintaining a normal CO (3.5 L/min–5.5 L/min) is very important for normal blood circulation of the human body.

In turn, changes in the ventricular function affect changes in the pressure and flow in various parts of the body. The waves of Pa, Psvc, Pivc, Qsvc, and Qivc are of no pulsation in 1.0VR, which is determined by the surgical characteristics of 1.0VR (Jarvis et al., 2016) and is consistent with the clinical practice. With the increase of PVR, Pa of all three surgical methods increases, resulting in different degrees of pulmonary hypertension (Palazzini et al., 2017). Psvc in 1.5VR′ is greater than Pivc due to the characteristics of 1.5VR′ (Bhattarai et al., 2017). mPsvc\mPivc of 1.5VR′ is the largest among the three kinds of procedures, that is because in 1.5VR′, the superior vena cava anastomoses to the pulmonary artery, and Psvc increases due to the influence of Pa (Bhattarai et al., 2017). During the period Ts, the right ventricle is in systole, resulting in Ppa greater than Psvc in 1.5VR′, then more blood would flow from the pulmonary artery to the superior vena cava; thus, the waveform of Qsvc is negative during Ts. However, the superior vena cava in 2VR is connected to the right atrium, and the negative waveform of Qivc during the period of Td is due to the active contraction of the right atrium. Moreover, mPsvc\mPivc is the reason for the change of mQvc\mQivc which has the smallest value in 1.5VR′, this will lead to a significant decrease in blood perfusion in the upper body.

In addition, Qti is closely related to the ventricular function. The “E peak” and “A peak” of Qti waveform are generated by the active systole of the right ventricle and right atrium, respectively, so the time of occurrence of the peak is different. With the increase of PVR, the waveform peak of Qti changes from "E peak" to “A peak,” which indicates that PVR can affect the right ventricular function to some extent. In reference (Murayama et al., 2019), the ratio of velocity between “E peak” and “A peak” is used to quantify the ventricular diastolic function.

LIMITATIONS

A major limitation of this study is related to the model we established. The model constructed in this essay is relatively simple and does not take into account the factors of interventricular interaction, valve movement and coronary circulation of the great clinical value, although it effectively captures physiological changes. Some scholars have used computational models to verify the importance of interventricular interaction (Korakianitis and Shi, 2006a; Lin et al., 2019) and valve movement (Korakianitis and Shi, 2006a). However, 1.5VR that is generally selected for patients based on their cardiac appearance is characterized by the right ventricle being much smaller than the left one, so the interventricular interaction can be ignored. The other limitation is the lumped parameter, which is retrieved from the value of normal people in literature. However, the parameter for CHD is different from that of the normal people. Due to the limited cases of patients with reoperation after 1.5VR failure, it is difficult to obtain actual clinical data. It is well-known that the lumped parameters determined by the normal people are somewhat different from those of a patient, but the interaction between the peripheral tissues of the human body is almost the same, so the lumped parameters determined by a normal person can be used for patients. In addition, only PVR changes are allowed in the simulation process, while other parameters remain unchanged. It has been reported that PVR changes are caused by pulmonary vascular histology, and the resulting pulmonary hypertension will also affect the physiological properties of other parts, such as decreased pulmonary vascular compliance, etc. (Dragu et al., 2015). In future studies, we can analyze the preoperative data of more patients to solve this problem.

CONCLUSION

By constructing the LPM of the reoperation after 1.5VR failure, we investigated the three kinds of surgical procedures, including the 2VR, 1.5VR′, and 1.0VR. Through MATLAB simulation analysis, the hemodynamic differences among the three kinds of surgical procedures are quantitatively revealed at different PVR. In this paper, we mainly focus on some values which are the ventricular stroke work, EF, Cardiac Output and pressure and flow rate of the superior and inferior vena cava, which can directly or indirectly reflect the function of the heart. Using these values, we can describe the hemodynamics of reoperation after 1.5VR failure under different PVR. The ventricular stroke work, EF and mCO of the changing rate are important parameters that can reflect the sensitivity of different surgical procedures to PVR. Comprehensive analyses of the above-mentioned parameters show that PVR has a greater impact on 1.5VR′ and 1.0VR. Therefore, the selection of reoperation strategies should be mainly based on the development of pulmonary vasculature. To be noted, the definite outcomes of related procedures need to be verified by further experiments or clinic data.

DATA AVAILABILITY STATEMENT

All datasets generated for this study are included in the article/supplementary material.

AUTHOR CONTRIBUTIONS

YF designed and simulated the LPM of virtual surgery, performed the data analysis, and prepared the initial draft manuscript under the instruction of AQ. YY and XF provided the support of clinical knowledge. AQ subsequently revised the manuscript. All authors approved the final submitted version.

FUNDING

This work was supported by the National Natural Science Foundation of China to AQ (11772015) and the Beijing Municipal Administration of Hospitals Clinical medicine Development of special funding support (XMLX201845).

REFERENCES

Akkaya, G., Bilen, Ç., Tuncer, O. S., and Atay, Y. (2019). Surgical treatment of Ebstein anomaly: a unicenter experience. *Sayfalar* 58, 161–165.

Barron, D. J. (2018). Is one-and-a-half better than two. *Transl. Pediatr.* 7, 9–10. doi: 10.21037/tp.2017.08.04

Bhattarai, A., Dedja, A., Vida, V. L., Cavallin, F., Padalino, M. A., Thiene, G., et al. (2017). Right atrium and superior vena cava pressure measurements in a novel animal model to study one and a half ventricle repair as compared to Fontan type procedure. *J. Coll. Med. Sci. Nepal* 12, 143–149. doi: 10.3126/jcmsn.v12i4.16412

Burkhoff, D., and Tyberg, J. V. (1993). Why does pulmonary venous pressure rise after onset of LV dysfunction: a theoretical analysis. *Am. J. Physiol.* 265, 1819–1828.

Contou, D., Parrot, A., Khalil, A., and Fartoukh, M. (2014). Azygos vein enlargement and cavo-suprahepatic regurgitation in massive pulmonary embolism. *Intensive Care Med.* 40, 434–435. doi: 10.1007/s00134-013-3179-2

Corsini, C., Baker, C., Kung, E., Schievano, S., Arbia, G., Baretta, A., et al. (2014). An integrated approach to patient-specific predictive modeling for single ventricle heart palliation. *Comput. Methods Biomech. Biomed. Eng.* 17, 1572–1589. doi: 10.1080/10255842.2012.758254

Corsini, C., Migliavacca, F., Hsia, T.-Y., and Pennati, G. (2018). The influence of systemic-to-pulmonary arterial shunts and peripheral vasculatures in univentricular circulations: focus on coronary perfusion and aortic arch hemodynamics through computational multi-domain modeling. *J. Biomech.* 79, 97–104. doi: 10.1016/j.jbiomech.2018.07.042

Di Molfetta, A., Ferrari, G., Filippelli, S., Fresiello, L., Iacobelli, R., Gagliardi, M. G., et al. (2015). Use of ventricular assist device in univentricular physiology: the role of lumped parameter models. *Artif. Organs* 40, 444–453. doi: 10.1111/aor.12583

Dragu, R., Rispler, S., Habib, M., Sholy, H., Hammerman, H., Galie, N., et al. (2015). Pulmonary arterial capacitance in patients with heart failure and reactive pulmonary hypertension. *Eur. J. Heart Fail.* 17, 74–80. doi: 10.1002/ejhf.192

Duanmu, Z., Yin, M., Fan, X., Yang, X., and Luo, X. (2018). A patient-specific lumped-parameter model of coronary circulation. *Sci. Rep.* 8, 1–10.

Heldt, T., Shim, E. B., Kamm, R. D., and Mark, R. G. (2002). Computational modeling of cardiovascular response to orthostatic stress. *J. Appl. Physiol.* 92, 1239–1254. doi: 10.1152/japplphysiol.00241.2001

Jarvis, K., Schnell, S., Barker, A. J., Garcia, J., Lorenz, R., Rose, M., et al. (2016). Evaluation of blood flow distribution asymmetry and vascular geometry in patients with Fontan circulation using 4-D flow MRI. *Pediatr. Radiol.* 46, 1507–1519. doi: 10.1007/s00247-016-3654-3

Korakianitis, T., and Shi, Y. (2006a). Effects of atrial contraction, atrioventricular interaction and heart valve dynamics on human cardiovascular system response. *Med. Eng. Phys.* 28, 762–779. doi: 10.1016/j.medengphy.2005.11.005

Korakianitis, T., and Shi, Y. (2006b). A concentrated parameter model for the human cardiovascular system including heart valve dynamics and atrioventricular interaction. *Med. Eng. Phys.* 28, 613–628. doi: 10.1016/j.medengphy.2005.10.004

Li, B., Wang, W., Mao, B., and Liu, Y. (2019). A method to personalize the lumped parameter model of coronary artery. *Int. J. Comput. Methods* 16, 385–404.

Lin, A. C. W., Seale, H., Hamilton-Craig, C., Morris, N. R., and Strugnell, W. (2019). Quantification of biventricular strain and assessment of ventriculo–ventricular interaction in pulmonary arterial hypertension using exercise cardiac magnetic resonance imaging and myocardial feature tracking. *J. Mag. Reson. Imaging* 49, 1427–1436. doi: 10.1002/jmri.26517

Liu, J., Qiu, L., Zhu, Z., Chen, H., and Hong, H. (2011). Cone reconstruction of the tricuspid valve in Ebstein anomaly with or without one and a half ventricle repair. *Thorac. Cardiovasc. Surg.* 141, 1178–1183. doi: 10.1016/j.jtcvs.2011.01.015

Ma, L. C., Liu, Y. J., Zhao, X., Ren, X., Bai, F., Ding, J., et al. (2014). Hemodynamic influence of different pulmonary stenosis degree in glenn procedure: a numerical study. *Adv. Mech. Eng.* 6, 268–275.

Malhotra, A., Agrawal, V., Patel, K., Shah, M., Sharma, K., Sharma, P., et al. (2018). Ebstein's Anomaly: "The One and a Half Ventricle Heart". *Braz. J. Cardiovasc. Surg.* 33, 353–361.

Murayama, M., Iwano, H., Tsujinaga, S., Sarashina, M., Ishizaka, S., Chiba, Y., et al. (2019). Tricuspid regurgitation occurring in the early-diastolic phase in a case of heart failure: insights from echocardiographic and invasive hemodynamic findings. *Echocardiography* 36, 1771–1775. doi: 10.1111/echo.14458

Palazzini, M., Dardi, F., Manes, A., Bacchi Reggiani, M. L., Gotti, E., Rinaldi, A., et al. (2017). Pulmonary hypertension due to left heart disease: analysis of survival according to the haemodynamic classification of the 2015 ESC/ERS guidelines and insights for future changes. *Eur. J. of Heart Fail.* 20, 248–255. doi: 10.1002/ejhf.860

Peng, H., Xiao, Y., Deng, X., Luo, J., Hong, C., and Qin, X. (2016). The warburg effect: a new story in pulmonary arterial hypertension. *Clin. Chim. Acta* 461, 53–58. doi: 10.1016/j.cca.2016.07.017

Preger, L., Hooper, T. I., Steinbach, H. L., and Hoffman, J. I. E. (1969). Width of azygos vein related to central venous pressure. *Radiology* 93, 521–523. doi: 10.1148/93.3.521

Ruigrok, D., Meijboom, L. J., Westerhof, B. E., Huis in ' t Veld, A., van der Bruggen, C. E. E., Marcus, J. T., et al. (2019). Right ventricular load and function in chronicthromboembolic pulmonary hypertension: differences between proximal and distal chronicthromboembolic pulmonary hypertension. *Am. J. Respir. Crit. Care Med.* 199, 1163–1166. doi: 10.1164/rccm.201808-1562le

Sharma, V., Burkhart, H. M., Cetta, F., Hagler, D. J., Phillips, S. D., and Dearani, J. A. (2012). Fontan conversion to one and one half ventricle repair. *Anna. Thorac. Surg.* 94, 1269–1274. doi: 10.1016/j.athoracsur.2012.04.060

Shimizu, S., Shishido, T., Une, D., Kamiya, A., Kawada, T., Sano, S., et al. (2010). Right ventricular stiffness constant as a predictor of postoperative hemodynamics in patients with hypoplastic right ventricle: a theoretical analysis. *J. Physiol. Sci.* 60, 205–212. doi: 10.1007/s12576-010-0086-y

Smith, B. W., Chase, J. G., Nokes, R. I., Shaw, G. M., and Wake, G. (2004). Minimal haemodynamic system model including ventricular interaction and travel valve dynamics. *Med. Eng. Phys.* 26, 131–139. doi: 10.1016/j.medengphy.2003.10.001

Suga, H., and Sagawa, K. (1974). Instantaneous pressure-volume relationships and their ratio in the excised. Supported canine left ventricle. *Circ. Res.* 35, 117–126. doi: 10.1161/01.res.35.1.117

Suga, H., Sagawa, K., and Shoukas, A. A. (1973). Load independence of the instantaneous pressure-volume ratio of the canine left ventricle and effects of epinephrine and heart rate on the ratio. *Circ. Res.* 32, 314–322. doi: 10.1161/01.res.32.3.314

Surkova, E., Muraru, D., Genovese, D., Aruta, P., Palermo, C., and Badano, L. P. (2019). Relative prognostic importance of left and right ventricular ejection fraction in patients with cardiac diseases. *J. Am. Soc. Echocardiogr.* 32, 1407–1415.

Talwar, S., Siddharth, B., Choudhary, S. K., and Airan, B. (2018). One and half ventricle repair: rationale, indications, and results. *Indian J. Thorac. Cardiovasc. Surg.* 34, 370–380. doi: 10.1007/s12055-017-0628-5

Verhoeff, K., and Mitchell, J. R. (2017). Cardiopulmonary physiology: why the heart and lungs are inextricably linked. *Adv. Physiol. Educ.* 41, 348–353. doi: 10.1152/advan.00190.2016

Wright, L. K., Knight, J. H., Thomas, A. S., Oster, M. E., St Louis, J. D., and Kochilas, L. K. (2019). Long-term outcomes after intervention for pulmonary atresia with intact ventricular septum. *Heart* 105, 1007–1013. doi: 10.1136/heartjnl-2018-314124

Zhang, X. Y., Wu, D. D., Mao, B. Y., Li, B., Yang, H. S., and Liu, Y. J. (2019). Hemodynamic mechanism of "blood stolen" phenomenon in coronary artery aneurysm. *J.Mech. Med. Biol.* 19, 1–13.

Zhao, X., Liu, Y. J., Ding, J. L., Ren, X. C., Bai, F., Zhang, M. Z., et al. (2015). Hemodynamic effects of the anastomoses in modified Blalock-Taussig shunt: a numerical study using 0D/3D coupling method. *J. Mech. Med. Biol.* 15, 1–18.

Conflict of Interest: The authors declare that the research was conducted in the absence of any commercial or financial relationships that could be construed as a potential conflict of interest.

frontiers
in Physiology

ORIGINAL RESEARCH
published: 19 March 2020
doi: 10.3389/fphys.2020.00198

Multi-Band Surgery for Repaired Tetralogy of Fallot Patients With Reduced Right Ventricle Ejection Fraction: A Pilot Study

Han Yu[1]*, Pedro J. del Nido[2,3], Tal Geva[4,5], Chun Yang[6], Zheyang Wu[6], Rahul H. Rathod[4], Xueying Huang[7], Kristen L. Billiar[8] and Dalin Tang[1,6]*

[1] School of Biological Science and Medical Engineering, Southeast University, Nanjing, China, [2] Department of Cardiac Surgery, Boston Children's Hospital, Boston, MA, United States, [3] Department of Surgery, Harvard Medical School, Boston, MA, United States, [4] Department of Cardiology, Boston Children's Hospital, Boston, MA, United States, [5] Department of Pediatrics, Harvard Medical School, Boston, MA, United States, [6] Mathematical Sciences Department, Worcester Polytechnic Institute, Worcester, MA, United States, [7] School of Mathematical Sciences, Xiamen University, Xiamen, China, [8] Department of Biomedical Engineering, Worcester Polytechnic Institute, Worcester, MA, United States

OPEN ACCESS

Edited by:
Wei Sun,
Georgia Institute of Technology,
United States

Reviewed by:
Jieyun Bai,
Jinan University, China
Xiaoyu Luo,
University of Glasgow,
United Kingdom

****Correspondence:***
Han Yu
yuhtalent@outlook.com
Dalin Tang
dtang@wpi.edu

Specialty section:
This article was submitted to
Computational Physiology
and Medicine,
a section of the journal
Frontiers in Physiology

Received: *16 September 2019*
Accepted: *20 February 2020*
Published: *19 March 2020*

Citation:
Yu H, del Nido PJ, Geva T,
Yang C, Wu Z, Rathod RH, Huang X,
Billiar KL and Tang D (2020)
Multi-Band Surgery for Repaired
Tetralogy of Fallot Patients With
Reduced Right Ventricle Ejection
Fraction: A Pilot Study.
Front. Physiol. 11:198.
doi: 10.3389/fphys.2020.00198

Introduction: Right ventricle (RV) failure is one of the most common symptoms among patients with repaired tetralogy of Fallot (TOF). The current surgery treatment approach including pulmonary valve replacement (PVR) showed mixed post-surgery outcomes. A novel PVR surgical strategy using active contracting bands is proposed to improve the post-PVR outcome. In lieu of testing the risky surgical procedures on real patients, computational simulations (virtual surgery) using biomechanical ventricle models based on patient-specific cardiac magnetic resonance (CMR) data were performed to test the feasibility of the PVR procedures with active contracting bands. Different band combination and insertion options were tested to identify optimal surgery designs.

Method: Cardiac magnetic resonance data were obtained from one TOF patient (male, age 23) whose informed consent was obtained. A total of 21 finite element models were constructed and solved following our established procedures to investigate the outcomes of the band insertion surgery. The non-linear anisotropic Mooney–Rivlin model was used as the material model. Five different band insertion plans were simulated (three single band models with different band locations, one model with two bands, and one model with three bands). Three band contraction ratios (10, 15, and 20%) and passive bands (0% contraction ratio) were tested. RV ejection fraction was used as the measure for cardiac function.

Results: The RV ejection fraction from the three-band model with 20% contraction increased to 41.58% from the baseline of 37.38%, a 4.20% absolute improvement. The RV ejection fractions from the other four band models with 20% contraction rate were 39.70, 39.45, and 40.70% (two-band) and 39.17%, respectively. The mean RV stress and strain values from all of the 21 models showed only modest differences (5–11%).

Conclusion: This pilot study demonstrated that the three-band model with 20% band contraction ratio led to 4.20% absolute improvement in the RV ejection fraction, which is considered as clinically significant. The passive elastic bands led to the reduction of the RV ejection fractions. The modeling results and surgical strategy need to be further developed and validated by a multi-patient study and animal experiments before clinical trial could become possible. Tissue regeneration techniques are needed to produce materials for the contracting bands.

Keywords: tetralogy of fallot, pulmonary valve replacement, heart failure, virtual surgery, mechanical model, active contraction band

INTRODUCTION

Heart failure is a severe cardiac problem which could lead to high morbidity and mortality despite the optimal medical and electrical therapies available today (Fang et al., 2015). TOF is a common congenital heart disease. The major symptoms of TOF include ventricle septal defect, RV outflow obstruction, overriding aorta, and right ventricular hypertrophy. Currently, patients born with TOF could expect survival into adulthood after surgical repair (Bacha et al., 2001). Many long-time repaired TOF survivors are left with residual hemodynamic lesions including pulmonary regurgitation and high ventricle blood pressure, which are major causes of late-onset heart failure (Kim and Emily, 2016). The surgery for pulmonary regurgitation, PVR, showed mixed post-surgery outcomes, with some patients who recovered their RV function and had an increase in the RV ejection fraction but with some who did not (Vliegen et al., 2002; Tang et al., 2015). Del Nido proposed a scar removal and RV remodeling technique to improve post-PVR surgical outcome. In their clinical trial (NIH 5P50HL074734, Geva and del Nido), 64 patients with repaired TOF and who fulfilled the defined criteria for PVI/PVR were randomly assigned to undergo either PVI/PVR alone ($n = 34$) or PVI/PVR with surgical RV remodeling ($n = 30$). After the RV remodeling and the RV volume reduction procedures by removing, replacing, or reducing the scar and patch (non-contracting tissue) in the outflow area of the RV, the RV ejection fraction improvement was insignificant (Geva et al., 2010). Due to the complexity of the RV structure and the surgical procedures, effective PVR procedures are needed to improve the post-PVR outcome.

Computational modeling plays a vital role in cardiovascular research for better understanding of the cardiac biological mechanism and for potential clinical usage. Many investigators have made great contributions to ventricle modeling, including the Continuity package and the Physiome Project. The early cardiac stimulation model was introduced by Peskin et al. with an immersed boundary method (Peskin, 1977, 1989). A well-developed active ventricle model was introduced by McCulloch et al. (1992) and Costa et al. (1999). A novel, robust method to couple finite element (FE) models of cardiac mechanics to system models of the circulation was developed by Kerckhoffs et al. (2007). The early magnetic resonance imaging (MRI)-based mechanical ventricle models were included by Axel (2002) and Saber et al. (2001). The advancement of computational modeling made it for patient-specific ventricle models to be used in realistic applications, surgical designs, and clinical decision-making processes. Since computational models require knowledge for ventricle material properties, Sacks and Chuong (1993) and Billiar and Sacks (2000) developed biaxial mechanical testing techniques to acquire ventricle anisotropic material properties. Deng et al. (2018) used a CT-based mechanical fluid–solid interaction (FSI) ventricle model. Their results indicated that high blood pressure difference and shear stress on mitral valve leaflets might directly initiate motion in hypertrophic obstructive cardiomyopathy. Sun's group has published extensively on quantifying myocardium and valve material properties, valve mechanics, and their impact on ventricle functions (Murdock et al., 2018; Kong et al., 2018; Sulejmani et al., 2019). We introduced a RV model for patients with TOF with a fluid–structure interaction (Tang et al., 2008; Tang et al., 2013; Yang et al., 2013; Tang et al., 2015; Yu et al., 2019). Our investigations included searching and identifying surgical options, possible factors which could improve post-PVR cardiac outcome prediction. The impact of patch size, stiffness, scar tissue removal, and RV remodeling was studied (Tang et al., 2008; Tang et al., 2013; Yang et al., 2013). Using data from computational models for 16 patients with TOF, it was found that, among the mechanical and geometrical factors considered, mechanical stress may be the best predictor for post-PVR cardiac outcome (Tang et al., 2015). Yu et al. (2019) used patient-specific CMR data from six healthy volunteers and 16 TOF patients and estimated the RV material stiffness parameter values. Their results indicated that the mean end-ejection effective YM value of TOF patients was 78.6% higher than that of the healthy group (1,952 vs. 1,093 kPa, $p = 0.016$). The mean end-ejection YM value from the worse-outcome TOF group was 59.5% higher than that from the better-outcome TOF group (2,400 vs. 1504 kPa, $p = 0.008$). Active contracting band insertion models using one band were also introduced using CMR data from one TOF patient to investigate the effect of band material stiffness variations, band length, and active contraction (Yang et al., 2013). The initial results were promising.

In this paper, we continue our effort to test the feasibility of the novel PVR surgical procedures using active contracting bands to improve the post-PVR cardiac outcome. A total of

---

Abbreviations: CMR, cardiac magnetic resonance, LV, left ventricle, PVI, pulmonary valve insertion, PVR, pulmonary valve replacement, RV, right ventricle, TOF, tetralogy of fallot, YM, young's modulus.

21 models combining five different band insertion options with passive and active bands and three different contraction ratios were constructed using CMR data from one repaired TOF patient to find the potential possible benefit of active contracting bands.

MATERIALS AND METHODS

Data Acquisition

Cardiac magnetic resonance data were provided by the Boston Children's Hospital from their clinical RV surgical remodeling trial (NIH 5P50HL074734, Geva and delNido). Written informed consent was obtained from the participants. The CMR image was acquired from one TOF patient (age, 22.5 years; gender, male) before and after PVR surgery using electrocardiography-gated, breath-hold, steady-state, cine precession MRI (slice thickness: 6–8 mm, interslice gap: 0–2 mm, 30 frames per cardiac cycle). The patch, scar, and valve were located based on cine MRI, flow data, and delayed enhancement CMR and further verified by the surgeon (PJdN, over 30 years of experience) who performed the PVR surgery. The endocardial and epicardial borders were traced manually and analyzed using commercially available software QMass (QMass, Medis Medical Imaging Systems, Leiden, Netherlands) for the entire cardiac cycle containing 30 time points, each with a 3D CMR data set. Simpson's method was applied to calculate the end-diastolic volume (EDV), the end-systolic volume (ESV), the stroke volume, and the ejection fraction. Blood pressure in the RV was measured via cardiac catheterization procedures. **Figure 1** shows the selected CMR slices together with segmented contour plots, zero-load ventricle geometries, reconstructed 3D RV/LV geometry with scar, patch and myocardium fiber orientation, and measured ventricle pressure conditions from the patient. The details about our pre-shrinking process to obtain zero-load geometry and 3D geometry reconstruction procedures are given in the "Governing Equations for Our RV/LV/Patch/Band Models" section. The demographic data are given in **Table 1**.

TABLE 1 | Demographic data of the TOF patient.

Age (year)	22.5
Gender	Male
Heart rate (beats/min)	56
Maximum RV pressure (mmHg)	31.4
Minimum RV pressure (mmHg)	2.16
RV EDV (ml)	406.9
RV ESV (ml)	254.5
Pre-op RV EF (%)	37.46
RV SV (ml)	152.4

Novel PVR Surgical Strategy Using Active Contracting Band and Feasibility Study Using Band Models

One major reason why TOF patients have poor RV cardiac function performance (normally measured by ejection fraction) is the weakened contractility of their RV tissue. We hypothesized that adding active contracting band(s) to the ventricle could improve its contractility and cardiac function. We are using our modeling approach to test the feasibility of this hypothesis. A total of 21 computational band models based on patient-specific CMR data with different band designs (location, number of bands, and percent of contraction rate) were constructed to investigate the impact of band insertion surgery. These models included five different band insertion plans (plans A–E, **Figure 2**) combined with passive elastic bands and active contracting bands with three different band contraction ratios (10, 15, and 20% band zero-stress length reduction). Plan A has a band at the anterior to the middle of the papillary muscle (PM). Plan B uses a band at the posterior to the middle of the PM. Plan C has two bands

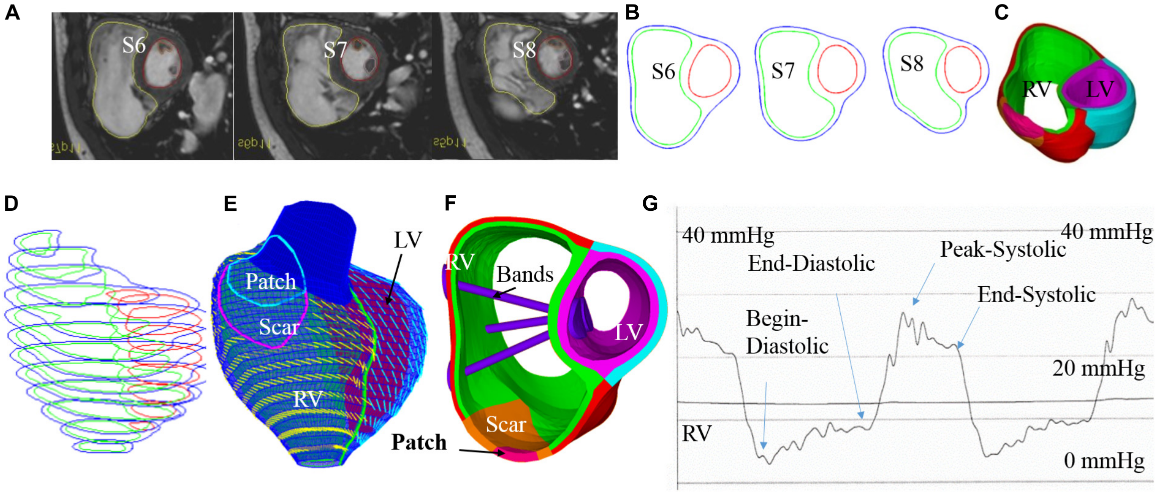

FIGURE 1 | Cardiac magnetic resonance-based model construction process and pressure conditions. **(A)** Selected CMR slices from a patient, end of systole. **(B)** Segmented contours. **(C)** Two-layer structure. **(D)** Zero-load geometry. **(E)** Model with fiber orientations. **(F)** Ventricle with three bands inserted. **(G)** Recorded RV pressure profile. This figure was made with components from Figure 1 in Yu et al. (2019) with copyright held under a creative commons license.

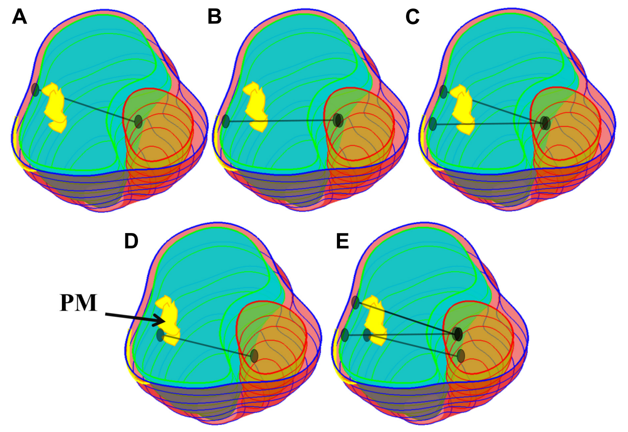

FIGURE 2 | Five band insertion surgical plans. **(A)** Plan A: A band at anterior to the middle of PM. **(B)** Plan B: A band at posterior to the middle of PM. **(C)** Plan C: Double bands, plans A and B combined. **(D)** Plan D: A band at the base of the PM. **(E)** Plan E: Combination of plans C and D. PM, papillary muscle. Colors used: light blue, RV inner surface; green, LV inner surface; yellow, papillary muscle; black, band.

with plans A and B combined. Plan D has a band at the base of the PM. Plan E is a three-band model with all the three single bands combined. A summary of the band models is given in **Table 2**.

The idea of passive and active bands models was introduced by Dr. del Nido and a paper with several one-band models was published (Yang et al., 2013). The zero-stress length (denoted by *L*) of the passive band was equal to the distance between the two locations on the ventricle wall from the zero-load no-band model where the band would be placed (100% of *L*). All active contracting bands had *L* as their "relaxed" zero-stress length and shortened to their contracted zero-stress length by 90, 85, and 80% of *L*, respectively. Due to their ability to actively shorten and relax, they can help the ventricle to contract during systole phase but would not resist the ventricle's relaxation in the diastolic phase (see **Figure 3**). The active contracting bands would contract and relax with the ventricle, which means that the zero-stress band length and the material parameters would change with ventricle contraction and relaxation.

This paper mainly aims to demonstrate the potential benefit of actively contracting bands if such materials could be made available. In our modeling process of the actively contracting band, the zero-stress band length was 80, 85, or 90% *L* in the contracted state of the band, corresponding to the contraction ratio of 20, 15, or 10%, respectively. At the end of the diastole phase, the zero-stress band length would be relaxed to *L*. In addition to active contraction and relaxation, the band would also have elastic expansion and contractions, in conjunction with the ventricle contractions and expansions.

TABLE 2 | Band model summary, band location and numbers, contraction ratios, and zero-load band length for all 21 RV/LV models.

Models	Plan	Band no.	Contraction ratio	Zero-load band length (cm)	Band location
Baseline	–	0	–	–	–
A000	A	1	Passive	3.94 (100%L)	Anterior to the middle of PM
A010	A	1	10%	3.54 (90%L)	Anterior to the middle of PM
A015	A	1	15%	3.35 (85%L)	Anterior to the middle of PM
A020	A	1	20%	3.15 (80%L)	Anterior to the middle of PM
B000	B	1	Passive	4.02 (100%L)	Posterior to the middle of PM
B010	B	1	10%	3.61 (90%L)	Posterior to the middle of PM
B015	B	1	15%	3.41 (85%L)	Posterior to the middle of PM
B020	B	1	20%	3.21 (80%L)	Posterior to the middle of PM
C000	C	2	Passive	3.94, 4.02 (100%L)	Plan A and B combined
C010	C	2	10%	3.54, 3.61 (90%L)	Plan A and B combined
C015	C	2	15%	3.35, 3.41 (85%L)	Plan A and B combined
C020	C	2	20%	3.15, 3.21 (80%L)	Plan A and B combined
D000	D	1	Passive	3.16 (100%L)	The base of the PM
D010	D	1	10%	2.85 (90%L)	The base of the PM
D015	D	1	15%	2.69 (85%L)	The base of the PM
D020	D	1	20%	2.52 (80%L)	The base of the PM
E000	E	3	Passive	3.94, 4.02, and 3.16 (100%L)	Combination of plan C and D
E010	E	3	10%	3.54, 3.61, and 2.85 (90%L)	Combination of plan C and D
E015	E	3	15%	3.35, 3.41, and 2.69 (85%L)	Combination of plan C and D
E020	E	3	20%	3.15, 3.21, and 2.52 (80%L)	Combination of plan C and D

PM, papillary muscle.

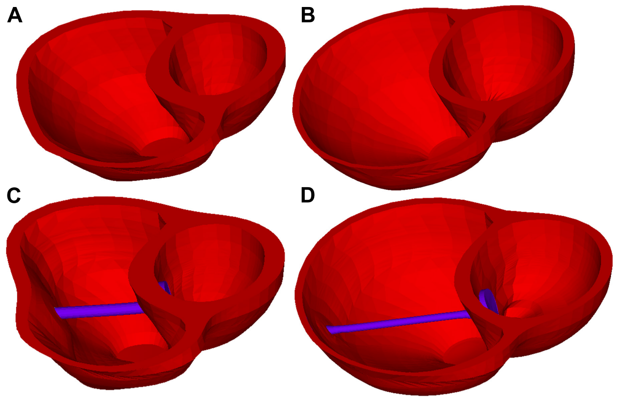

FIGURE 3 | Right ventricle /LV/band models at end-ejection (minimum RV volume) and end-filling (maximum RV volume). **(A)** Baseline model at end-ejection. **(B)** Baseline model at end-filling. **(C)** Model D020 (active band model) at end-ejection. **(D)** Model D020 (active band model) at end-filling.

Governing Equations for Our RV/LV/Patch/Band Models

For simplicity and efficiency in the model construction cost, structure-only models were used in this paper, which are sufficient to simulate and quantify the ventricle deformation and volume changes. Our models included RV, LV, patch (with RV outflow track and scar), and bands, so the name RV/LV/patch/band may be used for convenience when proper. Both the RV and the LV were included since it is difficult to keep the RV in its shape without the support of the LV or the artificially imposed constraints. Scar tissue and patch were included and whose shape and location were carefully reviewed by the surgeon (PN) and the radiologist (TG). The models with different band numbers and locations were considered. Ventricle tissue (myocardium) was assumed to be hyperelastic, anisotropic, nearly incompressible, and homogeneous. The patch, scar, and band materials were assumed to be hyperelastic, isotropic, nearly incompressible, and homogeneous. The non-linear Mooney–Rivlin model was used to describe the non-linear anisotropic and isotropic material properties (Yang et al., 2013; Yu et al., 2018). The measured right and LV blood pressure values were implemented on the right and the LV inner surfaces, respectively. The governing equations for our RV/LV/patch/band models were given by Tang et al. (2008):

$$\rho v_{i,tt} = \sigma_{ij,j}, \quad i, j = 1, 2, 3; \;\; \text{sum over } j, \tag{1}$$

$$\varepsilon_{ij} = \frac{1}{2}\left(v_{i,j} + v_{j,i} + v_{\alpha,i}v_{\alpha,j}\right), \quad i, j, = 1, 2, 3, \tag{2}$$

$$p\big|_{RV} = p_{RV}\,(t)\,, \;\; p\big|_{LV} = p_{LV}\,(t) \tag{3}$$

The isotropic Mooney–Rivlin strain energy function is given by:

$$W = c_1\,(I_1 - 3) + c_2\,(I_2 - 3) + D_1\left[\exp\left(D_2\,(I_1 - 3)\right) - 1\right] \tag{4}$$

where I_1 and I_2 are the first and second strain invariants given by:

$$I_1 = \sum C_{ii}, \;\; I_2 = \frac{1}{2}\left(I_1^2 - C_{ij}C_{ij}\right) \tag{5}$$

where $C = [C_{ij}] = X^T X$ is the right Cauchy–Green deformation tensor, $X = [Xij] = \partial[x/a, \; (x_i)$ is the current position,(a_i) is the original position, and c_i and D_i are the material parameters chosen to match the experimental or the patient-specific CMR measurements. The strain energy function for the anisotropic modified Mooney–Rivlin model was obtained by adding an additional anisotropic term in Eq. (4) (Tang et al., 2008):

$$W = c_1\,(I_1 - 3) + c_2\,(I_2 - 3) + D_1\left[\exp\left(D_2\,(I_1 - 3)\right) - 1\right] + \frac{K_1}{K_2}\left[exp\,(I_4 - 1)^2 - 1\right] \tag{6}$$

where $I_4 = C_{ij}(n_f)_i(n_f)_j$, C_{ij} is the Cauchy–Green deformation tensor, n_f is the fiber direction, and K_1 and K_2 are the material constants. With the parameters well chosen, the modified Mooney–Rivlin model could fit the direct measurement of the experiment stress–strain data from our biaxial test on the myocardium (Yu et al., 2018). The material parameter values are given in **Table 3**. The ventricle material parameter values were determined to fit the CMR-measured volume data. Stress–stretch curves are shown in **Figure 4**. It should be noted that both the patch and the scar materials were assumed to be isotropic. In **Figure 4B**, the myocardium fiber and the cross-fiber curves were made using equal stretch ratios in both the fiber and the cross-fiber directions so that it was possible to make 2D stress–stretch curves.

The orientation of the myofibrils caused the myocardial tissue to exhibit mechanical anisotropy. Since patient-specific fiber orientation data were not available, we chose to construct a two-layer RV/LV model and set fiber orientation angles using the fiber angles published by Sanchez-Quintana et al. (1996), Nash and Hunter (2000), and Hunter et al. (2003) and available data in human. In our two-layer models, the left ventricular fiber orientation was approximately −60° (relative to the circumferential direction) at the outer layer and +80° at the inner layer. The RV fiber orientation was set at −45° at the outer layer and at +40° at the inner layer (see **Figures 1**, **5**).

Pre-shrink Process and Myocardium Material Parameters for Patient-Specific CMR-Based Model

Under *in vivo* conditions, the left and the RVs are under pressure and their zero-load ventricular geometries were unknown from

TABLE 3 | Summary of the parameter values of the Mooney–Rivlin models for all materials, isotropic and anisotropic models (c_2 = 0 kPa).

Material/model	c_1 (kPa)	D_1 (kPa)	D_2	K_1 (kPa)	K_2
Patch (isotropic)	38.45	38.45	9.0	0	–
Scar (isotropic)	19.23	19.23	9.0	0	–
Myocardium, end-ejection					
RV/LV inner layer	3.82	1.20	3.0	18.28	3.0
RV/LV outer layer	4.36	1.12	3.0	17.76	3.2
Myocardium, end-filling					
RV/LV inner layer	2.95	0.93	3.0	14.12	3.0
RV/LV outer layer	3.37	0.87	3.0	13.72	3.2

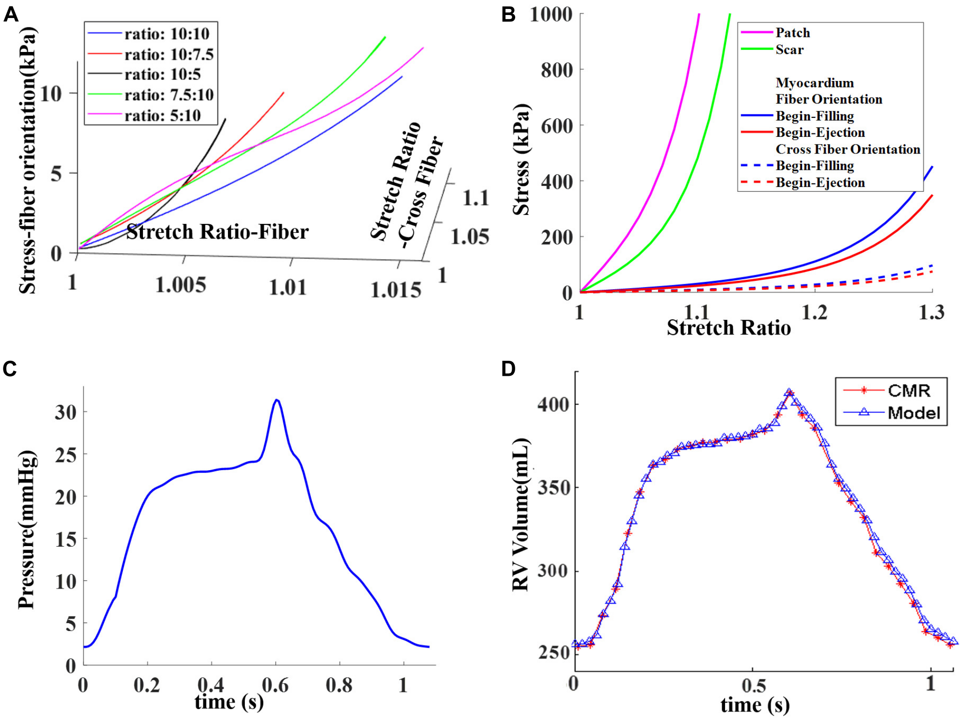

FIGURE 4 | Material stress–stretch curves and pressure conditions used in the paper and computational RV volume curve matching CMR-measured data. **(A)** Stress–stretch curves from Mooney–Rivlin models fitting data from biaxial test in fiber orientation. Five curves for five different stress ratios (stress in fiber direction vs. stress in cross-fiber direction) were plotted. **(B)** Stress–stretch curves for patch, scar, and myocardium in both fiber and cross-fiber directions for comparison purpose. Myocardium fiber and cross-fiber curves were made using equal stretch ratios in both fiber and cross-fiber directions. **(C)** Blood pressure in RV chamber. **(D)** Computed RV volume from baseline model matching CMR-measured volume. **(C)** was taken from Figure E1 C in Yang et al. (2013), with permission.

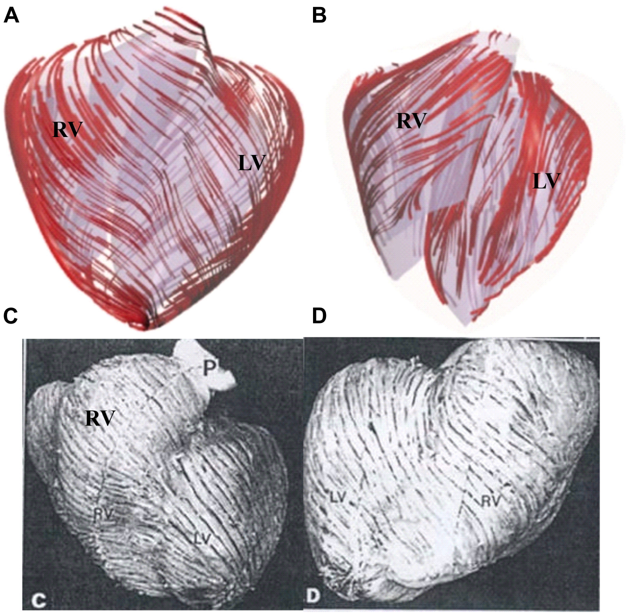

FIGURE 5 | Ventricle fiber orientation. **(A)** Pig ventricle: epicardium. **(B)** Pig ventricle: endocardium. **(C)** Human heart from a TOF patient: front view. **(D)** Human heart, back view. This figure was made with components from Figures 3A–D in Yang et al. (2013), with permission.

in vivo CMR images. Thus, in our model construction process, a pre-shrink process was applied to the *in vivo* begin-diastole ventricular geometries to generate the zero-stress geometry for the computational simulation so that, after the pressure was applied, the ventricle could approximately regain its *in vivo* morphology. Shrinking is achieved by shrinking each slice (short-axis direction) with a short-axis shrinking rate and by reducing the slice distances (long-axis direction) with a long-axis shrinking rate. The shrinkage for the inner slice contour was 2–3% based on the RV EDV, RV ESV, and blood pressure. The outer slice contour shrinkage was determined to conserve the total ventricular wall mass. The outer slice contour shrinkage was smaller than the inner slice contour to keep the ventricle tissue total volume (mass) conserved. After the pre-shrink process was implemented, the parameters in Eq. (6) for myocardium were adjusted iteratively until a good agreement between the computational and the CMR-measured volume data was found (error <0.2%). The details were described in Tang et al. (2008, 2013, 2015), Yang et al. (2013), and Yu et al. (2018).

Solution Methods, Data Extraction, and Model List

The 21-band models were constructed and solved by ADINA (ADINA R&D, Watertown, MA, United States) using unstructured finite elements and the Newton–Raphson iteration method. The simulation procedures were continued until the differences in the solutions between the last two periods became less than 0.1%. Our experience indicated that three periods were enough (solutions for periods 2 and 3 were almost identical). The solutions for the last period were accepted for analysis. The maximum principal stress and strain (both are scaler functions) were used as the representative stress/strain variables. The maximum principal stress and strain values from all RV inner surface points (100 evenly spaced points from each slice of the RV inner surface) were extracted from the model and their mean values at begin-filling (BF) and begin-ejection (BE) were recorded for comparison. The RV stress, strain, and pressure reach their minimum and maximum in a cardiac cycle, respectively.

Mesh analyses were performed for each model so that the solutions became stable and mesh-independent. The mesh analysis was accomplished by decreasing the mesh size until the solution differences in stress/strain from two consecutive meshes were less than 1%. The RV stress and strain errors from one sample model with different element numbers are given in **Table 4**. Stress and strain errors were defined by L_1-norm errors between solutions from two consecutive meshes. The details were described in Yu et al. (2019).

The RV ejection fraction was used as the index (marker) for evaluating ventricle cardiac function. The difference between the pre-operation and the post-operation RV ejection fraction, ΔEF, was used to qualify post-PVR surgery cardiac function improvement:

$$\Delta\text{EF} = \text{Post-PVR EF} - \text{Pre-PVR EF}. \qquad (7)$$

Pre-PVR no-band RV/LV model was constructed and used as the baseline model. Models "AXXX," "BXXX" to " EXXX" corresponded to the five band insertion surgery plans with four active contraction ratios of 0, 10, 15, and 20%, respectively, where "XXX" represented the band contraction ratio and "000" represented the RV/LV models with no-contraction passive bands. The simulation results are presented in the "Results" section.

RESULTS

The analyses of the 4D (time +3D) ventricle stress and strain data are overly complicated. Data at two critical time points, i.e. begin-filling and begin-ejection, were selected for analyses and comparative studies. The RV begin-filling and begin-ejection volume, ejection fraction, ejection fraction change from pre-PVR to post-PVR (ΔEF), and mean stress and strain values are given in **Table 5**. For the patient under consideration, the RV ejection fraction from our baseline no-band model was 37.38%, agreeing well with the EF data (37.46%) from direct CMR measurement.

TABLE 4 | Stress and strain errors from models with different mesh numbers.

Element number	Stress error (%)	Strain error (%)
8451	8.66	10.19
12470	4.80	3.64
16956	3.54	2.45
20630	2.50	2.39
25550	1.33	1.66
30554	0.98	0.81

Passive Band Had Negative Impact on Right Ventricle Function

Initially, one might think that an elastic band may be able to help the ventricle to contract and improve the ejection fraction. That was proven not true for a reason we did not think of: while it could be true that the band would help the ventricle to contract during systole by its elastic contraction, the band would also be holding the ventricle during diastole and resisting its expansion. The ventricle would not be able to reach its no-band maximum end-diastiole volume.

Our results indicated that the ejection fractions from those passive band models had significant decreases after the passive bands were inserted. The ΔEF for the passive band models A000, B000, C000, D000, and E000 were −1.00, −1.26, −2.65, −2.73, and −3.60%, respectively. The ejection fraction losses were caused by the decrease of the RV begin-ejection volume (the same as the end-diastole volume). The begin-ejection RV volume of the passive band models was 2.2, 2.5, 5.2, 6.0, and 8.25% lower than that from the baseline model. The baseline begin-ejection RV volume was 406.80 ml, while the band model begin-ejection volumes were A000—397.95 ml, B000—397.02 ml, C000—386.57 ml, D000—383.79 ml, and E000—375.78 ml.

Active Contractional Bands Improved the Right Ventricle Ejection Fraction

Results shown in indicated that plan E (three bands) with a band contraction ratio of 20% (model E020) improved the RV ejection fraction to 41.59%, which represented 4.20% absolute improvement or 11.24% relative improvement compared to the baseline EF value. The ejection fractions for plans A–D with band contraction ratios of 20% were 39.70, 39.45, 40.70, and 39.17%, respectively. It was clear that plan E with three bands had the best EF improvement, and plan C with two bands had the second best EF improvement. Plans A, B, and D (single with different locations) had similar EF improvements. Plan A was slightly better in general among the three (except B010) because the band location was more balanced.

Three different contraction ratios were applied on the band: 10, 15, and 20%. The surgeries with a band contraction ratio of 20% had the best improvement on EF, as expected. The same relations were also found among the models of surgery plans A, B, C, and D. The ploy-lines/bar plots of RV stress and EF vs. band contraction ratio are shown in **Figure 6**.

Band Location Could Lead to Different RV Stress and Strain Distributions

The ventricle stress and strain variance caused by the inserted bands was small and insignificant. **Table 5** shows that the RV mean stress values (unit in kPa) at begin-ejection from the five band models (A020–E020) with 20% band contraction ratio were

TABLE 5 | Right ventricle ejection fraction and wall stress/strain data from 21 models: five surgery plans combined with passive and active bands of three different contraction ratios and a RV/LV model with no band.

Models	Begin-filling			Begin-ejection			EF (%)	ΔEF (%)
	RV volume (ml)	Stress (kPa)	Strain	RV volume (ml)	Stress (kPa)	Strain		
Baseline	254.74	3.05	0.031	406.80	64.21	0.288	37.38	–
A000	253.19	2.96	0.031	397.95	60.97	0.288	36.38	−1.00
A010	249.29	3.02	0.030	406.35	61.72	0.291	38.65	1.27
A015	247.16	3.08	0.031	406.27	61.68	0.291	39.16	1.78
A020	244.90	3.17	0.033	406.15	61.64	0.291	39.70	2.32
B000	253.63	3.01	0.031	397.02	60.74	0.285	36.12	−1.26
B010	250.40	3.07	0.031	409.08	64.72	0.291	38.79	1.41
B015	248.44	3.10	0.031	407.15	64.72	0.285	38.98	1.60
B020	246.47	3.16	0.032	407.07	64.72	0.285	39.45	2.07
C000	252.30	2.83	0.029	386.57	57.00	0.274	34.73	−2.65
C010	246.80	2.93	0.029	405.09	63.17	0.287	39.07	1.69
C015	243.81	3.05	0.031	405.96	63.92	0.289	39.94	2.56
C020	240.64	3.21	0.033	405.83	63.98	0.289	40.70	3.32
D000	250.80	2.74	0.030	383.79	55.25	0.284	34.65	−2.73
D010	247.52	2.68	0.029	402.73	63.56	0.302	38.54	1.16
D015	245.60	2.73	0.029	402.79	63.67	0.301	39.03	1.65
D020	243.71	2.92	0.031	400.63	64.86	0.306	39.17	1.79
E000	248.83	2.82	0.028	375.78	54.60	0.278	33.78	−3.60
E010	242.37	3.01	0.030	402.81	67.33	0.301	39.83	2.45
E015	238.86	3.18	0.032	402.66	67.47	0.301	40.68	3.30
E020	235.13	3.39	0.035	402.45	67.76	0.302	41.58	4.20

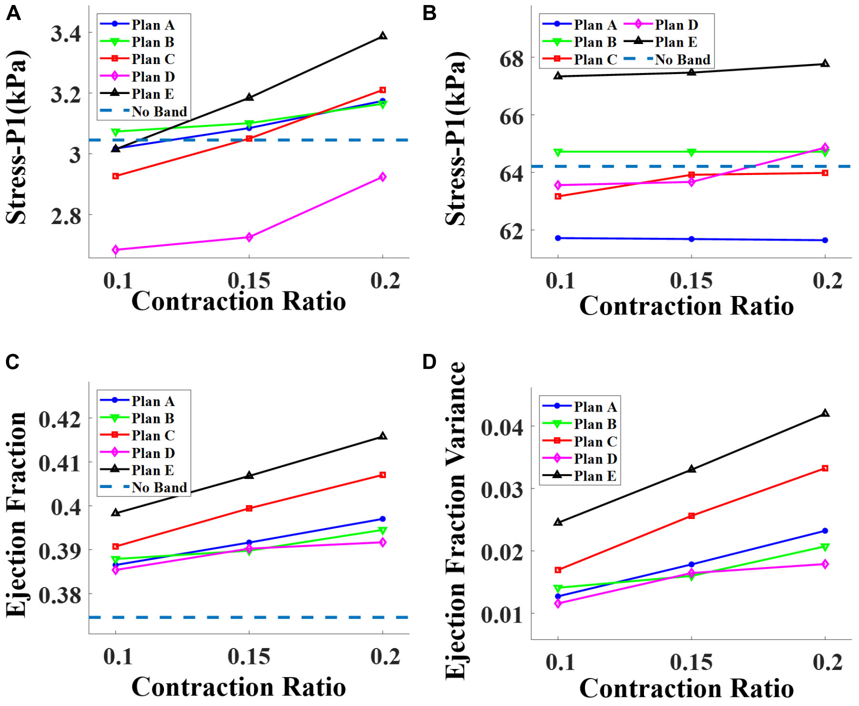

FIGURE 6 | Impact of contraction ratio on RV wall stress, ejection fraction, and ejection fraction improvement with band insertion surgery. **(A)** Begin-filling stress. **(B)** Begin-ejection stress. **(C)** Ejection fraction. **(D)** Ejection fraction improvement.

61.64, 64.72, 63.98, 64.86, and 67.76 kPa, respectively, compared to the baseline mean stress value at 64.21 kPa. The RV mean strain values at begin-ejection from the five band models (A020–E020) with 20% band contraction ratio were 0.291, 0.285, 0.289, 0.306, and 0.302 compared to the baseline mean stress value at 0.288. The RV mean stress and strain values at begin-filling were

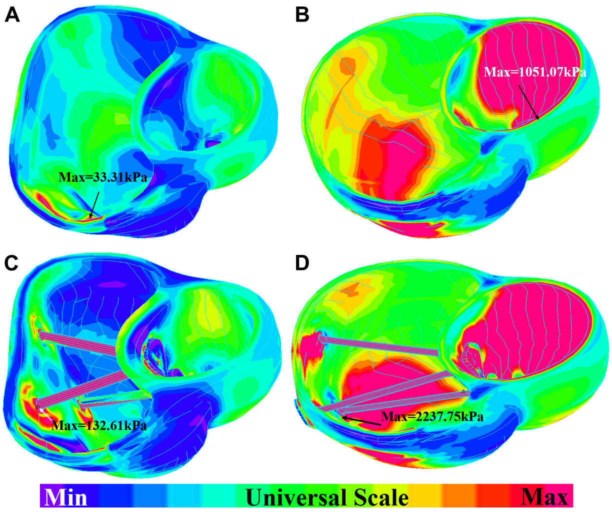

FIGURE 7 | Short-axis view: ventricle stress plots (stress-P_1) of baseline model and model E020. **(A)** Baseline model at begin-filling. **(B)** Baseline model at begin-ejection. **(C)** Model E020 at begin-filling. **(D)** Model E020 at begin-ejection.

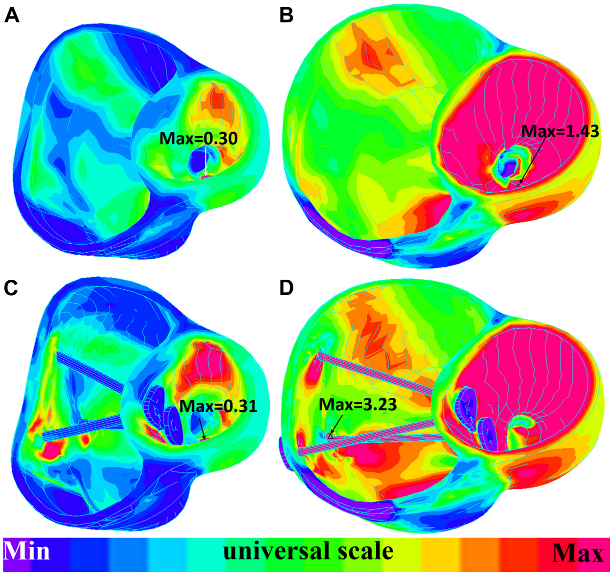

FIGURE 8 | Short-axis view: ventricle strain plots (strain-P_1) of baseline model and model E020. **(A)** Model E020 at begin-filling. **(B)** Model E020 at begin-ejection. **(C)** Baseline model at begin-filling. **(D)** Baseline model at begin-ejection.

small and their relative differences were also small. Overall the band insertion did not cause differences to the RV mean stress/strain values.

The impact of band insertion can be better observed by the stress/strain local distributions. **Figures 7–9** give the stress number and locations. The local stress/strain behaviors can be important band surgical suture considerations.

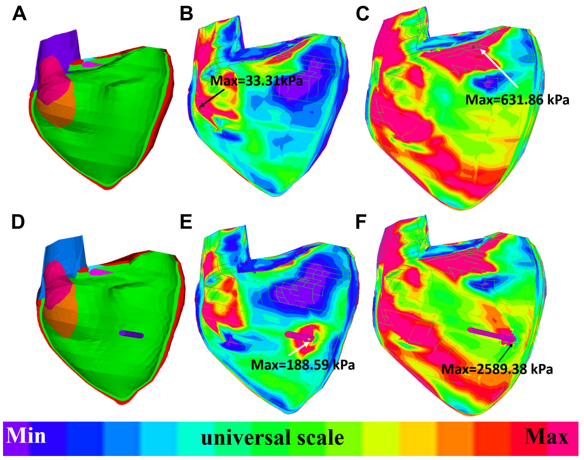

FIGURE 9 | Long-axis cut-surface: stress-P_1 band plots of baseline model and model B020. **(A)** Zero-load geometry of baseline model. **(B)** Baseline model at begin-filling. **(C)** Baseline model at begin-ejection. **(D)** Zero-load geometry of model B020. **(E)** Model B020 at begin-filling. **(F)** Model B020 at begin-ejection.

DISCUSSION

PVR Surgical Options and Challenge for Band Insertion Strategy

While PVR surgery has to be performed for repaired TOF patients in their lives, improving post-PVR cardiac function remains a challenge due to the complexities in surgical procedures, patch material, RV geometry, and remodeling process after PVR. We have demonstrated that band insertion with active contracting bands has good potential for possible improvements. Our modeling study showed that active contractional bands could improve the RV ejection fraction from 37.38 to 41.58% for the patient studied. This is an absolute improvement of 4.20% or a relative improvement of 11.24%. This compares favorably with the published drug trials to treat heart failure in which an improvement of 3 to 4% in LVEF resulted in significant improvement in functional capacity (Aleksova et al., 2012). Combined with scar trimming, patch optimization, and RV remodeling in PVR surgery, the band insertion technique may have further improvement in post-PVR cardiac function.

As we tried to demonstrate the feasibility of the band insertion strategies, the availability of the active contracting bands is an issue. Myocardium tissue regeneration has been an active research area in recent years. Ideally, the active contraction bands would be made of myocardium which could contract synchronized with the ventricle contraction. Currently, one viable solution is to use stem cells and biomaterial to generate an active contraction band made of contractional filament. Huge efforts had been devoted into cardiac repair and regeneration with biomaterial scaffolds such as fibrin or collagen (Barsotti et al., 2011; Cui et al., 2016). Proulx et al. (2011) described a band made of fibrin that could be seeded with mesenchymal stem cells and stitched through a collagen gel. A contracting band may be made by seeding these fibrin bands with contractile cells or stem cells. The details were discussed in our previous work (Tang et al., 2013).

Like many popular commercial mechanical ventricle assist devices for ventricular heart failure such as Impella RP (Abiomed, Danvers, MA, United States), HeartMate II (St. Jude Medical, Minneapolis, MN, United States) or HeartWare HVAD (HeartWare, Framingham, MA, United States), active contractional bands aim to help the ventricle to contract and push more blood to flow into the aorta or the pulmonary artery. These commercial ventricle assist devices have made great contributions to heart failure treatment with massive clinical cases (Sabashnikov et al., 2014; Anderson et al., 2015). RV heart failure has become a major clinical problem for TOF patients as the surgeries greatly extended their life expectancy (Wald et al., 2015). However, ventricle assist devices have not gained widespread use in adult patients with RV heart failure caused by a congenital heart disease due to many potential barriers (Everitt et al., 2015; Wald et al., 2015). Instead of using a pump draining blood from the ventricle and delivering it to the pulmonary artery or the artery directly, active contractional band insertion surgery presents an innovative method by helping the ventricle in squeezing more blood into the pulmonary artery.

Optimization of Band Contraction Ratio, Number, and Location

Reduction of RV ejection fraction with elastic passive bands indicated that passive band surgery might not be an optimal surgery treatment for TOF patients. The PVR surgery with more bands and higher active contraction ratios had better improvement in recovering the RV function. However, in our work, the active band contraction ratios (10, 15, and 20%) were only our hypothetical numbers. An early theoretical analysis by Gordon et al. (1966) indicated that the contraction ratio of the sarcomere could reach about 40%. With higher contraction ratio, greater improvements in the RV ejection fraction is possible. In order to test the band performance under an extreme condition of 40% band zero-load contraction ratio, an experiment was conducted, showing that the ejection fraction of the RV model after surgery plan E could reach 45.33%, providing a 7.87% absolute improvement. The ejection fractions of plans A, B, C, and D were 42.78, 41.83, 44.15, and 42.10%, respectively. However, normally, the myocardium sarcomere active contraction ratio could hardly be so extreme. This experiment simply aimed to explore the maximum ability of the band to improve the RV function. It should be noted that the band contraction should be consistent with the ventricle contraction. Meanwhile, the RV stress of plan E and the 40% band active contraction was 32.13% higher than that of the baseline. The results are shown in **Table 6**. Extreme band contraction could cause damage to the ventricle wall and defeat our purpose. Compared to plans A and B, plan D had much lower RV stress values and their differences in △EF were small. Thus, it is reasonable to believe that plan D may be the optimal surgery plan if only one band was used in the surgery. The RV stress values of model E010 was below the base value and most of the band models and yet its RV ejection fraction improvement was higher than model C010 and all the models with one band, from which a hypothesis can be drawn: multi-band surgeries with low band contraction ratios could have better performance than single-band surgeries with higher band contraction ratios.

At least, under the current circumstances, the passive bands could increase the RV stress and decrease the RV EF, causing damage to the ventricle wall and a negative effect on the RV function. For active band surgery plans, plan E (three-band model) with an active band contraction ratio of 20% had the best performance on improving the RV EF.

Model Validation

Model validation is a key step for all modeling work. For our modeling effort, validation takes several stages. The first stage

TABLE 6 | Right ventricle EF and wall stress/strain from models of band active contraction ratio of 40%.

Surgery plan	Begin-filling			Begin-Ejection			EF (%)	ΔEF (%)
	RV volume (ml)	Stress (kPa)	Strain	RV volume (ml)	Stress (kPa)	Strain		
A	233.76	3.62	0.038	408.59	60.61	0.29	42.79	5.33
B	236.44	3.40	0.039	406.45	64.18	0.28	41.83	4.37
C	225.76	3.96	0.045	404.21	65.13	0.29	44.15	6.69
D	230.04	3.19	0.035	397.34	87.45	0.31	42.11	4.65
E	217.96	4.03	0.046	398.68	68.84	0.30	45.33	7.87

TABLE 7 | Impact of myocardium fiber orientation RV stress and strain values.

RV fiber		Inner layer: 160° Outer layer: 75°	Inner layer: 100° Outer layer: 15°	Inner layer: 40° Outer layer: −45°
Begin-filling	Stress (kPa)	3.27	3.13	3.05
	Strain	0.032	0.033	0.031
Begin-ejection	Stress (kPa)	73.96	61.03	64.21
	Strain	0.295	0.307	0.288

is validation of our no-band model using available *in vivo* MRI-measured RV volume. The RV/LV models were constructed with material parameters chosen to match patient-specific RV volume data. With this patient-specific RV/LV model, the band models were constructed (by adding bands to the validated RV/LV models) to conduct our feasibility study. The validation of these band models would require results and data from patients who would have received those surgeries with contracting bands. Those data are currently not available. In fact, this feasibility study is aimed to obtain pilot data to support further effort in investigations in this direction, including tissue regeneration effort to produce the contracting band and actual surgical experimentation using animal models (pigs). The purpose of using computer-simulated virtual surgeries is to avoid direct experimentation on patients. That is the value of our approach.

Model Limitations and Future Directions

Several limitations should be acknowledged in our modeling study: (a) only one patient's data were used in this study. The band insertion benefits may vary from patient to patient. A multi-patient study should be conducted to help us draw more valid conclusions and further verify and confirm our findings; (b) the fluid–structure interaction should be included to obtain both blood flow and myocardium stress and strain data; (c) both the tricuspid valve and the pulmonary valve mechanics were not included; (d) data shown in **Table 7** indicate that the RV stress and strain values could be affected by myocardium fiber orientations. Patient-specific TOF RV/LV myocardium fiber orientations should be acquired and used in our future models; (e) the pre-shrink method applied to *in vivo* ventricle geometry obtained from CMR data to obtain approximate zero-load geometries could alter the shape of the ventricle when *in vivo* pressure was applied; (f) band stress and strain data were not available since the variance of zero-load length during band contraction and relaxation was not considered; (g) in our stimulation, the band did not change the RV blood pressure; and (h) in our future study, the band material parameters will be identical to the healthy myocardium as described in Yu et al. (2018).

DATA AVAILABILITY STATEMENT

All datasets generated for this study are included in the article/supplementary material.

ETHICS STATEMENT

Written informed consent was obtained from the individual(s) for the publication of any potentially identifiable images or data included in this article.

AUTHOR CONTRIBUTIONS

PN, TG, and RR collected the data. HY, CY, ZW, XH, and DT computed the modeling and analyzed the results. KB provided the biaxial test experiment data. HY and DT wrote the manuscript.

FUNDING

This research was supported during this study in part by the National Natural Science Foundation of China (Grants 11672001 and 81571691) and the Postgraduate Research and Practice Innovation Program of Jiangsu Province (KYCX19_0110).

REFERENCES

Aleksova, A., Masson, S., Maggioni, A. P., Lucci, D., Urso, R., Staszewsky, L., et al. (2012). Effects of candesartan on left ventricular function, aldosterone and BNP in chronic heart failure. *Cardiovasc. Drugs Ther.* 26, 131–143. doi: 10.1007/s10557-012-6370-8

Anderson, M. B., Goldstein, J., Milano, C., Morris, L. D., Kormos, R. L., Bhama, J., et al. (2015). Benefits of a novel percutaneous ventricular assist device for right heart failure: the prospective RECOVER RIGHT study of the Impella RP device. *J. Heart Lung Transplant.* 34, 1549–1560. doi: 10.1016/j.healun.2015.08.018

Axel, L. (2002). Biomechanical dynamics of the heart with MRI. *Annu. Rev. Biomed. Eng.* 4, 321–347. doi: 10.1146/annurev.bioeng.4.020702.153434

Bacha, E. A., Scheule, A. M., Zurakowski, D., Erickson, L. C., Hung, J., Lang, P., et al. (2001). Long-term results after early primary repair of tetralogy of Fallot. *J. Thorac. Cardiovasc. Surg.* 122, 154–161. doi: 10.1067/mtc.2001.115156

Barsotti, M. C., Felice, F., Balbarini, A., and Stefano, R. D. (2011). Fibrin as a scaffold for cardiac tissue engineering. *Biotechnol. Appl. Biochem.* 58, 301–310. doi: 10.1002/bab.49

Billiar, K. L., and Sacks, M. S. (2000). Biaxial mechanical properties of the natural and glutaraldehyde treated aortic valve cusp–Part I: experimental results. *J. Biomech. Eng.* 122, 23–30. doi: 10.1115/1.429624

Costa, K. D., Takayama, Y., McCulloch, A. D., and Covell, J. W. (1999). Laminar fiber architecture and three dimensional systolic mechanics in canine ventricular myocardium. *Am. J. Physiol.* 276, H595–H607. doi: 10.1152/ajpheart.1999.276.2.H595

Cui, Z., Yang, B., and Li, R. K. (2016). Application of biomaterials in cardiac repair and regeneration. *Engineering* 2, 141–148. doi: 10.1016/j.eng.2016.01.028

Deng, L., Huang, X., Yang, C., Lyu, B., Duan, F., Tang, D., et al. (2018). Numerical simulation study on systolic anterior motion of the mitral valve in hypertrophic obstructive cardiomyopathy. *Int. J. Cardiol.* 266, 167–173. doi: 10.1016/j.ijcard.2018.01.062

Everitt, M. D., Donaldson, A. E., Stehlik, J., Kaza, A. K., Budge, D., Alharethi, R., et al. (2015). Would access to device therapies improve transplant outcomes for adults with congenital heart disease? Analysis of the united network for organ sharing (UNOS). *J. Heart Lung Transplant.* 30, 395–401. doi: 10.1016/j.healun.2010.09.008

Fang, J. C., Ewald, G. A., Allen, L. A., Butler, J., Westlake, Canary CA, Colvin-Adams, M., et al. (2015). Advanced (Stage D) heart failure: a statement from the heart failure society of America guidelines committee. *J. Card. Fail.* 21, 519–534. doi: 10.1016/j.cardfail.2015.04.013

Geva, T., Gauvreau, K., Powell, A. J., Cecchin, F., Rhodes, J., Geva, J., et al. (2010). Randomized trial of pulmonary valve replacement with and without right ventricular remodeling surgery. *Circulation* 122, S201–S208. doi: 10.1161/CIRCULATIONAHA.110.951178

Gordon, A. M., Huxley, A. F., and Julian, F. J. (1966). The variation in isometric tension with sarcomere length in vertebrate muscle fibres. *J. Physiol.* 184, 170–192. doi: 10.1113/jphysiol.1966.sp007909

Hunter, P. J., Pullan, A. J., and Smaill, B. H. (2003). Modeling total heart function. *Annu. Rev. Biomed. Eng.* 5, 147–177. doi: 10.1146/annurev.bioeng.5.040202.121537

Kerckhoffs, R. C., Neal, M. L., Gu, Q., Bassingthwaighte, J. B., Omens, J. H., and McCulloch, A. D. (2007). Coupling of a3D finite element model of cardiac ventricular mechanics to lumped systems models of the systemic and pulmonic circulation. *Ann. Biomed. Eng.* 35, 1–18. doi: 10.1007/s10439-006-9212-7

Kim, Y. Y., and Emily, Rl (2016). Approach to residual pulmonary valve dysfunction in adults with repaired tetralogy of Fallot. *Heart* 102, 1520–1526. doi: 10.1136/heartjnl-2015-309067

Kong, F., Pham, T., Martin, C., McKay, R., Primiano, C., Hashim, S., et al. (2018). Finite element analysis of tricuspid valve deformation from multi-slice computed tomography images. *Ann. Biomed. Eng.* 46, 1112–1127. doi: 10.1007/s10439-018-2024-8

McCulloch, A. D., Waldman, L., Rogers, J., and Guccione, J. M. (1992). Large-scale finite element analysis of the beating heart. *Crit. Rev. Biomed. Eng.* 20, 427–449.

Murdock, K., Martin, C., and Sun, W. (2018). Characterization of mechanical properties of pericardium tissue using planar biaxial tension and flexural deformation. *J. Mech. Behav. Biomed. Mater.* 77, 148–156. doi: 10.1016/j.jmbbm

Nash, M. P., and Hunter, P. J. (2000). Computational mechanics of the heart, from tissue structure to ventricular function. *J. Elast.* 61, 113–141. doi: 10.1007/0-306-48389-0_4

Peskin, C. S. (1977). Numerical analysis of blood flow in the heart. *J. Comput. Phys.* 25, 220–252. doi: 10.1016/0021-9991(77)90100-0

Peskin, C. S. (1989). A three-dimensional computational method for blood flow in the heart. *J. Comput. Phys.* 81, 372–405. doi: 10.1016/0021-9991(89)90213-1

Proulx, M. K., Carey, S. P., Ditroia, L. M., Jones, C. M., Fakharzadeh, M., Guyette, J. P., et al. (2011). Fibrin microthreads support mesenchymal stem cell growth while maintaining differentiation potential. *J. Biomed. Mater. Res. A* 96, 301–312. doi: 10.1002/jbm.a.32978

Sabashnikov, A., Mohite, P. N., Zych, B., Popov, A.-F., Fatullayev, J., and Zeriouh, M. (2014). Outcomes in patients receiving heart mate II versus HVAD left ventricular assist device as a bridge to transplantation. *Transplant. Proc.* 46, 1469–1475. doi: 10.1016/j.transproceed.2013.12.057

Saber, N. R., Gosman, A. D., Wood, N. B., Kilner, P. J., Charrier, C. L., and Firman, D. N. (2001). Computational flow modeling of the left ventricle based on in vivo MRI data: initial experience. *Ann. Biomed. Eng.* 29, 275–283. doi: 10.1114/1.1359452

Sacks, M. S., and Chuong, C. J. (1993). Biaxial mechanical properties of passive right ventricular free wall myocardium. *J. Biomech. Eng.* 115, 202–205. doi: 10.1115/1.2894122

Sanchez-Quintana, D., Anderson, R. H., and Ho, S. Y. (1996). Ventricular myoarchitecture in tetralogy of Fallot. *Heart* 17, 280–286. doi: 10.1136/hrt.76.3.280

Sulejmani, F., Pokutta-Paskaleva, A., Salazar, O., Karimi, M., and Sun, W. (2019). Mechanical and structural analysis of the pulmonary valve in congenital heart defects: a presentation of two case studies. *J. Mech. Behav. Biomed. Mater.* 89, 9–12. doi: 10.1016/j.jmbbm.2018.08.053

Tang, D., Yang, C., del Nido, P. J., Zuo, H., Rathod, R. H., Huang, X., et al. (2015). Mechanical stress is associated with right ventricular response to pulmonary valve replacement in patients with repaired tetralogy of Fallot mechanical stress. *J. Thorac. Cardiovasc. Surg.* 151, 687–694. doi: 10.1016/j.jtcvs.2015.09.106

Tang, D., Yang, C., Geva, T., and del Nido, P. J. (2008). Patient-specific MRI-based 3D FSI RV/LV/Patch models for pulmonary valve replacement surgery and patch optimization. *J. Biomech. Eng.* 130:041010. doi: 10.1115/1.2913339

Tang, D., Yang, C., Geva, T., Rathod, R. H., Yamauchi, H., Gooty, V., et al. (2013). A multiphysics modeling approach to develop right ventricle pulmonary valve replacement surgical procedures with a contracting band to improve ventricle ejection fraction. *Comput. Struct.* 122, 78–87. doi: 10.1016/j.compstruc.2012.11.016

Vliegen, H. W., Van Straten, A., De Roos, A., Roest, A. A., Schoof, P. H., Zwinderman, A. H., et al. (2002). Magnetic resonance imaging to assess the hemodynamic effects of pulmonary valve replacement in adults late after repair of tetralogy of Fallot. *Circulation* 106, 1703–1707. doi: 10.1161/01.cir.0000030995.59403.f8

Wald, R. M., Valente, A. M., and Marelli, A. (2015). Heart failure in adult congenital heart disease: emerging concepts with a focus on tetralogy of Fallot. *Trends Cardiovasc. Med.* 25, 422–432. doi: 10.1016/j.tcm.2014.11.011

Yang, C., Tang, D., Geva, T., Rathod, R. H., Yamauchi, H., Gooty, V., et al. (2013). Using contracting band to improve right ventricle ejection fraction for patients with repaired tetralogy of Fallot, a modeling study using patient-specific CMR-based two-layer anisotropic models of human right and left ventricles. *J. Thorac. Cardiovasc. Surg.* 145, 285–293.

Yu, H., Tang, D., Geva, T., Yang, C., Wu, Z., Rathod, R. H., et al. (2018). Patient-specific in vivo right ventricle material parameter estimation for patients with tetralogy of Fallot using MRI-based models with different zero-load diastole and systole morphologies. *Int. J. Cardiol.* 276, 93–99. doi: 10.1016/j.ijcard.2018.09.030

Yu, H., Tang, D., Geva, T., Yang, C., Wu, Z., Rathod, R. H., et al. (2019). Ventricle stress/strain comparisons between Tetralogy of Fallot patients and healthy using models with different zero-load diastole and systole morphologies. *PLoS One* 14:e0220328. doi: 10.1371/journal.pone.0220328

Conflict of Interest: The authors declare that the research was conducted in the absence of any commercial or financial relationships that could be construed as a potential conflict of interest.

frontiers
in Physiology

ORIGINAL RESEARCH
published: 31 March 2020
doi: 10.3389/fphys.2020.00265

Transmural Remodeling of Cardiac Microstructure in Aged Spontaneously Hypertensive Rats by Diffusion Tensor MRI

Archontis Giannakidis[1,2,3]* **and Grant T. Gullberg**[2,4]

[1] School of Science and Technology, Nottingham Trent University, Nottingham, United Kingdom, [2] Life Sciences Division, Lawrence Berkeley National Laboratory, Berkeley, CA, United States, [3] National Heart & Lung Institute, Imperial College London, London, United Kingdom, [4] Department of Radiology and Biomedical Imaging, University of California, San Francisco, San Francisco, CA, United States

The long-standing high blood pressure (also known as hypertension) overworks the heart. Microstructural remodeling is a key factor of hypertensive heart disease progression. Diffusion tensor magnetic resonance imaging (DT-MRI) is a powerful tool for the rapid noninvasive nondestructive delineation of the cardiomyocyte organization. The spontaneously hypertensive rat (SHR) is a well-established model of genetic hypertension. The goal of this study was to employ high-resolution DT-MRI and the SHR animal model to assess the transmural layer-specific remodeling of myocardial microstructure associated with hypertension. *Ex vivo* experiments were performed on excised formalin-fixed hearts of aged SHRs ($n = 4$) and age-matched controls ($n = 4$). The DT-MRI-derived fractional anisotropy (FA), longitudinal diffusivity (λ_L), transversal diffusivity (λ_T), and mean diffusivity (MD) served as the readout parameters investigated at three transmural zones (i.e., endocardium, mesocardium, and epicardium). The helix angles (HAs) of the aggregated cardiomyocytes and the orientation of laminar sheetlets were also studied. Compared with controls, the SHRs exhibited decreased epicardial FA, while FA changes in the other two transmural regions were insignificant. No substantial differences were observed in the diffusivity parameters and the transmural course of HAs between the two groups. A consistent distribution pattern of laminar sheetlet orientation was not identified for either group. Our findings are in line with the known cellular microstructure from early painstaking histological studies. Biophysical explanations of the study outcomes are provided. In conclusion, our experimental findings indicate that the epicardial microstructure is more vulnerable to high blood pressure leading to more pronounced changes in this region during remodeling. DT-MRI is well-suited for elucidating these alterations. The revealed transmural nonuniformity of myocardial reorganization may shed light on the mechanisms of the microstructure-function relationship in hypertension progression. Our results provide insights into the management of patients with systemic arterial hypertension, thus prevent the progression toward heart failure. The findings of this study should be acknowledged by electromechanical models of the heart that simulate the specific cardiac pathology.

Keywords: myocardium, microstructure, remodeling, left ventricle, diffusion tensor MRI, hypertension

Edited by:
Yunlong Huo,
Shanghai Jiao Tong University, China

Reviewed by:
Arun V. Holden,
University of Leeds, United Kingdom
Dongliang Zhao,
Peking University, China

***Correspondence:**
Archontis Giannakidis
archontis.giannakidis@ntu.ac.uk

Specialty section:
This article was submitted to Computational Physiology and Medicine,
a section of the journal Frontiers in Physiology

Received: *07 October 2019*
Accepted: *09 March 2020*
Published: *31 March 2020*

Citation:
Giannakidis A and Gullberg GT (2020) Transmural Remodeling of Cardiac Microstructure in Aged Spontaneously Hypertensive Rats by Diffusion Tensor MRI. Front. Physiol. 11:265.
doi: 10.3389/fphys.2020.00265

1. INTRODUCTION

Elevated blood pressure in the arteries (also known as hypertension) is a serious condition that can lead to heart failure, stroke, kidney failure, and blindness among others[1]. More than 1 in 5 adults live with hypertension all around the globe, and complications from persistent high blood pressure account for 12.8% of the total of all deaths worldwide every year[2]. On top of that, the related disability puts a huge burden on medical care budgets. The treatment of hypertension is an important healthcare priority throughout the world[3].

Focussing on the heart, the chronic elevated arterial pressure adversely affects the cardiac function by compromising the organ's ability to work as a pump which escalates into heart failure. But a key determinant of the heart's pumping function is its unique three-dimensional (3D) microstructural organization (Arts et al., 1979). Therefore, and from a clinical perspective, depicting the remodeling of cardiomyocyte arrangement in hypertension is of vital significance, as this would provide us with a novel insight on the structure-function relationship allowing us to better interpret and model the cardiac behavior in this pathology.

The development of experimental pre-clinical models of left ventricular pressure overload has been very helpful for the study of the microstructural remodeling in hypertension (Lerman et al., 2005). The spontaneously hypertensive rat (SHR) (Okamoto and Aoki, 1963), which exhibits a type of hypertension that is analogous to essential hypertension in humans, is by far the most popular animal model. Early descriptions of the cardiac tissue alterations in the SHR model were based on gross dissection and microscopy (Kawamura et al., 1976; Engelmann et al., 1987). However, and in spite of being very enlightening with regard to cardiomyocyte alignment, this conventional approach is burdensome, tedious, destructive, inherently two-dimensional (2D), susceptible to processing artifacts, and of low spatial resolution (Hsu et al., 2010). Clearly, there is great clinical utility in acquiring the myocardial microstructural remodeling in hypertension by finding a way around the limitations of histology.

Diffusion tensor magnetic resonance imaging (DT-MRI) has emerged (Basser et al., 1994) as a powerful non-invasive non-destructive modality that infers the orientation-dependent microstructure of tissues such as the myocardium by relating the preferential self-diffusion of water molecules to the MRI signal attenuation. Compared to histology, DT-MRI provides far more measurement points in much shorter acquisition times (Winslow et al., 2000). To date, DT-MRI has been employed to assess myocardial microstructure in humans (Reese et al., 1995) and animal models (Healy et al., 2011; Teh et al., 2017), as well as to characterize cardiac pathologies like ischemia (Wu et al., 2006). There are several studies (Hales et al., 2011, 2012; Gilbert et al., 2012; Bernus et al., 2015; Teh et al., 2016, 2017) which have applied DT-MRI to rat hearts.

Given that some stimuli in hypertension have been shown (McCrossan et al., 2004) to produce a transmurally-varied cellular response, in this study we use aged SHRs and DT-MRI to test the hypothesis that the impact of long-standing elevated blood pressure on the cardiomyocyte arrangement depends upon the transmural depth. Because of the inherently low signal-to-noise ratio (SNR) and motion artifacts that currently hamper the high-spatial-resolution DT-MRI of the beating heart within a realistic time frame (Hsu et al., 2010), our investigation was performed *ex vivo*.

The findings of this study are expected to deeepen our understanding of the mechanisms by which microstructural changes make for the progressive deterioration in cardiac function in hypertensive disease. This understanding is currently weak (Wang et al., 2016). The results are also anticipated to enhance our ability to design therapeutic strategies for the effective management of patients with systemic arterial hypertension, and thus prevent the progression toward heart failure. Finally, our findings will also be useful in the development of more accurate subject-specific image-driven electromechanical models of the hypertensive heart. As a matter of fact, few recent modeling studies (Wang et al., 2015, 2016) of the rodent ventricle physiology have already recognized the lack of high-resolution cardiac microstructure data that could be used as input toward constructing constitutive modeling frameworks of the passive myocardium in hypertension.

2. MATERIALS AND METHODS

2.1. Study Population and Animal Model

The study population comprised 4 male SHRs, and 4 sex-matched Wistar Kyoto rats (WKYs) that served as the controls. SHR (Okamoto and Aoki, 1963) is a well-established genetic model of hypertension. It clones many crucial attributes of the progression of human hypertensive heart disease toward decompensated heart failure, whereas its treatment using angiotensin-converting-enzyme inhibitors is as effective as in humans (Cingolani et al., 2003). Male SHRs were chosen because they have significantly higher blood pressure than the female ones (Maranon and Reckelhoff, 2013). All analyzed rats were at the end of the aging phase (17–18 months old) in the time of heart excision. The endpoint selected for imaging and subsequent quantitative analysis of the microstructural remodeling corresponds to early systolic failure, which is a distinct disease stage of the hypertensive heart disease in humans as well (LeGrice et al., 2012). The animals were bought from the Charles River Laboratories (Wilmington, MA, USA). All animal procedures conformed to the guidelines set forth by the Animal Welfare Research Committee of Lawrence Berkeley National Laboratory.

2.2. Heart Preparation

Under deep isoflurane-inhalation anesthesia, each intact heart was rapidly removed from the chest and flushed with warmed isotonic saline. Once the heart was rinsed, it was weighed and instantaneously placed in 60cc of 10% buffered formalin (Sigma-Aldrich Corp., St. Louis, MO, USA) to induce tissue fixation at a contraction state. All hearts of this study were approximately

---

[1] https://www.nhs.uk/conditions/high-blood-pressure-hypertension/

[2] https://www.who.int/gho/ncd/risk_factors/blood_pressure_prevalence_text/en/

[3] https://www.who.int/features/qa/82/en/

in the same state of contraction as confirmed by measurements of the mean ventricular wall thickness (Omann et al., 2019). The whole-body weight before excision was also recorded. The period between harvest and imaging was approximately 1 week, following the advice on cardiac specimen preparation by Giannakidis et al. (2016a). Before euthanasia, and as part of a separate study (Hernandez et al., 2013), the living rats were imaged using a small animal PET/CT scanner (Inveon dedicated PET docked with CT in the multi-modality platform; Siemens Medical Solutions) and the ^{18}F-FDHROL radiotracer to evaluate the left-ventricular ejection fraction (EF). EF was measured using the clinical cardiac software Myovation designed for the Xeleris workstation (GE Healthcare).

2.3. Imaging

Whole heart imaging was carried out at the Small Animal MRI Imaging Facility of the University of Utah using a 7T horizontal bore MRI scanner (Bruker BioSpin, Ettlingen, Germany) interfaced with the Paravision 5.1 software package. All MRI acquisitions were performed at typical room temperature, approximately 20°C. For imaging, each heart was placed in a sealed 5-mL standard syringe filled with Fomblin (Solvay Solexis, West Deptford, NJ, USA) to increase contrast and eliminate susceptibility artifacts near the boundaries of the myocardium. Hearts were secured inside the containers using gauze to prevent the specimen from floating in the container. The long axis of each heart was aligned with the x-axis of the scanner. A custom-made radio frequency (RF) coil (single turn solenoid, wrapped around the syringe) was used for signal transmission and reception.

To acquire the DT-MRI data, a standard 3D spin echo readout sequence was used with the following parameters: echo time (TE) = 19.224 ms, pulse repetition time (TR) = 500 ms. Diffusion encoding was carried out using a pair of trapezoidal gradient pulses with parameters: gradient duration (δ) = 4 ms, inter-gradient separation (Δ) = 10 ms, rise time = 0.25 ms, maximum strength of the gradient pulse (G) = 30 G/cm, resulting in a nominal b value of 1,000 s/mm^2, accounting for all imaging gradients and cross-terms between imaging and diffusion gradients. The diffusion-induced signal decay was measured along 12 optimized (Papadakis et al., 1999) directions. All diffusion measurements were preceded by the acquisition of one reference (B0) image. The number of signal averages that was acquired was one and the total scan duration for each heart was approximately 17 h. The field of view (FOV) was 27 × 15.5 × 15.5 (mm), with a data matrix size = 169 × 97 × 97, resulting in an isotropic resolution of 0.160 mm.

The SNR was measured in the B0 image of each dataset as the mean signal of the myocardium in the central slice of the dataset divided by the standard deviation of the noise (measured outside the myocardium), multiplied by the factor 0.655

$$SNR_{(b=0)} = 0.655\frac{Mean(myocardium)}{Standard\ Deviation(Background\ Noise)} \tag{1}$$

where the factor 0.655 was used to account for the fact that the SNR was estimated on the magnitude data and the mean of the noise is not zero (Rician noise) (Henkelman, 1985).

2.4. Data Analysis

Five short-axis slices, evenly-spaced between the left ventricular base and apex, were analyzed for each heart. Endocardial and epicardial contours were semi-automatically acquired in the B0 images using cubic splines (de Boor, 1978). Extra care was taken to exclude papillary muscles. To assess whether the left ventricular cardiomyocytes respond uniformly to their hypertensive environment, each profile was divided into three transmural zones of equal thickness (i.e., epicardium, mesocardium, endocardium) (**Figure 1**).

The rank two symmetric diffusion tensors were estimated on a pixel-by-pixel basis over the myocardial tissue region using the diffusion signal attenuation data, the reference data, and a custom-made multi-variate nonlinear least-squares curve fitting algorithm (Hsu et al., 1998). Following this, the tensor at each voxel was diagonalised to yield the three eigenvalues d_1, d_2, d_3 (where $d_1 \geq d_2 \geq d_3$), and the corresponding eigenvectors $\boldsymbol{e}_1, \boldsymbol{e}_2, \boldsymbol{e}_3$. The eigenvectors represent the three principal axes of diffusion, whereas each eigenvalue is equal to the rate of diffusion along the direction that the paired eigenvector points. Therefore, any voxel, at which the diffusion tensor diagonalisation resulted in at least one negative eigenvalue, was excluded on thermodynamic grounds. The longitudinal diffusivity (λ_L), transversal diffusivity (λ_T), mean diffusivity (MD) and fractional anisotropy (FA) were subsequently derived from the three eigenvalues using the following formulae, respectively:

$$\lambda_L = d_1 \tag{2}$$

$$\lambda_T = \frac{d_2 + d_3}{2} \tag{3}$$

$$MD = \frac{d_1 + d_2 + d_3}{3} \tag{4}$$

$$FA = \sqrt{\frac{3[(d_1 - MD)^2 + (d_2 - MD)^2 + (d_3 - MD)^2]}{2[(d_1)^2 + (d_2)^2 + (d_3)^2]}}. \tag{5}$$

FA is a measure that describes the degree of deviation of a diffusion tensor from the isotropic tensor. In addition, since it was shown (Hsu et al., 1998) that the primary eigenvector of the diffusion tensor coincides with the local cardiomyocyte orientation, then, λ_L represents the water diffusivity parallel to the long axes of cardiomyocytes, while λ_T corresponds to water diffusivity perpendicular to the axonal myocardial cells. λ_L is considered to represent cell axonal integrity, whereas λ_T is regarded as a measure of cell integrity along its diameter (myelin integrity). To quantitatively compare the differences in the above parameters between the two groups, the mean values were computed for each of the three transmural zones across the five short-axis slices.

Apart from the degree of anisotropy and magnitude of water diffusion, its orientation was also studied. To this end, helix angle (HA) maps were determined, where HA is defined (Scollan et al., 1998) as the angle between the cardiac short-axis plane and the projection of the primary eigenvector

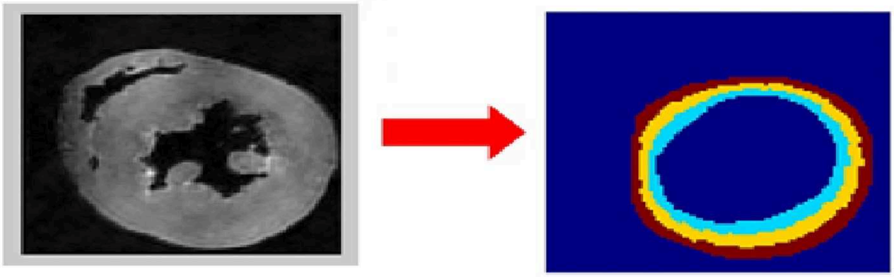

FIGURE 1 | Determination of the region of interest (ROI). The left ventricular wall was segmented semi-automatically in the B0 dataset (left image). Extra care was taken to exclude papillary muscles. The three transmural sectors (endocardium in cyan, mesocardium in yellow, epicardium in brown) were defined evenly spanning the left ventricular wall (right image).

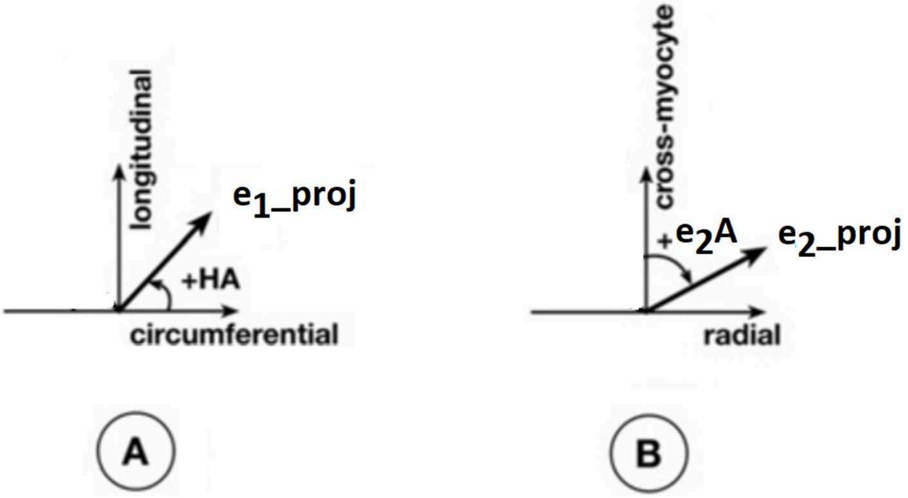

FIGURE 2 | Definitions of helix angle (HA) and angle of the secondary eigenvector of diffusion relative to the local wall tangent. **(A)** HA is the angle between the circumferential direction (which is tangential to the wall with a counter-clockwise direction when viewed from base to apex) and the radial projection of the primary eigenvector e_1 to the local wall tangent. HA takes values in the range −90° to 90°, being positive (right-handed helix) if rotated counter-clockwise from the circumferential as viewed from the outside, and negative (left-handed helix) if rotated clockwise. The longitudinal direction is parallel to the left-ventricular long-axis and pointing toward the base. **(B)** To calculate the angle of the secondary eigenvector of diffusion relative to the local wall tangent, we first calculated the cross-myocyte plane as the one being perpendicular to the primary eigenvector. The pertinent angle is then given by the angle between the projection of the secondary eigenvector e_2 onto this plane and the cross-myocyte direction. This angle takes values in the range [−90°, 90°], being positive if rotated clockwise from the cross-myocyte direction when viewed in the more circumferential direction, and negative if rotated counter-clockwise. The radial direction is obtained by the cross-product of the circumferential and longitudinal directions, described above, pointing outwards.

onto the epicardial tangent plane (**Figure 2**). Such maps have been frequently employed to characterize the classic helix-like orientation pattern of the aggregated cardiomyocytes within the left ventricular wall. To quantitatively compare the differences in HAs between the two groups, we computed the percentages of left-handed cardiomyocytes (i.e., cells with HAs between $-90°$ and $-30°$), circumferential cardiomyocytes (i.e., cells with HAs between $-30°$ and $30°$), and right-handed cardiomyocytes (i.e., cells with HAs between $30°$ and $90°$) for our region of interest (ROI). Finally, assuming (Nielles-Vallespin et al., 2017) that the cross-myocyte components of water diffusion are constrained by the laminar microstructures of the myocardium, we estimated the angles of the secondary eigenvector of diffusion relative to the local wall tangent plane (**Figure 2**), as described in Ferreira et al. (2014) for both control and diseased hearts.

All comparison tools that were employed in this study conform to previous findings (Giannakidis et al., 2016b) on the tensor manifold for cardiac DT-MRI data.

2.5. Statistical Analysis

To test the statistical significance of the differences in the mean parameter values between the two groups, the nonparametric Mann–Whitney test was employed. To assess dissimilarities in the HA distributions between the SHRs and WKYs, we used the chi-squared test for independence. A value of $p<0.05$ was considered statistically significant.

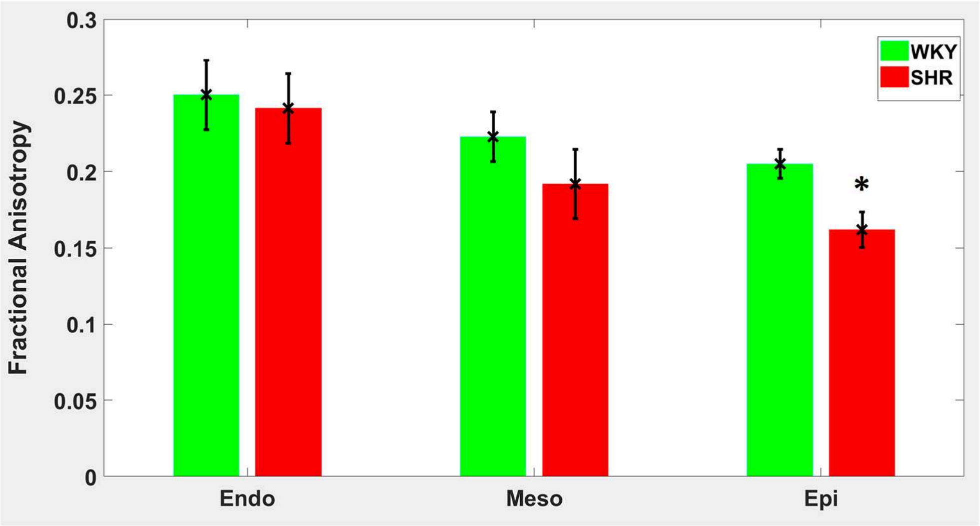

FIGURE 3 | Fractional anisotropy (FA) average in each group for the three transmural zones (i.e., endocardium, mesocardium, epicardium). Every zonal average is represented by a bar graph with corresponding standard deviations as error bars. $^*p < 0.05$ compared with controls.

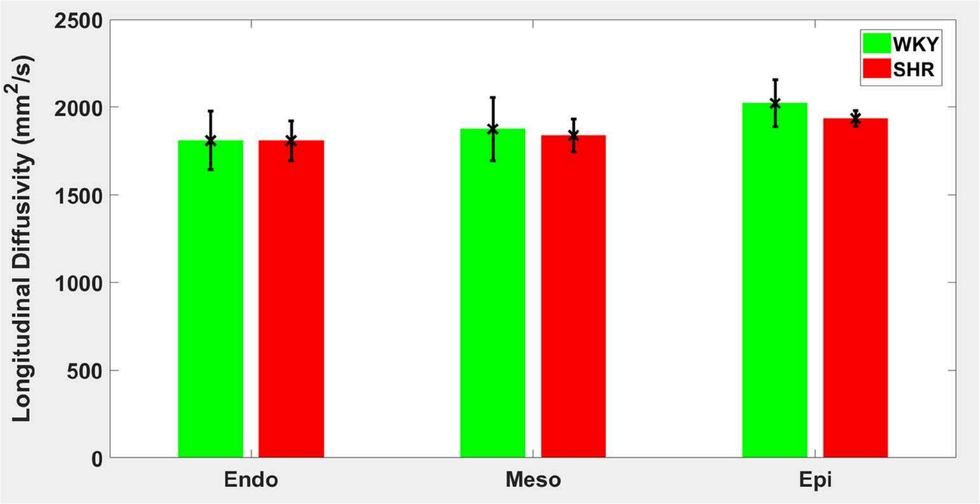

FIGURE 4 | Longitudinal diffusivity (λ_L) average in each group for the three transmural zones (i.e., endocardium, mesocardium, epicardium). Every zonal average is represented by a bar graph with corresponding standard deviations as error bars. The unit of λ_L is mm^2/s.

All computations described in section 2 were performed using in-house code written in Matlab (Mathworks, Natick, MA, USA).

3. RESULTS

The average heart-to-body weight ratio was 0.6550% for the SHRs vs. 0.3450% for the WKYs ($p = 0.0286$), confirming the development of left ventricular hypertrophy in the SHRs at the time of our experiments. The mean SNR for the B0 images was approximately 90 in both groups. The average EF was 69% for the WKYs and 50% for the SHRs, confirming that the SHRs were in borderline heart failure stage.

Hypertension gave rise to a statistically significant decrease in epicardial FA ($p = 0.0286$), when compared to controls (**Figure 3**). The same remodeling was observed in the other two transmural zones, but the changes did not reach the statistical significance level (**Figure 3**). No statistically significant differences were found in the mean λ_L, λ_T, and MD values between the two groups (**Figures 4–6**), even though the mean λ_T and MD values were generally larger in SHRs than the controls (**Figures 5**, **6**). By performing Pearson coefficient analysis, it turned up that there was no significant correlation ($p = 0.3615$) between the degree of cardiac hypertrophy and epicardial FA. A summary of the quantitative comparison results with respect to the degree of

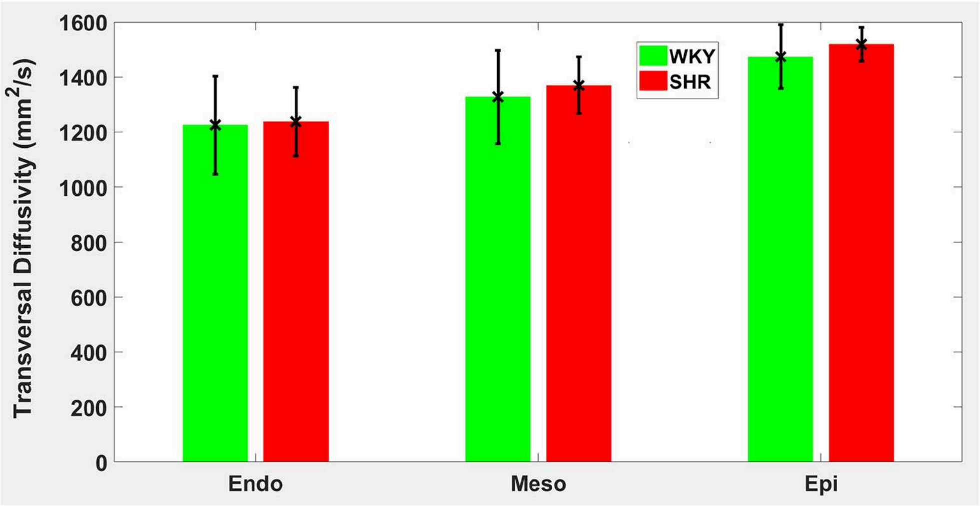

FIGURE 5 | Transversal diffusivity (λ_T) average in each group for the three transmural zones (i.e., endocardium, mesocardium, epicardium). Every zonal average is represented by a bar graph with corresponding standard deviations as error bars. The unit of λ_T is mm^2/s.

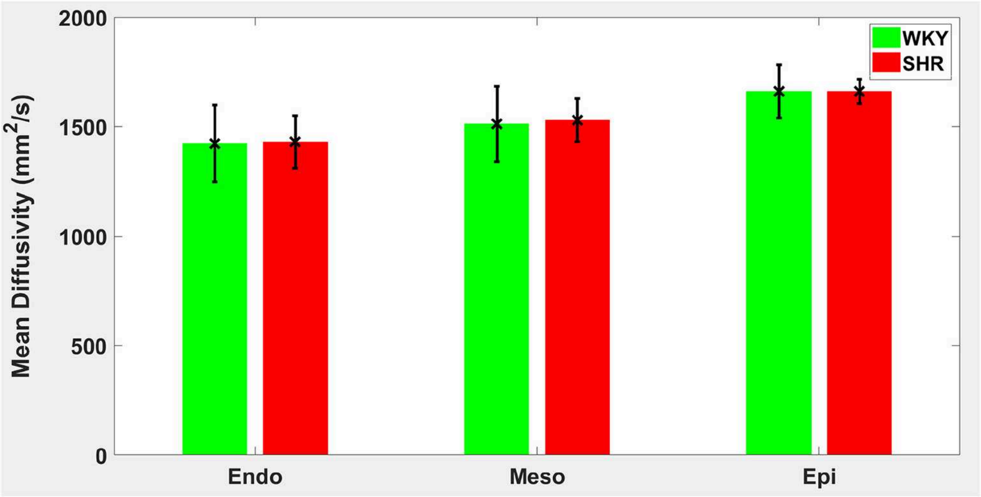

FIGURE 6 | Mean diffusivity (MD) average in each group for the three transmural zones (i.e., endocardium, mesocardium, epicardium). Every zonal average is represented by a bar graph with corresponding standard deviations as error bars. The unit of MD is mm^2/s.

anisotropy and magnitude of water diffusion is presented in **Table 1**.

The classic transition of HAs (namely, from negative values at the epicardium to zero at the mesocardium to positive values at the endocardium) was preserved after hypertension (**Figure 7**). By running the chi-squared test for independence on the HA distributions, we found that we cannot reject the null hypothesis that there is no association between HA distribution and status ($p = 0.9829$) (**Table 2**). Finally, a consistent distribution pattern of the angles of the secondary eigenvector with respect to the local wall tangent plane was not identified for either group (**Figure 8**).

4. DISCUSSION

Unrelenting high blood pressure brings the left ventricle to a pathological pressure overload state which, when left uncontrolled, mediates cardiac remodeling and dysfunction (Weber et al., 1987; Crozatier and Hittinger, 1988; Yazaki et al., 1989). In this paper, our aim was to use the SHR animal model and DT-MRI to assess the transmural layer-specific remodeling of cardiac microstructure associated with hypertension.

This is the first exhaustive and unbiased group study of the cardiac microstructural reorganization in the SHR using DT-MRI. A previous cardiac DT-MRI study (Giannakidis et al., 2013) compared only one SHR and one WKY. Another related study

TABLE 1 | A summary of the quantitative results of the comparison between WKYs and SHRs with respect to the degree of anisotropy and magnitude of water diffusion.

		WKY mean ± std	**SHR** mean ± std	***p*-value**
FA	endo	0.2502 ± 0.0228	0.2413 ± 0.0228	0.3429
	meso	0.2226 ± 0.0162	0.1918 ± 0.0226	0.1143
	epi	0.2050 ± 0.0095	0.1619 ± 0.116	0.0286
λ_L	endo	1,811 ± 166	1,809 ± 114	1.0000
	meso	1,875 ± 180	1,839 ± 94	1.0000
	epi	2,022 ± 133	1,935 ± 44	0.3429
λ_T	endo	1,225 ± 178	1,237 ± 123	1.0000
	meso	1,327 ± 170	1,370 ± 103	0.4857
	epi	1,474 ± 117	1,519 ± 62	0.4857
MD	endo	1,423 ± 174	1,431 ± 121	1.0000
	meso	1,513 ± 173	1,529 ± 98	0.6857
	epi	1,661 ± 122	1,661 ± 56	0.8857

All parameter values are expressed as group averages for the specific transmural zone ± standard deviations. FA is fractional anisotropy, λ_L is longitudinal diffusivity, λ_T is transversal diffusivity, MD is mean diffusivity. All diffusivity values are in mm^2/s.

(Tran et al., 2016) examined only the tissue orientation in SHRs, however, its results are biased in the sense that the same healthy (WKY) hearts were used both for creating the atlas and for the atlas-based comparison with the newly added SHRs.

A main finding of our study was that hypertension gave rise to a statistically significant decrease in epicardial FA, when compared to controls. The same remodeling trend was observed in the other two transmural zones, but the changes did not reach the statistical significance level. Such a transmural inhomogeneity of microstructural remodeling is in line with an early laborious tissue morphometry study (Engelmann et al., 1987) of the SHR model that reported on the presence of distinct, small foci of necrotic cells that were more pronounced in epicardial regions compared to other transmural layers. The transmural layer-specific cellular necrosis ensues as a result of the fact that cardiomyocytes at the outer layer of the heart are less protected from damage, compared to endocardial and mesocardial cells, due to their increased distance from the oxygen diffusing chamber following hypertensive ventricular hypertrophy (Engelmann et al., 1987; LeGrice et al., 2012). Areas of necrotic tissue are typically consistent with lower FA values, as validated in cerebral infarction (Pierpaoli et al., 1993). This diminished number of cardiomyocytes might act as a mechanism involved in the loss of contractile mass and function when hypertensive heart disease patients transition from adaptation to heart failure (Gonzalez et al., 2006; Díez and Frohlich, 2010). In general, decreases in FA can be multifactorial with swollen cardiomyocytes, cellular disarray, increases in collagen etc. having important roles and, indeed, similar FA decreases have been manifested in other cardiac pathologies such as infarction (Wu et al., 2006), dilated cardiomyopathy (Li et al., 2009), and hypertrophic cardiomyopathy (Tseng et al., 2006). A further observation of this study was that no substantial differences in diffusivity values were detected between SHRs and their normotensive equivalents.

With regards to tissue orientation, we found that the classic transmural transition of HAs was preserved after hypertension. A further quantitative analysis showed that there was no association between HA distribution and health status. This result is in agreement with a focal microscopy study (Pope, 2011) that reported insignificant differences in the transmural gradients of cardiomyocyte orientations between WKYs and SHRs.

Lastly, a consistent distribution pattern of the angles of the secondary eigenvector with respect to the local wall tangent plane was not identified for either group. This might be due to the overly complex structure of the myocardial laminar sheetlets that necessitate longer diffusion time. Another possible interpretation is that the simplistic unimodal Gaussian diffusion assumption made by DT-MRI does not satisfy the sheetlet imaging demands, and more advanced diffusion protocols, such as Q-ball imaging (Tuch, 2004), should be used when trying to elucidate this highly impenetrable structure. Further investigation of this finding is required.

The progression of hypertensive heart disease toward heart failure is a complex and multifaceted process. As well as changes in cardiac microstructure, many other pathogenetic mechanisms have been held responsible for the adverse effect on cardiac function (Brilla, 1994). These include metabolic abnormalities, interstitial remodeling, and changes in neurohormonal systems. In a longitudinal PET study (Hernandez et al., 2013) carried out using the same animal cohort as the present study, the SHRs exhibited statistically significant alterations in myocardial substrate metabolism characterized by increased glucose and fatty acid utilizations as early as in 8 months of age, followed by an increased reliance on glucose metabolism with the advancement of hypertrophy and heart failure. These changes were correlated with increases in blood flow and alterations in overall cardiac function. The findings of the present study are in line with these results.

Our results are of great clinical relevance. The manifested transmural nonuniformity of the response of rodent myocardial microstructure to hypertension suggests that there is a necessity to assess the cardiomyocyte arrangement (not only at numerous time points but also) at various depths across the left ventricular wall in order to fully understand and characterize the behavior of the whole organ in hypertension.

The fact that the imaging experiments of this investigation were performed when the SHRs were at the early systolic failure stage of the hypertensive heart disease hints that our findings could also be used to help identify those patients for whom it is required to adopt therapeutic strategies that prevent the progresion toward heart failure. Examples of such treatment might be the blunting of intracellular apoptotic pathways and the stimulation of cellular survival mechanisms that slow down the cell death processes (Gonzalez et al., 2006).

Computer-based electromechanical modeling of the heart at multiple scales is being extensively used in the literature (Markhasin et al., 2003; Vadakkumpadan et al., 2010; Sermesant

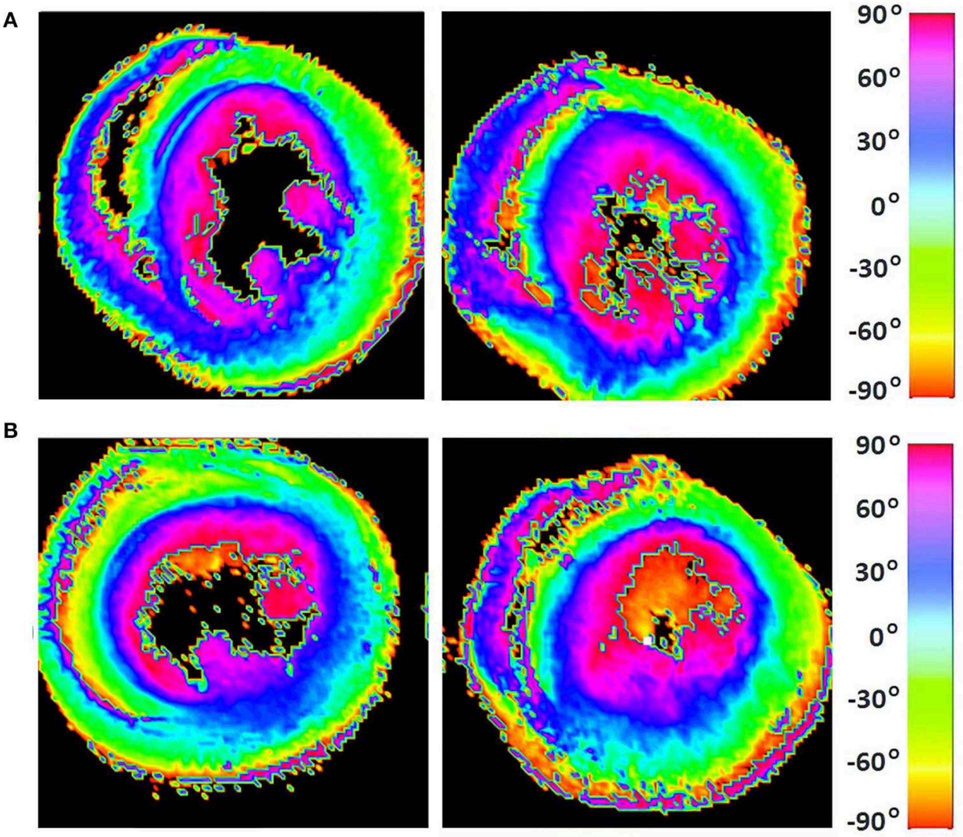

FIGURE 7 | Visualization of helix angle (HA) maps from **(A)** two representative WKYs, **(B)** two representative SHRs. The displayed short-axis slices are from the equatorial region of each heart.

TABLE 2 | A summary of the quantitative results of the comparison between WKYs and SHRs with respect to helix angle (HA) distribution.

	LHC mean ± std	CC mean ± std	RHC mean ± std
WKYs	16.7183 ± 3.1028	56.1480 ± 3.1986	27.1195 ± 2.1782
SHRs	16.6137 ± 3.9436	55.0974 ± 7.1503	28.2771 ± 5.3936
p-value		0.9829	

All parameter values are proportions (%) and are expressed as group averages for the specific orientation band ± standard deviations. LHC is left-handed cardiomyocytes, CC is circumferential cardiomyocytes, and RHC is right-handed cardiomyocytes. The observed chi-squared test statistic is greater than the critical value.

et al., 2012) in order to better understand the function of this complex organ. Given that a major goal of these modeling studies is to accurately simulate pathology, our findings are expected to be important for investigating the mechanisms for the cardiac function degradation in hypertensive heart disease. These mechanisms remain poorly understood to date (Wang et al., 2016). Considering that one needs to account for myocardial microstructure changes to explain differences in chamber compliance, our high-resolution results could be used for the development of more realistic subject-specific constitutive modeling frameworks toward determining the role that microstructural remodeling plays in the passive mechanical function of the heart during the progression of this disease (Wang et al., 2015, 2016). In addition, our results might be important for modeling studies of cardiac electrophysiology (Franzone et al., 1998; Muzikant and Henriquez, 1998) such as, for example, when one tries to determine the organ's predisposition to arrhythmia while still in the compensated state of hypertension (Evans et al., 1995).

This study has few limitations. At first, there is a lack of validation of our findings through histology. Nevertheless, the revealed differences were consistent with findings from early laborious cellular morphometry studies on the same animal model. Next, the small number of animals in both groups is also a weakness. However, the distinctness of the hypertension effects on epicardial FA was highlighted by the observed statistically significant differences between the two groups. The use of formalin fixation may also form a limiting factor in imaging studies. Our chosen duration of tissue exposure to formalin before imaging nonetheless does not appear to amend the DT-MRI parameters when compared to *in vivo* imaging (Giannakidis et al., 2016a). The fact that an animal model was used may also be viewed as a caveat, and a cautious approach is mandatory when findings in animal models are being extrapolated to human

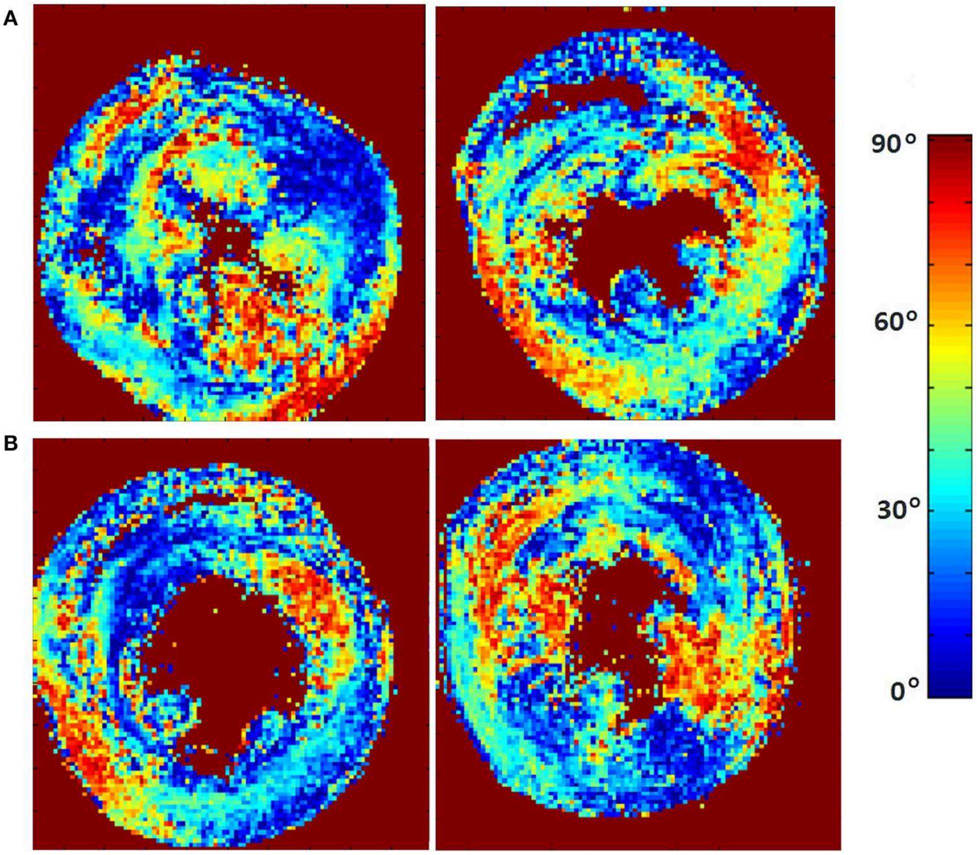

FIGURE 8 | Visualization of the absolute angle maps of the second eigenvector of diffusion relative to the local wall tangent from **(A)** two representative WKYs, **(B)** two representative SHRs. The displayed short-axis slices are from the equatorial region of each heart.

hypertension. However, we believe that the differences between rat and human physiology do not adversely affect our goal, since previous results showed (Lerman et al., 2005) that the SHR model mimics many of the pathophysiology seen in hypertensive heart disease in humans. Another shortcoming of this paper was that only aged (17–18 months old) rats were analyzed. A future DT-MRI study should investigate more phases of the SHR remodeling to shed more light on the time course of hypertensive heart disease. An inherent error of our imaging technique is that a voxel volume of 0.160 mm^3 was sampled. Bearing in mind the average cardiomyocyte size of $20 \times 20 \times 80\ \mu\text{m}^3$ (Okabe et al., 1999), this means that the primary eigenvector in each voxel of our study represents the mean direction of approximately 128 cardiomyocytes. Noise is another source of error in MRI experiments. However, due to the very high SNR achieved in our experiments, it is unlikely that noise has caused any bias. ROI measurements can also induce errors related to reproducibility. Finally, another limitation of this study is that we have not included any measurements of the haemodynamic state of the animals before they were killed. In fact, we tried early in our study to obtain blood pressure measurements of the rats using an external non-invasive method (Ohta et al., 2017). However, we found that this was very difficult, and a lot of effort and preparation time was required in order to maintain the correct environment which was necessary to ensure the accuracy of the small animal data. We actually obtained high blood pressure readings ($>$ 150 mm Hg) for the SHR model, but it was difficult to know if the readings reflected the true blood pressure since the animals exhibited significant stress during the measurement (Jamieson et al., 1997). Likewise, the invasive method to obtain blood pressure measurements in small animals has many disadvantages despite being more accurate (Parasuraman and Raveendran, 2012). In this case, anesthesia is required to perform catheterization which may also lead to haemodynamic changes. In addition, it is a very laborious process, as it necessitates tracheostomy and cannulation of carotid artery. Therefore, we decided on not including any blood pressure measurements in this study. There is nevertheless abundant evidence in the literature (Kawamura et al., 1976) that the 17–18 month old SHRs have long-standing high blood pressure (their blood pressure is significantly higher than in the controls since 7 weeks old). Accordingly, we cannot tell whether more hypertension related to larger decreases in epicardial FA. However, we found that there was no significant correlation between the degree of cardiac hypertrophy and epicardial FA.

In summary, the transmural microstructural nonuniformity of the rodent myocardial response to hypertension gave rise to measurable differences in the DT-MRI-derived FA. The epicardium is more vulnerable to high blood pressure leading to more pronounced microstructural alterations in this region during remodeling. Our observations corroborate previous labor-intensive cellular morphometry studies. Spatial factors are important for fully understanding the heart's behavior in hypertension. Our findings could be useful for the improved management of patients with systemic arterial hypertension, thus prevent further damage. The results of this study are timely and their incorporation in models of cardiac electrophysiology and biomechanics may lead to more robust frameworks that simulate this pathology.

DATA AVAILABILITY STATEMENT

The datasets generated for this study can be found in figshare repository (https://figshare.com/articles/Ex_vivo_cardiac_DT-MRI_rat_study_-_LBNL/11663301).

ETHICS STATEMENT

The animal study was reviewed and approved by Animal Welfare Research Committee of Lawrence Berkeley National Laboratory.

AUTHOR CONTRIBUTIONS

GG conceived and designed the study, and wrote the paper. AG analyzed the data, wrote the software used in analyses, and wrote the paper. All authors agree to be accountable for the content of the work.

FUNDING

The work was supported in part by The National Institutes of Health under Grant R01 EB007219, and The Director, Office of Science, Office of Biological and Environmental Research, Medical Sciences Division of the U.S. Department of Energy under Contract No. DE-AC02-05CH11231.

ACKNOWLEDGMENTS

We thank Kathleen Brennan, DVM, in the Department of Radiotracer Development And Imaging Technology at Lawrence Berkeley National Laboratory for preparation of the excised heart samples, and Edward W. Hsu in the Department of Bioengineering at the University of Utah for acquiring the diffusion tensor MRI datasets used in this study.

REFERENCES

Arts, T., Reneman, R. S., and Veenstra, P. C. (1979). A model of the mechanics of the left ventricle. *Ann. Biomed. Eng.* 7, 299–318. doi: 10.1007/BF02364118

Basser, P. J., Mattiello, J., and LeBihan, D. (1994). MR diffusion tensor spectroscopy and imaging. *Biophys. J.* 66, 259–267. doi: 10.1016/S0006-3495(94)80775-1

Bernus, O., Radjenovic, A., Trew, M. L., LeGrice, I. J., Sands, G. B., Magee, D. R., et al. (2015). Comparison of diffusion tensor imaging by cardiovascular magnetic resonance and gadolinium enhanced 3D image intensity approaches to investigation of structural anisotropy in explanted rat hearts. *J. Cardiovasc. Mag. Reson.* 17:31. doi: 10.1186/s12968-015-0129-x

Brilla, C. G. (1994). The cardiac structure-function relationship and the renin-angiotensin-aldosterone system in hypertension and heart failure. *Curr. Opin. Cardiol.* 9, S2–S11. doi: 10.1097/00001573-199407000-00002

Cingolani, O. H., Yang, X.-P., Cavasin, M. A., and Carretero, O. A. (2003). Increased systolic performance with diastolic dysfunction in adult spontaneously hypertensive rats. *Hypertension* 41, 249–254. doi: 10.1161/01.HYP.0000052832.96564.0B

Crozatier, B., and Hittinger, L. (1988). Mechanical adaptation to chronic pressure overload. *Eur. Heart J.* 9, 7–11. doi: 10.1093/eurheartj/9.suppl_E.7

de Boor, C. (1978). *A Practical Guide to Splines*. New York, NY: Springer-Verlag.

Díez, J., and Frohlich, E. D. (2010). A translational approach to hypertensive heart disease. *Hypertension* 55, 1–8. doi: 10.1161/HYPERTENSIONAHA.109.141887

Engelmann, G. L., Vitullo, J. C., and Gerrity, R. G. (1987). Morphometric analysis of cardiac hypertrophy during development, maturation, and senescence in spontaneously hypertensive rats. *Circul. Res.* 60, 487–494. doi: 10.1161/01.RES.60.4.487

Evans, S. J., Levi, A. J., and Jones, J. V. (1995). Wall stress induced arrhythmia is enhanced by low potassium and early left ventricular hypertrophy in the working rat heart. *Cardiovasc. Res.* 29, 555–562. doi: 10.1016/S0008-6363(96)88534-8

Ferreira, P. F., Kilner, P. J., McGill, L.-A., Nielles-Vallespin, S., Scott, A. D., Ho, S. Y., et al. (2014). *In vivo* cardiovascular magnetic resonance diffusion tensor imaging shows evidence of abnormal myocardial laminar orientations and mobility in hypertrophic cardiomyopathy. *J. Cardiovasc. Magn. Reson.* 16:87. doi: 10.1186/s12968-014-0087-8

Franzone, P. C., Guerri, L., Pennacchio, M., and Taccardi, B. (1998). Spread of excitation in 3-D models of the anisotropic cardiac tissue. II. Effects of fiber architecture and ventricular geometry. *Math. Biosci.* 147, 131–171. doi: 10.1016/S0025-5564(97)00093-X

Giannakidis, A., Gullberg, G. T., Pennell, D. J., and Firmin, D. N. (2016a). Value of formalin fixation for the prolonged preservation of rodent myocardial microanatomical organization: Evidence by MR diffusion tensor imaging. *Anat. Record* 299, 878–887. doi: 10.1002/ar.23359

Giannakidis, A., Melkus, G., Yang, G., and Gullberg, G. T. (2016b). On the averaging of cardiac diffusion tensor MRI data: the effect of distance function selection. *Phys. Med. Biol.* 61, 7765–7786. doi: 10.1088/0031-9155/61/21/7765

Giannakidis, A., Rohmer, D., Veress, A. I., and Gullberg, G. T. (2013). "Diffusion tensor magnetic resonance imaging-derived myocardial fiber disarray in hypertensive left ventricular hypertrophy: visualization, quantification and the effect on mechanical function," in *Cardiac Mapping, 4th Edn.*, eds M. Shenasa, G. Hindricks, M. Borggrefe, G. Breithardt, and M. E. Josephson (Chichester: Wiley-Blackwell), 574–588. doi: 10.1002/9781118481585.ch53

Gilbert, S. H., Benoist, D., Benson, A. P., White, E., Tanner, S. F., Holden, A. V., et al. (2012). Visualization and quantification of whole rat heart laminar structure using high-spatial resolution contrast-enhanced MRI. *Amer. J. Physiol. Heart Circulat. Physiol.* 302, H287–H298. doi: 10.1152/ajpheart.00824.2011

Gonzalez, A., Ravassa, S., Lopez, B., Loperena, I., Querejeta, R., and Díez, J. (2006). Apoptosis in hypertensive heart disease: a clinical approach. *Curr. Opin. Cardiol.* 21, 288–294. doi: 10.1097/01.hco.0000231397.64362.70

Hales, P. W., Burton, R. A. B., Bollensdorff, C., Mason, F., Bishop, M., Gavaghan, D., et al. (2011). Progressive changes in T_1, T_2 and left–ventricular histo–architecture in the fixed and embedded rat heart. *NMR Biomed.* 24, 836–843. doi: 10.1002/nbm.1629

Hales, P. W., Schneider, J. E., Burton, R. A. B., Wright, B. J., Bollensdorff, C., and Kohl, P. (2012). Histo-anatomical structure of the living isolated rat heart in two contraction states assessed by diffusion tensor MRI. *Prog. Biophys. Mol. Biol.* 110, 319–330. doi: 10.1016/j.pbiomolbio.2012.07.014

Healy, L. J., Jiang, Y., and Hsu, E. W. (2011). Quantitative comparison of myocardial fiber structure between mice, rabbit, and sheep using diffusion tensor cardiovascular magnetic resonance. *J. Cardiovasc. Magn. Reson.* 13:74. doi: 10.1186/1532-429X-13-74

Henkelman, R. M. (1985). Measurement of signal intensities in the presence of noise in MR images. *Med. Phys.* 12, 232–233. doi: 10.1118/1.595711

Hernandez, A. M., Huber, J. S., Murphy, S. T., Janabi, M., Zeng, G. L., Brennan, K. M., et al. (2013). Longitudinal evaluation of left ventricular substrate metabolism, perfusion, and dysfunction in the spontaneously hypertensive rat model of hypertrophy using microPET/CT imaging. *J. Nucl. Med.* 54, 1938–1945. doi: 10.2967/jnumed.113.120105

Hsu, E. W., Healy, L. J., Einstein, D. R., and Kuprat, A. P. (2010). "Imaging-based assessment and modeling of the structures of the myocardium," in *Computational Cardiovascular Mechanics*, eds J. M. Guccione, G. S. Kassab, and M. B. Ratcliffe (Boston, MA: Springer), 23–39.

Hsu, E. W., Muzikant, A. L., Matulevicius, S. A., Penland, R. C., and Henriquez, C. S. (1998). Magnetic resonance myocardial fiber-orientation mapping with direct histological correlation. *Am. J. Physiol. Heart Circul. Physiol.* 274, H1627–H1634. doi: 10.1152/ajpheart.1998.274.5.H1627

Jamieson, M. J., Gonzales, G. M., Jackson, T. I., Koerth, S. M., Romano, W. F., Tan, D.-X., et al. (1997). Evaluation of the IITC tail cuff blood pressure recorder in the rat against intraarterial pressure according to criteria for human devices. *Am. J. Hyperten.* 10, 209–216. doi: 10.1016/S0895-7061(96)00321-4

Kawamura, K., Kashii, C., and Imamura, K. (1976). Ultrastructural changes in hypertrophied myocardium of spontaneously hypertensive rats. *Japanese Circulat. J.* 40, 1119–1145. doi: 10.1253/jcj.40.1119

LeGrice, I. J., Pope, A. J., Sands, G. B., Whalley, G., Doughty, R. N., and Smaill, B. H. (2012). Progression of myocardial remodeling and mechanical dysfunction in the spontaneously hypertensive rat. *Amer. J. Physiol. Heart Circul. Physiol.* 303, H1353–H1365. doi: 10.1152/ajpheart.00748.2011

Lerman, L. O., Chade, A. R., Sica, V., and Napoli, C. (2005). Animal models of hypertension: an overview. *J. Laborat. Clin. Med.* 146, 160–173. doi: 10.1016/j.lab.2005.05.005

Li, W., Lu, M., Banerjee, S., Zhong, J., Ye, A., Molter, J., et al. (2009). *Ex vivo* diffusion tensor MRI reflects microscopic structural remodeling associated with aging and disease progression in normal and cardiomyopathic Syrian hamsters. *NMR Biomed.* 22, 819–825. doi: 10.1002/nbm.1394

Maranon, R., and Reckelhoff, J. F. (2013). Sex and gender differences in control of blood pressure. *Clin. Sci.* 125, 311–318. doi: 10.1042/CS20130140

Markhasin, V. S., Solovyova, O., Katsnelson, L. B., Protsenko, Y., Kohl, P., and Noble, D. (2003). Mechano-electric interactions in heterogeneous myocardium: development of fundamental experimental and theoretical models. *Prog. Biophys. Mol. Biol.* 82, 207–220. doi: 10.1016/S0079-6107(03)00017-8

McCrossan, Z. A., Billeter, R., and White, E. (2004). Transmural changes in size, contractile and electrical properties of SHR left ventricular myocytes during compensated hypertrophy. *Cardiovasc. Res.* 63, 283–292. doi: 10.1016/j.cardiores.2004.04.013

Muzikant, A. L., and Henriquez, C. S. (1998). Bipolar stimulation of a three-dimensional bidomain incorporating rotational anisotropy. *IEEE Trans. Biomed. Eng.* 45, 449–462. doi: 10.1109/10.664201

Nielles-Vallespin, S., Khalique, Z., Ferreira, P. F., de Silva, R., Scott, A. D., Kilner, P., et al. (2017). Assessment of myocardial microstructural dynamics by *in vivo* diffusion tensor cardiac magnetic resonance. *J. Am. Coll. Cardiol.* 69, 661–676. doi: 10.1016/j.jacc.2016.11.051

Ohta, H., Ohki, T., Kanaoka, Y., Koizumi, M., and Okano, H. J. (2017). Pitfalls of invasive blood pressure monitoring using the caudal ventral artery in rats. *Sci. Rep.* 7:41907. doi: 10.1038/srep41907

Okabe, M., Kawamura, K., Terasaki, F., and Hayashi, T. (1999). Remodeling of cardiomyocytes and their branches in juvenile, adult, and senescent spontaneously hypertensive rats and Wistar Kyoto rats: comparative morphometric analyses by scanning electron microscopy. *Heart Vessels* 14, 15–28. doi: 10.1007/BF02481739

Okamoto, K., and Aoki, K. (1963). Development of a strain of spontaneously hypertensive rats. *Japanese Circulat. J.* 27, 282–293. doi: 10.1253/jcj.27.282

Omann, C., Agger, P., Bogh, N., Laustsen, C., Ringgaard, S., Stephenson, R. S., et al. (2019). Resolving the natural myocardial remodelling brought upon by cardiac contraction; a porcine *ex-vivo* cardiovascular magnetic resonance study of the left and right ventricle. *J. Cardiovasc. Magn. Reson.* 21:35. doi: 10.1186/s12968-019-0547-2

Papadakis, N. G., Xing, D., Huang, C. L.-H., Hall, L. D., and Carpenter, T. A. (1999). A comparative study of acquisition schemes for diffusion tensor imaging using MRI. *J. Magn. Reson.* 137, 67–82. doi: 10.1006/jmre.1998.1673

Parasuraman, S., and Raveendran, R. (2012). Measurement of invasive blood pressure in rats. *J. Pharmacol. Pharmacotherapeut.* 3, 172–177. doi: 10.4103/0976-500X.95521

Pierpaoli, C., Righini, A., Linfante, I., Tao-Cheng, J. H., Alger, J. R., and Chiro, G. D. (1993). Histopathologic correlates of abnormal water diffusion in cerebral ischemia: diffusion-weighted MR imaging and light and electron microscopic study. *Radiology* 189, 439–448. doi: 10.1148/radiology.189.2.8210373

Pope, A. (2011). *Characterising myocardial remodelling in hypertensive heart disease. Structural and functional changes in the spontaneously hypertensive rat*. (Ph.D. thesis). University of Auckland, Department of Physiology, Auckland, New Zealand.

Reese, T. G., Weisskoff, R. M., Smith, R. N., Rosen, B. R., Dinsmore, R. E., and Wedeen, V. J. (1995). Imaging myocardial fiber architecture *in vivo* with magnetic resonance. *Magn. Reson. Med.* 34(6):786–791. doi: 10.1002/mrm.1910340603

Scollan, D. F., Holmes, A., Winslow, R., and Forder, J. (1998). Histological validation of myocardial microstructure obtained from diffusion tensor magnetic resonance imaging. *Amer. J. Physiol. Heart Circulat. Physiol.* 275, H2308–H2318. doi: 10.1152/ajpheart.1998.275.6.H2308

Sermesant, M., Chabiniok, R., Chinchapatnam, P., Mansi, T., Billet, F., Moireau, P., et al. (2012). Patient-specific electromechanical models of the heart for the prediction of pacing acute effects in CRT: a preliminary clinical validation. *Med. Image Anal.* 16, 201–215. doi: 10.1016/j.media.2011.07.003

Teh, I., McClymont, D., Burton, R. A. B., Maguire, M. L., Whittington, H. J., Lygate, C. A., et al. (2016). Resolving fine cardiac structures in rats with high-resolution diffusion tensor imaging. *Sci. Rep.* 6:30573. doi: 10.1038/srep30573

Teh, I., McClymont, D., Zdora, M.-C., Whittington, H. J., Davidoiu, V., Lee, J., et al. (2017). Validation of diffusion tensor MRI measurements of cardiac microstructure with structure tensor synchrotron radiation imaging. *J. Cardiovasc. Magn. Reson.* 19:31. doi: 10.1186/s12968-017-0342-x

Tran, N., Giannakidis, A., Gullberg, G. T., and Seo, Y. (2016). Quantitative analysis of hypertrophic myocardium using diffusion tensor magnetic resonance imaging. *J. Med. Imaging* 3:046001. doi: 10.1117/1.JMI.3.4.046001

Tseng, W.-Y. I., Dou, J., Reese, T. G., and Wedeen, V. J. (2006). Imaging myocardial fiber disarray and intramural strain hypokinesis in hypertrophic cardiomyopathy with MRI. *J. Magn. Reson. Imaging* 23, 1–8. doi: 10.1002/jmri.20473

Tuch, D. S. (2004). Q-ball imaging. *Magn. Reson. Med.* 52, 1358–1372. doi: 10.1002/mrm.20279

Vadakkumpadan, F., Arevalo, H., Prassl, A. J., Chen, J., Kickinger, F., Kohl, P., et al. (2010). Image-based models of cardiac structure in health and disease. *Wiley Interdiscip. Rev. Syst. Biol. Med.* 2, 489–506. doi: 10.1002/wsbm.76

Wang, V. Y., Niestrawska, J. A., Wilson, A. J., Sands, G. B., Young, A. A., LeGrice, I. J., et al. (2016). Image-driven constitutive modeling of myocardial fibrosis. *Int. J. Comput. Methods Eng. Sci. Mech.* 17, 211–221. doi: 10.1080/15502287.2015.1082675

Wang, V. Y., Wilson, A. J., Sands, G. B., Young, A. A., LeGrice, I. J., and Nash, M. P. (2015). "Microstructural remodelling and mechanics of hypertensive heart disease," in *International Conference on Functional Imaging and Modeling of the Heart*, eds H. van Assen, P. Bovendeerd, and T. Delhaas (Maastricht: Springer), 382–389.

Weber, K. T., Clark, W. A., Janicki, J. S., and Shroff, S. G. (1987). Physiologic versus pathologic hypertrophy and the pressure-overloaded myocardium. *J. Cardiovasc. Pharmacol.* 10, S37–S50. doi: 10.1097/00005344-198700106-00006

Winslow, R. L., Scollan, D. F., Holmes, A., Yung, C. K., Zhang, J., and Jafri, M. S. (2000). Electrophysiological modeling of cardiac ventricular function: from cell to organ. *Annu. Rev. Biomed. Eng.* 2, 119–155. doi: 10.1146/annurev.bioeng.2.1.119

Wu, M.-T., Tseng, W.-Y. I., Su, M.-Y. M., Liu, C.-P., Chiou, K.-R., Wedeen, V. J., et al. (2006). Diffusion tensor magnetic resonance imaging mapping the fiber architecture remodeling in human myocardium after infarction: correlation with viability and wall motion. *Circulation* 114, 1036–1045. doi: 10.1161/CIRCULATIONAHA.105.545863

Yazaki, Y., Tsuchimochi, H., Kurabayashi, M., and Komuro, I. (1989). Molecular adaptation to pressure overload in human and rat hearts. *J. Mol. Cell. Cardiol.* 21, 91–101. doi: 10.1016/0022-2828(89)90775-X

Conflict of Interest: The authors declare that the research was conducted in the absence of any commercial or financial relationships that could be construed as a potential conflict of interest.

frontiers in Physiology

ORIGINAL RESEARCH
published: 16 April 2020
doi: 10.3389/fphys.2020.00323

Hemodynamic Mechanism of Coronary Artery Aneurysm High Occurrence on Right Coronary Artery

Dandan Wu[1], Sirui Wang[1], Jinsheng Xie[2], Boyan Mao[1], Bao Li[1], Chunbo Jin[1], Yue Feng[1], Gaoyang Li[1] and Youjun Liu[1]*

[1] College of Life Science and Bioengineering, Beijing University of Technology, Beijing, China, [2] Beijing Anzhen Hospital, Capital Medical University, Beijing, China

The abnormal diameter of the coronary artery is twice or more than the normal diameter, which is a coronary artery aneurysm (CAA). According to the clinical statistics, CAA shows high occurrence on right coronary artery (RCA). The most common cause of CAA in adults is atherosclerosis, which destroys the elastic fibers in the middle layer of the blood vessel. Under the intravascular pressure, the weak wall bulges outward and form CAA. This article aims to explain the hemodynamic mechanism of coronary artery aneurysm shows high occurrence on RCA. Occurrence of CAA was simulated by the volume growth of coronary artery. Firstly, a 0–3D multi-scale model of normal coronary artery was constructed to obtain the hemodynamic environments of coronary artery. Then, fluid-structure interaction of normal and atherosclerotic blood vessel was performed to obtain volume growth rate of the coronary artery. Atherosclerosis was simulated by modifying Young's modulus in middle layer of the blood vessel. Finally, creep simulation was performed to compare the deformation of the blood vessels under the accumulation of time. Under normal condition, the volume growth rate of the RCA is 2.28 times and 1.55 times of the LAD and the LCX. After atherosclerosis, the volume growth rate of the RCA was 2.69 times and 2.12 times of the LAD and the LCX. And the volume growth rate of the RCA was 3.85 times and 3.45 times of the LAD and the LCX after further deepening of atherosclerosis. The expansion time above the average volume growth rate of the RCA, the LAD and the LCX respectively were 0.194, 0.168 and 0.179 s. The RCA is 2.06 times the original, the LAD and LCX are 1.53 times and 1.56 times after 10 years in creep simulation. It can be concluded that the RCA is more prone to aneurysms originated from the larger expansion of the RCA under normal physiological condition, and the larger expansion is magnified under atherosclerosis condition with destroyed vessel elasticity, and further magnified during the time accumulated viscoelastic creep to develop to aneurysm eventually.

Keywords: coronary artery aneurysm, high occurrence on right coronary artery, geometric multi-scale model, fluid-structure interaction, creep simulation

Edited by:
Yunlong Huo,
Shanghai Jiao Tong University, China

Reviewed by:
Shengzhang Wang,
Fudan University, China
Guangyu Zhu,
Xi'an Jiaotong University, China

****Correspondence:***
Youjun Liu
lyjlma@bjut.edu.cn

Specialty section:
This article was submitted to Computational Physiology and Medicine, a section of the journal Frontiers in Physiology

Received: *22 September 2019*
Accepted: *20 March 2020*
Published: *16 April 2020*

Citation:
Wu D, Wang S, Xie J, Mao B, Li B, Jin C, Feng Y, Li G and Liu Y (2020) Hemodynamic Mechanism of Coronary Artery Aneurysm High Occurrence on Right Coronary Artery. Front. Physiol. 11:323. doi: 10.3389/fphys.2020.00323

INTRODUCTION

The abnormal diameter of the coronary artery is twice or more than the normal diameter, which is a coronary aneurysm (Syed, 1997; Pahlavan and Niroomand, 2006; Jariwala et al., 2018) (Coronary Artery Aneurysm, CAA).

The most common cause of CAA in adults is atherosclerosis, which destroys the elastic fibers in the middle layer of the blood vessel. Under the intravascular pressure, weak wall bulges outward and forms CAA (Anabtawi and De Leon, 1974; Demopoulos et al., 1997; Baman et al., 2004). Pan et al. (2014) detected 697 coronary artery ectasia (CAE) patients. There were totally 878 dilated coronary arteries, and the main branch of right coronary artery (RCA) was mostly involved (41.80%), followed by the main branch of left anterior descending artery (LAD) (25.40%), the main branch of left circumflex artery (LCX) (21.64%), and the left main coronary artery (LM) (4.78%). It can be seen that the coronary aneurysm presents high occurrence on RCA. But due to the rareness of coronary aneurysm, there are only a few reports of clinical cases and their treatment (Swaye et al., 1983; Dahhan, 2015). The hemodynamic mechanism of CAA is not sufficient. So why does coronary aneurysm present high occurrence on right coronary artery?

The formation of CAA is a complex physiological process. The occurrence of CAA in adults is mainly due to atherosclerosis involving the middle layer of blood vessels. Therefore, three-layer blood vessels were established and the young's modulus of the middle blood vessels were modified to simulate atherosclerosis. Two aspects of simulation were performed to explain that the RCA prone to form CAA. Firstly, the deformation of vessel wall can be directly reflected by Fluid-structure Interaction numerical simulation. By comparing the volume growth rate of the RCA, the LAD and the LCX in normal condition and atherosclerosis, whether RCA prone to expand could be judged. Secondly, the formation of coronary artery aneurysm is cumulative. Creep numerical simulation was performed to predict whether RCA is prone to form CAA.

MATERIALS AND METHODS

Firstly, a 0–3D geometric multi-scale model of normal coronary artery was constructed to obtain the hemodynamic environments of the RCA, LAD, and LCX. Then, fluid-structure interaction was performed under the normal condition and the atherosclerosis. Atherosclerosis was simulated by modifying Young's modulus in middle layer of the blood vessel. Finally, creep simulation was performed to simulate the formation of CAA.

Multi-Scale Numerical Simulation

In this study, a geometric multi-scale method (Zhao et al., 2014) is used to couple the 0D lumped parameter model with the three-dimensional coronary artery model for fluid dynamics simulation., The CT image of the coronary artery were imported to Mimics software and the 3D model reconstruction was performed by using the threshold segmentation method and manual segmentation method, respectively. Coronary artery models were eventually reconstructed in FREEFORM software based on the research objectives combined with previous actual case reports. The 0D lumped parameter model refers to the findings of Taylor et al. (2013) and has been used many times in our previous studies, and its accuracy has been confirmed (Stergiopulos et al., 1996; Zhao et al., 2016). The lumped parameter model in this study can be divided into three modules: heart module, aorta module and coronary artery module. See the right side of **Figure 1**. The parameter values of each component were based on the research of Kim et al. on coronary artery modeling (Kim et al., 2010), and the values were adjusted by genetic algorithm (Li et al., 2018). The systolic and diastolic pressure, and cardiac output of the model were adjusted to match the physiological reality of the patient, and made the flow of each branch of coronary artery conform to the principles proposed by Kim: The total coronary arterial flow accounts for 4% of the patient's cardiac output. And then, the flow of each branch of the coronary artery is was then proportional to the cubic of the diameter of the branch (Kim et al., 2010). Values of 0D lumped parameters are show in **Table 1**.

As shown in **Figure 1**, the 3D model is coupled with the entrance and exit of the 0D model to form a geometric multi-scale model. The 3D model was meshed by the CFX module in ANSYS, and the meshing method was a hexahedral mesh. At the same time, it is assumed in the simulation that the blood vessel is a rigid wall that is impermeable, and the blood is an incompressible Newtonian fluid. The dynamic viscosity of blood is 0.0035 Pa·s and the density of blood is 1060 kg/m^3, which is an unsteady laminar flow and calculated according to the existing method (Zhao et al., 2014). The hemodynamic parameters of the coronary arteries are finally obtained. These hemodynamic parameters, such as flow and pressure, were applied to the fluid-structure interaction numerical simulation as boundary conditions.

Two-Way Fluid-Structure Interaction

CAA occurs mostly in trunk of coronary artery and less frequently in branches. In the objective-specific 3D coronary model, the models for the RCA, LAD, and LCX were built, as shown in **Figure 1**. Since LM is relatively short and the incidence of CAA is extremely low, the model of LM was not built.

The fluid-structure interaction model is divided into a blood vessel model and a fluid model. First, the blood vessels shown in **Figure 2** were thickened by GEOMAGIC software to obtain a three-layer blood vessel model consisting of the inner layer, the middle layer and the outer layer. In clinical statistics, there was no significantly difference in the wall thickness of RCA, LAD, and LCX. The total thicknesses of the three-layer vessel models were 0.95 mm. The thickness of the inner layer and the outer layer is 0.3 mm and the thickness of the middle layer is 0.35 mm (Li and Guo, 2017). Boolean operations are then performed on the blood vessel models in SOLIDWORKS software to tailor the fluid models. After the model is established, the two-way fluid-structure interaction was performed in ANSYS WORKBENCH software. The coupling module consisted of Transient Structural module and Fluid Flow module. Material setup, meshing, and analysis setup are performed in the Transient Structural module for the blood vessel model. The structure of the three-layer

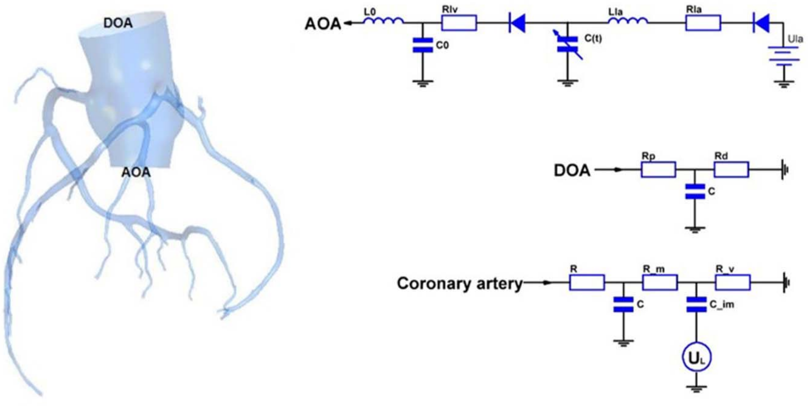

FIGURE 1 | Geometric multi-scale model of normal coronary arteries.

TABLE 1 | 0D part parameter value.

Heart module	**Branch**	R_{la}	R_{lv}	L_{la}	L_1	C_1
		0.00375	0.0075	0.000285	0.0037	0.95
Aorta module	**Branch**	R_p	R_d	C_{doa}	C_{doa_a}	
		0.10285	0.9196	2.2653	0.0005	
Coronary artery module	**Branch**	R	R_m	R_v	C	C_{im}
	a	78.6	127.52	44.51	0.00124	0.01269
	b	95.6	155.52	44.51	0.00124	0.01269
	c	83.52	136.28	42.01	0.00124	0.01269
	d	110.6	180.52	44.51	0.00124	0.01269
	e	95.6	155.52	44.51	0.00137	0.00909
	f	95.6	155.52	44.51	0.00137	0.00909
	g	79.26	129.51	65	0.00124	0.01269
	h	100.26	163.51	65	0.00124	0.01269
	i	79.26	129.51	40	0.00124	0.01269
	j	79.26	129.51	40	0.00137	0.00909
	k	79	129	60	0.00124	0.01269
	l	131.25	135.51	60	0.00137	0.00909
	m	131.25	135.51	70	0.00137	0.00909
	n	130	212	88.75	0.00124	0.01269
	o	130	212	60	0.00137	0.00909
	p	150	244	60.15	0.0001	0.0354
	q	175.5	283	60	0.0001	0.0354
	r	155.5	244	40	0.0001	0.0354

The unit of resistance R is mmHg·s/mL, and the unit of blood flow inertia L is mmHg·s^2/mL, the unit of vascular compliance C is mL/mmHg.

blood vessel models exhibits different properties. The Young's modulus of the inner and outer layer was about 3 times lower than the middle layer. Therefore, we referenced (Gao et al., 2006; Watanabe and Matsuzawa, 2006) and Maier et al. (2010), who reported that the ratio of Young's modulus of the inner layer, the middle layer and the outer layer is 1/3/1, so the Young's modulus of the inner, middle and outer layer was set to Ei = 0.9 MPa, Em = 2.7 MPa, and Eo = 0.9 MP, respectively, and the Poisson's ratio was set to 0.45.

Mesh independency test was performed, for example, the RCA vessel model in **Figure 2**. The mesh sizes of the blood vessel were set to 0.3, 0.1, and 0.05 mm. Fluid-structure interactions were performed for three groups of models with different mesh sizes. The error rate of the calculation results of the three groups of models is within 5%. In order to reduce the calculation time and increase the calculation speed, the mesh size is chosen to be 0.3 mm. The mesh number of the RCA, LAD, and LCX are 167521, 84839, and 324997.

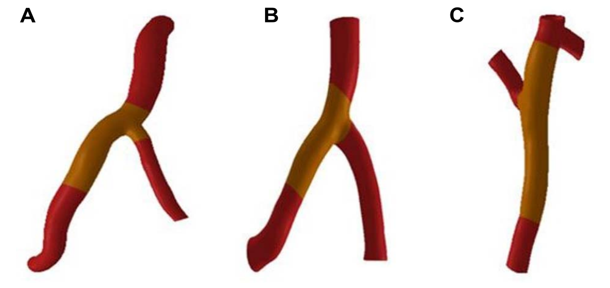

FIGURE 2 | Blood vessel models. **(A)** RCA **(B)** LAD **(C)** LCX.

Binding constraints were imposed between the layers of blood vessels. A cylindrical coordinate system was established at the entrance and exit of the blood vessels to restrain the circumferential and axial displacement of the blood vessels, so that the blood vessels could freely expand radially. The fluid setting was then made in the Fluid Flow module. The fluid density is 1060 kg/m^3 and the dynamic viscosity is 0.0035 Pa·s. The fluid boundary conditions were taken from the previous 0–3D multi-scale numerical calculations. The calculation type is transient, taking the normal cardiac cycle $T = 0.8$ s.

The flow boundary of the fluid inlet and the pressure boundary of the fluid outlet were given. The boundary settings are shown in **Figure 3**.

The deformation of the RCA, the LAD and the LCX under normal Young's modulus is obtained from fluid-structure interaction. Through fluid-structure interaction simulation under normal condition, it was found that the maximum deformation of the RCA, LAD, and LCX was at the bifurcation position. The length of atherosclerosis site is 20 mm. The orange marker area in **Figure 2** is the coronary atherosclerosis site.

Due to atherosclerosis involves the middle layer of the blood vessels, the elastic fibers in the middle wall of the blood vessels are destroyed. Atherosclerosis is simulated by modifying Young's modulus in middle layer of the blood vessel. When the middle layer of the blood vessels is damaged, the ability of the blood vessels to resist deformation is weakened, which can be modified by reducing the Young's modulus. The specific Young's modulus of the atherosclerotic site is not available and is related to the degree of coronary expansion. It is assumed that the Young's modulus is 1/10 and 1/100 which are 0.27 and 0.027 MPa, respectively. Non-atherosclerosis sites are consistent with the normal blood vessels. The fluid-structure interaction was performed in the same manner on different models of atherosclerosis. The volume growth rate of the RCA, the LAD and the LCX under normal condition and atherosclerotic condition were compared.

Creep Simulation

When the ability of the blood vessels to resist deformation is weakened, creep will occur with time, due to the viscoelasticity of blood vessels. A creep simulation was adopted to analyze this process. The relaxation and creep functions of the power law form have been well fitted to the experimental results of certain materials and have been widely adopted by researchers of high molecular materials. Since the temperature and stress are constant, creep rate is only related to time. The Time Hardening theory from engineering data of ANSYS WORKBENH was chosen, which is related to

$$\varepsilon_{cr} = C_1 \sigma^{C_2} t^{C_3} e^{-C_4/T} \tag{1}$$

Where ε_{cr} is creep rate, C_1–C_4 are constants, σ is stress, and T is temperature. Li et al. (2013) performed the uniaxial creep experimental data of human cerebral arteries under 18700 and 22500 Pa. The time-strain curve at the average arterial pressure under 12500 Pa is obtained by linear interpolation of the creep experimental data under 18700 and 22500 Pa, shown in **Figure 4**. The C$_1$–C$_4$ were obtained by fitting the strain-stress curve under 12500 Pa. Fitting results are $C_1 = 2.35e^{-6}$, $C_2 = 0.6808$,

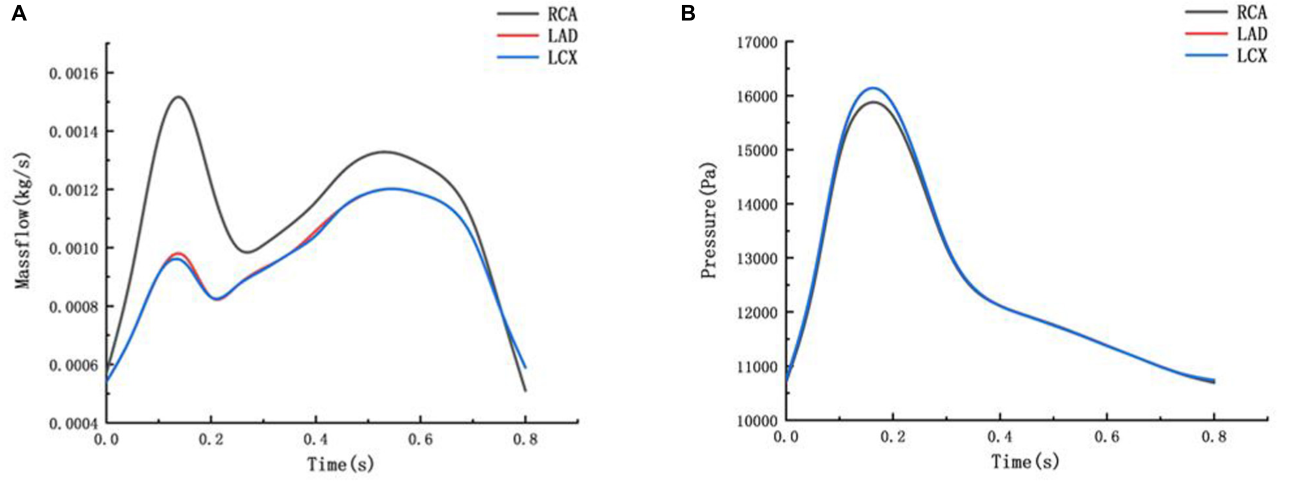

FIGURE 3 | Mass flow and Pressure boundary **(A)** mass flow boundary of inlet **(B)** pressure boundary of outlet.

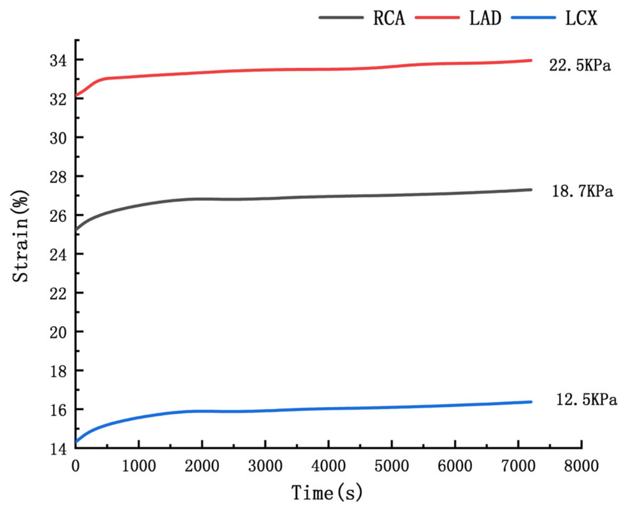

FIGURE 4 | Arterial strain-time curve.

$C_3 = 0.3273$, $C_4 = 0$. The RCA, the LAD and the LCX models are identical to the previous blood vessel model of the two-way fluid-structure interaction. The periodic load shown in **Figure 3** was applied to the RCA, the LAD, and the LCX models, and the creep simulation was calculated to be 150,000 s.

RESULTS

Two-Way Fluid-Structure Interaction

The expansion results of the middle layer of the vessel wall under different atherosclerosis degree were calculated. The maximum deformation moment of RCA, LAD, and LCX models is 0.15. The deformation contours were derived at this time, as shown in **Figures 5–7**.

From the deformation contour at the maximum time 0.15 s, it could be seen that the deformation of the RCA, the LAD and the LCX is increased after the degree of atherosclerosis is increased. The deformation of the atherosclerotic site in RCA is much larger than that in LAD and LCX. The volume growth rate curves of the atherosclerotic site in the RCA, the LAD, and the LCX could be plotted in the cardiac cycle. Volume growth rate is the ratio of increased volume to original volume after expansion, as shown in **Figure 8**. In a cardiac cycle, the volume growth rate of the atherosclerotic site in the RCA was larger than the LAD and LCX.

The average volume growth rates of blood vessels within a cardiac cycle were compared, as shown in. **Figure 9**. Under normal conditions, the average volume growth rates of the atherosclerotic site in the RCA, the LAD, and the LCX respectively were: 4.56, 2, and 2.93% in a cardiac cycle. When the middle layer of the blood vessels was damaged and the Young's modulus was reduced to 0.27 MPa, the average volume growth rate of atherosclerotic site in the RCA, the LAD, and the LCX were 10.4, 3.86, and 4.90% respectively in a cardiac cycle. When the middle layer of the blood vessels was damaged and the Young's modulus was reduced to 0.027 MPa, the average volume growth rate of atherosclerotic site in the RCA, the LAD, and the LCX respectively were 18.4, 4.78, and 5.32% in a cardiac cycle. Under normal condition, the volume growth rate of the RCA is 2.28 times and 1.55 times of the LAD and the LCX. After atherosclerosis, the volume growth rate of the RCA was 2.69 times and 2.12 times of the LAD and the LCX. And the volume growth rate of the RCA was 3.85 times and 3.45 times of the LAD and the LCX after further deepening of atherosclerosis. It can be seen from the volume growth curve in a cardiac cycle that vasodilation is more obvious in systole. The volume growth curves in systole (0—0.3 s) of the RCA, the LAD, and the LCX could be plotted. The average volume growth rates of the RCA, the LAD, and the LCX in systole respectively were 5.26, 2.28, and 3.46%. These were shown in **Figure 10**. The auxiliary lines from the intersection of average line of the RCA and volume growth curve of the RCA to X axis were plotted. It can be seen that the time when volume growth rate of the RCA is higher than the average was longer than the LAD and

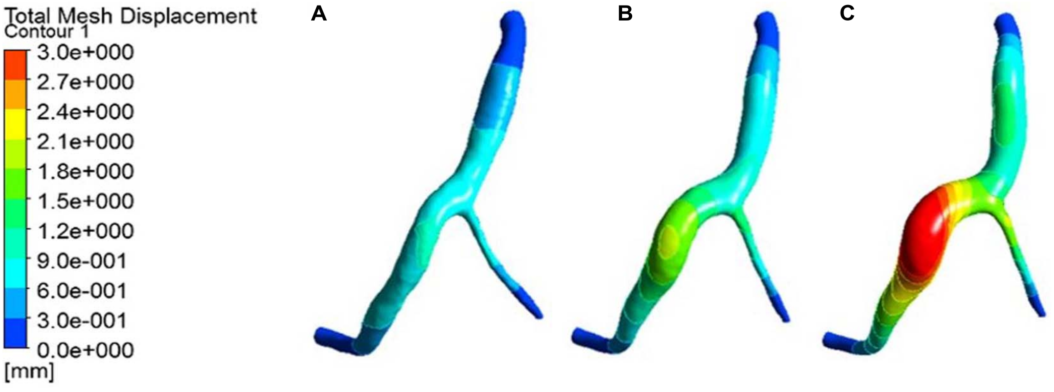

FIGURE 5 | Deformation contour of the RCA in maximum time. **(A)** normal condition; **(B)** the Young's modulus of the atherosclerotic site is 0.27MPa; **(C)** the Young's modulus of the atherosclerotic site is 0.027 MPa.

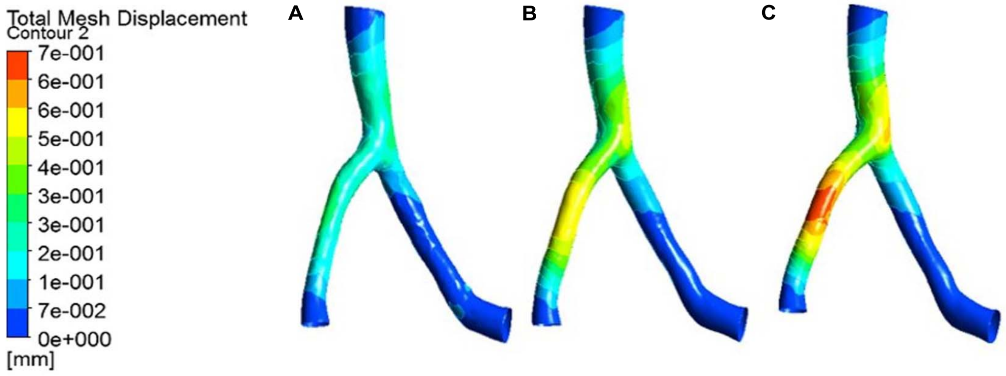

FIGURE 6 | Deformation contour of the LAD in maximum time. **(A)** normal condition; **(B)** the Young's modulus of the atherosclerotic site is 0.27MPa; **(C)** the Young's modulus of the atherosclerotic site is 0.027 MPa.

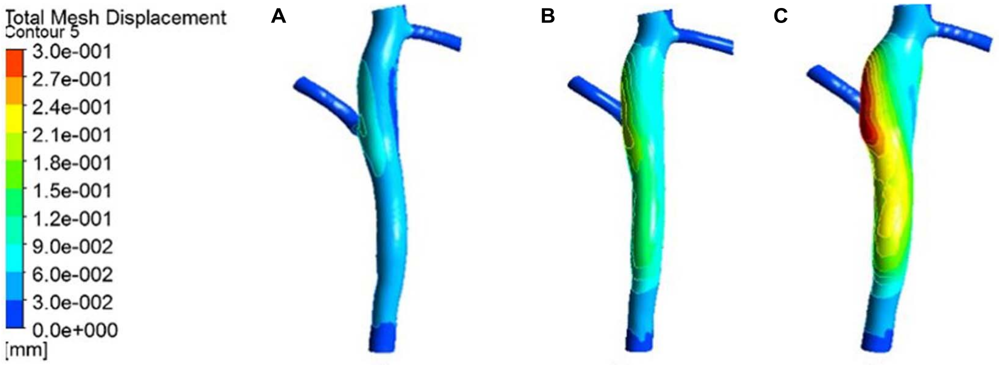

FIGURE 7 | Deformation contour of the LCX in maximum time. **(A)** normal condition; **(B)** the Young's modulus of the atherosclerotic site is 0.27MPa; **(C)** the Young's modulus of the atherosclerotic site is 0.027 MPa.

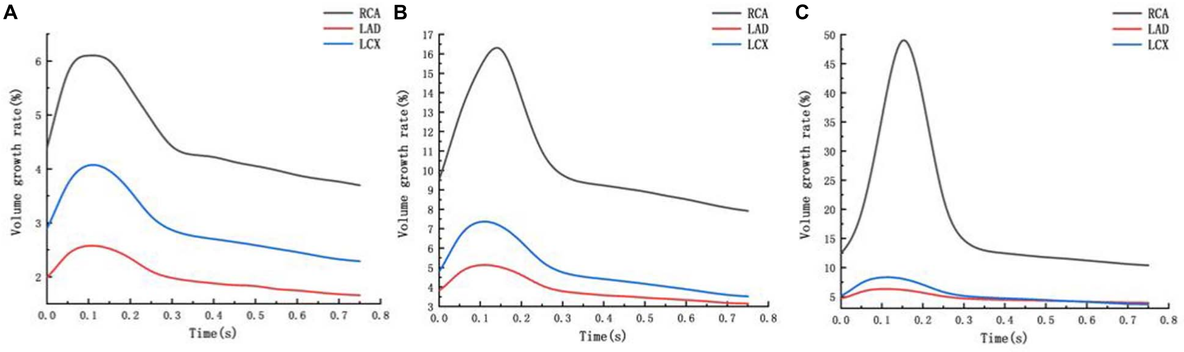

FIGURE 8 | Volume growth rate curve **(A)** normal condition **(B)** the Young's modulus of the atherosclerotic site is 0.27MPa **(C)** the Young's modulus of the atherosclerotic site is 0.027 MPa.

the LCX, which respectively were 0.027—0.221 s, 0.052—0.22 s, and 0.033—0.212 s.

Creep Simulation

The deformation curves of the RCA, LAD, and LCX were obtained by creep simulation. As shown in **Figure 11**, it could be seen that the deformation of the RCA was larger than the LAD and the LCX.

Deformation functions of the RCA, LAD, and LCX were obtained by fitting the curve in **Figure 11**.

$$D_{RCA} = 4.67e^{-4}t^{0.01841}$$

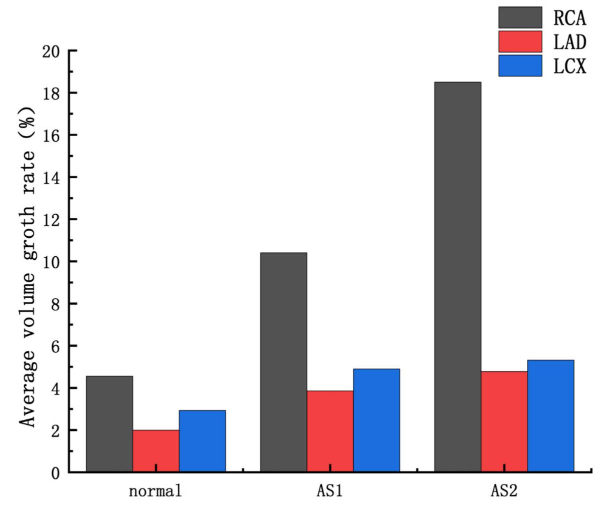

FIGURE 9 | Average volume growth rate: AS1: the Young's modulus of the atherosclerotic site is 0.27MPa; AS2: the Young's modulus of the atherosclerotic site is 0.027 MPa.

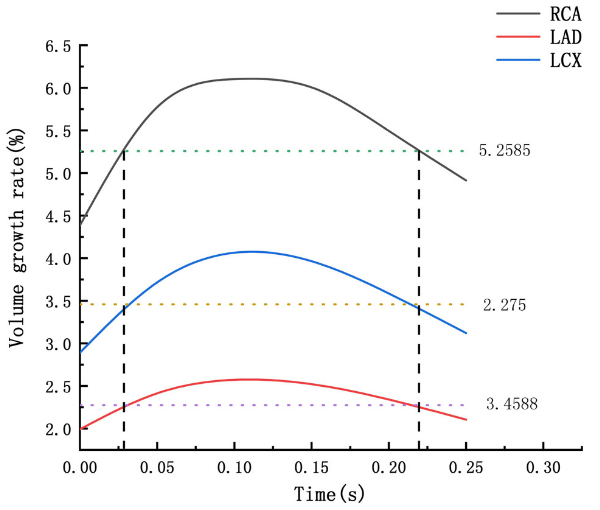

FIGURE 10 | Volume growth rate in systole.

$$D_{LAD} = 2.52e^{-4}t^{0.01561}$$

$$D_{LCX} = 2.63e^{-4}t^{0.01728}$$

Through the function we can predict that after 10 years, the RCA is 2.06 times the original, the LAD and LCX are 1.53 times and 1.56 times. It indicated that the RCA is more likely to form CAA than the LAD and LCX.

DISCUSSION

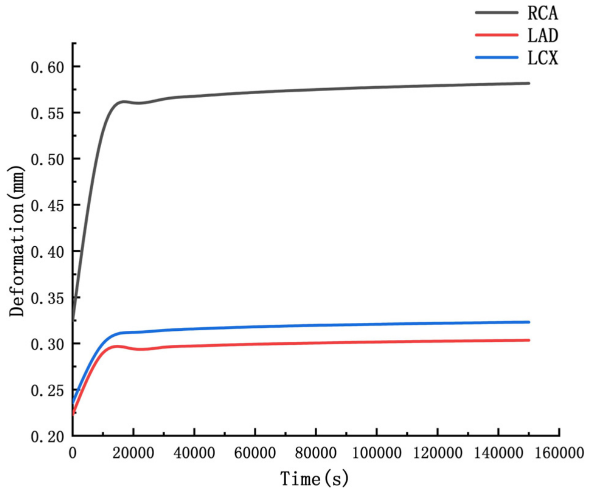

FIGURE 11 | Curve of deformation.

At present, the study of coronary aneurysms is more common in a few clinical reports, and its hemodynamic mechanism research is still insufficient. From clinical statistics, coronary aneurysms can be found to be highly focal and easily occur in the RCA. The formation of CAA is a complex physiological process. The Fluid-structure Interaction numerical simulations were performed to compare the expansion ability of the RCA, the LAD and LCX. The Creep simulations were performed to predict the formation of CAA. These simulations attempt to explain the hemodynamic mechanism of coronary artery aneurysm easily occurring on RCA The average volume growth rate of the RCA under normal condition and atherosclerosis both larger than the LAD and the LCX, shown in **Figure 9**. In the Fluid-structure Interaction numerical simulations, there is almost no difference between the material of the blood vessels and the pressure in the vessels. It can be considered that the structural difference makes the RCA prone to expand. Coronary diameter statistics were performed on 167 subjects. The average diameter of the RCA, the LAD and the LCX respectively are 2.95 ± 060, 2.14 ± 0.43, and 2.26 ± 0.41 mm. It can be seen that the average diameter of the RCA is greater than the LAD and the LCX. The larger average diameter of the RCA leads it prone to expand. From **Figure 9**, it can be seen that under normal condition, the volume growth rate of the RCA is 2.28 times and 1.55 times of the LAD and the LCX. After atherosclerosis, the volume growth rate of the RCA was 2.69 times and 2.12 times of the LAD and the LCX. And the volume growth rate of the RCA was 3.85 times and 3.45 times of the LAD and the LCX after further deepening of atherosclerosis. It indicates that the larger expansion is magnified under atherosclerosis condition with destroyed vessel elasticity. As well as, it can be seen that the time above average volume growth rate in systole of the RCA, LAD, and LCX respectively were 0.194, 0.168, and 0.179 s, shown in **Figure 10**. In Creep simulations, this accumulation of the time difference leads the RCA reaching to 2.06 times, while the LAD and the LCX respectively were 1.53 times and 1.56 times after 10 years. So it can be considered that the RCA is more prone to aneurysms originated from the larger expansion of the RCA under normal physiological condition, and the larger expansion is magnified under atherosclerosis condition with destroyed vessel elasticity, and further magnified during the time accumulated viscoelastic creep to develop to aneurysm eventually.

There are some limitations in our study. The formation of CAA is a complex physiological process. Many physiological factors have not been considered. Human blood vessels are anisotropic, and stress-strain are not a simple linear relationship. The linear elastic material given in the article is indeed not as suitable as the superelastic material in reflecting the deformation of blood vessels. Due to the limitation of calculation cost, the simulation time of the creep process is 150,000 s. We can only give the trend of coronary artery dilation, but cannot really simulate the formation of CAA. The differences in the location and structure of atherosclerosis were not considered in this study. With the expansion of the blood vessel, wall shear stress at the site of atherosclerosis decreases, which may lead to intimal hyperplasia, deepening of atherosclerosis, and affecting coronary dilation. However, the potential interaction between low wall shear stress and coronary dilation has not yet been clarified, and further work is needed. These problems will continue to be explored in future research.

CONCLUSION

In this article, numerical simulations show that RCA is more likely to expand to form CAA, which is consistent with clinical statistics. The RCA is more prone to aneurysms originated from the larger expansion of the RCA under normal physiological condition, and the larger expansion is magnified under atherosclerosis condition with destroyed vessel elasticity, and further magnified during the time accumulated viscoelastic creep to develop to aneurysm eventually.

DATA AVAILABILITY STATEMENT

The raw data supporting the conclusions of this article will be made available by the authors, without undue reservation, to any qualified researcher.

AUTHOR CONTRIBUTIONS

DW participated in all the work and wrote the manuscript. YL contributed conception and design of the study. SW organized the database. BM and BL performed the statistical analysis. CJ and YF collected relevant documents. GL provided guidance on research methods and language. All authors contributed to manuscript revision, read and approved the submitted version.

FUNDING

This research is supported by the National Natural Science Foundation of China (11772016, 11832003, and 11472022).

ACKNOWLEDGMENTS

Thanks for all the authors and partners for their contributions to this article.

REFERENCES

Anabtawi, I. N., and De Leon, J. A. (1974). Arteriosclerotic aneurysms of the coronary arteries. *J. Thor. Cardiovasc. Surg.* 68, 226–228.

Baman, T. S., Cole, J. H., Devireddy, C. M., and Sperling, L. S. (2004). Risk factors and outcomes in patients with coronary artery aneurysms. *Am. J. Cardiol.* 93, 1549–1551.

Dahhan, A. (2015). Coronary artery ectasia in atherosclerotic coronary artery disease, inflammatory disorders, and sickle cell disease. *Cardiovasc. Ther.* 33, 79–88. doi: 10.1111/1755-5922.12106

Demopoulos, V. P., Olympios, C. D., Fakiolas, C. N., Pissimissis, E. G., Economides, N. M., Adamopoulou, E., et al. (1997). The natural history of aneurysmal coronary artery disease. *Heart* 78, 136–141.

Gao, F., Guo, Z., Sakamoto, M., and Matsuzawa, T. (2006). Fluid-structure interaction within a layered aortic arch model. *J. Biol. Phys.* 32, 435–454. doi: 10.1007/s10867-006-9027-7

Jariwala, P., Padmakumar, E. A., and Krishnaprasad, A. R. (2018). Acutecoronary syndrome secondary to coronary artery aneurysms: case reports and review. *Ihj Cardiovasc. Case Rep.* 2, 85–90.

Kim, H. J., Vignon-Clementel, I. E., Coogan, J. S., Figueroa, C. A., Jansen, K. E., Taylor, C. A., et al. (2010). Patient-specific modeling of blood flow and pressure in human coronary arteries. *Ann. Biomed. Eng.* 38, 3195–3209. doi: 10.1007/s10439-010-0083-6

Li, B., Wang, W., Mao, B., and Liu, Y. (2018). A method to personalize the lumped parameter model of coronary artery. *Int. J. Compu. Methods* 2018:184 2004.

Li, D. Y., Xu, D. H., Li, P., Wei, J., Yang, K., and Zhao, C. H. (2013). Viscoelastic evaluation of fetal umbilical vein for reconstruction of middle cerebral artery. *Chin. Neuroregen. Res* 32, 3055–3062. doi: 10.3969/j.issn.1673-5374.2013.32.009

Li, N., and Guo, T. (2017). "A multi-layer finite element model based on anisotropic hyperelastic of coronary artery and it's application," in *Proceedings of the International Conference on Bioinformatics and Biomedical Engineering (iCBBE2011)*, Kyoto.

Maier, A., Gee, M. W., Reeps, C., Eckstein, H. H., and Wall, W. A. (2010). Impact of calcifications on patient-specific wall stress analysis of abdominal aortic aneurysms. *Biomech. Model. Mechanobiol.* 9, 511–521. doi: 10.1007/s10237-010-0191-0

Pahlavan, P. S., and Niroomand, F. (2006). Coronary artery aneurysm: a review. *Clin. Cardiol.* 29, 439–443.

Pan, Z. X., Wang, Y. T., Dou, K. F., You, S. J., and Song, W. H. (2014). Clinical characteristics of 669 hospitalized patient with Coronary expansion (CAE). *Chin. J. Mol. Cardiol.* 14, 1120–1123.

Stergiopulos, N., Meister, J. J., and Westerhof, N. (1996). Determinants of stroke volume and systolic and diastolic aortic pressure. *Am. J. Physiol. Heart Circul. Physiol.* 270, H2050–H2059.

Swaye, P. S., Fisher, L. D., Litwin, P., Vignola, P. A., Judkins, M. P., Kempet, H. G., et al. (1983). Aneurysmal coronary artery disease. *Circulation* 67:134.

Syed, M. M. (1997). Coronary artery aneurysm: a review. *Prog. Cardiovasc. Dis.* 40, 77–84.

Taylor, C. A., Fonte, T. A., and Min, J. K. (2013). Computational fluid dynamics applied to cardiac computed tomography for noninvasive quantification of fractional flow reserve: scientific basis. *J. Am. Coll. Cardiol.* 61, 2233–2241.

Watanabe, F. M., and Matsuzawa, T. (2006). Stress analysis in a layered aortic arch model under pulsatile blood flow. *Biomed. Eng. Online* 5:25.

Zhao, X., Liu, Y., Ding, J., Bai, F., Ren, X., Ma, L., et al. (2014). Numerical study of bidirectional glenn with unilateral pulmonary artery stenosis. *J. Mech. Med. Biol.* 14:1450056.

Zhao, X., Liu, Y., Li, L., Wang, W., Xie, J., and Zhao, Z. (2016). Hemodynamics of the string phenomenon in the internal thoracic artery grafted to the left anterior descending artery with moderate stenosis. *J. Biomech.* 49, 983–991.

Conflict of Interest: The authors declare that the research was conducted in the absence of any commercial or financial relationships that could be construed as a potential conflict of interest.

frontiers in Physiology

ORIGINAL RESEARCH
published: 30 April 2020
doi: 10.3389/fphys.2020.00324

Analysis of Cardiac Amyloidosis Progression Using Model-Based Markers

Wenguang Li[1], Alan Lazarus[1], Hao Gao[1], Ana Martinez-Naharro[2], Marianna Fontana[2], Philip Hawkins[2], Swethajit Biswas[3], Robert Janiczek[3], Jennifer Cox[3], Colin Berry[4], Dirk Husmeier[1] and Xiaoyu Luo[1]*

[1] School of Mathematics and Statistics, University of Glasgow, Glasgow, United Kingdom, [2] Centre for Amyloidosis and Acute Phase Proteins, University College London, London, United Kingdom, [3] GlaxoSmithKline plc, Stevenage, United Kingdom, [4] British Heart Foundation Glasgow Cardiovascular Research Centre, University of Glasgow, Glasgow, United Kingdom

Deposition of amyloid in the heart can lead to cardiac dilation and impair its pumping ability. This ultimately leads to heart failure with worsening symptoms of breathlessness and fatigue due to the progressive loss of elasticity of the myocardium. Biomarkers linked to the clinical deterioration can be crucial in developing effective treatments. However, to date the progression of cardiac amyloidosis is poorly characterized. There is an urgent need to identify key predictors for disease progression and cardiac tissue function. In this proof of concept study, we estimate a group of new markers based on mathematical models of the left ventricle derived from routine clinical magnetic resonance imaging and follow-up scans from the National Amyloidosis Center at the Royal Free in London. Using mechanical modeling and statistical classification, we show that it is possible to predict disease progression. Our predictions agree with clinical assessments in a double-blind test in six out of the seven sample cases studied. Importantly, we find that multiple factors need to be used in the classification, which includes mechanical, geometrical and shape features. No single marker can yield reliable prediction given the complexity of the growth and remodeling process of diseased hearts undergoing high-dimensional shape changes. Our approach is promising in terms of clinical translation but the results presented should be interpreted with caution due to the small sample size.

Keywords: cardiac amyloidosis, left ventricle, model-based markers, classification, strain and stress, shape analysis, MRI

Edited by:
Wenchang Tan,
Peking University, China

Reviewed by:
Vicky Y. Wang,
The University of Auckland,
New Zealand
Joakim Sundnes,
Simula Research Laboratory, Norway

***Correspondence:**
Xiaoyu Luo
Xiaoyu.luo@glasgow.ac.uk

Specialty section:
This article was submitted to
Computational Physiology and
Medicine,
a section of the journal
Frontiers in Physiology

Received: *19 October 2019*
Accepted: *20 March 2020*
Published: *30 April 2020*

Citation:
Li W, Lazarus A, Gao H, Martinez-Naharro A, Fontana M, Hawkins P, Biswas S, Janiczek R, Cox J, Berry C, Husmeier D and Luo X (2020) Analysis of Cardiac Amyloidosis Progression Using Model-Based Markers. Front. Physiol. 11:324.
doi: 10.3389/fphys.2020.00324

1. INTRODUCTION

Amyloidosis occurs when proteins that take abnormal forms known as amyloid deposits build up in the tissues. These deposits are composed of abnormal protein fibers that accumulate more quickly than they are cleared away, and thus interfere with the structure and function of affected organs throughout the body. These include the heart, liver, skin, lungs, kidneys, and nervous system (Gertz et al., 2013). When amyloid fibrils infiltrate in myocardium, the ventricles will show impaired contraction and relaxation. This is known as cardiac amyloidosis. The most prevalent forms of cardiac amyloidosis are known as Transthyretin-related (ATTR) and immunoglobulin light chain (AL) amyloidosis (formerly known as primary amyloidosis). Untreated cardiac amyloid, particularly the AL type, can be life-threatening, the median survival of patients is half a year from the onset of heart failure (Grogan et al., 2017).

The left ventricle (LV) with amyloid becomes firm, rubbery and stiff, similar to hypertrophic cardiomyopathy (Kholova and Niessen, 2005). Further, the ventricular wall is thickened (Carroll et al., 1982; Kholova and Niessen, 2005; Quarta et al., 2012; Martinez-NaharrO et al., 2018), particularly in the interventricular septum (Frenzel et al., 1986), but the ventricular cavity does not dilate much (Kholova and Niessen, 2005). Hence, the functional defect in amyloidosis is associated to the "stiff heart" syndrome, with the LV end-diastolic pressure rising to at least 10 mmHg higher than normal subjects (Chew et al., 1975; Swanton et al., 1977). As a result, the amyloidosis myocardium material properties also altered (Petre et al., 2005).

With effective treatments, it is hoped that amyloid deposits can gradually diminish in patients. However, although various anti-amyloid drugs are being researched, none has been introduced into routine clinical practice. A standing challenge in developing anti-amyloid drugs is the difficulty of reliably assessing the disease progression non-invasively and within in a short follow-up duration, because subtle changes inside tissues with reduced amyloid deposits are not always visible in clinical images, such as cardiac magnetic resonance (CMR) imaging.

Using Doppler echocardiography, Koyama et al. found that the early impairment in systolic function of a cardiac amyloidosis heart can be reflected by changed longitudinal strain and strain rate (Koyama et al., 2003). Both circumferential and longitudinal strains are found to be substantially lower in an amyloidosis LV, compared with a normal, or hypertrophic cardiomyopathy LV (Sun et al., 2009; Buss et al., 2012). CMR images are used to diagnose cardiac amyloid with late gadolinium enhancement (LGE) (Vogelsberg et al., 2008; Liu et al., 2013; Dungu et al., 2014) or delayed enhancement (White et al., 2014). Based on CMR basal and apical short-axis images, White et al. showed that the peak LV twist rate and untwist rates are significantly lower in patients with cardiac amyloid LV (White et al., 2014). Nucifora et al. (2014) measured the circumferential strain of 61 amyloidosis patients using tagging CMR and found the peak circumferential strain could be a potential clinical biomarker.

In previous studies, strain and material stiffness were found to be associated with cardiac amyloidosis. However, there is much to be done on understanding the disease progression of cardiac amyloid. Needless to say, finding a reliable classification based on suitable biomarkers is crucially important in assessing the effectiveness of amyloidosis treatments and any clinical trials for new drugs. Despite major research development of computational cardiac models, which can provide a rich set of biomarkers, it is perhaps surprising that very little modeling effort has focused on cardiac amyloidosis (Chapelle et al., 2015), and no studies considered the relation to amyloidosis disease progression.

The aim of this work is to carry out an image-derived mechanical and statistical modeling approach for LVs with amyloidosis progression. We systemically checked multiple factors, including the strains, stresses, p-V curve, LV shape, and volume of a group of amyloidosis patients before and after treatment. The biomechanical modeling analysis was blind to the clinical assessment, and the classification based on the multiple factors compares favorably with the clinical observation. To the best of the authors' knowledge, this is the first time that cardiac amyloidosis progression has been studied in a combined mechanical and statistical approach, based on longitudinal images of real patients during treatments.

2. METHODS

2.1. CMR-Based LV Model Construction

2.1.1. CMR Imaging

The study consists of CMR images from seven cardiac amyloidosis patients before treatment (baseline) and at 6 or 9 months after the treatment (follow-up). The information of all patients is in **Table 1**. Each patient has been clinically classified as recovery, worsening, and stable (no obvious change). The assessment was based on the clonal response to chemotherapy and progression/regression on the extracellular volume. The biomechanical modeling analysis in this paper is blind to the clinical assessment and the CMR imaging acquisition, briefly summarized in **Appendix A.1**, has been described in detail elsewhere (Fontana et al., 2015).

2.1.2. Ventricular Model Reconstruction

A prolate spherical coordinate system is used to reconstruct the LV geometry following the steps in Liu et al. (2009). Short-axis and long-axis cine images (Figure A1) at a total of 13 time instants in diastole are used to warp the LV geometry. The LV wall boundaries are manually segmented using an in-house Matlab code (Gao et al., 2017), and all short-axis LV wall boundaries are aligned to the images of the horizontal long axis, the vertical long axis, and the left ventricular outflow tract, respectively. In order to align the LV geometries along the long-axis at different times, we first determine the distance between the most-basal short-axis image and the mitral annulus ring, denoted as d_t at time t. Following this, the most-basal short-axis image is moved toward the annulus ring along the long axis with a distance of $d_\mathrm{t} - \min(d_i)$, ($i = 1, ...13$, representing the i^{th} short axis image at diastole). Note that the long axis is defined by connecting the center of the LV base and the apex. In order to align the LV geometries circumferentially, the angles of right ventricular insertion points are defined in the basal plane (corresponding to the most-basal short-axis image), v_1 near the

TABLE 1 | Cardiac amyloidosis patients and treatment details.

Case	Age	Sex	Weight (kg)	Blood pressure (mmHg)		Gadolinium dosage (mL)	
	Baseline		Baseline	Baseline	Follow-up	Baseline	Follow-up
1	62	M	110	79/42	96/61	22	17.8
2	55	F	78.9	106/71	131/80	15.8	16
3	54	F	75	115/68	108/71	16.2	15
4	70	M	67.8	94/62	96/61	13.6	13.1
5	65	M	57	111/69	107/71	11.4	12.3
6	59	F	87.8	112/69	129/83	17.6	21
7	72	M	75.4	106/66	108/71	15.1	11.5

inferior segment, and v_2 near the anterior segment, as shown in **Figure 1** at two different time instances. Then, for LV geometries at different times, the basal plane is aligned by matching the insertion points at v_1, and the same number of elements are assigned to the septum circumferentially when generating the layered hexhedron mesh. **Figure 2** shows the reconstructed LV at early-diastole, right after isovolumetric relaxation when the mitral valve just opens and the ventricular pressure is the lowest, for all patients both before and after treatment. This choice of reference configuration has been used in the literature (Genet et al., 2014; Gao et al., 2017).

A rule-based approach (Potse et al., 2006) is adopted to generate myofiber structure within the LV wall, with fibers varied linearly from -60^o at the epicardium to 60^o at the endocardium, and the sheet angle from -45^o at the epicardium to 45^o at the endocardium (see **Figure 3A**). Because the reconstructed LV geometries are fitted to one standard template mesh after long-axis and circumferential alignment, we may reasonably assume that elements with the same index from LV models at different times are co-registered. As shown in **Figure 3B**, three short-axis planes are further defined for extracting strains. Within each selected plane, 20 regions distributed equally along the circumferential direction are selected to obtain regional-average strains. In total, 60 circumferential strains are measured from CMR derived LV models.

Since each LV geometry has the same mesh connectivity, after co-registration of all LV geometries, a mapping can be established for every element of the LV geometry at different time frames. The deformation gradient related to the first time frame (at early-diastole) can be readily calculated as $\mathbb{F} = \frac{\partial \mathbf{x}}{\partial \mathbf{X}}$, where $\mathbf{X}$ and $\mathbf{x}$ are position vectors at the first and later time frames, respectively. We further obtain the circumferential direction ($\mathbf{c}$) locally with respect to the long axis, and the transmural direction ($\mathbf{r}$) pointing from endocardium to epicardium, and then the local longitudinal direction $\mathbf{l} = \mathbf{r} \times \mathbf{c}$, which follows local geometrical curvature (Gao et al., 2014a). This enables us to compute the circumferential and longitudinal strains as $E_{\mathrm{cc}} = \mathbf{c} \cdot (\frac{1}{2}(\mathbb{F}^T\mathbb{F} - \mathbf{I})\,\mathbf{c})$ and $E_{\mathrm{ll}} = \mathbf{l} \cdot (\frac{1}{2}(\mathbb{F}^T\mathbb{F} - \mathbf{I})\,\mathbf{l})$, in which $\mathbf{I}$ is the identity matrix. Note the reference state for strain calculation is early-diastole, not end-diastole which is usually adopted in clinics.

2.2. Personalized Biomechanical LV Model

2.2.1. Constitutive Law

We use the Holzapfel-Ogden strain energy function to describe myocardial passive properties (Holzapfel and Ogden, 2009),

$$\Psi = \frac{a}{2b}\exp(b(I_1 - 3)) + \sum_{i=\mathrm{f,s}} \frac{a_i}{2b_i}[\exp(b_i(\max(I_{4i}, 1) - 1)^2) - 1] + \frac{a_{\mathrm{fs}}}{2b_{\mathrm{fs}}}[\exp(b_{\mathrm{fs}} I_{8\mathrm{fs}}^2 - 1)] \tag{1}$$

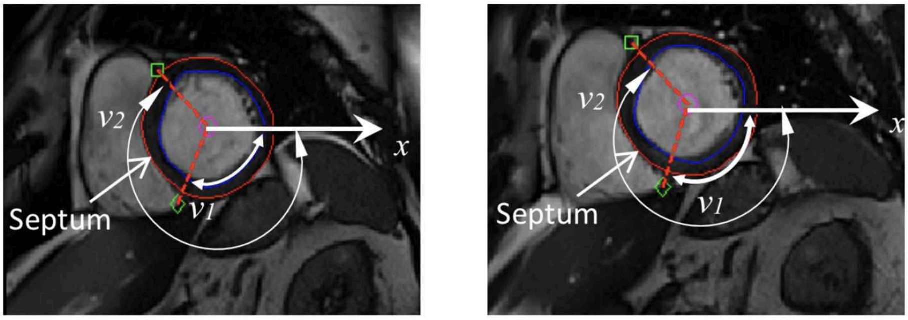

FIGURE 1 | Definition of right ventricular insertion points at the basal plane in order to align LV geometries circumferentially at different time instances.

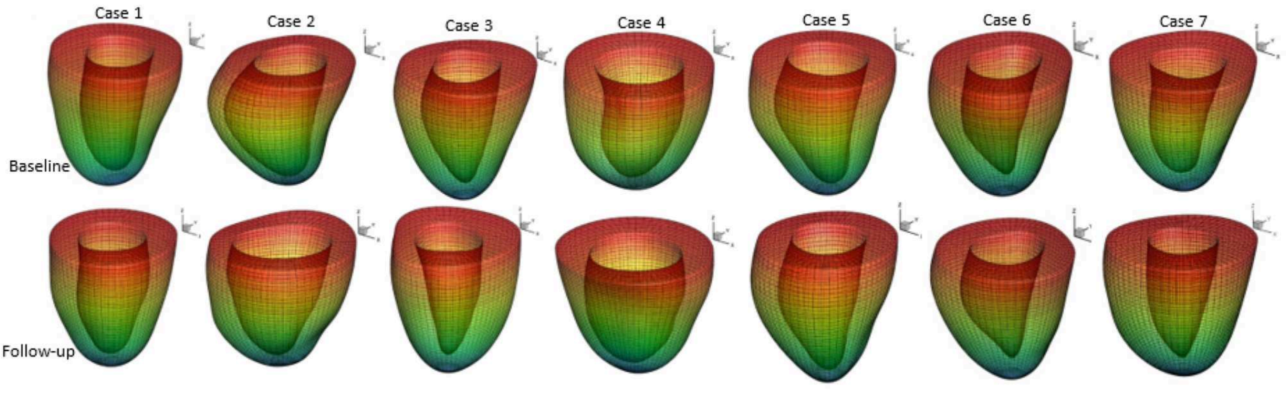

FIGURE 2 | Generated LV geometrical models based on the CMR images and their meshes at early-diastole of seven patients in baseline and follow-up scans.

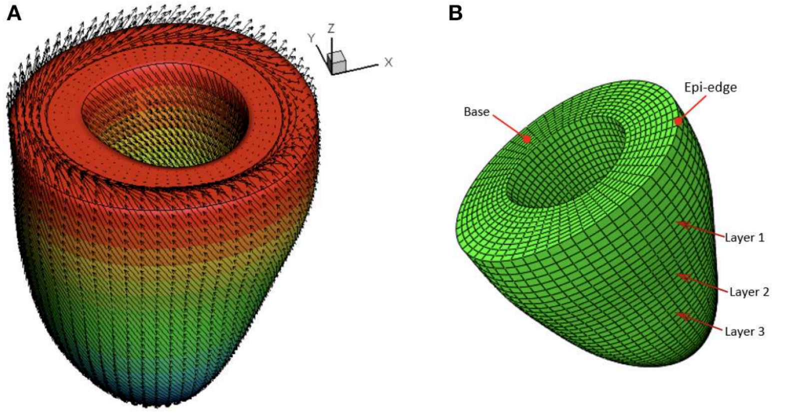

FIGURE 3 | Schematic illustration of myofiber orientation **(A)** and selected three layers in the LV wall **(B)**.

TABLE 2 | Wall volume ratio and estimated end-diastolic pressure of the amyloidosis patients.

	V_{wall}/V_{LV}		P_{ED} (mmHg)	
Case	**Baseline**	**Follow-up**	**Baseline**	**Follow-up**
1	2.2066	2.4505	17.38	15.65
2	1.5379	1.8881	10.91	13.39
3	2.7021	3.8163	19.17	27.07
4	1.9746	1.6576	14.01	11.76
5	2.2003	2.6155	15.57	18.55
6	3.2463	3.196	23.03	22.67
7	3.5	5.0283	24.83	35.67

where a, b, a_f, b_f, a_s, b_s, a_fs, b_fs are patient-dependent material parameters, and I_j ($j = 1, 4\mathrm{f}, 4\mathrm{s}$) are invariants of the right Cauchy-Green tensor. A more detailed description of the model (1) can be found in Holzapfel and Ogden (2009) and its applications in LV modeling should be referred to Göktepe et al. (2011), Wang et al. (2013), Gao et al. (2014b), and Wang et al. (2014). Differentiation of the strain energy function (1) with respect to the displacements and applying constraints related to various conservation laws leads to a set of equations that define the cardiac dynamics. These equations are solved numerically using finite element discretization, implemented in ABAQUS software 6.11.

2.2.2. Boundary Conditions

Early-diastole is used as the reference configuration. The following boundary conditions are applied at the most basal plane (see **Figure 3B**),

$$\begin{cases} u_x^{\mathrm{edge}}(t) = u_x^{\mathrm{CMR}}(t), \quad u_y^{\mathrm{edge}}(t) = u_y^{\mathrm{CMR}}(t), \\ u_z^{\mathrm{edge}}(t) = 0, \qquad \text{on the epicardial edge} \\ u_z^{\mathrm{base}}(t) = 0, \qquad \text{excluding the epicardial edge} \end{cases} \tag{2}$$

where u_x^{edge}, u_y^{edge}, u_x^{CMR}, u_y^{CMR} are the displacements in the x and y directions determined from the model and the CMR images at the epicardial edge in the most basal plane (see **Figure 3B**).

The diastolic pressure profile is assumed to be linear between zero at early-diastole ($t = 0\,\mathrm{s}$) and P_{ED} at end-diastole ($t = 1\,\mathrm{s}$), following (Steendijk et al., 2004). t here is a pseudo simulation time. The values of P_{ED} should be patient-specific. However, as the pressure measurements are invasive, this information is not available from *in vivo* studies. On the other hand, the literature suggests that all amyloidosis patients have increased wall thickness and higher pressure compared with normal subjects (Kholova and Niessen, 2005; Quarta et al., 2012; Martinez-NaharrO et al., 2018). Hence, we assume P_{ED} is proportional to scaled LV wall volume as follows:

$$\frac{P_{\mathrm{ED}}}{P_{\mathrm{EDm}}} = \frac{V_{\mathrm{wall}}/V_{\mathrm{LV}}}{(V_{\mathrm{wall}}/V_{\mathrm{LV}})^m}, \tag{3}$$

where P_{EDm} is the mean end-diastolic pressure, taken to be 19 mmHg based on measurements in Plehn et al. (1992) and Boufidou et al. (2010). $V_{\mathrm{wall}}/V_{\mathrm{LV}}$ is the ratio of the LV wall volume to the LV chamber volume. Its mean value $(V_{\mathrm{wall}}/V_{\mathrm{LV}})^m$ at early-diastole before treatment is 2.678. The scaled P_{ED} for each patient is listed in **Table 2**. This range of pressure values seems to be consistent with clinical observations of amyloidosis patients (Bhuiyan et al., 2011).

2.2.3. Parameter Inference

For each amyloidosis patient, the material parameters in Equation (1) are inferred by using an optimization algorithm through minimizing an objective function (the difference between the model and imaged-derived P-V curve and circumferential strains). Sensitivity analysis in our previous study (Gao et al., 2015) shows the ranking order of the parameters, from the most significant to the least, is

$$a > a_{\mathrm{fs}} > a_{\mathrm{f}} > b_{\mathrm{f}} > b \gg b_{\mathrm{fs}} > a_{\mathrm{s}} \approx b_{\mathrm{s}}. \tag{4}$$

This allows us to divide the parameters in Equation (1) into two groups, the first group includes a, b, a_{f}, b_{f}, a_{fs}, and the second group involves a_{s}, b_{s}, b_{fs}. The first group may be determined with higher accuracy than the second group because of the higher sensitivity to clinical measurements, although this may not be true all the time as the material model is strongly nonlinear. As such, a two-step approach is used. In the first step, parameters of the first group are determined by minimizing the following objective function with the parameters in the second group taking the values from Gao et al. (2015) for healthy volunteers estimated at $P_{\mathrm{EDm}} = 8$ mmHg ($a_{\mathrm{s}} = 0.5426\,\mathrm{kPa}$, $b_{\mathrm{s}} = 1.5998$, $b_{\mathrm{fs}} = 3.3900$):

$$\begin{cases} F_{\mathrm{VE}} = F_V + F_E \\ F_V = w_v \sum\limits_{i=1}^{n_{\mathrm{time}}} [(V_i^{\mathrm{FEA}} - V_i^{\mathrm{CMR}})/V_i^{\mathrm{CMR}}]^2 \\ F_E = \frac{w_E}{n_{\mathrm{layer}}\, n_{\mathrm{reg}}} \sum\limits_{k=1}^{n_{\mathrm{layer}}} \sum\limits_{j=1}^{n_{\mathrm{reg}}} \sum\limits_{i=1}^{n_{\mathrm{time}}} (\bar{E}\mathrm{cc}_{i,j,k}^{\mathrm{FEA}} - \bar{E}\mathrm{cc}_{i,j,k}^{\mathrm{CMR}})^2 \end{cases} \tag{5}$$

where n_{layer} is the number of layers considered, $n_{\mathrm{layer}} = 3$ indexed by k; n_{time} is the number of time steps, $n_{\mathrm{time}} = 13$ indexed by j; n_{reg} is the number of regions in each layer considered, $n_{\mathrm{reg}} = 20$ indexed by i; V_i^{FEA}, V_i^{CMR} are the LV chamber volumes from the FEA and CMR images, respectively; $\bar{E}\mathrm{cc}_{i,j,k}^{\mathrm{FEA}}$, $\bar{E}\mathrm{cc}_{i,j,k}^{\mathrm{CMR}}$ are the mean circumferential strains in 20 regions from the FEA and CMR images, respectively; w_v, w_E are the weights. Note we do not include the longitudinal strains in our objective function because the uncertainty of estimating longitudinal strains is much larger than the circumferential strains. This is because the simplified long-axial alignment we use does not account for the out-of-plane motion along the long axis. We are unable to quantify the out-of-plane motion due to the lack of necessary features in cine images. 3D strain imaging such as tagging allows one to include longitudinal strains (Nikou et al., 2016) or the displacement fields (Asner et al., 2016) in the objective function, but it is not used routinely in clinics. It is for this reason many published studies using *in vivo* cine images mainly used measured volume (Genet et al., 2014; Palit et al., 2018), or regional circumferential strains along with measured volume in the objective function (Gao et al., 2015).

After obtaining the optimal five constants in the first group, we proceed to infer all parameters but found a_{s}, b_{s}, and b_{fs} are insensitive to the optimization. Therefore we first focus on the ratios of parameters: $a_{\mathrm{s}}/a_{\mathrm{fs}}$, $a_{\mathrm{f}}/a_{\mathrm{s}}$, $b_{\mathrm{s}}/b_{\mathrm{fs}}$, $b_{\mathrm{f}}/b_{\mathrm{s}}$. A range of values for these ratios can be found from the literature (Gao et al., 2015; Palit et al., 2018) from which we derive the linear regressions,

$$\begin{cases} a_{\mathrm{s}}/a_{\mathrm{fs}} = 1.72\, a_{\mathrm{f}}/a_{\mathrm{s}} - 3.65 \\ b_{\mathrm{s}}/b_{\mathrm{fs}} = -0.43\, b_{\mathrm{f}}/b_{\mathrm{s}} + 1.61 \end{cases} . \tag{6}$$

The first equation of (6) shows that a_{s} is the only unknown after the first optimization step,

$$a_{\mathrm{s}} = \frac{1}{2}\left[1.72 a_{\mathrm{fs}} + \sqrt{(3.65\, a_{\mathrm{fs}})^2 + 4 \times 1.72\, a_{\mathrm{f}} a_{\mathrm{fs}}}\,\right]. \tag{7}$$

In the second equation of (6), two unknowns remain, b_{s} b_{fs}. Let $\xi = b_{\mathrm{f}}/b_{\mathrm{fs}}$, we write

$$\begin{cases} b_{\mathrm{s}} = b_{\mathrm{f}}/\xi \\ b_{\mathrm{fs}} = \frac{b_{\mathrm{f}}}{\xi(1.61 - 0.43\xi)} \end{cases} . \tag{8}$$

It is easy to see that $\xi \in [1.44, \quad 2.96]$ from data in Gao et al. (2015) and Palit et al. (2018). Thus in the second step, ξ is optimized by minimizing the objective function F_E in Equation (5).

The flowchart of the two-step optimization method and the inferred parameters are given in **Appendix A.2**. The uncertainties of these parameters are evaluated using the residual bootstrap method (Efron and Tibshirani, 1986), as described in **Appendix A.2**.

2.3. Shape Analysis and Statistical Classification

For feature comparison between the amyloidosis patients and control, we make use of the LV geometries of 26 healthy subjects from our previous study (Gao et al., 2017). Basic characteristics for the healthy volunteers are: ages: 45±15, sex (male: female): 15 : 11, systolic blood pressure (mmHg): 145.6 ± 31.4, diastolic blood pressure (mmHg): 83 ± 15, LV EF(%):57 ± 5, LV end-diastolic-volume (mL): 126 ± 21, LV end-systolic-volume (mL): 55±14. Geometry reconstruction follows the same procedure as for the amyloidosis patients (see section 2.1.2). All the LV geometries are fitted to one template LV mesh, with 5,792 vertices from the endocardial and epicardial surfaces, extracted from CMR images with the same imaging orientation as shown in **Figure 4** (i.e., the chest wall in the left side of the short-axis images). Note the vertices inside the ventricular wall are excluded, and each vertex has three coordinate components. Thus, a Cartesian coordinate representation lies in the 17,376 dimensional space, necessitating the use of dimensionality reduction techniques for consideration of the geometry in the context of classification and data visualization (see **Figure 4**).

To analyse the LV shape change, we first need to represent the LV in a low dimensional space. Principal component analysis (PCA) relies on, successively, finding the principal directions of variation in the data where the amount of variation explained by the eigenvectors (principal components) can be quantified using the corresponding eigenvalues (Bishop, 2006). If we begin with data in n dimensions, then projecting onto the first $m < n$ principal components provides us with a lower dimensional representation of the data while preserving variations in the data captured by these first m principal components. By construction, PCA assumes a linear mapping into the lower dimensional space and constrains the principal directions of variation to be orthogonal to one another (Shlens, 2014). Similarly, there is an implicit assumption of Gaussianity since we assume that dependence between data points is fully specified by the first two moments (mean and variance). These limitations of PCA can be overcome by considering a more flexible, non-linear, dimensionality reduction technique. Methods such as an autoencoding neural network could be considered however, for sparse data sets, as available in our study, parameter tuning will either lead to overfitting, or (if properly regularized) lose the non-linear model flexibility that motivated the method in the first place. For visualization purposes, t-Distributed Stochastic Neighbor Embedding (t-SNE) (van der Maaten and Hinton, 2008) provides a non-linear projection of the data into a lower dimensional space by minimizing a KL divergence between conditional probabilities of nearest neighbors in both spaces. However, since an explicit transformation is never learned, the method is limited to only data visualization. More details of dimensional reduction is given in **Appendix A.3**.

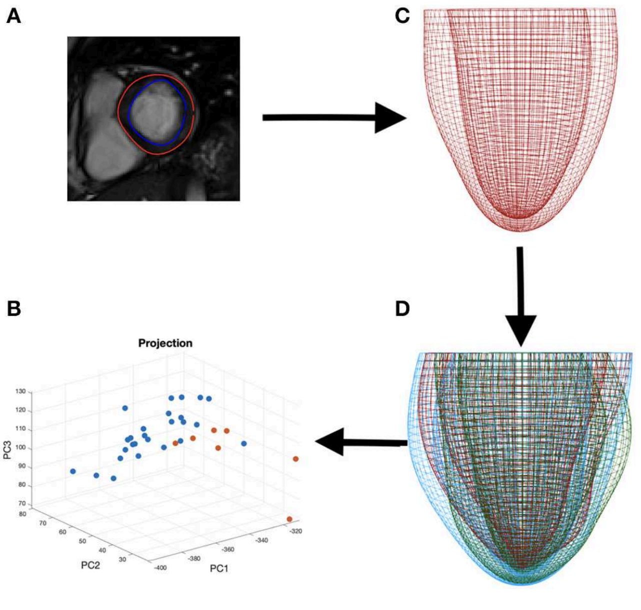

FIGURE 4 | The process of data segmentation and dimensionality reduction. First we segment the outer and inner walls of the LV **(A)** allowing us to construct a mesh representation of the LV **(C)**. We then extract the main variations in a sample of LVs **(D)** allowing us to represent the geometries in a lower dimensional space **(B)**.

For the purpose of classification, we can first consider a supervised method similar to PCA, namely linear discriminant analysis (LDA) (Bishop, 2006). Whereas PCA finds the direction of maximal variation without taking classes into account, LDA attempts to find a lower dimensional projection for separation of the two classes (in this case, healthy volunteers and amyloidosis patients). LDA is restricted by assumptions of linearity and Gaussianity. To overcome these constraints, we will also consider a kernel support vector machine (SVM), which allows for the possibility of non-linear boundaries between the groups in the dataset by the introduction of a kernel function (Murphy, 2012).

3. RESULTS

3.1. Analysis of Mechanical Features

3.1.1. Material Parameters

The optimization procedure is given in **Appendix A.2**, followed by uncertainty quantification using the bootstrap method. The inferred material parameters for the seven patients and the corresponding errors are listed in **Table 5**, and **Tables A2, A3.** However, it is not easy to see the pattern of parameter changes directly given the potential correlations between these parameters, and the lack of uniqueness. To assess the mechanical features, below we analyze the mechanical response of the cardiac amyloidosis patients during the disease progression using our FE models with the inferred parameters.

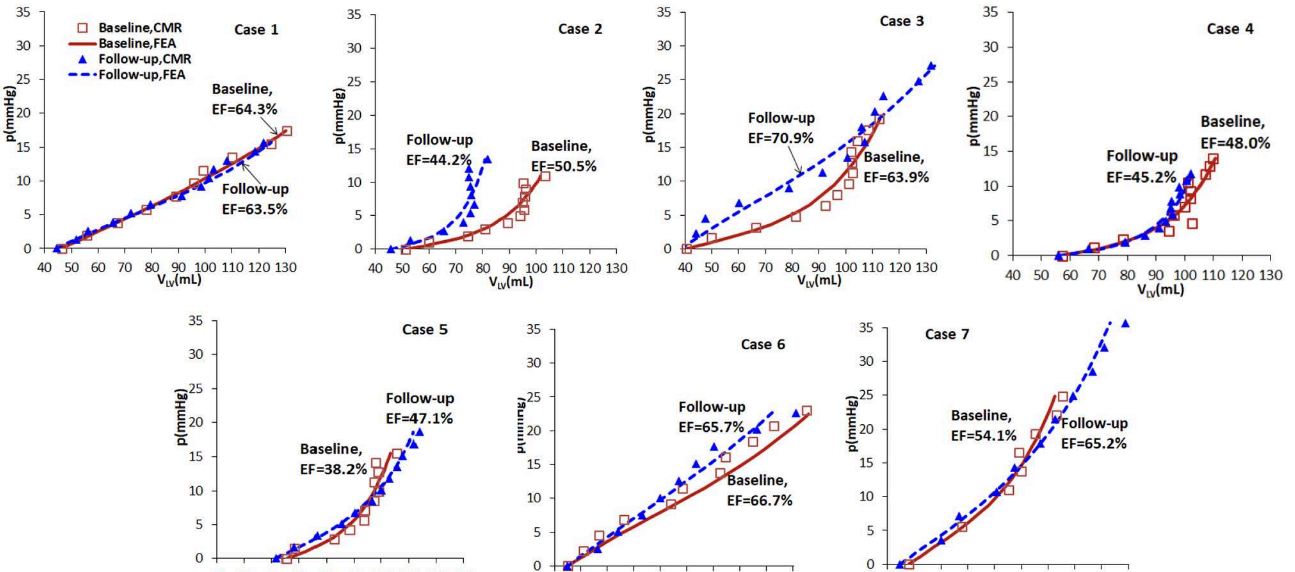

FIGURE 5 | p-V curves of the seven cases in baseline (red) and follow-up (blue), from CMR images (symbols) and FE models (lines).

3.1.2. p-V Curve

Based on the wall-thickness scaled P_{ED}, the p-V curves estimated from the FE models are shown in **Figure 5**, which are compared with the corresponding results when the volume is estimated directly from CMR images. **Figure 5** shows that there are little changes in the p-V curves of Cases 1, 4, 5, 7 from baseline to follow-up, but dramatic changes for Cases 2, 3, 6. The end-diastolic volumes of Cases 3, 5, and 7 increased compared to the baseline values, suggesting a ventricular dilation, while the end-diastolic volumes of Cases 1, 2, 4, and 6 decreased, especially for Case 2.

3.1.3. Stress-Stretch Response

The myocardium stress-stretch response along the myofiber direction for each patient can now be obtained from a pseudo uni-axial test of the myocardium using the material parameters estimated with perfectly aligned myofibers in one direction. The results are plotted in **Figure 6**. The stress-stretch curves

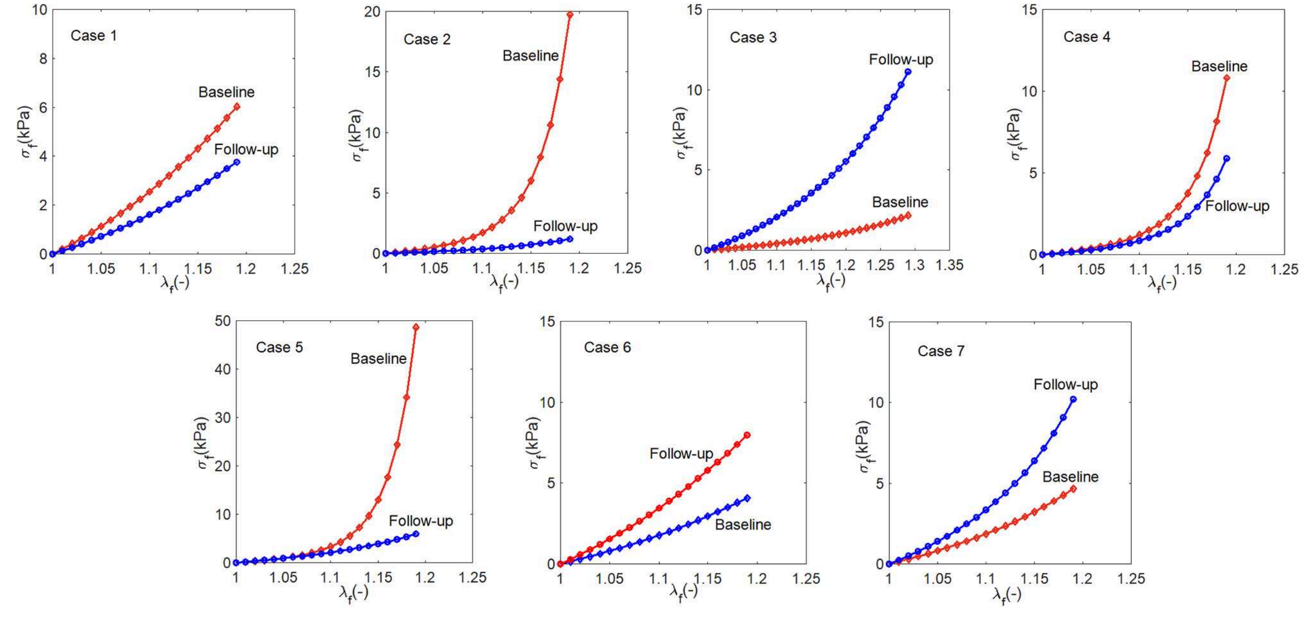

FIGURE 6 | The stress-stretch responses of the patients at the baseline (red) and follow-up (blue).

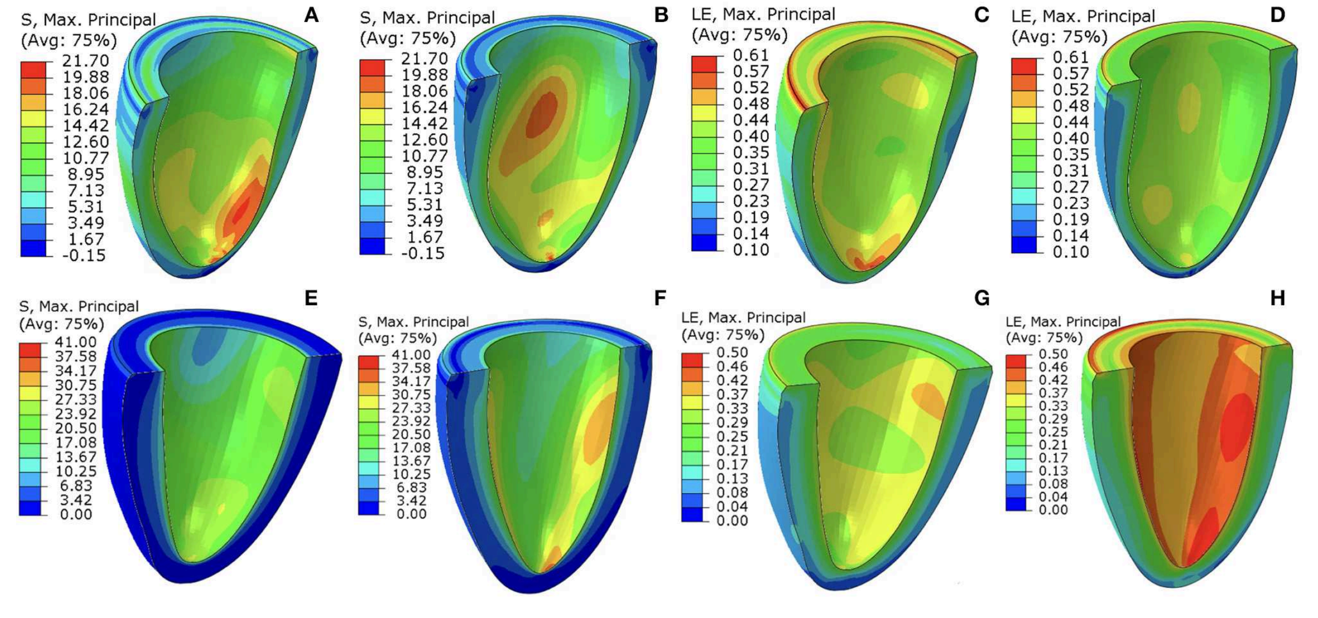

FIGURE 7 | The first principal stress contours at baseline **(A,E)** and follow-up **(B,F)**. The corresponding (logarithmic) strain contours are shown in **(C,D,G,H)**. **(A–D)** are for Case 1, **(E–H)** are for Case 7. The unit of the stresses is kPa.

of Cases 1, 2, 4, 5, and 6 in the follow-up are less stiff than in the baseline, in contrast to Cases 3 and 7. Note that in Case 6, the difference in the baseline and follow-up is very small.

3.1.4. 3D Strain and Stress Distribution

Figure 7 shows the first principal strain and stress of two different patients (Case 1 and Case 7) at baseline and follow-up. Clearly, the progression is very different in these two subjects. In Case 1, the first principal strain is slightly lower in the follow-up (**Figure 7B**) compared to the baseline (**Figure 7A**), particularly in the apical region. The strain patterns are somewhat different, but the maximum strain does not increase in the follow-up (**Figure 7C** vs. **Figure 7D**). However, for Case 7, there is a dramatic increase in the first principal stress level in the follow-up (**Figure 7E**) from the baseline **Figure 7F**. The strain patterns are also very different. In terms of the LV shape, not much change is seen in Case 1, but significant axial elongation is observed in Case 7.

3.2. Shape Analysis

PCA permits an intuitive representation of the variations in the data via the modes of variation (See **Appendix A.3**, top of **Figure A3**), obtained by perturbing the mean LV shape along each of the principal components. For our dataset, mode 1 is clearly related to overall size of the LV, mode 2 appears to represent thickness of the LV wall and mode 3 is related to the horizontal shape. Considering the absence of group indicators in this method, it is interesting to observe the second mode of variation, showing that within the dataset one of the largest sources of LV variation appears to be wall thickness. In the central plot on the bottom of **Figure A3** we see the projection of the data onto this second principal component where, as expected, there is some separation of the amyloidosis patients from the healthy volunteers once we isolate this source of variation. This separation can also be observed by considering the median distance (wall thickness) between points on the epicardium and endocardium of healthy volunteers and amyloidosis patients, found to be 0.77 and 1.11 cm for healthy volunteers and amyloidosis patients respectively. Letting wall thickness be taken as the median distance between the epicardium and endocardium walls, we obtain a $p < 0.05$ for a test of a difference between median wall thickness of healthy volunteers and amyloidosis patients using Mood's median test (these results are consistent with a t-test and a rank sum test).

Before studying amyloidosis progression prediction, we perform classification of the seven amyloidosis patients at baseline compared with a set of 26 healthy volunteers based on geometries alone, assessing the performance of LDA and a kernel SVM. Sensitivity (the ratio of the correctly predicted positive observations to all observations in the positive class) and specificity (the ratio of correctly predicted negative observations to all observations in the negative class) scores for these methods, obtained using a leave-one-out cross validation (LOOCV) procedure, are given in **Table 3** along with an overall accuracy quantification obtained using the F_1 score:

TABLE 3 | Sensitivity, specificity, and F1 scores for classifying geometries using LDA and Kernel SVM.

Method	LDA	Kernel SVM
Specificity	0.92	1
Sensitivity	0.71	0.86
F_1	0.71	0.92

$$F_1 = 2\frac{TP}{2TP + FP + FN} \tag{9}$$

where TP is number of true positives, FP is number of false positives and FN is number of false negatives. The F1 score is the harmonic mean of the precision (the ratio of correctly predicted positive observations to the total predicted positive observations) and the recall (also called sensitivity). We use the harmonic rather than the arithmetic mean to penalize the improvement of one of the scores at the expense of the other.

Accuracy of both the linear and non-linear methods is encouraging, suggesting the discriminative properties of the LV geometry with regards to amyloidosis.

3.3. Classification and Prediction

3.3.1. Selected Markers for Classification

The analysis above shows that no single marker provides a clear indication for disease progression. A combination of multiple features must be considered. To this end, we summarize the representative markers below that may contribute to the growth and remodeling of myocardium.

1. $V_{\text{wall}}/V_{\text{LV}}$, which reflects the wall thickness change relative to the ventricular volume. A lower value of $V_{\text{wall}}/V_{\text{LV}}$ means the wall becomes thinner (recovery);
2. $\bar{E}_{\text{cc}}$, the circumferential strain at end-diastole averaged from the three planes. A larger value of $\bar{E}_{\text{cc}}$ indicates that the LV is more compliant in the circumferential direction (recovery);
3. $\bar{E}_{\text{ll}}$, the longitudinal strain at end-diastole averaged from the three planes. A larger value of $\bar{E}_{\text{ll}}$ indicates that the LV is more compliant in the longitudinal direction (recovery);
4. $\bar{\sigma}_1$, the principal stress at end-diastole averaged from the three planes. A lower value of $\bar{\sigma}_1$ means the tissue is less stressed (recovery);
5. W, work done by pressure during diastolic filling, because it is not straightforward to compare different p-V curves, we compare the area-under-the-curve, which is defined as

$$W = \int_0^{\text{diastole}} p \, dV_{\text{LV}}.$$

A higher value of W in the follow-up means more work is required to maintain the heart function, corresponding to worsening.

6. The average slope $\bar{f}$ of the stress-stretch curve $\sigma - \lambda$. A steeper $\sigma - \lambda$ in the follow-up indicates the myocardium becomes stiffer (worsening).
7. Shape features, obvious shape changes compared to control indicate worsening.

The markers used for follow-up cardiac amyloidosis status prediction are divided into three classes: (1) geometrical markers (features 1–3), (2) biomechanical markers (features 4–6), and (3) LV shape markers (feature 7). Geometrical markers include normalized LV wall thickness, which has been applied clinically. Biomechanical markers are discussed in section 3.2.

3.3.2. Shape Classification and Prediction

We first study the amyloidosis patient recovery using shape features. As we do not know what is a "healthier" shape for LV, we make use of the control data from our previous study (Gao et al., 2017). The analysis is conducted by projecting the seven patients onto LDA components and measuring distances from the group of healthy volunteers before and after treatment. Pre-processing with PCA is necessary, removing collinearity and preventing singularities in the LDA calculations (this is the result of all meshes being formed by the same base LV mesh). **Figure 8** presents these distances where a negative gradient is a sign of movement toward healthy volunteers. Only patients 1, 5, 6, and 7 appear to improve as a result of the treatment. This analysis is performed using leave-one-out-cross-validation where in each case one amyloidosis patient is left out of the training set. These movements toward or away from healthy volunteers provide the shape marker in **Table 4** where values of the six markers in the previous section are also provided. Further details on computation of the first six markers are provided in **Appendix A.2**.

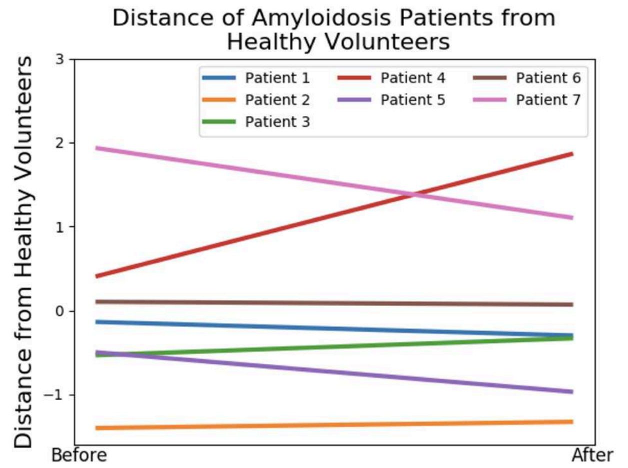

FIGURE 8 | Shape analysis of the amyloidosis patients. This plot was produced using LDA during an initial analysis of the data, before any patient recovery labels were known. The y-axis provides a measure of distance from the group of healthy volunteers and the x-axis provides two timepoints: before and after treatment.

Now that we have quantified the shape features, we can summarize the changes of all the markers from our model in **Table 4**. The original values of these markers at the baseline and follow up as well as the uncertainty quantification are provided in **Appendix A.4**.

4. DISCUSSION

Using a modeling approach, we have studied the predictive power of the mechanical and geometric markers with respect to amyloidosis classification. Of great interest is the relation of amyloidosis progression with these markers, and which ones have greater predictive power. We find that, due to the complexity of the LV disease, no single marker can provide the whole picture of the disease progression. Indeed, as shown in **Table 4**, some markers give opposite predictions for the same case. To overcome this issue, we made use of the recovery score for each patient based on the predictions of all the markers studied.

Table 5 summarizes the results of predicting recovery of amyloidosis patients. The recovery score refers to a classification done based on **Table 4**, which was found before the patient labels were made available. The recovery score is obtained as the proportion of "better" predictions in **Table 4**. In other words, we take the number of recovery scores and divide by the total so if a patient is said to recover by 3 out of 7 markers, then the recovery score is 3/7. The small sample size here severely limits significance of these results, but by consulting a committee of weak classifiers we seek to obtain more conclusive results. All patients were diagnosed with heart failure and all of them had NYHA class 2 at presentation. However, some cases (e.g., Case 1) became class 1 after treatment, and others (e.g., case number 7) became class 3 on the second follow up. Hence, the clinical assessments can be made. This is used to compare to our recovery score in **Table 4**, with a good overall agreement, particularly in cases (1, 3, 4, 6, 7). Notice that although we have computed the recovery scores, we do not know the corresponding range of recovery scores to the clinical statuses (of recovery, stable or worsening). If we declare all scores above 0.5 correspond to stable or recovery, then 6 out of 7 predictions are accurate. Case 2 is predicted wrong, but the score is almost at the boundary.

Despite the encouraging results from the double blind test shown in **Table 5**, limitations of our work must be discussed. This is a proof of concept study in the goal of classifying disease progression after treatment in amyloidosis patients. Thus, although the concept of the approach is deemed to be rather promising, it is important to exercise caution when interpreting the statistical results presented in this paper, as the lack of data reduces significance of the statistical analysis, as well as the dimensionality reduction results.

There are two issues that can impact the stress values we estimate. The first is that it is known that the eight parameters in the HO model are coupled and not independent. Therefore, each parameter may not be uniquely determined. However, it is not the individual change of the parameters that we look for, but the collective effects of all the parameters. For example, it has been shown that the stress-strain curves can be more robustly

TABLE 4 | Classification for the amyloidosis patients based on various markers.

Marker	$V_{\mathrm{wall}}/V_{\mathrm{LV}}$	$\bar{E}_{\mathrm{cc}}$	$\bar{E}_{\mathrm{ll}}$	W	$\bar{\sigma}_1$	$\bar{f}$	**Shape**
Case	**(Follow-up − Baseline)/Baseline × 100%**						
1	11.05	10.66 (0.06)	−10.72 (0.092)	−18.86 (0.05)	−18.20 (0.11)	−33.86 (0.12)	down
2	22.77	25.24 (0.10)	−51.86 (0.12)	−13.51 (0.03)	−38.59 (0.18)	−92.69 (0.09)	up
3	41.2	−4.77 (0.03)	65.03 (0.16)	168.22 (0.06)	39.79 (0.31)	428.19 (2.26)	up
4	−16.05	2.65 (0.10)	−10.63 (0.11)	−30.70 (0.11)	−6.53 (0.07)	−40.92 (0.69)	up
5	18.87	70.20 (0.18)	7.26 (0.18)	108.82 (0.09)	−8.50 (0.07)	−93.09 (0.08)	down
6	−1.55	−29.86 (0.03)	0.74 (0.06)	−14.37 (0.04)	13.36 (0.03)	193.59 (1.52)	down
7	43.67	9.33 (0.08)	83.90 (0.14)	154.70 (0.15)	42.12 (0.17)	168.10 (2.45)	down
Better:	4,6	1,2,4,5,7	3,5,6,7	1,2,4,6	1,2,4,5	1,2,4,5	1,5,6,7
Worse:	1,2,3,5,7	3,6	1,2,4	3,5,7	3,6,7	3,6,7	2,3,4

The criterion for improvement for the first 6 markers is based on physiology, as described in section 3.3.1. The criterion for improvement for "shape" (last column) is based on the statistical analysis described in section 3.3.2. The uncertainty intervals for the biomechanical markers (columns 5–7) are obtained from the residual bootstrap analysis described in ***Appendix A.2, A.4****. Note the sign of the values does not change when taking this uncertainty into account.*

TABLE 5 | Model predication vs. clinical assessment.

Patient	**1**	**2**	**3**	**4**	**5**	**6**	**7**
Recovery score	0.71	0.57	0.14	0.57	0.71	0.71	0.43
Clinical assessment	Recovery	Worsening	Worsening	Stable	Stable	Recovery	Worsening

The higher the score, the more likely is the recovery, and vice versa.

estimated despite the inter-correlations of the parameters, as shown in our previous study (Gao et al., 2015), for different measurement noise levels or initial values. To quantify the parameter uncertainty in our paper, we have carried out a residual bootstrap analysis (Efron and Tibshirani, 1986). Our uncertainty quantification follows a three-tier approach. At the bottom tier, we apply the residual bootstrap analysis to estimate the estimation uncertainty of the biomechanical parameters, which are defined below Equation (1). The methodological details are described in **Appendix A.2**. Note that the bootstrap analysis takes two effects into consideration: intrinsic uncertainty as a consequence of measurement noise, and algorithmic uncertainty as a consequence of potential convergence of the optimization algorithm to local optima of the objective function. At the middle tier, we use the bootstrap distributions of the biomechanical parameter estimates from the bottom tier to obtain the corresponding distributions of the biomechanical markers, which were introduced in section 3.3.1. The results can be found in **Appendix A.4**. At the highest tier, we use the uncertainty of the biomechanical markers to determine the uncertainty of the recovery scores. The methodological details can be found in **Appendix A.4**, and the results are in **Table 4**.

The second issue is the significant assumption we made on the end-of-diastole pressure for the patients since invasive pressure measurements are not available. We assumed that there is a proportional relationship between the pressure and wall volume, inspired by data from the literature. This assumption increased the uncertainty of the final stress values we computed. However, we would like to state that it is not the absolute stress values, but the relative change (follow up vs. acute), that matters in our evaluations. Clearly, **Table 4** shows that the recovery scores are not affected by the uncertainty intervals since, within the interval provided by the uncertainty propagation outlined in **Appendix A.4**, the recovery indicator does not change. We also estimated the recovery scores based on markers from the image-based strain and shape analysis alone, and found that the prediction is not as good, in that two cases (1 and 7) are predicted wrong if we exclude the stresses related markers. However, we noted that some of the individual scores give nearly opposite results. For example, in **Table 4**, two strain and shape indicators show that case 7 is getting better, but the three stress and wall thickness indicators show it is getting worse. Hence, not all indicators give a positive contribution to the overall score. This highlights the complexity of the pathological system, and indicates that no single biomarker studied is able to predict the amyloidosis progression. We tentatively suggest that competing mechanisms may be in play during patients' recovery. For instance, the increased strains (showing recovering) in Case 7 are accompanied by the increased stresses (showing worsening). This may imply that the more stiffened myocardium over-weights the benefits of the smaller strains. Therefore, it seems that multiple markers are required to give a balanced view for the overall picture. We remark again that our observations need to be supported by a larger sample size, as with a small sample size it is difficult to distinguish systematic effects from random fluctuations.

Other modeling limitations should also be mentioned. In this paper, amyloidosis LV is regarded as homogeneous material. The loaded early diastolic configuration is used as the reference configuration which excludes the effect of residual stresses. Our alignment of LV geometries at different times is based on a simplified linear registration approach. Nonlinear methods, such as deformable registration approaches (Rueckert et al., 1999), the large deformation deformetric metric mapping (Durrleman et al., 2014), may provide more accurate geometry co-registrations. These issues need to be addressed in future work.

5. CONCLUSION

A proof of concept analysis of cardiac amyloidosis progression has been obtained by projecting a group of amyloidosis patients onto linear discriminant analysis components and measuring distances from the group of healthy volunteers before and after treatment. Extensive mechanical, geometrical, and shape markers are included in the analysis for the first time for cardiac amyloidosis patients. A promising agreement with clinical observation is achieved in predicting disease progression following medical treatments in a double blind test. Although these results should be interpreted with caution due to a small sample size, the methodology of using statistical analysis and multiple markers, in particular the shape analysis, can play a powerful role in clinical translation in the future when used in large samples with new and automatic image segmentation methods.

DATA AVAILABILITY STATEMENT

All datasets generated for this study are included in the article/**Supplementary Material**.

ETHICS STATEMENT

Ethical approval was obtained from the Joint University College London/University College London Hospitals Research Ethics Committee (REC reference: 07/H0715/101). All research-related procedures were performed in accordance with local guidelines and regulations. The patients/participants provided their written informed consent to participate in this study.

AUTHOR CONTRIBUTIONS

XL, HG, and DH designed the study. WL and AL developed the mechanical and statistical models. AM-N, MF, and PH acquired the CMR scans. SB, RJ, and JC initiated the research idea and helped with image analysis. CB provided clinical insight. All participated in writing the manuscript.

FUNDING

This research was supported by the Engineering and Physical Sciences Research Council (EP/N014642/1, EP/S030875, EP/S020950/1), the British Heart Foundation Grant (Project Grant PG/14/64/31043, PG/11/2/28474), the National Health Service, and the Chief Scientist Office, and the British Heart Foundation Centre of Research Excellence Award (CoE RE/186134217). DH was supported by a grant from the Royal Society of Edinburgh, award no. 62335.

ACKNOWLEDGMENTS

We thank the patients who participated in this study.

SUPPLEMENTARY MATERIAL

The Supplementary Material for this article can be found online at: https://www.frontiersin.org/articles/10.3389/fphys.2020.00324/full#supplementary-material

REFERENCES

Asner, L., Hadjicharalambous, M., Chabiniok, R., Peresutti, D., Sammut, E., Wong, J., et al. (2016). Estimation of passive and active properties in the human heart using 3D tagged MRI. *Biomech. Model. Mechanobiol.* 15, 1121–1139. doi: 10.1007/s10237-015-0748-z

Bhuiyan, T., Helmke, S., Patel, A. R., Ruberg, F. L., Packman, J., Cheung, K., et al. (2011). Pressure-volume relationships in patients with transthyretin (ATTR) cardiac amyloidosis secondary to V122I mutations and wild-type transthyretin: Transthyretin cardiac amyloid study (TRACS). *Circulation* 4, 121–128. doi: 10.1161/CIRCHEARTFAILURE.109.910455

Bishop, C. M. (2006). *Pattern Recognition and Machine Learning (Information Science and Statistics)*. Berlin; Heidelberg: Springer-Verlag.

Boufidou, A., Mantziari, L., Paraskevaidis, S., Karvounis, H., Nenopoulou, E., Manthou, M.-E., et al. (2010). An interesting case of cardiac amyloidosis initially diagnosed as hypertrophic cardiomyopathy. *Hellenic J. Cardiol.* 51, 552–557. Available online at: https://www.hellenicjcardiol.org/archive/full_text/2010/6/2010_6_552.pdf

Buss, S. J., Emami, M., Mereles, D., Korosoglou, G., Kristen, A. V., Voss, A., et al. (2012). Longitudinal left ventricular function for prediction of survival in systemic light-chain amyloidosis: incremental value compared with clinical and biochemical markers. *J. Am. Coll. Cardiol.* 60, 1067–1076. doi: 10.1016/j.jacc.2012.04.043

Carroll, J. D., Gaasch, W. H., and McAdam, K. P. (1982). Amyloid cardiomyopathy: characterization by a distinctive voltage/mass relation. *Am. J. Cardiol.* 49, 9–13. doi: 10.1016/0002-9149(82)90270-3

Chapelle, D., Felder, A., Chabiniok, R., Guellich, A., Deux, J.-F., and Damy, T. (2015). "Patient-specific biomechanical modeling of cardiac amyloidosis–a case study," in *International Conference on Functional Imaging and Modeling of the Heart* (Maastricht: Springer), 295–303. doi: 10.1007/978-3-319-20309-6_34

Chew, C., Ziady, G. M., Raphael, M. J., and Oakley, C. M. (1975). The functional defect in amyloid heart disease: the "stiff heart" syndrome. *Am. J. Cardiol.* 36, 438–444. doi: 10.1016/0002-9149(75)90891-7

Dungu, J. N., Valencia, O., Pinney, J. H., Gibbs, S. D., Rowczenio, D., Gilbertson, J. A., et al. (2014). CMR-based differentiation of AL and ATTR cardiac amyloidosis. *JACC* 7, 133–142. doi: 10.1016/j.jcmg.2013.08.015

Durrleman, S., Prastawa, M., Charon, N., Korenberg, J. R., Joshi, S., Gerig, G., et al. (2014). Morphometry of anatomical shape complexes with dense deformations and sparse parameters. *NeuroImage* 101, 35–49. doi: 10.1016/j.neuroimage.2014.06.043

Efron, B., and Tibshirani, R. (1986). Bootstrap methods for standard errors, confidence intervals, and other measures of statistical accuracy. *Stat. Sci.* 1, 54–75. doi: 10.1214/ss/1177013815

Fontana, M., Pica, S., Reant, P., Abdel-Gadir, A., Treibel, T. A., Banypersad, S. M., et al. (2015). Prognostic value of late gadolinium enhancement cardiovascular magnetic resonance in cardiac amyloidosis. *Circulation* 132, 1570–1579. doi: 10.1161/CIRCULATIONAHA.115.016567

Frenzel, H., Schwartzkopff, B., Kuhn, H., Lösse, B., Thormann, J., Hort, W., et al. (1986). Cardiac amyloid deposits in endomyocardial biopsies: light microscopic, ultrastructural, and immunohistochemical studies. *Am. J. Clin. Pathol.* 85, 674–680. doi: 10.1093/ajcp/85.6.674

Gao, H., Aderhold, A., Mangion, K., Luo, X., Husmeier, D., and Berry, C. (2017). Changes and classification in myocardial contractile function in the left ventricle following acute myocardial infarction. *J. R. Soc. Interface* 14:20170203. doi: 10.1098/rsif.2017.0203

Gao, H., Carrick, D., Berry, C., Griffith, B. E., and Luo, X. (2014a). Dynamic finite-strain modelling of the human left ventricle in health and disease using an immersed boundary-finite element method. *IMA J. Appl. Math.* 79, 978–1010. doi: 10.1093/imamat/hxu029

Gao, H., Li, W., Cai, L., Berry, C., and Luo, X. (2015). Parameter estimation in a holzapfel–ogden law for healthy myocardium. *J. Eng. Math.* 95, 231–248. doi: 10.1007/s10665-014-9740-3

Gao, H., Wang, H., Berry, C., Luo, X., and Griffith, B. E. (2014b). Quasi-static image-based immersed boundary-finite element model of left ventricle under diastolic loading. *Int. J. Numer. Methods Biomed. Eng.* 30, 1199–1222. doi: 10.1002/cnm.2652

Genet, M., Lee, L. C., Nguyen, R., Haraldsson, H., Acevedo-Bolton, G., Zhang, Z., et al. (2014). Distribution of normal human left ventricular myofiber stress at end diastole and end systole: a target for *in silico* design of heart failure treatments. *J. Appl. Physiol.* 117, 142–152. doi: 10.1152/japplphysiol.00255.2014

Gertz, M., Dispenzieri, A., Grogan, M., Kumar, S., Leung, N., Maurer, M., et al. (2013). *Amyloidosis Awareness.* Amyloidosis Support Groups.

Göktepe, S., Acharya, S., Wong, J., and Kuhl, E. (2011). Computational modeling of passive myocardium. *Int. J. Numer. Methods Biomed. Eng.* 27, 1–12. doi: 10.1002/cnm.1402

Grogan, M., Dispenzieri, A., and Gertz, M. A. (2017). Light-chain cardiac amyloidosis: strategies to promote early diagnosis and cardiac response. *Heart* 103, 1065–1072. doi: 10.1136/heartjnl-2016-310704

Holzapfel, G. A., and Ogden, R. W. (2009). Constitutive modelling of passive myocardium: a structurally based framework for material characterization. *Philos. Trans. R. Soc. Lond. A Math. Phys. Eng. Sci.* 367, 3445–3475. doi: 10.1098/rsta.2009.0091

Kholova, I., and Niessen, H. (2005). Amyloid in the cardiovascular system: a review. *J. Clin. Pathol.* 58, 125–133. doi: 10.1136/jcp.2004.017293

Koyama, J., Ray-Sequin, P. A., and Falk, R. H. (2003). Longitudinal myocardial function assessed by tissue velocity, strain, and strain rate tissue doppler echocardiography in patients with al (primary) cardiac amyloidosis. *Circulation* 107, 2446–2452. doi: 10.1161/01.CIR.0000068313.67758.4F

Liu, D., Hu, K., Niemann, M., Herrmann, S., Cikes, M., Störk, S., et al. (2013). Impact of regional left ventricular function on outcome for patients with al amyloidosis. *PLoS ONE* 8:e56923. doi: 10.1371/journal.pone.0056923

Liu, Y., Wen, H., Gorman, R. C., Pilla, J. J., Gorman, J. H. III, Buckberg, G., et al. (2009). Reconstruction of myocardial tissue motion and strain fields from displacement-encoded MR imaging. *Am. J. Physiol. Heart Circul. Physiol.* 297, H1151–H1162. doi: 10.1152/ajpheart.00074.2009

Martinez-NaharrO, A., Hawkins, P. N., and Fontana, M. (2018). Cardiac amyloidosis. *Clin. Med.* 18, s30–s35. doi: 10.7861/clinmedicine.18-2-s30

Murphy, K. P. (2012). *Machine Learning: A Probabilistic Perspective.* The MIT Press.

Nikou, A., Dorsey, S. M., McGarvey, J. R., Gorman, J. H., Burdick, J. A., Pilla, J. J., et al. (2016). Computational modeling of healthy myocardium in diastole. *Ann. Biomed. Eng.* 44, 980–992. doi: 10.1007/s10439-015-1403-7

Nucifora, G., Muser, D., Morocutti, G., Piccoli, G., Zanuttini, D., Gianfagna, P., et al. (2014). Disease-specific differences of left ventricular rotational mechanics between cardiac amyloidosis and hypertrophic cardiomyopathy. *Am. J. Physiol. Heart Circul. Physiol.* 307, H680–H688. doi: 10.1152/ajpheart.00251.2014

Palit, A., Bhudia, S. K., Arvanitis, T. N., Turley, G. A., and Williams, M. A. (2018). *In vivo* estimation of passive biomechanical properties of human myocardium. *Med. Biol. Eng. Comput.* 56, 1615–16317. doi: 10.1007/s11517-017-1768-x

Petre, R. E., Quaile, M. P., Wendt, K., Houser, S. R., Wald, J., Goldman, B. I., et al. (2005). Regionally heterogeneous tissue mechanics in cardiac amyloidosis. *Amyloid* 12, 246–250. doi: 10.1080/13506120500386824

Plehn, J. F., Southworth, J., and Cornwell III, G. G. (1992). Atrial systolic failure in primary amyloidosis. *N. Engl. J. Med.* 327, 1570–1573. doi: 10.1056/NEJM199211263272205

Potse, M., Dubé, B., Richer, J., Vinet, A., and Gulrajani, R. M. (2006). A comparison of monodomain and bidomain reaction-diffusion models for action potential propagation in the human heart. *IEEE Trans. Biomed. Eng.* 53, 2425–2435. doi: 10.1109/TBME.2006.880875

Quarta, C., Kruger, J., and Falk, R. (2012). Cardiac amyloidosis. *Clin. Med.* 126, e178–e182. doi: 10.1161/CIRCULATIONAHA.111.069195

Rueckert, D., Sonoda, L. I., Hayes, C., Hill, D. L., Leach, M. O., and Hawkes, D. J. (1999). Nonrigid registration using free-form deformations: application to breast MR images. *IEEE Trans. Med. Imaging* 18, 712–721. doi: 10.1109/42.796284

Shlens, J. (2014). *A Tutorial on Principal Component Analysis.*

Steendijk, P., Tulner, S. A., Wiemer, M., Bleasdale, R. A., Bax, J. J., van der Wall, E. E., et al. (2004). Pressure–volume measurements by conductance catheter during cardiac resynchronization therapy. *Eur. Heart J. Suppl.* 6(Suppl. D), D35–D42. doi: 10.1016/j.ehjsup.2004.05.012

Sun, J. P., Stewart, W. J., Yang, X. S., Donnell, R. O., Leon, A. R., Felner, J. M., et al. (2009). Differentiation of hypertrophic cardiomyopathy and cardiac amyloidosis from other causes of ventricular wall thickening by two-dimensional strain imaging echocardiography. *Am. J. Cardiol.* 103, 411–415. doi: 10.1016/j.amjcard.2008.09.102

Swanton, R. H., Brooksby, A. I., Davies, M. J., Coltart, D. J., Jenkins, B. S., and Webb-Peploe, M. M. (1977). Systolic and diastolic ventricular function in cardiac amyloidosis: studies in six cases diagnosed with endomyocardial biopsy. *Am. J. Cardiol.* 39, 658–664. doi: 10.1016/S0002-9149(77)80125-2

van der Maaten, L., and Hinton, G. (2008). Visualizing data using t-SNE. *JMLR* 9, 2579–2605.

Vogelsberg, H., Mahrholdt, H., Deluigi, C. C., Yilmaz, A., Kispert, E. M., Greulich, S., et al. (2008). Cardiovascular magnetic resonance in clinically suspected cardiac amyloidosis: noninvasive imaging compared to endomyocardial biopsy. *J. Am. Coll. Cardiol.* 51, 1022–1030. doi: 10.1016/j.jacc.2007.10.049

Wang, H., Gao, H., Luo, X., Berry, C., Griffith, B., Ogden, R., et al. (2013). Structure-based finite strain modelling of the human left ventricle in diastole. *Int. J. Numer. Methods Biomed. Eng.* 29, 83–103. doi: 10.1002/cnm.2497

Wang, H., Luo, X., Gao, H., Ogden, R., Griffith, B., Berry, C., et al. (2014). A modified holzapfel-ogden law for a residually stressed finite strain model of the human left ventricle in diastole. *Biomech. Model. Mechanobiol.* 13, 99–113. doi: 10.1007/s10237-013-0488-x

White, J. A., Kim, H. W., Shah, D., Fine, N., Kim, K.-Y., Wendell, D. C., et al. (2014). CMR imaging with rapid visual T1 assessment predicts mortality in patients suspected of cardiac amyloidosis. *JACC Cardiovasc. Imaging* 7, 143–156. doi: 10.1016/j.jcmg.2013.09.019

Conflict of Interest: RJ and JC were employed by the company GlaxoSmithKline, plc, UK. The University of Glasgow holds research and/or consultancy agreements with Siemens Healthcare and GlaxoSmithKline plc for work done by XL, CB, and others.

frontiers in Physiology

ORIGINAL RESEARCH
published: 07 May 2020
doi: 10.3389/fphys.2020.00432

A Comprehensive Engineering Analysis of Left Heart Dynamics After MitraClip in a Functional Mitral Regurgitation Patient

Andrés Caballero[1], Wenbin Mao[1], Raymond McKay[2], Rebecca T. Hahn[3] and Wei Sun[1]*

[1] Tissue Mechanics Laboratory, The Wallace H. Coulter Department of Biomedical Engineering, Georgia Institute of Technology and Emory University, Atlanta, GA, United States, [2] Division of Cardiology, The Hartford Hospital, Hartford, CT, United States, [3] Division of Cardiology, Columbia University Medical Center, New York, NY, United States

OPEN ACCESS

Edited by:
Rajat Mittal,
Johns Hopkins University,
United States

Reviewed by:
Zhaoming He,
Texas Tech University, United States
Vicky Y. Wang,
The University of Auckland,
New Zealand

***Correspondence:**
Wei Sun
wei.sun@bme.gatech.edu

Specialty section:
This article was submitted to
Computational Physiology
and Medicine,
a section of the journal
Frontiers in Physiology

Received: 29 November 2019
Accepted: 08 April 2020
Published: 07 May 2020

Citation:
Caballero A, Mao W, McKay R,
Hahn RT and Sun W (2020) A
Comprehensive Engineering Analysis
of Left Heart Dynamics After MitraClip
in a Functional Mitral Regurgitation
Patient. Front. Physiol. 11:432.
doi: 10.3389/fphys.2020.00432

Percutaneous edge-to-edge mitral valve (MV) repair using MitraClip has been recently established as a treatment option for patients with heart failure and functional mitral regurgitation (MR), which significantly expands the number of patients that can be treated with this device. This study aimed to quantify the morphologic, hemodynamic and structural changes, and evaluate the biomechanical interaction between the MitraClip and the left heart (LH) complex of a heart failure patient with functional MR using a fluid-structure interaction (FSI) modeling framework. MitraClip implantation using lateral, central and double clip positions, as well as combined annuloplasty procedures were simulated in a patient-specific LH model that integrates detailed anatomic structures, incorporates age- and gender-matched non-linear elastic material properties, and accounts for mitral chordae tethering. Our results showed that antero-posterior distance, mitral annulus spherecity index, anatomic regurgitant orifice area, and anatomic opening orifice area decreased by up to 28, 39, 52, and 71%, respectively, when compared to the pre-clip model. MitraClip implantation immediately decreased the MR severity and improved the hemodynamic profile, but imposed a non-physiologic configuration and loading on the mitral apparatus, with anterior and posterior leaflet stress significantly increasing up to 210 and 145% during diastole, respectively. For this patient case, while implanting a combined central clip and ring resulted in the highest reduction in the regurgitant volume (46%), this configuration also led to mitral stenosis. Patient-specific computer simulations as used here can be a powerful tool to examine the complex device-host biomechanical interaction, and may be useful to guide device positioning for potential favorable clinical outcomes.

Keywords: mitral valve, MitraClip, fluid-structure interaction, functional mitral regurgitation, heart failure, patient-specific, edge-to-edge, annuloplasty

INTRODUCTION

The mitral valve (MV) repair technique using MitraClip (Abbott, Santa Clara, CA, United States) is the most common percutaneous treatment option for patients with symptomatic mitral regurgitation (MR) at high surgical risk (Mauri et al., 2013). Although MitraClip was recently approved by the U.S. Food and Drug Administration (FDA) for use in heart failure patients with functional MR, two large randomized clinical trials showed apparently conflicting results. While the COAPT trial showed that MitraClip was associated with a lower rate of hospitalization for heart failure and lower all-cause mortality within 24 months of follow-up, compared with using medical therapy alone (Stone et al., 2018), the MITRA-FR trial did not show significant differences between the intervention and control groups (Obadia et al., 2018).

Differences in the two clinical trials are likely to be related to threshold values for MR severity, medical management, operator experience and most importantly, proper patient selection (Goldberg, 2019); with markedly improved outcomes in the setting of a disproportionately larger severity of MR relative to left ventricle (LV) volumes after optimizing medical therapy (Grayburn et al., 2019). Indeed, several studies have shown that persistence of moderate-to-severe MR after MitraClip is associated with a considerably higher 1-year mortality (Lim et al., 2014; Sorajja et al., 2017; Ailawadi et al., 2019), such that MR reduction to moderate or less is of paramount importance. Thus, it is clear that for a successful MitraClip therapy: (i) a multidisciplinary heart team needs to be involved, (ii) procedural techniques need to be optimized, (iii) a better mechanistic understanding of device-host interaction is needed, and (iv) physicians need to perform careful patient selection and individualize treatments in accordance with patient characteristics.

To support this multidisciplinary approach, patient-specific computer simulations for transcatheter cardiac interventions can help to better understand the complex biomechanical inter-dependence between the device and the human host, predict device performance (efficacy), and possible complications (safety) (de Jaegere et al., 2019). Computer simulations using finite element (FE) and fluid-structure interaction (FSI) analyses have been useful in assessing MV biomechanics under healthy and diseased conditions, as well as in evaluating the functional effects of different surgical and transcatheter MV repair techniques (Wang et al., 2014; Caballero et al., 2018, 2019b, 2020; Sacks et al., 2019; Kong et al., 2020). While several computer studies have modeled the edge-to-edge and MitraClip procedures under degenerative or primary MR (Mansi et al., 2012; Zhong et al., 2014; Sturla et al., 2015; Morgan et al., 2017; Sturla et al., 2017; Prescott et al., 2019), to the best of our knowledge, no computer FSI study has to date evaluated the impact of MitraClip on left heart (LH) dynamics under functional MR. Previously, Lau et al. (2011) investigated the effect of the edge-to-edge surgical technique on an idealized MV model with a dilated static mitral annulus (MA) and healthy chordae structure with no leaflet tethering.

In this study, a previously validated patient-specific LH model with functional MR and heart failure (Caballero et al., 2019a) was used to: (1) simulate and evaluate MitraClip implantation with different clipping configurations and combined annuloplasty procedures, and (2) investigate the post-procedure LH dynamics throughout the cardiac cycle in order to quantify the acute changes in MR severity and assess the immediate biomechanical outcomes of the MitraClip procedure. Albeit a single patient case, we believe that this study offers a novel and detailed engineering analysis that could shed some light on the biomechanical impact of MitraClip on cardiac function in heart failure patients with significant MR. Further development and validation of such computer models could provide useful information toward proper patient selection and procedural optimization for treatment with transcatheter MV repair devices.

MATERIALS AND METHODS

Patient-Specific LH Model With Functional MR

In this study, we employed a patient-specific LH model with functional MR, heart failure and reduced LV ejection fraction (LVEF) rigorously developed and validated in Caballero et al. (2019a). The use of de-identified patient clinical data for this study was approved by an Institutional Review Board. Briefly, cardiac multi-slice computed tomography (MSCT) images of a patient referred for transcatheter AV replacement (TAVR) were retrospectively collected from Hartford Hospital (Hartford, CT). Transthoracic echocardiographic (echo) examination revealed moderate-to-severe functional MR, with restricted posterior mitral leaflet (PML) motion and reduced leaflet coaptation, resulting in a posteriorly directed regurgitant jet. The LVEF was estimated to be 25%. The LV thickness was normal but the chamber was dilated with severe global hypokinesis with regional variation. The LA was dilated despite a normal antero-posterior diameter. Classical low-flow, low-gradient severe aortic stenosis (AS) was also found, with a bicuspid aortic valve (AV) with fused left and right coronary cusps.

The patient-specific LH model, as shown in **Figure 1A**, is composed of the ascending aorta, aortic root, AV, calcification, MV, and LV and left atrium (LA) endocardial walls. Additionally, the computer model comprises detailed mitral chordae structure and distribution, accurate leaflet geometry and thickness, dynamic MA and chordae origins, anisotropic hyperelastic material models, and human age- and gender-matched material properties. Chordae tethering forces due to papillary muscle (PM) displacement were accounted for accurate modeling of MV dynamics under functional MR, as previously presented in Pham et al. (2017). Further details on medical imaging segmentation, 3D model reconstruction, constitutive modeling, and model validation can be found in **Supplementary Material**.

MitraClip and Annuloplasty FE Modeling

The clip device was modeled as two rectangular rigid plates mimicking the design and dimensions of the real MitraClip, as seen in **Figure 1B**. The length of each plate was 9 mm and the width was 5 mm. A reference node was defined at the middle bottom edge of each plate, allowing each arm to rotate with respect to its own reference node. A connector element connecting the two reference nodes was defined in order to impose mutual kinematic constraints. During the simulations, the relative motion of the two clip arms was constrained by the connector element to prevent relative displacement between them. Based on the location of the regurgitant gap, three MitraClip placement locations were simulated in this study: (i)

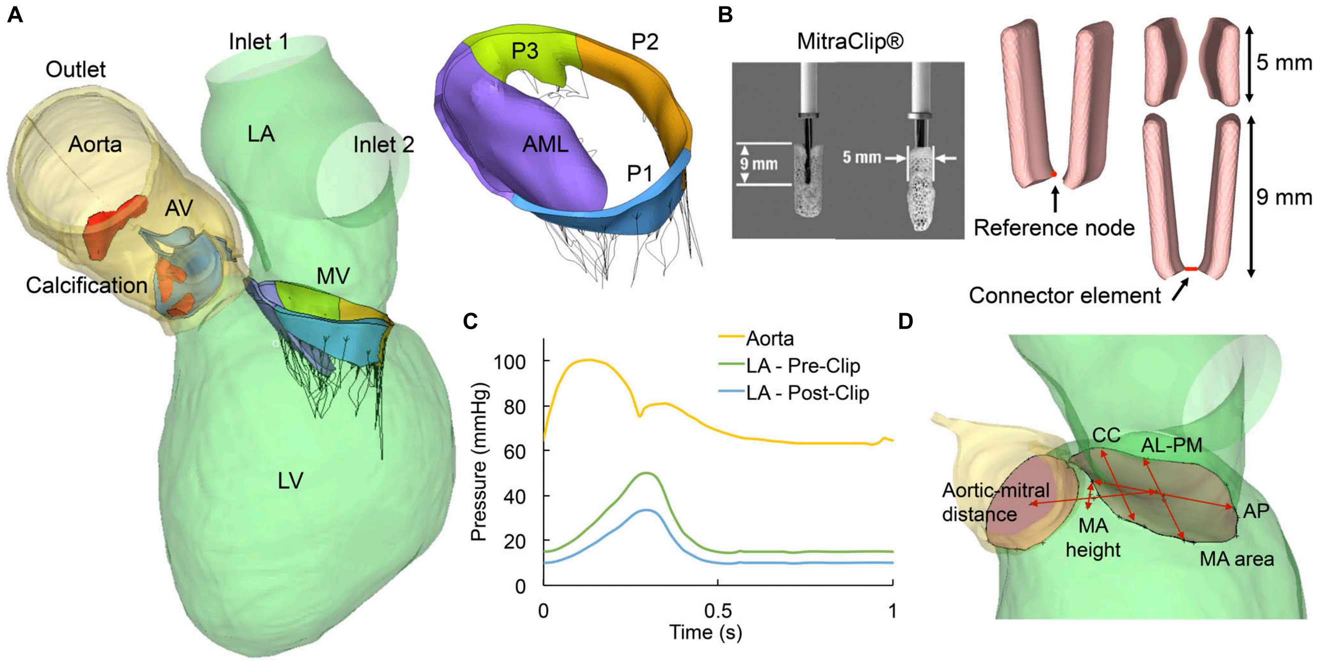

FIGURE 1 | (A) Patient-specific LH model, **(B)** Real and simulated MitraClip devices, **(C)** Aortic and LA pressure waveforms, **(D)** MV geometrical parameters. AV, aortic valve; LV, left ventricle; LA, left atrium; MV, mitral valve; AML, anterior mitral leaflet; PML, posterior mitral leaflet is divided into lateral P1 scallop, central P2 scallop and medial P3 scallop.

lateral positioning, between the anterior mitral leaflet (AML) and P1 scallop, (ii) central positioning, between the AML and P2 scallop, and (iii) double positioning, by combining lateral and central clips.

Because multiple mechanistic etiologies of MR frequently coexist, there is a high clinical interest in combining or sequentially staging transcatheter approaches to eliminate MR, such as combined MitraClip with percutaneous annuloplasty (Rogers et al., 2018). Due to the lack of geometrical data for these novel transcatheter rings, the 3D profile of a well-established surgical annuloplasty ring (Carpentier-Edwards Classic) known to successfully treat functional MR by reducing the antero-posterior annular diameter was used in this study. Following the selection guidelines (Borghetti et al., 2000), a 38 ring size was chosen based on the surface area of the device and the AML. However, rather than modeling the implantation of the actual ring with its full cross-sectional geometry, ring implantation was simplified by displacing the nodes of the MA to the 3D shape of the ring, as previously presented in Kong et al. (2018). The 3D ring shape and dimensions were obtained from literature. Combined annuloplasty ring implantation was simulated for the central and double clip models. The MV repair procedures were modeled in three major FE steps:

Step 1: MV Closure

Simulation of MV closure under systolic pressure and chordae tethering has been described in detail in our previous studies (Pham et al., 2017; Kong et al., 2018). Briefly, since the heart failure patient had moderate-to-severe MR with PML tethering and dilated LV, pre-existing forces within the chordae at diastole were modeled in the first sub-step of the simulation. Thus, before running the FE simulation, a total of 8 posterior chordae were shortened by translating the chordae origins toward the MA plane along the original direction of the chordae. At the beginning of the step, those chordae origins were initially displaced to their original locations to generate the tethering tension. After those chordae origins reached their original locations on the PM tips, a rough contact with no separation behavior was enforced to connect the chordae with the PM tips (Pham et al., 2017). The reaction force on each node of the MA was output at the end of this first sub-step. Next, the dynamic motion of the MA and chordae origins from diastole to systole obtained from the MSCT images was applied as a nodal displacement boundary condition (Pham et al., 2017). The clinically measured trans-mitral pressure gradient of 114 mmHg was then applied to the ventricular surface of the leaflets to simulate MV closure. At the end of this step, the two MitraClip arms rotated so that the clip opened at 120 degrees.

Step 2: Clip Grasping

Clip grasping to the mitral leaflets was modeled at diastole when the valve just started to open. Initially, displacement boundary conditions on the MA and chordae were applied so that the mitral apparatus restored to a diastolic position and the leaflets opened due to the release of the pressure on the ventricular surface. Next, the MA nodal displacement boundary condition was replaced by the MA reaction forces obtained in Step 1 from the pretension simulation at diastole to account for the tension within the MA during diastole. Meanwhile, to grasp the leaflets, the two clip arms rotated back to a closed position until a gap of 4 mm was left between the upper end of the two arms (Magruder et al., 2016). At the end of the step, rough contact with no slippage and no separation behavior was initiated between the clip arms and the mitral leaflets. The arms remained mutually parallel but could rotate/tilt following the interaction with the leaflets.

Step 3: Annuloplasty Ring Implantation

To align the virtual ring with the MA plane, least-square planes were created for both the ring and the MA. Next, middle anterior and posterior portions of the ring were aligned with the middle anterior and posterior portions of the MA until the ring was positioned such that the anterior portion of the ring overlapped with the anterior MA, avoiding excessive displacement of the LV outflow tract (LVOT). Following ring alignment, a total of 18 node clusters uniformly distributed along the MA were identified as boundary nodes; each cluster contained 3 adjacent nodes. On the virtual ring, 18 uniformly distributed nodes were also identified. Suturing of the annuloplasty ring to the MA was simulated by imposing kinematic displacements on the 18 node clusters on the MA from their original locations to the locations of the 18 corresponding nodes identified on the virtual ring (Kong et al., 2018).

During all FE simulation steps that modeled the MitraClip and annuloplasty implantation procedures, nodes on the septal wall of the LV myocardium were fixed to prevent excessive cardiac motion. The rest of the LV was not constrained to allow deformation near the MA during the repair therapies. The resulting deformed LH geometries after MitraClip and annuloplasty procedures were extracted from the FE simulations and used to assess the post-procedure LH dynamics using FSI.

FSI Modeling of Pre- and Post-procedure LH Dynamics

The FSI modeling framework used in this study has been previously developed, validated and implemented to evaluate the LH dynamics under a variety of physiologic, pathologic and repaired states (Mao et al., 2016a, 2017; Caballero et al., 2017, 2018, 2019a,b). Briefly, the FSI approach combines smoothed particle hydrodynamics (SPH) for the blood flow and non-linear FE analysis for the heart valves. As seen in **Figure 1C**, time-dependent pressure boundary conditions were applied at the two LA inlets (pulmonary veins) and at the aortic outlet of the pre- and post-procedure models. In functional MR, the regurgitant volume in the LA results in an elevated V-wave pressure during systole (Mokadam et al., 2011). After MitraClip, the LA pressure decreased by 33% (Kuwata et al., 2019; Turyan Medvedovsky et al., 2019). On the outlet, a physiologic aortic pressure waveform was employed. These waveforms were fitted to match this particular patient's pressure values clinically measured (Caballero et al., 2019a).

Endorcardial LV and LA wall motion and chordae origins motion during the pre- and post-procedure FSI simulations were imposed as a time-dependent nodal displacement boundary condition based on the MSCT images (Caballero et al., 2017; Mao et al., 2017). This cardiac wall motion was kept the same for all pre- and post-procedure models, simulating immediate post-operative LH dynamics, without considering any possible cardiac remodeling mechanisms that occur over time after MV repair. SPH particles were uniformly distributed in the LH domain with a spatial resolution of 0.8 mm and given Newtonian blood properties with a density of σ = 1056 kg/m^3 and a dynamic viscosity of μ=0.0035 Pa.s. SPH particle sensitivity (Mao et al., 2016b; Caballero et al., 2017) and FE mesh sensitivity (Wang and Sun, 2013) studies were previously performed. The patient's heart rate was approximately 60 bpm, corresponding to a cardiac cycle of 1 s. Two cardiac cycles were conducted and the results from the second cycle were analyzed in this study. Abaqus/Explicit 6.17 (3DS, Dassault Systéms, Paris, France) was used for all FE and FSI simulations presented in this work.

Data Analysis

MV Geometrical Parameters

Morphologic changes in the MV during MitraClip were evaluated in terms of the geometrical parameters shown (**Figure 1D**). The following measurements were obtained during systole: (a) antero-posterior (AP) distance, (b) anterolateral-posteromedial (AL-PM) distance, (c) MA spherecity index (ASI), defined as the ratio between AP and AL-PM distances, (d) inter-commissural (CC) distance, (e) MA height to inter-commissural width ratio (AHCWR), defined as the ratio between MA height and CC distance, (f) MA area, and (g) aortic-mitral distance, defined as the centroid distance between the mitral and aortic annuli.

Fluid Parameters

The following hemodynamic parameters were quantified throughout the cardiac cycle: (a) stroke volume in the AV (SV_{AV}) and MV (SV_{MV}), obtained by integrating the positive aortic and mitral flow over time, respectively (**Figure 2**), (b) regurgitant volume in the AV (RV_{AV}) and MV (RV_{MV}), obtained by integrating the negative aortic and mitral flow over time, respectively (**Figure 2**). The regurgitant volume was defined as the sum of the valve closing and the leakage volumes, (c) regurgitant fraction, $RF_{MV} = RV_{MV}/LVSV$ where $LVSV$ is the total SV of the LV ($SV_{AV}+ RV_{MV}$), (d) MR severity, graded using the RF_{MV} criterion (Zoghbi et al., 2003), (e) LVEF, (f) LV mean systolic pressure (LV-MSP), (g) LV end-diastolic pressure (LV-EDP), (h) peak systolic pressure gradient (PSPG), (i) mean systolic pressure gradient (MSPG), (j) AV peak velocity, (k) AV effective orifice area, $EOA_{AV} = \frac{MSF}{51.6\sqrt{\text{MSPG}}}$, where MSF is the root mean square systolic flow rate (Saikrishnan et al., 2014), (l) peak diastolic pressure gradient (PDPG), (m) mean diastolic pressure gradient (MDPG), (n) E and A wave velocities, (o) MV effective orifice area, $EOA_{MV} = \frac{MDF}{31\sqrt{\text{MDPG}}}$, where MDF is the root mean square diastolic flow rate (Chandran et al., 2012), (p) MR mean pressure gradient (MR-MPG), q) MR mean velocity, and (r) effective regurgitant orifice area,

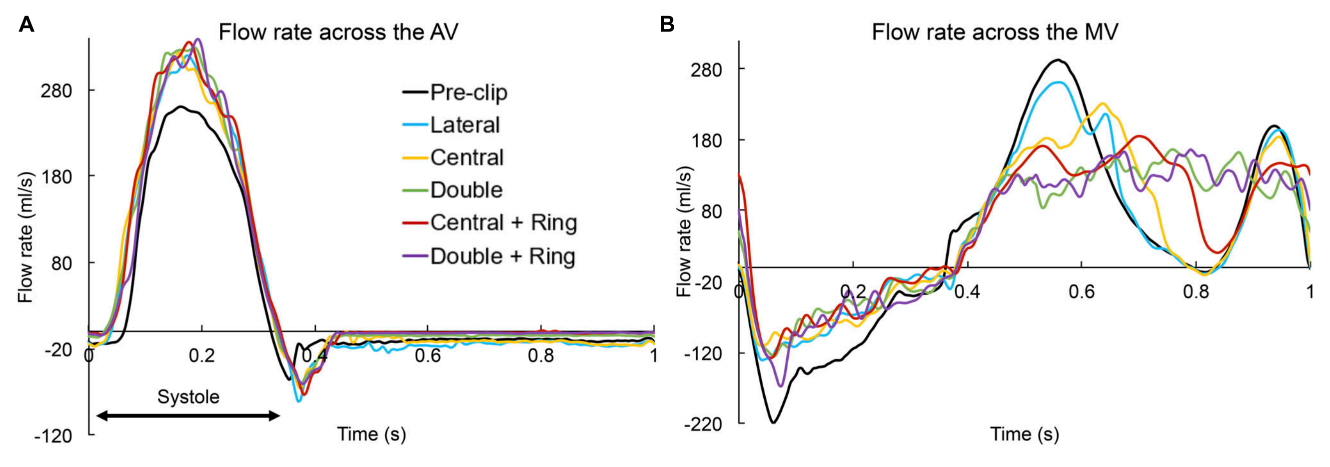

FIGURE 2 | Flow rate (ml/s) across the **(A)** AV and **(B)** MV throughout the cardiac cycle.

$EROA = \frac{MRF}{31\sqrt{MR - MPG}}$, where MRF is the root mean square regurgitant flow rate.

Structural Parameters

Pre- and post-procedure MV biomechanics were evaluated by the average maximum principal stress (S_I^{AVRG}) in the MV leaflets during peak systole and diastole. To avoid the bias caused by local high stress concentration, only the 99-percentile values of the peak stress values were evaluated (Auricchio et al., 2011). Moreover, MA regions were not included in the average stress calculation in order to avoid boundary effects. AML and PML chordae forces ($F_{chordae}$) were also reported. The force experienced by a particular chordae group was calculated as the sum of vectors representing the tension in each individual chorda attached to a specific leaflet. Finally, the anatomic MV orifice area (AMVOA) was quantified throughout the cardiac cycle. The least square plane of the MA was calculated at each time point of the cardiac cycle. The AMVOA was then measured as the projected 2D area of the mitral leaflets free edge on the MA least square plane. The anatomic regurgitant and opening orifice areas were obtained by selecting the minimum and maximum AMVOA values during systole and diastole, respectively.

RESULTS

MitraClip Impact on MV Geometry

Table 1 summarizes the changes in MV geometry during MitraClip implantation. The AP distance and ASI markedly decreased (>20%) for the central and double clip models, with or without ring. Similarly, the MA area and aortic-mitral distance had a tendency to decrease for all clip models, but these changes were only important for the double + ring model when compared to the pre-clip state. Furthermore, the AL-PM and CC distances showed a trend to increase after MV repair, however, these changes were relatively small and comparable before and after the procedure. Generally, using a lateral clip led to the smallest changes in MV geometry, while using a double clip + ring led to the biggest anatomic changes.

MitraClip Impact on Intraventricular Hemodynamics

Figure 2 shows the flow rate waveforms across the valves throughout the cardiac cycle for the pre- and post-clip models. The positive flow indicates the forward flow toward the aorta (**Figure 2A**) and the LV (**Figure 2B**) during systole and diastole, respectively. In contrast, the negative flow indicates the backward blood flow due to valve closure and regurgitation. Based on mass conservation and since blood is incompressible, $SV_{AV} + RV_{MV}$ during systole = $SV_{MV} + RV_{AV}$ during diastole (Mao et al., 2020). Additionally, **Table 2** summarizes the main hemodynamic parameters quantified for the pre- and post-clip models from the FSI simulations.

Several important findings can be quantified during systole: First, MitraClip therapy led to an immediate hemodynamic improvement by decreasing the RV_{AV}, and due to the coupled aortic-mitral valve dynamics and mass conservation, a concomitant increase in the forward SV_{AV} (**Table 2**). The greatest degree of MR improvement was for the central + ring model (46%). Moreover, all post-clip models can now be classified as moderate MR. Second, an increase in the LV-MSP of 8–13 mmHg was quantified immediately after MitraClip, reflecting the increase in the SV_{AV}. Third, the MR-MPG increased after the procedure (**Figure 3B**) due to a better closure of the mitral leaflets, the decrease in the LA pressure, and the increase in the LV-MSP. The peak MR velocity and EROA consequently decreased after MitraClip. Fourth, improvement in the systolic hemodynamic profile after clip implantation was also associated with a decrease in the PSPG and MSPG (**Figure 3A**), and an increase in the EOA_{AV}.

Similarly, important findings were quantified during the diastolic phase: First, narrowing of the MV orifice after MitraClip caused higher PDPG and MDPG (**Figure 3B**), as well as higher MV inflow velocities (**Table 2**). The MDPG increased from 1.35 mmHg pre-clip up to 9.2 mmHg when using a double

TABLE 1 | MV anatomical parameters pre- and post-clip.

	Pre-clip	Lateral	Central	Double	Central + Ring	Double + Ring
AP distance (mm)	34.37	31.90	27.37 (−20)	27.66 (−20)	25.28 (−26)	24.74 (−28)
AL-PM distance (mm)	39.83	41.96	43.28	43.51	45.71	46.80
ASI	0.86	0.76	0.63 (−27)	0.64 (−26)	0.55 (−36)	0.53 (−39)
CC distance (mm)	33.87	35.22	34.90	35.36	37.42	37.98
AHCWR	0.14	0.16	0.11	0.12	0.12	0.14
MA area (cm^2)	11.40	10.37	10.04	9.58	9.40	9.14 (−20)
Aortic-mitral distance (mm)	28.32	25.06	24.43	23.71	23.38	22.78 (−20)

Marked percentage variations (%) with respect to the pre-clip model are reported in parenthesis.

TABLE 2 | Pre- and post-clip LH hemodynamics.

	Pre-clip	Lateral	Central	Double	Central + Ring	Double + Ring
SV_{AV} (ml)	46.28	58.81	58.55	60.94	61.21	57.13
RV_{AV} (ml)	9.34	13.18	10.42	6.37	4.78	4.85
SV_{MV} (ml)	74.64	70.22	71.57	74.45	75.70	75.38
RV_{MV} (ml)	37.59	23.88	23.59	20.86	19.51	23.98
RF_{MV} (%)	44.82	28.88	28.72	25.50	24.17	29.56
MR severity (RF_{MV})	Moderate-to-severe	Moderate	Moderate	Moderate	Moderate	Moderate
LVEF (%)	28.55	28.15	27.96	27.84	27.47	27.61
LV-MSP (mmHg)	97.64	105.7	105.43	110.31	110.38	103.94
LV-EDP (mmHg)	15.96	9.67	8.39	0.03	0.92	0.01
PSPG (mmHg)	34.82	30.74	30.58	34.14	33.90	31.50
MSPG (mmHg)	23.97	20.97	20.7	21.68	21.34	20.84
AV peak velocity (m/s)	2.82	2.76	2.8	2.81	2.8	2.77
EOA_{AV} (cm^2)	0.77	0.94	0.93	0.95	0.96	0.93
PDPG (mmHg)	4.32	8.91	9.05	10.4	9.17	10.78
MDPG (mmHg)	1.35	4.33	6.16	9.17	7.47	9.2
E wave (m/s)	0.79	0.96, 1.46	1.41, 1.29	1.15, 0.92, 1.44	1.43, 1.36	1.2, 0.74, 1.47
A wave (m/s)	0.54	0.71, 1.2	1.30, 1.15		1.31, 1.28	
EOA_{MV} (cm^2)	4.1	2.19	1.76	1.32	1.53	1.32
MR-MPG (mmHg)	57.25	75.24	76.65	79.84	79.56	74.25
MR peak velocity (m/s)	5.42	4.81	4.83	4.9	4.89	4.82
EROA (cm^2)	0.5	0.28	0.26	0.24	0.24	0.28

E and A wave velocity values from left to right correspond to the double/triple orifices located from P1 to P3 scallops.

clip + ring. Second, MR reduction promoted a decrease in the preload, manifested by a decrease in the LV-EDP (**Figure 3C**). The double clip models presented the greatest decrease in LV preload. Third, as seen in **Figure 2B**, the MV inflow curve profile changed after repair. Due to the decrease in the EOA_{MV} and the greater resistance to flow in the multiple-orifice MV, there was a decrease in the early E-wave dominant flow. This decrease was more dominant for the double clip models, which presented the lowest EOA_{MV}.

Figure 4 shows the intraventricular velocity streamlines colored by velocity magnitude during peak systole. Due to restricted PML motion, the pre-clip model displayed a posteriorly directed regurgitant jet in the P1 region, which qualitatively and quantitatively matched the regurgitant jet measured clinically (Caballero et al., 2019a). The overall regurgitant jet direction was similar between pre- and post-clip states, with an eccentric "wall-hugging" jet that impinged the postero-lateral LA wall. The strength and velocity of the jet, however, decreased following MitraClip (**Table 2**). Moreover, when a double clip + ring was implanted, a second small regurgitant jet structure was visible in the postero-medial MA region, which supports the finding of the highest RV_{MV} between all post-clip models (**Table 2**).

Finally, **Figure 5** shows the velocity streamlines during peak diastole. Marked differences in the inflow flow structure and magnitude were observed pre- and post-clip, as well as between the different clip/ring configurations. Clip implantation significantly altered the intraventricular hemodynamics by creating a multiple-jet flow due to the double-orifice MV for the lateral and central clip models, and the triple-orifice MV for the double clip models. Moreover, the post-clip jets were not oriented toward the apex, but toward the LV wall where they impinged, leading to higher near-wall velocities than the pre-clip state, especially for the clip models with a ring. As shown

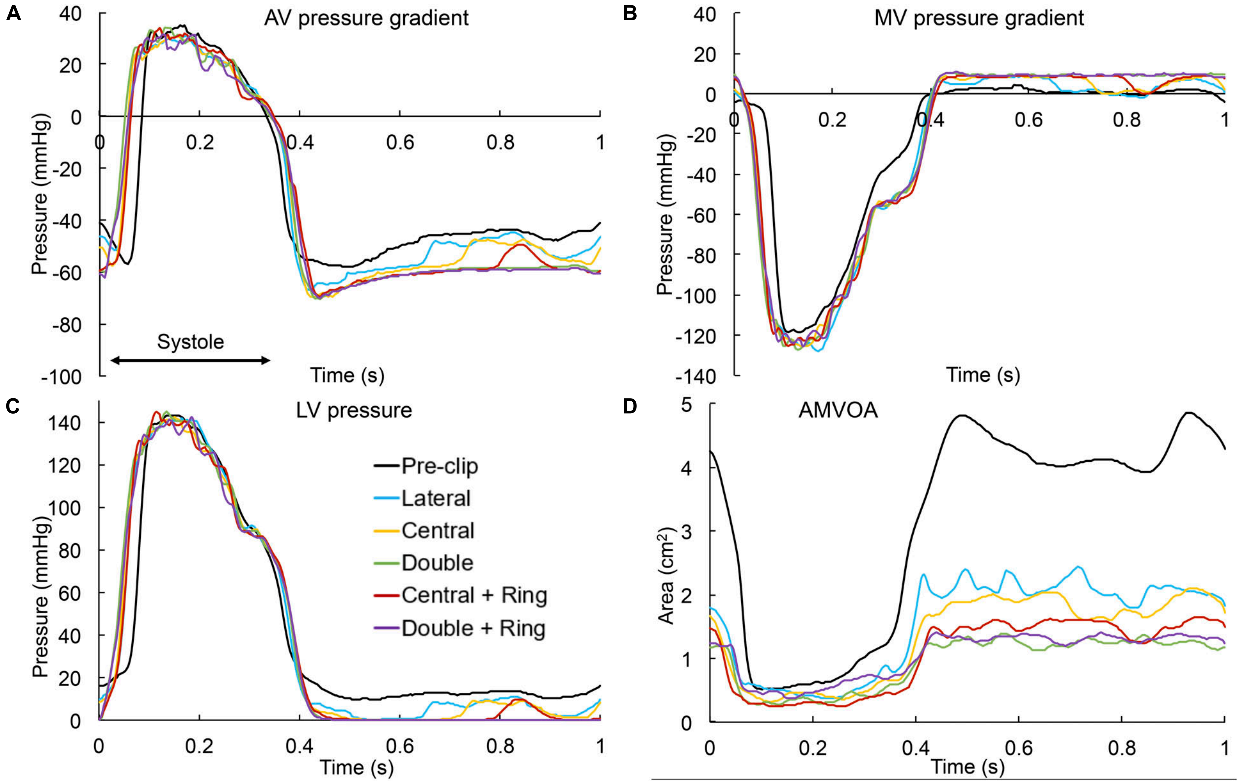

FIGURE 3 | (A) AV pressure gradient, **(B)** MV pressure gradient, **(C)** LV pressure, and **(D)** AMVOA throughout the cardiac cycle.

in **Table 2**, due to the reduced EOA_{MV}, the inflow jets had much higher velocities than the central jet observed before clip implantation.

MitraClip Impact on Tissue Mechanics

Table 3 and **Figure 6A** present the average stress in the mitral leaflets during peak systole. From **Figure 6A** it can be seen that both AML and PML were subjected to a higher systolic stress after the procedure. This increase in leaflet stress was significant (>50%) in the PML for all post-clip models except when using a central clip. Additionally, **Figure 7** shows the stress distribution across the MV leaflets at peak systole. Before clip implantation, peak stresses in the AML were located at the right and left trigones, while peak stresses for the PML were distributed along the MA region and close to the basal chordae insertion regions. Following clip attachment, areas of high stress concentration were relocated near the clip arms for all MitraClip configurations, and extended above the leaflet portion grasped by the clip arms toward the annular region. Repaired-induced leaflet stresses in areas remote from the devices were not significant.

Figure 6B presents the chordae tension during peak systole. Since this patient had a postero-lateral regurgitant gap with PML tethering, it can be seen that the pre- and post-clip models experienced a significantly higher total PML chordae tension when compared to AML chordae tension. After MitraClip, the chordae attached to the AML were subjected to a lower tension compared to the pre-clip model, while PML chordae were under a higher tension. These differences were significant (>50%) when two clips were implanted, with or without ring.

Regarding the diastolic phase, **Table 4** and **Figure 6C** show a significant increase (>50%) in AML and PML average stress for all post-clip models. Moreover, the central clip + ring model gave the lowest increase in leaflet stress, while the double clip model gave the highest increase. As seen in **Figure 8**, similar stress distribution patterns were observed in the MV leaflets for all post-clip models during diastole. In the AML, peak stresses relocated near the clip arms and along strut and marginal chordae insertion regions. In the PML, peak stresses extended from the free edge at the level of the clip arms toward the P2 annular region, close to the insertion of the basal chordae.

In regard to diastolic chordae forces, **Figure 6D** shows that although AML and PML chordae tension had a tendency to increase after the procedure, these changes we only important (>30%) for the double clip models. When comparing systolic and diastolic chordae forces (**Figures 6B,D**) between each pre- and post-clip model, we observed a higher chordae tension during diastole, which could be attributed to the diastolic restriction of the mitral leaflets caused by PM relocation and LV dilatation.

Finally, **Figure 3D** shows the AMVOA throughout the cardiac cycle. During systole, the AMVOA markedly decreased (>28%) from 0.51 cm^2 pre-clip up to 0.25 cm^2 after MV repair, with the highest reduction (52%) obtained for the central clip + ring model (**Table 3**). During diastole, the AMVOA decreased significantly (>50%) for all post-clip models, with the highest

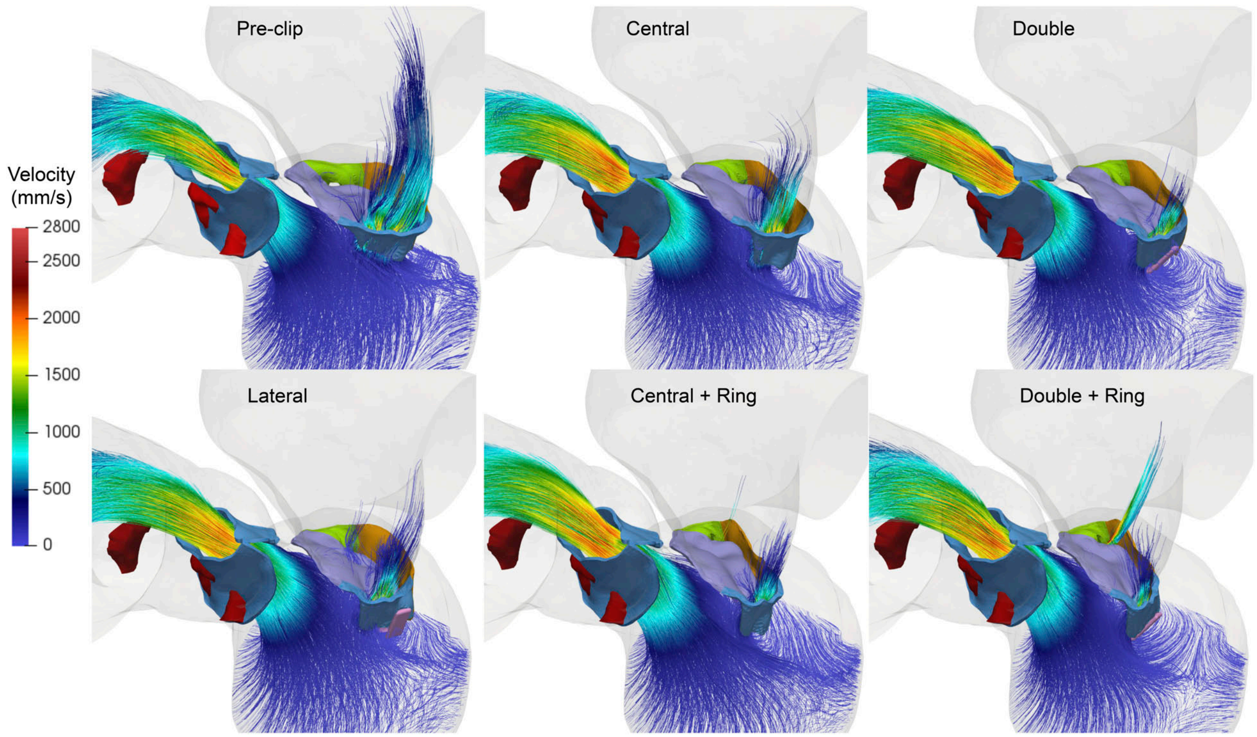

FIGURE 4 | Pre- and post-clip velocity showing the regurgitant jet structures during peak systole.

reduction (71%) quantified for the double clip models (**Table 4**). Furthermore, as seen in **Figure 3D**, the pre-clip double-peaked AMVOA curve waveform changed to a flat curve post-clip, similarly as the MV inflow curves seen **Figure 2B**.

DISCUSSION

The results of this first-in-human experience with patient-specific computer simulations of MitraClip under functional MR can be summarized as follows: First, MitraClip induced acute morphologic changes in the mitral apparatus. Clip implantation resulted in a marked decrease of the AP distance by up to 28%, together with a small increase of the AL-PM. Consequently, there was a significant reduction of the ASI by up to 39%, together with a non-significant decrease in the AHCWR and MA area, suggesting that MitraClip leads to a more elliptical and planar MA. Second, the immediate reduction in the RV_{MV} achieved by MitraClip resulted in an acute increase in the forward flow (>23%), a decrease in preload, and overall improved hemodynamic profile. For this patient case, while implanting a central clip + ring resulted in the highest MR reduction (46%), this configuration also led to mitral stenosis (MS) by increasing the MDPG to 7.47 mmHg. Third, the MV leaflets were subjected to a higher loading state throughout the cardiac cycle after the procedure, with a significant increase in the diastolic leaflet average stress by up to 210 and 145% for the AML and PML, respectively. All post-clip models resulted in a concentrated high stress pattern at the region of clip grasp. Fourth, MitraClip was accompanied by the reduction of the anatomic opening area by up to 71% for the double clip models, while the anatomic regurgitant area decreased by up to 52% for the central clip + ring model, resulting in improved but incomplete MV coaptation. Finally, MitraClip altered the temporal course of the MV inflow and AMVOA diastolic waveforms from double-peaked to more flattened curves.

Effects on MV Geometry

The acute effects of MitraClip on MV geometry under functional MR have been investigated in a few clinical studies using echo (Schmidt et al., 2013; Schueler et al., 2014; Noack et al., 2019b). Similar to these investigations, we found a marked reduction of the AP distance together with a relatively small increase of the AL-PM distance, especially when a ring was added (**Table 1**). These changes were accompanied by comparable changes in the CC distance pre- and post-clip (Donmez et al., 2019), and by a non-significant reduction in the MA area, as found in previous studies (Mantegazza et al., 2018; Noack et al., 2019b). Some studies, however, quantified a significant decrease of the MA area after MitraClip (Schmidt et al., 2013; Schueler et al., 2014). Nonetheless, this decrease in MA area appears to be secondary to reduced AP distance after the procedure. Our results suggest that reshaping of the MA with a significant reduction of the AP distance contributes to a reduction of MR after MitraClip, which might be an indicator of clinical benefit (Schueler et al., 2014; Patzelt et al., 2017; Schueler et al., 2017). As a whole, it appears that MitraClip limits MV further dilation by exerting traction on

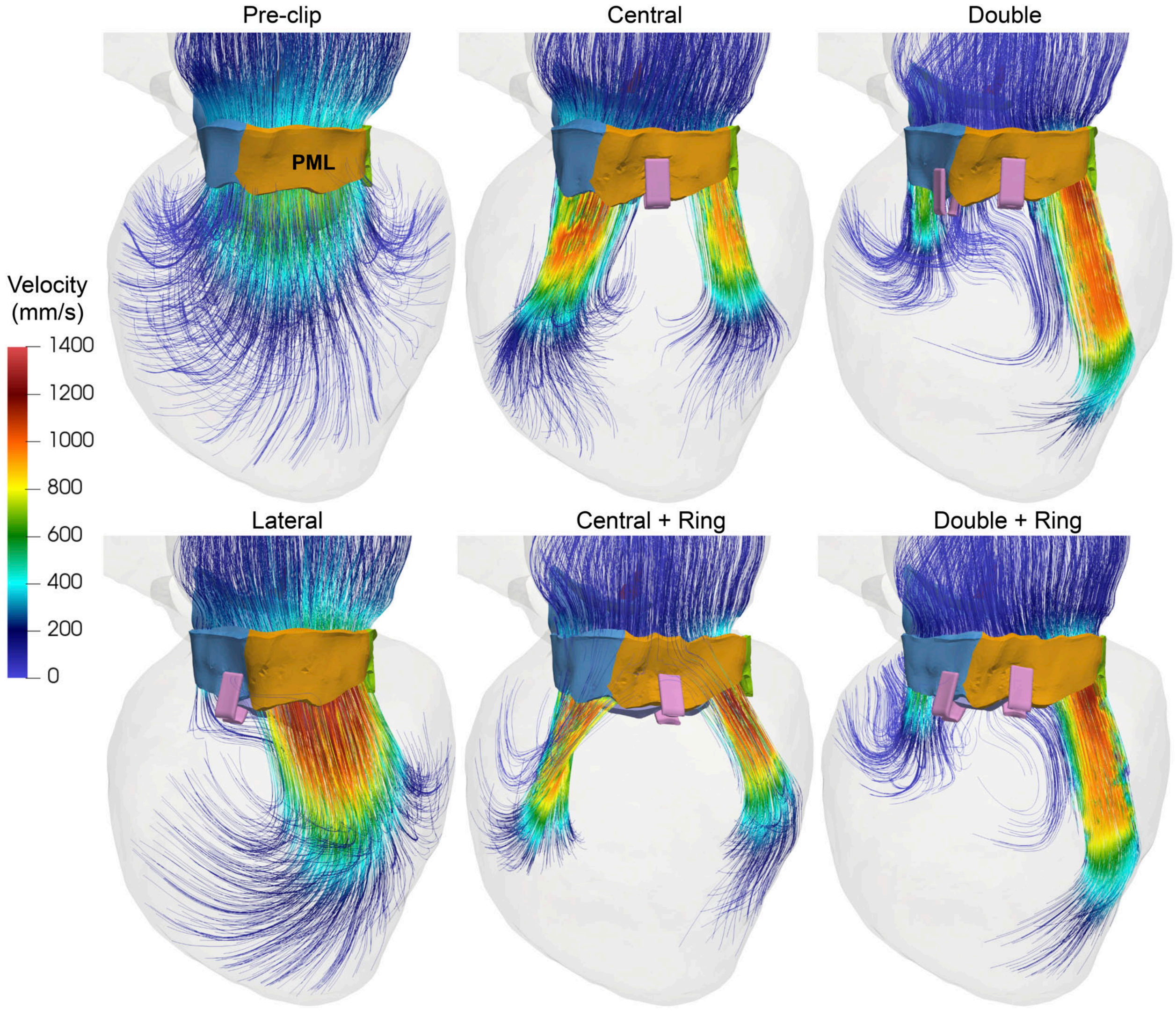

FIGURE 5 | Pre- and post-clip velocity showing the intraventricular blood flow during peak diastole.

the MA (Mantegazza et al., 2018); mainly in the antero-posterior direction. The small changes in the CC distance can be explained by the presence of the aortic-mitral continuity and the fibrous trigones, which is a region less prone to large deformations than the posterior MA, which is mainly muscular and more susceptible to dilation (McCarthy et al., 2010).

The decrease of the AP distance together with the increase in the AL-PM distance resulted in a significant reduction of the ASI in the central and double clip models, which confirms the reshaping of the MA from a rounder to a more oval shape. The reduction in the MA sphericity has been quantified in patients with functional MR undergoing surgical MV repair with annuloplasty ring (Mahmood et al., 2010). AHCWR and aortic-mitral distance also had a tendency to decrease after MitraClip, but these changes were comparable pre- and post-clip. The AHCWR is a measure of the MA non-planarity and describes its 3D shape. Our results suggest a flatter MA post-clip, which can be related with the increased LV pressure and the more elliptical MA (Jimenez et al., 2006; Warraich et al., 2012). Overall, these geometric findings might be of interest for future biomechanical studies to determine independent anatomic features that can be correlated to sustained procedural success.

Effects on MV Tissue Mechanics

MV leaflet stress increased throughout the cardiac cycle after MitraClip, especially in the vicinity of clip insertion (Zhang et al., 2019). More importantly, this increase was significant (50–210%) in all post-clip models during diastole (**Table 4** and **Figure 6C**). These results are congruent with the findings from Lau et al. (2011) that showed that during diastole the MV leaflet stress can be up to 200% higher after MitraClip when treating MA dilatation. This important local increase in leaflet peak stress could be a key factor in triggering mitral leaflet remodeling after MitraClip. *In vitro* studies have shown that increased leaflet stress

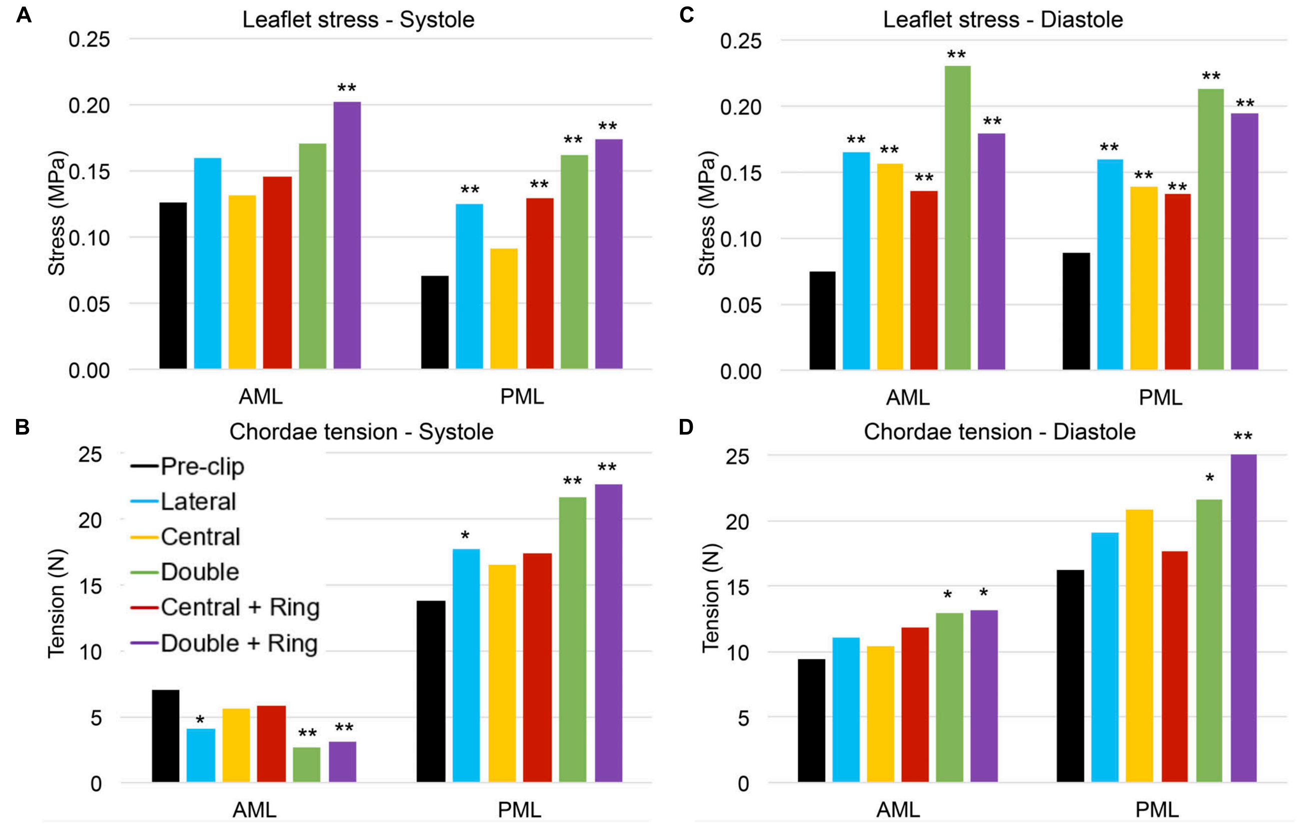

FIGURE 6 | (A) Average MV leaflet stress during peak systole, **(B)** Chordae tension during peak systole, **(C)** Average MV leaflet stress during peak diastole, and **(D)** Chordae tension during peak diastole. ** highlight a 50% increase/decrease with respect to the pre-clip model, and * highlight a 30% increase/decrease with respect to the pre-clip model.

can alter proteoglycan and collagen synthesis, resulting in leaflet thickening with an increased compliance (Quick et al., 1997; Kunzelman et al., 1998). Moreover, under *in vivo* conditions the MitraClip has been reported to gradually be encapsulated by connective tissue, have thicker fibrous capsules, and incite a fibrous reaction that results in the formation of a tissue bridge within the clip arms (Ladich et al., 2011).

Although AML and PML had comparable stress values for each post-clip model during diastole (**Table 4** and **Figure 6C**), the leaflets were subjected to abnormal stresses up to 52% higher with respect to the systolic phase (**Figure 6A**). For the clip models with ring, however, the leaflets were subjected to comparable stress values during systole and diastole. Thus, the use of an annuloplasty ring in combination with MitraClip appears to induce a more homogeneous stress state in the leaflets throughout the cardiac cycle. This key finding can have an important impact upon transcatheter MV repair techniques and their durability, whereby MitraClip is the only repair procedure currently performed.

Effects on Anatomic MV Orifice Area

We report, to our knowledge, the first set of time-dependent AMVOA measurements pre- and post-clip under different clipping configurations and combined annuloplasty procedures (**Figure 3D**). The computer-based approach implemented herein allowed us to directly quantify the true MV orifice area at the level of the leaflet free edge with high reproducibility and accuracy. Clinically, this parameter could be assumed to represent an invasive measurement using catheterization or the “ground truth.” Nevertheless, for better comparability with clinical data, we also quantified the EOA_{MV} and EROA by using the mathematical formulation that relates the pressure drop across the valve and the flow rate (Chandran et al., 2012; Saikrishnan et al., 2014). We measured a reduction in the EOA_{MV} and EROA after MitraClip by up to 68 and 52%, respectively (**Table 2**). Congruent with our results, a recent 3D TEE study by Noack et al. (2019b) found that the EOA_{MV} and EROA decreased by up to 65 and 67%, respectively. Previous works have shown a decrease in the EOA_{MV} of ~53% after the procedure (Altiok et al., 2012; Biaggi et al., 2013). In these studies, the EOA_{MV} was calculated with 3D planimetry in the proximity of the commissures, which can lead to an overestimation of the post-clip EOA_{MV}. This could help to explain the larger decrease in EOA_{MV} quantified in our study.

Clinical assessment of the continuous MV orifice area during MitraClip is technical challenging due to the 3D dynamic MV orifice, the limited capacity for echo measurement of areas below 0.5 cm^2, and the different TEE and Doppler-derived

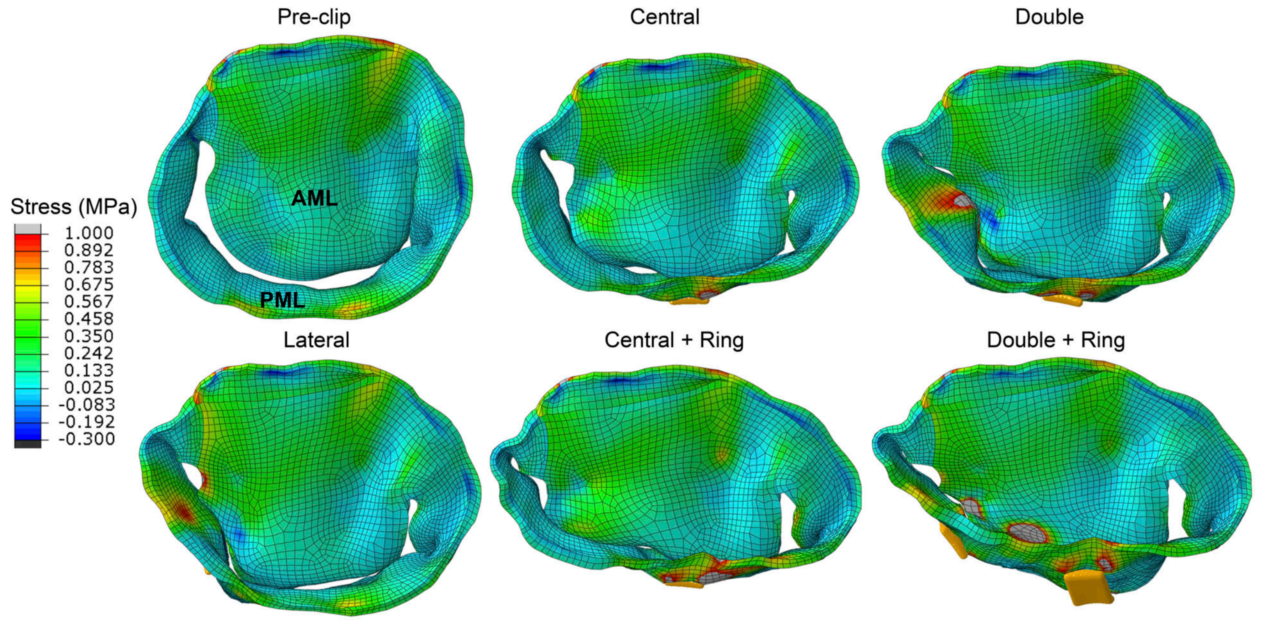

FIGURE 7 | Stress distribution on the MV leaflets during peak systole.

measurement techniques (Biaggi et al., 2013). When comparing our AMVOA values (**Tables 3**, **4**) with the EOA_{MV} and EROA values (**Table 2**), we observed the same trend toward a decrease of the MV opening and regurgitant orifice areas after MitraClip. However, we also quantified that overall, the echo-based method (EOA_{MV} and EROA) underestimates the true MV orifice (AMVOA) (Biaggi et al., 2013), especially the regurgitant orifice area, with an error up to 24% for the double clip + ring model. Interestingly, out study also showed that MitraClip therapy altered the temporal MV leaflet kinematics, especially during diastole. A seen in **Figure 3D**, before MitraClip, a twin-peaked AMVOA curve was quantified, which can be explained by early MV inflow (E wave) followed by atrial contraction (A wave). After clip implantation, the double-peaked AMVOA curve changed to a more flattened curve as more clips were implanted. Although some clinical studies have detected this diastolic flattening of the AMVOA curve, it was suggested this was caused by the prevalence of atrial fibrillation in the patients studied (Noack et al., 2019a). But unlike previous reports, we prescribed the same LA wall motion pre- and post-clip in our virtual patient-specific model. Thus, we hypothesize these diastolic changes in the profile of the AMVOA and MV inflow curves post-clip are related to the MS caused by the narrower and multiple-orifice MV.

Effects on Blood Flow Dynamics

Impact on Residual MR

The most important clinical hemodynamic parameters that determine MitraClip procedural success are residual MR and transmitral pressure gradient (MDPG). Even moderate MR after the procedure has been associated with increased mortality (Buzzatti et al., 2016), particularly in patients with impaired LV function and heart failure (Cheng et al., 2017). Indeed, residual MR is presented as one of the main drivers for worse patient outcome in the MITRA−FR trial, compared with the COAPT trial, with 50% residual MR ≥ 2 in MITRA−FR, and 31% residual MR ≥ 2 in COAPT after 1 year (Obadia et al., 2018; Stone et al., 2018). After MitraClip, all our post-procedure models decreased MR severity to moderate (**Table 2**). This finding of moderate MR would be considered a suboptimal clinical outcome (Paranskaya et al., 2013), leading to the consideration to deploy additional clips. As a general guideline, additional clips should not be placed if the patient has a mean MDPG $\geq$ 4 mmHg (Singh et al., 2015), which was the case for all our post-clip models. Regardless of whether 1 or more clips are deployed, current clinical MR assessment relies heavily on echo evaluation by integrating multiple parameters (Stone et al., 2015; Zoghbi et al., 2017; Mao et al., 2020), some of which are not validated in the specific MitraClip clinical scenario, are limited by operator dependence, or are difficult to obtain with TEE imaging (Krieger et al., 2016; Palmiero et al., 2017; Corrigan et al., 2018; Dietl et al., 2018).

Despite the reassuring data on efficacy and long-term durability of MitraClip, the proportion of patients with residual MR after therapy is not negligible. In light of the detrimental prognostic impact of MR, there is a high clinical interest in combining or sequentially staging transcatheter approaches to eliminate MR. Combined percutaneous therapies can be performed together at the time of initial treatment, or they can be staged for the treatment of persistent or recurrent MR (Rogers et al., 2018). For example, Latib et al. (2016) reported initially using 2 clips in a patient with functional MR, followed by staged CardioBand (Edwards Lifesciences, Irvine, CA, United States) transcatheter annuloplasty for persistent MR. In our study, the greatest degree of MR improvement was found for the central clip model followed by annuloplasty. From surgical experience, we

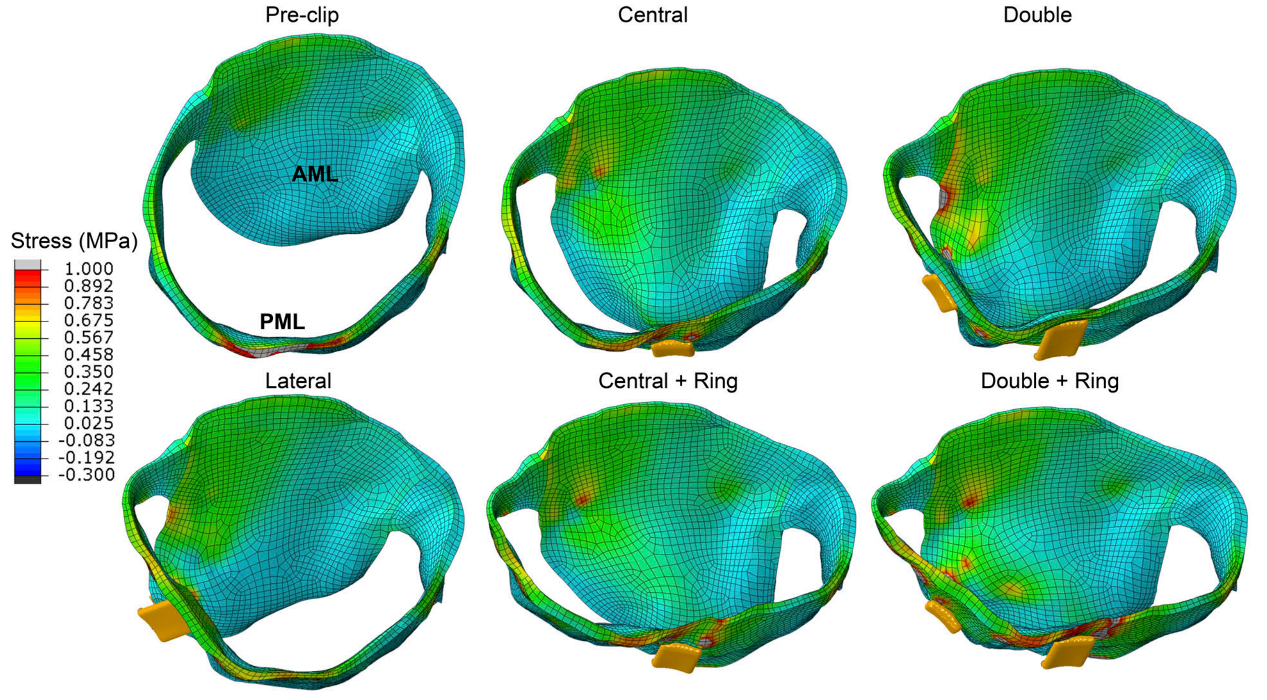

FIGURE 8 | Stress distribution on the MV leaflets during peak diastole.

know that annuloplasty as a part of MV repair stabilizes the MA and improves long-term results. In the near future and with the rapidly expanding arena of catheter-based technologies for MV repair, the combined application of multiple devices will increase the therapeutic arsenal, optimize results, and expand the pool of treatable patients to include those with multiple mechanistic etiologies of MR.

Impact on MV Diastolic Pressure Gradient

The benefit from MR reduction can be counterbalanced by the formation of MS, which is associated with the creation of a multiple-orifice MV (Herrmann et al., 2006; Boerlage-van Dijk et al., 2014). The abrupt change of a hemodynamic status from an elevated preload caused by MR, to an elevated after load caused by MS and the decrease of the low-impedance regurgitant flow into the LA can have a major impact on procedural outcomes. A recent study by Neuss and colleagues (Neuss et al., 2017) found that MS after MitraClip has a negative impact on long-term clinical outcomes. A cutoff value was found at 5 mmHg for invasively and 4.4 mmHg for echo measured MDPG. Based on the invasively threshold value, implantation of central and double clips, with or without ring, caused MS in our virtual patient models. In clinical practice, the pressure drop across the MV during MitraClip is usually calculated using the simplified Bernoulli equation and the maximum velocity measured by TEE or Doppler-derived echo (Bach, 2010; Zoghbi et al., 2009). Echo measurements are operator dependent and strongly influenced by LV function, LA compliance, and loading conditions (Kang et al., 2013). In addition, some Doppler methods have not been adequately validated in a multiple-orifice MV (Kar and Sharma, 2015). Considering these limitations, evaluation of directly measured hemodynamic parameters pre- and post-clip should be included to support decision making (Mao et al., 2020). In our study, all hemodynamic variables, including the MDPG and residual MR were quantified accurately and objectively using the pressure and velocity fields obtained from the simulation algorithms.

Impact on Intraventricular Hemodynamics

This study detected potentially harmful changes in the LV blood flow dynamics. While lateral clipping demonstrated a diastolic flow field closest to that of the pre-clip state, multiple diastolic jets were formed when central and double clips were implanted. The peak velocities across the MV were strongly affected by this multiple—orifice configuration (**Table 2**). From **Figure 5** it is clear that the jets impinged the LV wall with a deeper penetration as they were deviated laterally due to the reduction in the MV orifice area. Moreover, the inflow velocities, trans-mitral pressure gradients, and jet deflection angle further increased when a ring was added. This deflection can compromise the fluid mechanics such as rapid dissipation of the large anterior vortex (Hu et al., 2010; Jeyhani et al., 2018), and a higher energy loss (Hu et al., 2010; Du et al., 2014). Although previous computer and *in vitro* studies have provided initial insights on the LV flow after MitraClip (Redaelli et al., 2001; Shi and He, 2009), simplified models that considered idealized LV and MV geometries were used. An improved understanding of human host-MitraClip hemodynamics using patient-specific FSI models may help to optimize device placement. We are currently working on performing a quantitative analysis of the intraventricular

TABLE 3 | Pre- and post-clip MV biomechanics during peak systole.

	Pre-clip	Lateral	Central	Double	Central + Ring	Double + Ring
S_I^{AVRG} (MPa)						
AML	0.126	0.159 (26)	0.131 (5)	0.170 (35)	0.145 (16)	0.202 (61)
PML	0.071	0.125 (76)	0.091 (28)	0.162 (128)	0.129 (82)	0.174 (145)
$F_{chordae}$ (N)						
AML	7.04	4.07 (−42)	5.59 (−21)	2.66 (−62)	5.88 (−16)	3.16 (−55)
PML	13.79	17.71 (28)	16.50 (20)	21.62 (57)	17.36 (26)	22.62 (64)
AMOVA - Regurgitant orifice area (cm^2)	0.51	0.37 (−29)	0.32 (−38)	0.27 (−47)	0.25 (−52)	0.37 (−28)

Percentage variations (%) with respect to the pre-clip model are reported in parenthesis.

TABLE 4 | Pre- and post-clip MV biomechanics during peak diastole.

	Pre-clip	Lateral	Central	Double	Central + Ring	Double + Ring
S_I^{AVRG} (MPa)						
AML	0.074	0.165 (122)	0.156 (110)	0.230 (210)	0.135 (82)	0.179 (142)
PML	0.088	0.159 (80)	0.139 (57)	0.213 (141)	0.133 (50)	0.195 (120)
$F_{chordae}$ (N)						
AML	9.43	11.04 (17)	10.42 (11)	12.99 (38)	11.85 (26)	13.17 (40)
PML	16.25	19.06 (17)	20.92 (29)	21.65 (33)	17.63 (8)	27.81 (71)
AMVOA – Opening orifice area (cm^2)	4.85	2.46 (−49)	2.11 (−56)	1.4 (−71)	1.66 (−66)	1.42 (−71)

Percentage variations (%) with respect to the pre-clip model are reported in parenthesis.

energetic parameters associated with maladaptive changes and LV reshaping in these FSI models (Cimino et al., 2017; Filomena et al., 2019).

Clinical Implications

In daily MitraClip routine, the interventional team has to face several difficult situations from a decision-making standpoint: What should be done in case of residual MR?, what should be done in case of MR reduction, but a significant increase in the MDPG?, what is an acceptable compromise between these two parameters when implanting multiple clips? The answers to these questions are not always clear, suggesting that procedural assessment should be performed in a more integrated way. For example, real-time monitoring of LA pressure during MitraClip has been described as a helpful tool to predict clinical outcomes (Eleid et al., 2015; Horstkotte et al., 2016). Kuwata et al. (2019) demonstrated that an increased LA mean pressure was predictive of worse clinical outcomes at short-term follow-up, independent from echo findings. As intra-procedural decisions have a strong impact on short- and long-term outcomes and prognosis, the clinical message from these clinical studies is extremely relevant for the interventional community: evaluation of MitraClip should shift from a solely echo-based color Doppler assessment to a more hemodynamic-based approach.

To the best of our knowledge, this is the first patient-specific computer-based engineering study to quantify the coupled LH hemodynamics and tissue mechanics pre- and post-clip under different MitraClip/annuloplasty configurations throughout the cardiac cycle in a virtual human beating-heart. FSI modeling tools, as used in this study, are required to directly quantify the RV_{MV}, accurately simulate full dynamic AV-MV dynamics (Lau et al., 2010; Mao et al., 2016b), and shift the conventional MitraClip paradigm from a solely anatomic assessment, toward a more functional and physiologic approach based on objective biomechanical data. Much needed clinically relevant flow indicators can be obtained by applying the computer modeling framework herein proposed for the personalized assessment of MitraClip therapy, as well as to gain insight into the different clinical scenarios and implantation criteria currently critical for this procedure. Moreover, this modeling methodology could be easily applied to other structural MV interventions and newer device designs.

Limitations

The present study has several limitations. The main one is its small sample size. This work only used one previously validated patient-specific LH model with heart failure and functional MR (Caballero et al., 2019a), therefore no general statements can be made. A large cohort of patient-specific LH models under different MR conditions and MitraClip configurations would be necessary to draw conclusions with confidence. Second, simulations results were not validated against post-procedural clinical data, since the patient studied herein did not undergo a real MitraClip treatment. Nevertheless, this study allowed for a systematic investigation of various biomechanical scenarios resulting from combined MitraClip/annuloplasty procedures. Such well-controlled side-by-side comparisons under the same patient and loading conditions are challenging to obtain in a clinical setting. Third, annuloplasty procedures were simplified as nodal displacement boundary conditions on the MA, and the ring geometry was based on a surgical device. Fourth, some of the pressure and flow fluctuations seen in **Figures 2**, **3** after MitraClip implantation are thought to be caused by small numerical artifacts in the FSI simulations. Due to the use of prescribed cardiac wall motion and the assumption of incompressible fluid, a small compression in volume for a closed system can cause large changes in pressure and velocity. These fluctuations, however, damped out rapidly due to the viscous effect of the fluid. This numerical artifact could be resolved by including the shock-absorbing effect of the myocardium, and modeling its interaction with the blood considering active contraction. This is the subject of a study that we are currently undertaking. Finally, although cardiac tissue properties were age- and gender-matched, they were not patient-specific. Estimation of *in vivo* material parameters inversely from medical images would be ideal to produce more accurate predictive results (Liu et al., 2017).

CONCLUSION

Percutaneous MV repair using MitraClip has been established as an option for heart failure patients with functional MR who failed medical therapy. Feasibility and safety of MitraClip has been largely described in a variety of clinical trials and case-reports. Results concerning efficacy and durability, however, are not entirely satisfactory. Additionally, results tend to be less impressive immediately after the procedure compared to surgical MV repair. In this era of booming technology, the collaboration between industry and academia is of utmost importance in order to bring further advancements in the field of percutaneous treatment of MV disease. The objective of this study was to evaluate the acute LH hemodynamic, structural and morphologic changes after MitraClip/annuloplasty therapies. Although this patient-specific computer study provided further evidence to support that MitraClip is a viable approach to treat functional MR by reducing regurgitation severity and improving LV systolic function, clip implantation also imposed a non-physiologic configuration and loading on the LV-valve complex, especially during diastole. Comprehensive personalized engineering analyses, as performed in this study, can be a powerful and versatile tool that can pinpoint specific biomechanical implications and potentially play an important role in elucidating the optimal setting and efficacy of percutaneous MV repair procedures.

DATA AVAILABILITY STATEMENT

All datasets generated for this study are included in the article/**Supplementary Material**.

ETHICS STATEMENT

The studies involving human participants were reviewed and approved by Institutional Review Board of the Hartford Hospital. Written informed consent for participation was not required for this study in accordance with the national legislation and the institutional requirements.

AUTHOR CONTRIBUTIONS

AC and WS contributed to the conceptualization and project administration. AC contributed to the formal analysis, the methodology, the visualization, and the writing of the original draft. AC, WM, and WS contributed to the investigation. RM, RH, and WS contributed to the resources. WS contributed to the supervision. AC, WM, RM, RH, and WS contributed to the review and editing of the manuscript.

FUNDING

AC was in part supported by a Fulbright-Colciencias Fellowship.

ACKNOWLEDGMENTS

We would like to thank Jill J. Cloutier for her support in data collection. Special thanks to Samantha Kodikara and Brian Barrett for their data analysis support.

SUPPLEMENTARY MATERIAL

The Supplementary Material for this article can be found online at: https://www.frontiersin.org/articles/10.3389/fphys.2020.00432/full#supplementary-material

REFERENCES

Ailawadi, G., Lim, D. S., Mack, M. J., Trento, A., Kar, S., Grayburn, P. A., et al. (2019). One-year outcomes after MitraClip for functional mitral regurgitation. *Circulation* 139, 37–47. doi: 10.1161/CIRCULATIONAHA.119.040735

Altiok, E., Hamada, S., Brehmer, K., Kuhr, K., Reith, S., Becker, M., et al. (2012). Analysis of procedural effects of percutaneous edge-to-edge mitral valve repair by 2D and 3D echocardiography. *Circ. Cardiovasc. Imaging* 5, 748–755. doi: 10.1161/CIRCIMAGING.112.974691

Auricchio, F., Conti, M., De Beule, M., De Santis, G., and Verhegghe, B. (2011). Carotid artery stenting simulation: from patient-specific images to finite element analysis. *Med. Eng. Phys.* 33, 281–289. doi: 10.1016/j.medengphy.2010.10.011

Bach, D. S. (2010). Echo/Doppler evaluation of hemodynamics after aortic valve replacement: principles of interrogation and evaluation of high gradients. *JACC Cardiovasc. Imaging* 3, 296–304. doi: 10.1016/j.jcmg.2009.11.009

Biaggi, P., Felix, C., Gruner, C., Herzog, B. A., Hohlfeld, S., Gaemperli, O., et al. (2013). Assessment of Mitral valve area during Percutaneous mitral valve repair using the mitraclip system comparison of different echocardiographic methods. *Circ. Cardiovasc. Imaging* 6, 1032–1040. doi: 10.1161/Circimaging.113.000620

Boerlage-van Dijk, K., Van Riel, A. C., de Bruin-Bon, R. H., Wiegerinck, E. M., Koch, K. T., Vis, M. M., et al. (2014). Mitral inflow patterns after MitraClip implantation at rest and during exercise. *J. Am. Soc. Echocardiogr.* 27, 24–31. doi: 10.1016/j.echo.2013.09.007

Borghetti, V., Campana, M., Scotti, C., Domenighini, D., Totaro, P., Coletti, G., et al. (2000). Biological versus prosthetic ring in mitral-valve repair: enhancement of mitral annulus dynamics and left-ventricular function with pericardial annuloplasty at long term. *Eur. J. Cardiothorac. Surg.* 17, 431–439. doi: 10.1016/s1010-7940(00)00344-4

Buzzatti, N., De Bonis, M., Denti, P., Barili, F., Schiavi, D., Di Giannuario, G., et al. (2016). What is a "good" result after transcatheter mitral repair? Impact of 2+ residual mitral regurgitation. *J. Thorac. Cardiovasc. Surg.* 151, 88–96. doi: 10.1016/j.jtcvs.2015.09.099

Caballero, A., Mao, W., Liang, L., Oshinski, J., Primiano, C., McKay, R., et al. (2017). Modeling left ventricular blood flow using smoothed particle hydrodynamics. *Cardiovasc Eng Techn.* 8, 465–479. doi: 10.1007/s13239-017-0324-z

Caballero, A., Mao, W., McKay, R., Primiano, C., Hashim, S., and Sun, W. (2018). New insights into mitral heart valve prolapse after chordae rupture through fluid–structure interaction computational modeling. *Sci. Rep.* 8:17306. doi: 10.1038/s41598-019-44072-y

Caballero, A., Mao, W., McKay, R., and Sun, W. (2019a). The impact of balloon-expandable transcatheter aortic valve replacement on concomitant mitral regurgitation: a comprehensive computational analysis. *J. R. Soc. Interf.* 16:20190355. doi: 10.1098/rsif.2019.0355

Caballero, A., Mao, W., McKay, R., and Sun, W. (2019b). Transapical mitral valve repair with neochordae implantation: FSI analysis of neochordae number and complexity of leaflet prolapse. *Int. J. Numerical Methods Biomed. Eng.* 2019:e3297. doi: 10.1002/cnm.3297

Caballero, A., Mao, W., McKay, R., and Sun, W. (2020). The impact of self-expandable Transcatheter Aortic valve replacement on concomitant functional mitral regurgitation: a comprehensive engineering analysis*. *Struct. Heart* 1–13. doi: 10.1080/24748706.2020.1740365

Chandran, K. B., Rittgers, S. E., and Yoganathan, A. P. (2012). *Biofluid Mechanics: The Human Circulation*. Boca Raton, FL: CRC press.

Cheng, R., Dawkins, S., Tat, E., Makar, M., Hussaini, A., Makkar, R. R., et al. (2017). Relation of residual mitral regurgitation despite elevated mitral gradients to risk of heart failure hospitalization after MitraClip repair. *Am. J. Cardiol.* 120, 1595–1600. doi: 10.1016/j.amjcard.2017.07.027

Cimino, S., Palombizio, D., Cicogna, F., Cantisani, D., Reali, M., Filomena, D., et al. (2017). Significant increase of flow kinetic energy in "nonresponders" patients to cardiac resynchronization therapy. *Echocardiography* 34, 709–715. doi: 10.1111/echo.13518

Corrigan, F. E. III, Chen, J. H., Maini, A., Lisko, J. C., Alvarez, L., Kamioka, N., et al. (2018). Pulmonary venous waveforms predict rehospitalization and mortality after percutaneous mitral valve repair. *JACC* 12, 1905–1913. doi: 10.1016/j.jcmg.2018.07.014

de Jaegere, P., Rocatello, G., Prendergast, B. D., de Backer, O., Van Mieghem, N. M., and Rajani, R. (2019). Patient-specific computer simulation for transcatheter cardiac interventions: what a clinician needs to know. *Heart* 105(Suppl. 2), s21–s27. doi: 10.1136/heartjnl-2018-313514

Dietl, A., Prieschenk, C., Eckert, F., Birner, C., Luchner, A., Maier, L. S., et al. (2018). 3D vena contracta area after MitraClip© procedure: precise quantification of residual mitral regurgitation and identification of prognostic information. *Cardiovasc. Ultrasound* 16:1. doi: 10.1186/s12947-017-0120-9

Donmez, E., Salcedo, E. E., Quaife, R. A., Burke, J. M., Gill, E. A., and Carroll, J. D. (2019). The acute effects of edge-to-edge percutaneous mitral valve repair on the shape and size of the mitral annulus and its relation to mitral regurgitation. *Echocardiography* 36, 732–741. doi: 10.1111/echo.14284

Du, D., Jiang, S., Wang, Z., Hu, Y., and He, Z. (2014). Effects of suture position on left ventricular fluid mechanics under mitral valve edge-to-edge repair. *Biomed. Mater. Eng.* 24, 155–161. doi: 10.3233/BME-130795

Eleid, M. F., Sanon, S., Reeder, G. S., Suri, R. M., and Rihal, C. S. (2015). Continuous left atrial pressure monitoring during MitraClip: assessing the immediate hemodynamic response. *JACC Cardiovasc. Interv.* 8, e117–e119. doi: 10.1016/j.jcin.2015.02.010

Filomena, D., Cimino, S., Maestrini, V., Cantisani, D., Petronilli, V., Mancone, M., et al. (2019). Changes in intraventricular flow patterns after MitraClip implant in patients with functional severe mitral regurgitation. *J. Am. Soc. Echocardiogr.* 32, 1250–3e1. doi: 10.1016/j.echo.2019.05.022

Goldberg, S. L. (2019). Reflections on percutaneous therapies for secondary mitral regurgitation. *Cardiovasc. Revasc. Med.* 20, 528–529. doi: 10.1016/j.carrev.2019.02.027

Grayburn, P. A., Sannino, A., and Packer, M. (2019). Proportionate and disproportionate functional mitral regurgitation a new conceptual framework that reconciles the results of the MITRA-FR and COAPT trials. *JACC Cardiovasc. Imaging* 12, 353–362. doi: 10.1016/j.jcmg.2018.11.006

Herrmann, H. C., Rohatgi, S., Wasserman, H. S., Block, P., Gray, W., Hamilton, A., et al. (2006). Mitral valve hemodynamic effects of percutaneous edge-to-edge repair with the MitraClip^{TM} device for mitral regurgitation. *Catheter. Cardiovasc. Interv.* 68, 821–828. doi: 10.1002/ccd.20917

Horstkotte, J., Kloeser, C., Beucher, H., Schwarzlaender, E., von Bardeleben, R. S., and Boekstegers, P. (2016). Intraprocedural assessment of mitral regurgitation during the mitraclip procedure: impact of continuous left atrial pressure monitoring. *Catheter. Cardiovasc. Interv.* 88, 1134–1143. doi: 10.1002/ccd.26504

Hu, Y., Shi, L., Parameswaran, S., Smirnov, S., and He, Z. (2010). Left ventricular vortex under Mitral valve edge-to-edge repair. *Cardiovasc. Eng Techn.* 1, 235–243. doi: 10.1007/s13239-010-0022-6

Jeyhani, M., Shahriari, S., and Labrosse, M. (2018). Experimental investigation of left ventricular flow patterns after Percutaneous Edge-to-Edge mitral valve repair. *Artif. Organs* 42, 516–524. doi: 10.1111/aor.13020

Jimenez, J. H., Forbess, J., Croft, L. R., Small, L., He, Z., and Yoganathan, A. P. (2006). Effects of annular size, transmitral pressure, and mitral flow rate on the edge-to-edge repair: an in vitro study. *Ann. Thorac. Surg.* 82, 1362–1368. doi: 10.1016/j.athoracsur.2006.05.008

Kang, W. S., Choi, J. W., Kang, J. E., Chung, J. W., and Kim, S. H. (2013). Determination of mitral valve area with echocardiography, using intra-operative 3-dimensional versus intra- & post-operative pressure half-time technique in mitral valve repair surgery. *J. Cardiothor. Surg.* 8:98. doi: 10.1186/1749-8090-8-98

Kar, S., and Sharma, R. (2015). Current assessment of mitral regurgitation: not making the grade. *J. Am. Coll. Cardiol.* 65, 1089–1091. doi: 10.1016/j.jacc.2015.02.001

Kong, F., Caballero, A., McKay, R., and Sun, W. (2020). Finite element analysis of MitraClip procedure on a patient-specific model with functional mitral regurgitation. *J. Biomech.* 2020:109730. doi: 10.1016/j.jbiomech.2020.109730

Kong, F., Pham, T., Martin, C., Elefteriades, J., McKay, R., Primiano, C., et al. (2018). Finite element analysis of annuloplasty and papillary muscle relocation on a patient-specific mitral regurgitation model. *PLoS One* 13:e0198331. doi: 10.1371/journal.pone.0198331

Krieger, E. V., Lee, J., Branch, K. R., and Hamilton-Craig, C. (2016). Quantitation of mitral regurgitation with cardiac magnetic resonance imaging: a systematic review. *Heart* 102, 1864–1870. doi: 10.1136/heartjnl-2015-309054

Kunzelman, K. S., Quick, D. W., and Cochran, R. P. (1998). Altered collagen concentration in mitral valve leaflets: biochemical and finite element analysis. *Ann. Thorac. Surg.* 66 (6 Suppl), S198–S205. doi: 10.1016/s0003-4975(98)01106-0

Kuwata, S., Taramasso, M., Czopak, A., Luciani, M., Pozzoli, A., Ho, E., et al. (2019). Continuous direct left atrial pressure: intraprocedural measurement predicts clinical response following MitraClip therapy. *JACC Cardiovasc. Interv.* 12, 127–136. doi: 10.1016/j.jcin.2018.07.051

Ladich, E., Michaels, M. B., Jones, R. M., McDermott, E., Coleman, L., Komtebedde, J., et al. (2011). Endovascular Valve Edge-to-Edge Repair Study I. Pathological healing response of explanted MitraClip devices. *Circulation* 123, 1418–1427. doi: 10.1161/CIRCULATIONAHA.110.978130

Latib, A., Ancona, M. B., Ferri, L., Montorfano, M., Mangieri, A., Regazzoli, D., et al. (2016). Percutaneous direct annuloplasty with cardioband to treat recurrent mitral regurgitation after MitraClip implantation. *JACC Cardiovasc. Interv.* 9, e191–e192. doi: 10.1016/j.jcin.2016.06.028

Lau, K., Diaz, V., Scambler, P., and Burriesci, G. (2010). Mitral valve dynamics in structural and fluid–structure interaction models. *Med. Eng. Phys.* 32, 1057–1064. doi: 10.1016/j.medengphy.2010.07.008

Lau, K., Díaz-Zuccarini, V., Scambler, P., and Burriesci, G. (2011). Fluid–structure interaction study of the edge-to-edge repair technique on the mitral valve. *J. Biomech.* 44, 2409–2417. doi: 10.1016/j.jbiomech.2011.06.030

Lim, D. S., Reynolds, M. R., Feldman, T., Kar, S., Herrmann, H. C., Wang, A., et al. (2014). Improved functional status and quality of life in prohibitive surgical risk patients with degenerative mitral regurgitation after transcatheter mitral valve repair. *J. Am. Coll. Cardiol.* 64, 182–192. doi: 10.1016/j.jacc.2013.10.021

Liu, M., Liang, L., and Sun, W. (2017). A new inverse method for estimation of in vivo mechanical properties of the aortic wall. *J. Mech. Behav. Biomed. Mater.* 72, 148–158. doi: 10.1016/j.jmbbm.2017.05.001

Magruder, J. T., Crawford, T. C., Grimm, J. C., Fredi, J. L., and Shah, A. S. (2016). Managing mitral regurgitation: focus on the MitraClip device. *Med. Devices* 9, 53–60. doi: 10.2147/MDER.S86645

Mahmood, F., Gorman, J. H. III, Subramaniam, B., Gorman, R. C., Panzica, P. J., Hagberg, R. C., et al. (2010). Changes in mitral valve annular geometry after repair: saddle-shaped versus flat annuloplasty rings. *Ann. Thorac. Surg.* 90, 1212–1220. doi: 10.1016/j.athoracsur.2010.03.119

Mansi, T., Voigt, I., Georgescu, B., Zheng, X., Mengue, E. A., Hackl, M., et al. (2012). An integrated framework for finite-element modeling of mitral valve biomechanics from medical images: application to MitralClip intervention planning. *Med. Image Anal.* 16, 1330–1346. doi: 10.1016/j.media.2012.05.009

Mantegazza, V., Pasquini, A., Agati, L., Fusini, L., Muratori, M., Gripari, P., et al. (2018). Comprehensive assessment of mitral valve geometry and cardiac remodeling with 3-dimensional echocardiography after Percutaneous Mitral valve repair. *Am. J. Cardiol.* 122, 1195–1203. doi: 10.1016/j.amjcard.2018.06.036

Mao, W., Caballero, A., Hahn, R. T., and Sun, W. (2020). Comparative quantification of primary mitral regurgitation by computer modeling and simulated echocardiography. *Am. J. Physiol. Heart Circ. Physiol.* 318, H547–H557. doi: 10.1152/ajpheart.00367.2019

Mao, W., Caballero, A., McKay, R., Primiano, C., and Sun, W. (2017). Fully-coupled fluid-structure interaction simulation of the aortic and mitral valves in a realistic 3D left ventricle model. *PLoS One* 12:e0184729. doi: 10.1371/journal.pone.0184729

Mao, W. B., Li, K. W., Caballero, A., and Sun, W. (2016a). Fully-Coupled FSI simulation of bioprosthetic heart valve using smoothed particle hydrodynamics. *Cardiology* 134:178. doi: 10.1007/s13239-016-0285-7

Mao, W. B., Li, K., and Sun, W. (2016b). Fluid–structure interaction study of transcatheter aortic valve dynamics using smoothed particle hydrodynamics. *Cardiovasc. Eng. Technol.* 7, 374–388. doi: 10.1007/s13239-016-0285-7

Mauri, L., Foster, E., Glower, D. D., Apruzzese, P., Massaro, J. M., Herrmann, H. C., et al. (2013). 4-year results of a randomized controlled trial of percutaneous repair versus surgery for mitral regurgitation. *J. Am. Coll. Cardiol.* 62, 317–328. doi: 10.1016/j.jacc.2013.04.030

McCarthy, K. P., Ring, L., and Rana, B. S. (2010). Anatomy of the mitral valve: understanding the mitral valve complex in mitral regurgitation. *Eur. J. Echocardiogr.* 11, i3–i9. doi: 10.1093/ejechocard/jeq153

Mokadam, N. A., Stout, K. K., and Verrier, E. D. (2011). Management of acute regurgitation in left-sided cardiac valves. *Tex. Heart Inst. J.* 38, 9–19.

Morgan, A. E., Wozniak, C. J., Gulati, S., Ge, L., Grossi, E. A., Weinsaft, J. W., et al. (2017). Uneven MitraClip application does not increase leaflet stress in a finite element model. *JAMA Surg.* 152:111. doi: 10.1001/jamasurg.2016.3360

Neuss, M., Schau, T., Isotani, A., Pilz, M., Schopp, M., and Butter, C. (2017). Elevated Mitral Valve pressure gradient after MitraClip implantation deteriorates long-term outcome in patients with severe Mitral regurgitation and severe heart failure. *JACC Cardiovasc. Interv.* 10, 931–939. doi: 10.1016/j.jcin.2016.12.280

Noack, T., Janietz, M., Lurz, P., Kiefer, P., Sieg, F., Marin-Cuartas, M., et al. (2019a). Dynamic mitral valve geometry in patients with primary and secondary mitral regurgitation: implications for mitral valve repair. *Eur. J. Cardiothorac. Surg.* 56, 983–992. doi: 10.1093/ejcts/ezz096

Noack, T., Kiefer, P., Mallon, L., Lurz, P., Bevilacqua, C., Banusch, J., et al. (2019b). Changes in dynamic mitral valve geometry during Percutaneous edge–edge mitral valve repair with the MitraClip system. *J. Echocardiogr.* 17, 84–94. doi: 10.1007/s12574-018-0398-0

Obadia, J. F., Messika-Zeitoun, D., Leurent, G., Iung, B., Bonnet, G., Piriou, N., et al. (2018). Percutaneous repair or medical treatment for secondary mitral regurgitation. *N. Engl. J. Med.* 379, 2297–2306. doi: 10.1056/NEJMoa1805374

Palmiero, G., Ascione, L., Briguori, C., Carlomagno, G., Sordelli, C., Ascione, R., et al. (2017). The mitral-to-aortic flow-velocity integral ratio in the real world echocardiographic evaluation of functional mitral regurgitation before and after percutaneous repair. *J. Interv. Cardiol.* 30, 368–373. doi: 10.1111/joic.12401

Paranskaya, L., D'Ancona, G., Bozdag-Turan, I., Akin, I., Kische, S., Turan, G. R., et al. (2013). Residual mitral valve regurgitation after percutaneous mitral valve repair with the mitraclip® system is a risk factor for adverse one-year outcome. *Catheter. Cardiovasc. Interv.* 81, 609–617. doi: 10.1002/ccd.24586

Patzelt, J., Zhang, Y., Magunia, H., Ulrich, M., Jorbenadze, R., Droppa, M., et al. (2017). Improved mitral valve coaptation and reduced mitral valve annular size after percutaneous mitral valve repair (PMVR) using the MitraClip system. *Eur. Heart J. Cardiovasc. Imaging* 19, 785–791. doi: 10.1093/ehjci/jex173

Pham, T., Kong, F., Martin, C., Wang, Q., Primiano, C., McKay, R., et al. (2017). Finite element analysis of patient-specific mitral valve with mitral regurgitation. *Cardiovasc. Eng. Technol.* 8, 3–16. doi: 10.1007/s13239-016-0291-9

Prescott, B., Abunassar, C., Baxevanakis, K. P., and Zhao, L. (2019). Computational evaluation of mitral valve repair with MitraClip*.

Quick, D. W., Kunzelman, K. S., Kneebone, J. M., and Cochran, R. P. (1997). Collagen synthesis is upregulated in mitral valves subjected to altered stress. *ASAIO J.* 43, 181–186.

Redaelli, A., Guadagni, G., Fumero, R., Maisano, F., and Alfieri, O. (2001). A computational study of the hemodynamics after "edge-to-edge" mitral valve repair. *J. Biomech. Eng.* 123, 565–570. doi: 10.1115/1.1408938

Rogers, J. H., Boyd, W. D., Smith, T. W. R., Ebner, A. A., and Bolling, S. F. (2018). Combined MitraClip edge-to-edge repair with millipede IRIS Mitral annuloplasty. *JACC Cardiovasc. Interv.* 11, 323–324. doi: 10.1016/j.jcin.2017.11.007

Sacks, M., Drach, A., Lee, C. H., Khalighi, A., Rego, B., Zhang, W., et al. (2019). On the simulation of mitral valve function in health, disease, and treatment. *J. Biomech. Eng.* 141:070804. doi: 10.1115/1.4043552

Saikrishnan, N., Kumar, G., Sawaya, F. J., Lerakis, S., and Yoganathan, A. P. (2014). Accurate assessment of aortic stenosis: a review of diagnostic modalities and hemodynamics. *Circulation* 129, 244–253. doi: 10.1161/CIRCULATIONAHA.113.002310

Schmidt, F. P., von Bardeleben, R. S., Nikolai, P., Jabs, A., Wunderlich, N., Münzel, T., et al. (2013). Immediate effect of the MitraClip® procedure on mitral ring geometry in primary and secondary mitral regurgitation. *Eur. Heart J. Cardiovasc. Imaging* 14, 851–857. doi: 10.1093/ehjci/jes293

Schueler, R., Kaplan, S., Melzer, C., Ozturk, C., Weber, M., Sinning, J. M., et al. (2017). Impact of interventional edge-to-edge repair on mitral valve geometry. *Int. J. Cardiol.* 230, 468–475. doi: 10.1016/j.ijcard.2016.12.081

Schueler, R., Momcilovic, D., Weber, M., Welz, A., Werner, N., Mueller, C., et al. (2014). Acute changes of mitral valve geometry during interventional edge-to-edge repair with the MitraClip system are associated with midterm outcomes in patients with functional valve disease: preliminary results from a prospective single-center study. *Circ. Cardiovasc. Interv.* 7, 390–399. doi: 10.1161/CIRCINTERVENTIONS.113.001098

Shi, L., and He, Z. (2009). Hemodynamics of the mitral valve under edge-to-edge repair: an in vitro steady flow study. *J. Biomech. Eng.* 131:51010. doi: 10.1115/1.3118772

Singh, G. D., Smith, T. W., and Rogers, J. H. (2015). Multi-M itra C lip therapy for severe degenerative mitral regurgitation:"Anchor" technique for extremely flail segments. *Catheter. Cardiovasc. Interv.* 86, 339–346. doi: 10.1002/ccd.25811

Sorajja, P., Vemulapalli, S., Feldman, T., Mack, M., Holmes, D. R. Jr., Stebbins, A., et al. (2017). Outcomes with transcatheter Mitral valve repair in the United States: an STS/ACC TVT registry report. *J. Am. Coll. Cardiol.* 70, 2315–2327. doi: 10.1016/j.jacc.2017.09.015

Stone, G. W., Lindenfeld, J., Abraham, W. T., Kar, S., Lim, D. S., Mishell, J. M., et al. (2018). Transcatheter mitral-valve repair in patients with heart failure. *N. Engl. J. Med.* 379, 2307–2318. doi: 10.1056/NEJMoa1806640

Stone, G. W., Vahanian, A. S., Adams, D. H., Abraham, W. T., Borer, J. S., Bax, J. J., et al. (2015). Clinical trial design principles and endpoint definitions for Transcatheter Mitral valve repair and replacement: part 1: clinical trial design principles a consensus document from the Mitral Valve Academic Research Consortium. *J. Am. Coll. Cardiol.* 66, 278–307. doi: 10.1016/j.jacc.2015.05.046

Sturla, F., Redaelli, A., Puppini, G., Onorati, F., Faggian, G., and Votta, E. (2015). Functional and biomechanical effects of the Edge-to-Edge Repair in the Setting of Mitral regurgitation: consolidated knowledge and novel tools to gain insight into its Percutaneous implementation. *Cardiovasc. Eng. Technol.* 6, 117–140. doi: 10.1007/s13239-014-0208-4

Sturla, F., Vismara, R., Jaworek, M., Votta, E., Romitelli, P., Pappalardo, O. A., et al. (2017). In vitro and in silico approaches to quantify the effects of the Mitraclip® system on mitral valve function. *J. Biomech.* 50, 83–92. doi: 10.1016/j.jbiomech.2016.11.013

Turyan Medvedovsky, A., Tonchev, I., Tahiroglu, I., Lotan, C., Gilon, D., Planer, D., et al. (2019). MitraClip therapy in critically Ill patients with severe functional mitral regurgitation and refractory heart failure. *Struct. Heart* 2019, 1–6.

Wang, Q., Primiano, C., and Sun, W. (2014). Can isolated annular dilatation cause significant ischemic mitral regurgitation? Another look at the causative mechanisms. *J. Biomech.* 47, 1792–1799. doi: 10.1016/j.jbiomech.2014.03.033

Wang, Q., and Sun, W. (2013). Finite element modeling of mitral valve dynamic deformation using patient-specific multi-slices computed tomography scans. *Ann. Biomed. Eng.* 41, 142–153. doi: 10.1007/s10439-012-0620-6

Warraich, H. J., Chaudary, B., Maslow, A., Panzica, P. J., Pugsley, J., and Mahmood, F. (2012). Mitral annular nonplanarity: correlation between annular height/commissural width ratio and the nonplanarity angle. *J. Cardiothorac. Vasc. Anesth.* 26, 186–190. doi: 10.1053/j.jvca.2011.09.007

Zhang, Y., Wang, V. Y., Morgan, A. E., Kim, J., Handschumacher, M. D., Moskowitz, C. S., et al. (2019). Mechanical effects of MitraClip on leaflet stress and myocardial strain in functional mitral regurgitation–A finite element modeling study. *PLoS One* 14:e0223472. doi: 10.1371/journal.pone.0223472

Zhong, Q., Zeng, W., Huang, X., and Zhao, X. (2014). Finite element analysis for edge-to-edge technique to treat post-mitral valve repair systolic anterior motion. *Acta Bioeng. Biomech.* 16, 3–12.

Zoghbi, W. A., Adams, D., Bonow, R. O., Enriquez-Sarano, M., Foster, E., Grayburn, P. A., et al. (2017). Recommendations for noninvasive evaluation of native valvular regurgitation: a report from the American Society of echocardiography developed in collaboration with the society for cardiovascular Magnetic resonance. *J. Am. Soc. Echocardiogr.* 30, 303–371. doi: 10.1016/j.echo.2017.01.007

Zoghbi, W. A., Chambers, J. B., Dumesnil, J. G., Foster, E., Gottdiener, J. S., Grayburn, P. A., et al. (2009). Recommendations for Evaluation of Prosthetic Valves With Echocardiography and Doppler Ultrasound: a Report From the American Society of Echocardiography's Guidelines and Standards Committee and the Task Force on Prosthetic Valves, Developed in Conjunction With the American College of Cardiology Cardiovascular Imaging Committee, Cardiac Imaging Committee of the American Heart Association, the European Association of Echocardiography, a Registered Branch of the European Society of Cardiology, the Japanese Society of Echocardiography and the Canadian Society of Echocardiography, Endorsed by the American College of Cardiology Foundation, American Heart Association, European Association of Echocardiography, a Registered Branch of the European Society of Cardiology, the Japanese Society of Echocardiography, and Canadian Society of Echocardiography. *J Am Soc Echocardiogr.* 22, 975–1014. doi: 10.1016/j.echo.2009.07.013

Zoghbi, W. A., Enriquez-Sarano, M., Foster, E., Grayburn, P. A., Kraft, C. D., Levine, R. A., et al. (2003). Recommendations for evaluation of the severity of native valvular regurgitation with two-dimensional and Doppler echocardiography. *J. Am. Soc. Echocardiogr* 16, 777–802. doi: 10.1016/S0894-7317(03)00335-3

Conflict of Interest: WS was a co-founder and serves as the Chief Scientific Advisor of Dura Biotech. He receives compensation and owns equity in the company. RH was a speaker for Abbott Vascular, Boston Scientific, Edwards Lifesciences, Philips Healthcare, and on the advisory board/consultant for Edwards Lifesciences, Gore & Associates, Medtronic, and Navigate.

The remaining authors declare that the research was conducted in the absence of any commercial or financial relationships that could be construed as a potential conflict of interest.

frontiers in Physiology

ORIGINAL RESEARCH
published: 05 February 2021
doi: 10.3389/fphys.2021.503687

The Hemodynamic Mechanism of FFR-Guided Coronary Artery Bypass Grafting

Bao Li*[1], *Boyan Mao*[1,2], *Yue Feng*[1,3], *Jincheng Liu*[1], *Zhou Zhao*[4], *Mengyao Duan*[2] and *Youjun Liu*[1]

[1] College of Life Science and Bio-Engineering, Beijing University of Technology, Beijing, China, [2] The School of Life Sciences, Beijing University of Chinese Medicine, Beijing, China, [3] Department of Medical Equipment, Peking University First Hospital, Beijing, China, [4] Cardiac Surgery Department, PeKing University People's Hospital, Beijing, China

Edited by:
Wenchang Tan,
Peking University, China

Reviewed by:
Jacopo Biasetti,
CorWave SA, France
Xiaoyan Deng,
Beihang University, China
Hao Liu,
Chiba University, Japan

****Correspondence:***
Youjun Liu
lyjlma@bjut.edu.cn

Specialty section:
This article was submitted to Computational Physiology and Medicine, a section of the journal Frontiers in Physiology

Received: *09 October 2019*
Accepted: *07 January 2021*
Published: *05 February 2021*

Citation:
Li B, Mao B, Feng Y, Liu J, Zhao Z, Duan M and Liu Y (2021) The Hemodynamic Mechanism of FFR-Guided Coronary Artery Bypass Grafting.
Front. Physiol. 12:503687.
doi: 10.3389/fphys.2021.503687

Clinically, fractional flow reserve (FFR)-guided coronary artery bypass grafting (CABG) is more effective than CABG guided by coronary angiography alone. However, no scholars have explained the mechanism from the perspective of hemodynamics. Two patients were clinically selected; their angiography showed 70% coronary stenosis, and the FFRs were 0.7 (patient 1) and 0.95 (patient 2). The FFR non-invasive computational model of the two patients was constructed by a 0–3D coupled multiscaled model, in order to verify that the model can accurately calculate the FFR results. Virtual bypass surgery was performed on these two stenoses, and a CABG multiscaled model was constructed. The flow rate of the graft and the stenosis coronary artery, as well as the wall shear stress (WSS) and the oscillatory shear index (OSI) in the graft were calculated. The non-invasive calculation results of FFR are 0.67 and 0.91, which are close to the clinical results, which proves that our model is accurate. According to the CABG model, the flow ratios of the stenosis coronary artery to the graft of patient 1 and patient 2 were 0.12 and 0.42, respectively. The time-average wall shear stress (TAWSS) results of patient 1 and patient 2 grafts were 2.09 and 2.16 Pa, respectively, and WSS showed uniform distribution on the grafts. The OSI results of patients 1 and 2 grafts were 0.0375 and 0.1264, respectively, and a significantly high OSI region appeared at the anastomosis of patient 2. The FFR value of the stenosis should be considered when performing bypass surgery. When the stenosis of high FFR values is grafted, a high OSI region is created at the graft, especially at the anastomosis. In the long term, this can cause anastomotic blockage and graft failure.

Keywords: fractional flow reserve, coronary artery bypass grafting, hemodynamics, multiscale model, lumped parameter model

INTRODUCTION

Coronary artery bypass grafting (CABG) is a common surgical procedure for the treatment of myocardial ischemia (Beck, 1935; Vineberg, 1948). The surgeon uses an artery or vein of the patient to anastomose from the aorta to the distal end of the stenosis, so that blood flow can directly supply the distal myocardium through the graft, thereby achieving the purpose of treating myocardial ischemia. The main problem with CABG is the failure of the graft. One of the main reasons for graft failure, aside from technical causes, is that it anastomoses a less severe stenosis (Pellicano et al., 2010). Studies have shown that when the graft is anastomosed to a moderate stenosis, the damage rate is very high (Hanet et al., 1991; Sabik et al., 2003; Berger, 2004).

At present, it is mainly through imaging data, such as coronary angiography, that determines whether the stenosis is serious. However, some researchers used the fluorescent particle method to observe the graft and target coronary artery after CABG, finding that anatomical stenosis does not necessarily result in functional ischemia. A false estimate of the degree of ischemia affects the blood flow of the graft (Ferguson et al., 2013). Therefore, we need to functionally evaluate a stenosis. In this regard, fractional flow reserve (FFR) has been shown to be an effective complement to coronary angiography, which can determine whether coronary stenosis can actually trigger myocardial ischemia (Pijls et al., 1995, Pijls et al., 1996).

FFR has been widely used by cardiologists to guide percutaneous coronary intervention (PCI). But its use to guide CABG is still a very new area of research. Botman et al. (2007) prospectively studied the vascular permeability of 164 patients who underwent CABG 1 year after surgery and found that FFR-guided surgery had a graft failure rate of about one half of that under angiographic guidance. A study by Toth et al. (2013) found that doctors used FFR to guide surgical decisions, using fewer grafts for patients, and the incidence of angina pectoris in patients with FFR-guided CABG was significantly lower than that of the angiographic group after 3 years. In a follow-up study, they also found that CABG under FFR guidance had a significantly lower incidence of cardiovascular events after 6 years than the angiographic guide group (Stephane et al., 2018). The FFR guidelines play an important role in determining whether an angiogram shows moderate stenosis lesions requiring bypass and whether these lesions can affect the long-term effectiveness of grafting (Casselman et al., 2016).

According to the study, hemodynamics is a key factor affecting the permeability of the graft. The failure of the graft is mainly caused by atherosclerosis and intimal hyperplasia (Whittemore et al., 1981; Butany et al., 1998); poor hemodynamic factors are considered to be the most important factors in their occurrence and development (Bassiouny et al., 1992; Hofer et al., 1996). Therefore, it is clear that FFR guides the hemodynamic mechanism behind CABG, which can help to understand why FFR technology can help improve the permeability of graft and lay the foundation for further development of this technology.

MATERIALS AND METHODS

This study is aimed at the moderately sensitive stenosis of FFR; two patients with the same stenosis rate but different FFR values were selected. The 3D model of two patients' coronary artery and bypass grafting were reconstructed to conduct the simulation, respectively. The hemodynamic parameters in the graft of these two patients were obtained by numerical simulation to correctly analyze the hemodynamic mechanism of FFR-guided CABG.

Patient Clinical Data

In this study, two patients with moderate stenosis diagnosed by angiography were selected, and they also underwent invasive FFR. The stenosis of the first patient (patient 1) was located on the left anterior descending branch (LAD), and the stenosis of the second patient (patient 2) was located in the right coronary artery (RCA). Both stenosis diagnoses showed a stenosis rate of 70%. However, patient 1 had an FFR detection of 0.7 and patient 2 had a FFR of 0.95.

At the same time, we also obtained preoperative computed tomography angiography (CTA) data, as well as clinical basic information such as gender, age, heart rate, blood pressure, and cardiac output. Patient specific information is shown in **Table 1**.

Construction of FFR Non-invasive Computing Model

In order to study the hemodynamic effects of FFR on CABG surgery, we first need to construct a 0–3D coupled multi-scaled model with an FFR non-invasive calculation. The FFR non-invasive calculation method used in this study is based on the research results of Taylor et al. (2013), and its accuracy has been fully confirmed.

Using the patient's CTA data, we reconstructed a coronary 3D model of two patients, as shown in **Figure 1**. Mimics 17.0 was used in this study for 3D reconstruction. After the CTA image was imported into the software, the aorta and coronary artery regions were selected by threshold segmentation. The aorta and main coronary arteries could be separated by selecting the appropriate threshold. For small distal coronary arteries, manual adjustment was required. After selecting the desired region, the 3D model of the coronary artery system was reconstructed. When 3D reconstruction of the coronary arteries was completed, the

TABLE 1 | Patient clinical data.

	Gender	Age	Heart rate (times/min)	Blood pressure (mmHg)	Cardiac output (ml/min)	Stenosis rate	FFR
Patient 1	Male	56	77	120/70	4,675.6	70%	0.7
Patient 2	Male	53	62	124/74	5,032.3	70%	0.95

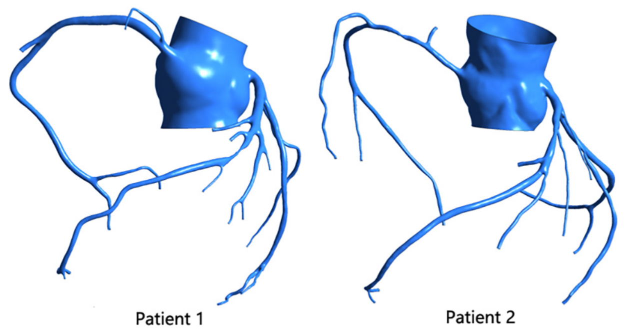

FIGURE 1 | Patient's coronary 3D model.

virtual surgical software Freeform was used to smooth the surface of the model, and then the reconstructed 3D model of the patient was obtained.

The model was meshed by the ANSYS ICEM CFD software. The models were meshed by the tetrahedral mesh method. The drawn mesh passed the grid sensitivity analysis. For the 3D model of the coronary artery, we assumed that the vessel wall was rigid, and the material properties of blood were set as adiabatic, isotropic, and incompressible Newtonian fluids. Its hemodynamic viscosity was 0.0035 Pas, and its density was 1,050 kg/m^3.

The multi-scale model coupled the 0D model to the 3D model, and the 0D model provided boundary conditions for the 3D model, as shown in **Figure 2** (taking patient 1 as an example). The 0D model uses the circuit structure to simulate the vascular network, simplifying the complex three-dimensional blood flow problem into a simple circuit-solving problem. We used resistors to simulate blood flow resistance, capacitors to simulate blood vessel elasticity, and inductors to simulate blood flow inertia.

The 0D model in **Figure 2** can be divided into three modules: the heart module, the aortic module, and the coronary module.

For the heart module, the purpose was to provide boundary conditions for the aortic inlet of the 3D model, so our heart model only included the left part of the heart and left out the right part. In the left heart, the blood enters the left ventricle through the left atrium via the mitral valve. Blood is pumped through the aortic valve to the aorta by compression of the left ventricle, which then completes the systemic circulation. The Ula part is a constant voltage source, which represents the pressure of the left atrium. This is because the pressure of the left atrium is small and does not fluctuate significantly with the cardiac cycle, so it can be replaced by a constant voltage source. The two diodes represent the mitral valve and the aortic valve from right to left, respectively, to ensure the single conduction of current. The resistance Rla and inductance Lla, respectively, represent the flow resistance and flow inertia through the mitral valve. Resistance Rlv represents the resistance of the blood flow through the aortic valve. C(t) is a time-varying capacitance that reflects the periodic contraction and relaxation of the left ventricle, and the change of its value is regulated by the relationship between the pressure and volume of the left ventricle. The functional relationship of $C(t)$ is as follows:

$$C(t) = \frac{1}{E(t)} \tag{1}$$

$$E\,(t) = (E_{max} - E_{min}) \cdot E_n(t_n) + E_{min} \tag{2}$$

$$E_n\,(t_n) = 1.55 \left[\frac{\left(\frac{t_n}{0.7}\right)^{1.9}}{1 + \left(\frac{t_n}{0.7}\right)^{1.9}} \right] \left[\frac{1}{1 + \left(\frac{t_n}{1.17}\right)^{21.9}} \right]$$

(*Stergiopuloset al.*, 1996) (3)

Among them, $t_n = \frac{t}{T_{max}}$, $T_{max} = 0.2 + 0.15t_c$, t_c represents the time of a cardiac cycle.

For the aortic module, the resistance R_P represents the arterial blood flow resistance; the resistance Rd represents the sum of the arterial end, the microcirculatory system, and the venous system resistance; and the capacitance C represents the arterial elasticity.

For the coronary module, unlike other blood vessels, the coronary vessels reach their peak blood flow during diastole. In order to simulate the special phenomenon of coronary artery, the effect of myocardial contraction needs to be taken into account in the lumped parameter model. The common practice is to add a pressure source synchronized with ventricular pressure into the lumped parameter model. The resistance R represents the coronary flow resistance, the resistance R_m represents the coronary microcirculation blood flow resistance, and the resistance R_v represents the coronary venous flow resistance. Capacitance C represents the elasticity of the coronary arteries, and capacitance C_{im} represents the elasticity of the coronary microcirculation. A voltage source is terminated at the capacitorC_{im}, and the change in value follows the change in left ventricular pressure.

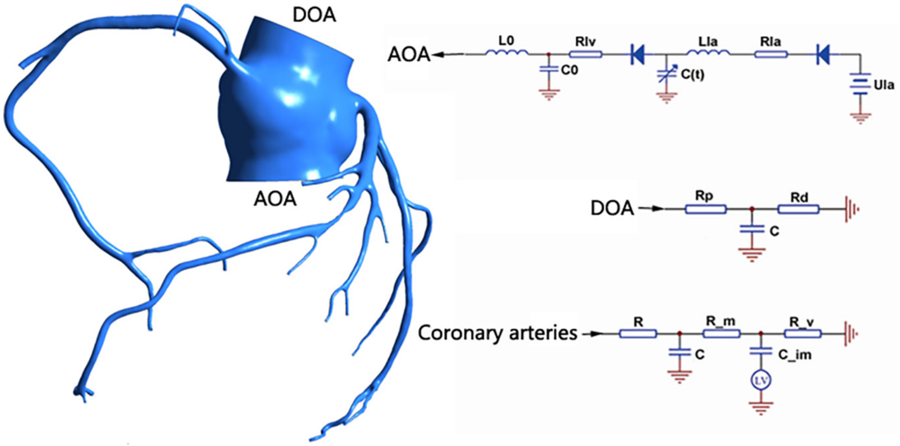

FIGURE 2 | 0–3D coupled multi-scale model.

The parameter values of each component in the lumped parameter model are based on the study of coronary artery modeling by Kim et al. (2010). After the structure of the lumped parameter model is determined, the problem of parameter selection should be solved. Firstly, using the data of systolic blood pressure, diastolic blood pressure, heart rate, and cardiac output of normal people, the aorta pressure waveform and cardiac output waveform of normal people were fitted and used as the two optimal target waveforms. In this process, two important points should be noted: (1) the total coronary flow accounted for 4% of the cardiac output, and the left coronary flow and the right coronary flow accounted for 60 and 40% of the total coronary flow, respectively; (2) the blood flow of the coronary artery branch was directly proportional to the 2.7 power of the coronary artery diameter. Secondly, taking the clinically measured aortic pressure and cardiac output as the optimization objectives, the sensitivity analysis was carried out on the parameters of the lumped-parameter model to find the parameters that had great influence on the optimization objectives. Finally, the measured systolic blood pressure, diastolic blood pressure, and heart rate were used to adjust the standard aortic pressure waveform; the root mean square error between the aortic pressure waveform and the simulated waveform, and the mean value of cardiac output were taken as the objective function; and the sensitive parameters in the model were optimized by a simulated annealing algorithm.

After adjusting the parameters according to the normal state, the coronary resistance was multiplied by 0.24 to simulate the maximum hyperemia after adenosine injection when measuring FFR.

This study used a specific interface condition and coupling algorithm to couple the 3D model with the lumped parameter model. The 3D model was calculated by ANSYS-CFX, the set parameter model was calculated based on the FORTRAN subroutine of CFX Junction Box, and the data transfer between the 3D model and the set parameter model utilized the CFX User CEL Function. The lumped parameter model provided a three-dimensional model with flow at the aortic inlet and pressure boundary conditions at each arterial outlet; after the 3D model was calculated, a pressure value was returned to the lumped parameter model at the entrance to the aorta. A flow value was returned to the lumped parameter model at each arterial exit in order for the lumped parameter model to complete the calculation.

Now, the multi-scale model of the 0–3D coupling of the complete coronary hyperemia state is completed. After the calculation, the pressure at the aorta and the distal end of the stenosis was extracted at 3 cm for the calculation of FFR.

Construction of CABG Model

The virtual surgery software Freeform was used to graft the stenosis of the two patients. The diameter of the graft was set to 3 mm, and the initial site of the bypass was the aortic root, as shown in **Figure 3**.

After the 3D model was constructed, the settings of the 0D model part and the 0–3D interface part became the same as the 2.2 part of the method. The difference is that in the CABG model, the coronary artery is in a normal state, so its resistance does not need to be multiplied by 0.24.

RESULTS

FFR Non-invasive Calculation Results

After the calculation was completed, the FFR value of the entire model was extracted. By comparing the FFR diagram of the two models, it can be seen that the color scale of patient 1 at both ends of the stenosis shows a significant difference, indicating that the FFR value has a significant reduction after the stenosis site. The color scales of patient 2 at the front and distal ends of the stenosis site change steadily, and there is no significant difference, indicating that the FFR value does not change significantly after the stenosis site. At the same time, the pressure at 3 cm from the distal end of the stenosis and the pressure in the aorta were extracted, and the ratio was defined as the FFR value of the stenosis. As shown in **Figure 4**, although the anatomical stenosis rate of both patients 1 and

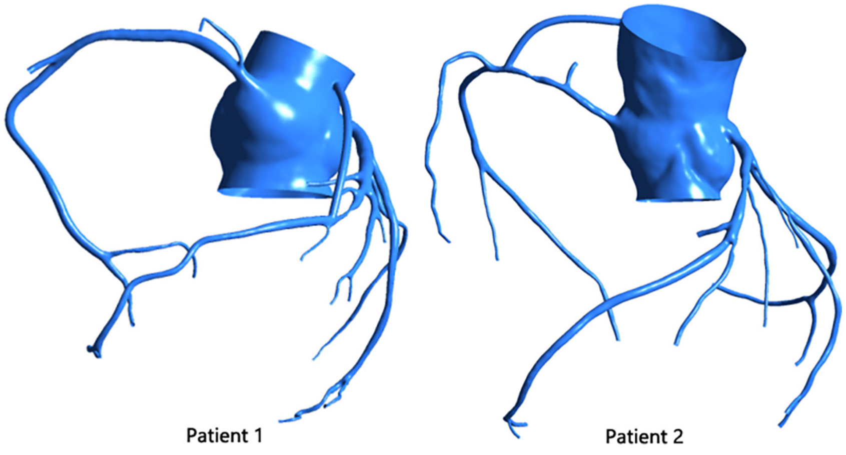

FIGURE 3 | Patient's CABG model.

2 was 70%, their FFR calculation results were quite different. Patient 1 had an FFR of 0.67, and patient 2 had an FFR of 0.91, which are close to their clinical measurements (0.7 and 0.95), indicating that the model reflects the true physiological condition. At the same time, it was also indicated that the stenosis of patient 1 caused downstream ischemia (FFR < 0.75), while the stenosis of patient 2 did not cause downstream ischemia (FFR > 0.8).

Hemodynamic Environment After CABG

Flow of Graft and Coronary Vessels

After calculating the CABG model, the blood flow waveforms of the middle segment of the graft and the stenosis coronary artery were extracted, as shown in **Figure 5**. The mean flow rate, as well as the ratio of stenosis coronary flow to graft flow, are shown in **Table 2**.

From the figure and the table, we can see that although the flow rate through the two grafts was not very different, the ratio of the flow rate of the stenosis coronary artery to the graft of patient 1 was 0.12, and the flow ratio of patient 2 was 0.42. This indicates that after the bypass surgery, the proportion of blood supply to the distal coronary artery in patient 1 was large, while the blood supply to the distal coronary artery in patient 2 was still a considerable proportion through the stenosis coronary artery. This reflects the presence of a strong competitive flow in patient 2, which severely reduces blood flow in the graft. Moreover, the negative flow in the waveform of patient 2 was also significantly greater than patient 1, which produces poor hemodynamic results.

TABLE 2 | The flow rate of graft and coronary artery.

	Graft (ml/min)	Coronary (ml/min)	Ratio
Patient 1	45.07	5.49	0.12
Patient 2	39.68	16.62	0.42

Results of WSS in the Graft

This study extracted time-averaged WSS (TAWSS) results from the grafts, as shown in **Figure 6**.

The TAWSS in the patient 1 graft was calculated to be 2.09 Pa, and the TAWSS in the patient 2 graft was 2.16 Pa. It can also be

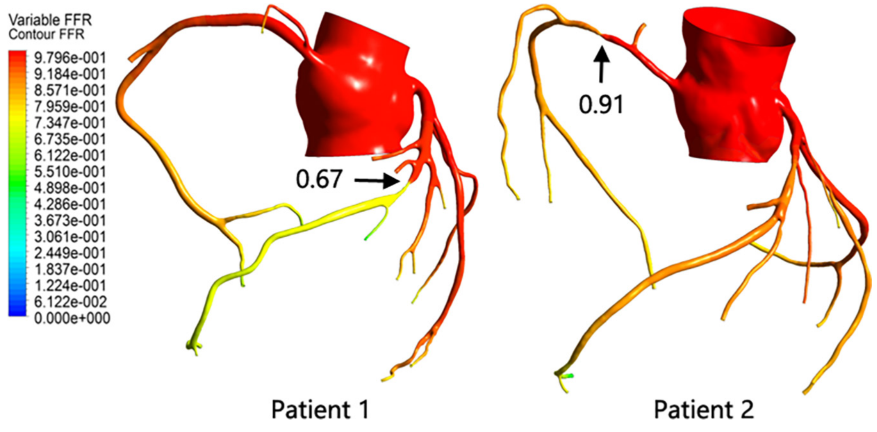

FIGURE 4 | Patient FFR calculation results.

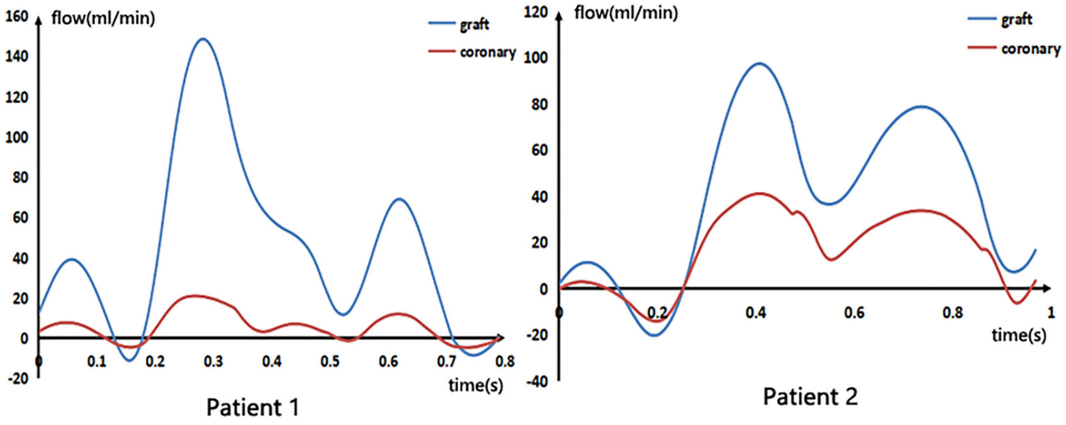

FIGURE 5 | Blood flow waveforms in the graft and stenosis of the patient.

seen from the figure that the WSS spatial distributions of the two were similar and were distributed approximately uniformly over the entire graft.

Results of Oscillatory Shear Index in the Graft

Oscillatory shear index (OSI) is also a commonly used hemodynamic parameter that characterizes the degree of oscillation of blood flow in a blood vessel, defined as

$$OSI = 0.5\left[1 - \frac{\left|\int_0^T \overrightarrow{WSS}dt\right|}{\int_0^T \left|\overrightarrow{WSS}\right|dt}\right] \tag{4}$$

The OSI results in the graft were extracted as shown in **Figure 7**. The OSI of patient 1 was calculated to be 0.0375, and the OSI of patient 2 was 0.1264. Patient 2 had an OSI value that was approximately three times that of patient 1. Moreover, according to **Figure 7**, it can be seen that not only was the mean OSI of patient 2 higher than that of patient 1, but a local high OSI region was also present at the anastomosis.

DISCUSSION

Analysis of Factors Affecting FFR

The narrowness of the same stenosis rate (70%) in the image information resulted in different functional results (FFR <0.75 or FFR >0.8). This shows that in addition to the stenosis rate factor, there are other factors that are also affecting stenosis functional outcome. For the two patients in this study, we can see that their stenosis length was not the same; patient 1 had a stenosis length of 10 mm, while patient 2 had a stenosis length of only 4 mm. Within a certain range, a longer stenosis length will result in a larger pressure drop. At the same time, the patients' heart rate, blood pressure, cardiac output, and other physiological parameters were also different, and these physiological parameters also had an impact on the calculation of FFR. In addition, the location of the stenosis of the two patients was different; the stenosis of patient 1 was in the LAD, and the stenosis of patient 2 was in the RCA. The myocardial area supplied by the LAD is larger than that of the RCA, which means that the distal microvessels of the LAD are more effective than the RCA after adenosine injection, which

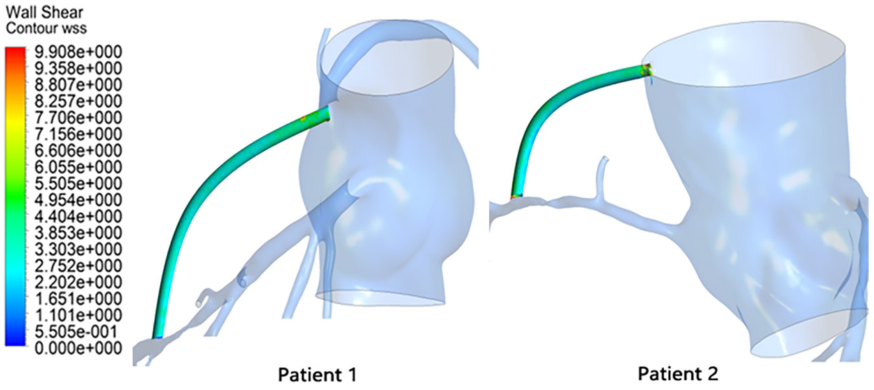

FIGURE 6 | TAWSS results in the graft.

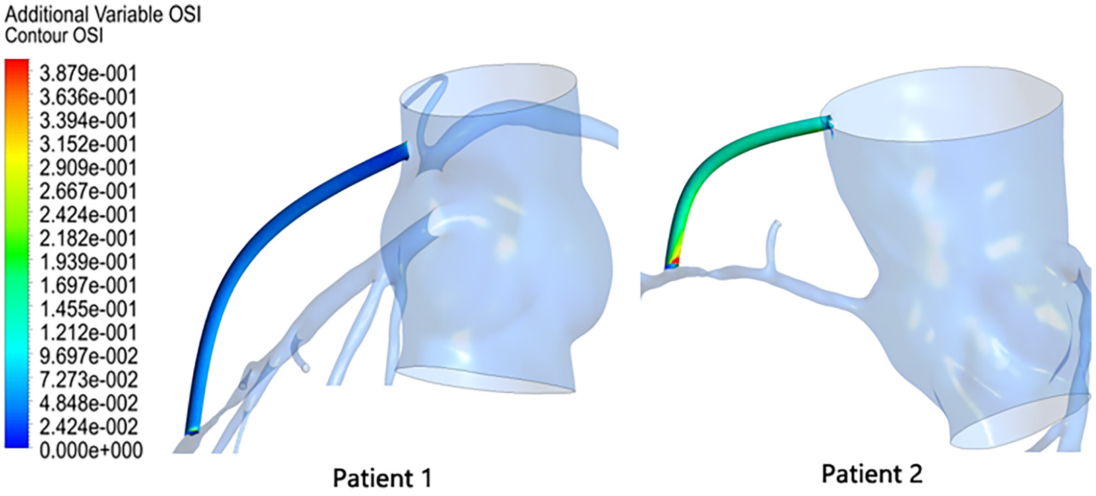

FIGURE 7 | OSI results in the graft.

makes the pressure drop on the LAD larger, which also affects the results of FFR.

Effect of FFR on Graft

By comparing the blood flow results of the simulated bypass of the two patients, it can be found that the biggest difference between the two was the flow ratio of the stenosis coronary artery to the graft. Patients with high FFR values have a higher ratio of stenosis coronary to graft flow. This means that the coronary artery divides a large part of the blood flow of the graft; that is, the competition flow is strong. However, this did not seem to affect the supply of blood flow to the distal end of the coronary artery. Even when observing the WSS of the graft, it was found that the competitive flow did not cause the WSS to be too low on the graft, nor was the WSS gradient form too large. So, does this mean that we cannot consider the FFR value when we graft? In other words, can we perform a preventive bypass surgery when the FFR shows that the stenosis is not serious?

By continuing to observe the results of OSI in the grafts, we found that this is not the case. By performing a bypass surgery on a high FFR stenosis, the OSI value in the graft is significantly higher. In this study, the OSI value in the patient 2 graft was three times that of patient 1. This will result in poor long-term permeability of the high FFR-narrow graft, and this inference is consistent with the clinical observations mentioned in the section "Introduction" of this article. At the same time, we can observe that the OSI in the graft is not evenly distributed but has a very high OSI region near its anastomosis. This will lead to the formation of intimal hyperplasia at the anastomosis, which will block the blood supply downstream of the coronary artery. Therefore, from a long-term perspective, prophylactic grafting when the FFR shows that the stenosis is not severe does not improve the supply of blood flow but also worsens the original blood supply.

To sum up, the most important role of FFR technology in CABG is to guide bypass surgery and decide whether to bypass a stenosis site. A purely anatomic diagnosis would result in a graft to a site of moderate stenosis, which would result in the failure of the graft. FFR, a functional diagnostic method, can avoid these failed bypass operations and improve the graft patency.

Limitation

In this paper, the relationship between FFR and graft hemodynamics was investigated using the data of two patients. This amount of data are insufficient to draw conclusions, and it was difficult to draw the cutoff value of FFR to determine whether a stenosis was suitable for bypass. In future studies, more cases should be introduced to verify the results, and a reasonable FFR cutoff value guiding coronary bypass surgery can also be explored.

CONCLUSION

When bypassing a stenosis with high FFR value, its adverse hemodynamic effects were mainly reflected in OSI. It produced a high OSI region in the graft, especially at the anastomosis. In the long term, this will cause anastomotic blockage and graft failure. FFR, a functional diagnostic method, can be introduced to avoid failed bypass surgery. Therefore, a quick evaluation of the CABG using FFR may be considered prior to bypass surgery, which will help improve the graft patency.

DATA AVAILABILITY STATEMENT

All datasets generated for this study are included in the article/supplementary material.

ETHICS STATEMENT

This study passed the inspection by the medical ethics committee of Peking University people's hospital. All participants gave signed informed consent.

AUTHOR CONTRIBUTIONS

BL was responsible for model calculation and manuscript revising. BM was responsible for modeling, calculation, data analysis, and article writing. YF assisted in data analysis and article writing. JL assisted in the establishment of the three-dimensional model. ZZ was responsible for providing experimental data. MD assisted in the article writing. YL was responsible for supervision. All authors contributed to the article and approved the submitted version.

FUNDING

This research was supported by the National Natural Science Foundation of China (11832003, 11772016, and 11472022), the Fundamental Research Funds for the Central Universities (2021-JYB-XJSJJ022), and the China Scholarship Council.

REFERENCES

Bassiouny, H. S., White, S., Glagov, S., Choi, E., Giddens, D. P., and Zarins, C. K. (1992). Anastomotic intimal hyperplasia: mechanical injury or flow induced. *J. Vasc. Surg.* 15, 708–716. doi: 10.1016/0741-5214(92)90019-5

Beck, C. S. (1935). The development of a new blood supply to the heart by operation. *Ann. Surg.* 102, 801–813. doi: 10.1097/00000658-193511000-00001

Berger, A. (2004). Long-term patency of internal mammary artery bypass grafts: relationship with preoperative severity of the native coronary artery stenosis. *Circulation* 110, II–36–II–40.

Botman, C. J., Schonberger, J., Koolen, S., Dib, N., Eric, E., Nico, P., et al. (2007). Does stenosis severity of native vessels influence bypass graft patency? a prospective fractional flow reserve–guided study. *Ann. Thorac. Surg.* 83, 2093–2097. doi: 10.1016/j.athoracsur.2007.01.027

Butany, J. W., David, T. E., and Ojha, M. (1998). Histological and morphometric analyses of early and late aortocoronary vein grafts and distal anastomoses. *Can. J. Cardiol.* 14, 671–677.

Casselman, F., Johan, V. D. M., Ferrara, A., and Barbato, E. (2016). The present day potential role of fractional flow reserve–guided coronary artery bypass graft surgery. *J. Thorac. Cardiovasc. Surg.* 151, 926–932. doi: 10.1016/j.jtcvs.2015.12.021

Ferguson, T. B., Chen, C., Babb, J. D., Jimmy, T. E., Ramesh, D., and John, M. C. (2013). Fractional flow reserve–guided coronary artery bypass grafting: can intraoperative physiologic imaging guide decision making? *J. Thorac. Cardiovasc. Surg.* 146, 824.e1–835.e1.

Hanet, C., Schroeder, E., Michel, X., Cosyns, J., Dion, R., Verhelst, R., et al. (1991). Flow-induced vasomotor response to tachycardia of the human internal mammary artery and saphenous vein grafts late following bypass surgery. *Circulation* 84(5 Suppl.), III268–III274.

Hofer, M., Rappitsch, G., Perktold, K., Trubel, W., and Schima, H. (1996). Numerical study of wall mechanics and fluid dynamics in end-to-side anastomoses and correlation to intimal hyperplasia - journal of biomechanics. *J. Biomech.* 29, 1297–1308. doi: 10.1016/0021-9290(96)00036-x

Kim, H. J., Vignonclementel, I. E., Coogan, J. S., Figueroa, C. A., Jansen, K. E., and Taylor, C. A. (2010). Patient-specific modeling of blood flow and pressure in human coronary arteries. *Ann. Biomed. Eng.* 38, 3195–3209. doi: 10.1007/s10439-010-0083-6

Pellicano, M., De, B. B., Toth, G. G., Filip, C., Wijns, W., and Barbato, E. (2010). Fractional flow reserve to guide and to assess coronary artery bypass grafting. *Eur. Heart J.* 38, 1959–1968.

Pijls, N., Gelder, B. V., Voort, P. V., Peels, K., Bracke, F. A., Bonnier, H. J., et al. (1995). Fractional flow reserve. A useful index to evaluate the influence of an epicardial coronary stenosis on myocardial blood flow. *Circulation* 92, 3183–3193. doi: 10.1161/01.cir.92.11.3183

Pijls, N. H. J., De Bruyne, B., Peels, K., Koolen, J. J., Koolen, B. J., Bonnier, H. J., et al. (1996). Measurement of fractional flow reserve to assess the functional severity of coronary-artery stenoses. *N. Engl. J. Med.* 334, 1703–1708. doi: 10.1056/nejm199606273342604

Sabik, J. F., Lytle, B. W., Blackstone, E. H., Khan, M., Penny, L. H., and Delos, M. C. (2003). Does competitive flow reduce internal thoracic artery graft patency? *Ann. Thorac. Surg.* 76, 1490–1496. doi: 10.1016/s0003-4975(03)01022-1

Stephane, F., Toth, G. G., Bernard, D. B., Nils, P. J., Barbato, E., Ivan, D., et al. (2018). Six-year follow-up of fractional flow reserve-guided versus angiography-guided coronary artery bypass graft surgery. *Circ. Cardiovas. Int.* 11:e006368.

Stergiopulos, N., Meister, J. J., and Westerhof, N. (1996). Determinants of stroke volume and systolic and diastolic aortic pressure. *Am. J. Physiol.* 270(6 Pt 2), H2050–H2059.

Taylor, C. A., Fonte, T. A., and Min, J. K. (2013). Computational fluid dynamics applied to cardiac computed tomography for noninvasive quantification of fractional flow reserve: scientific basis. *J. Am. Coll. Cardiol.* 61, 2233–2241. doi: 10.1016/j.jacc.2012.11.083

Toth, G., De Bruyne, B., Casselman, F., Frederic, D. V., Frank, V. P., Carlos, V. M., et al. (2013). Fractional flow reserve-guided versus angiography-guided coronary artery bypass graft surgery. *Circulation* 128, 1405–1411. doi: 10.1161/circulationaha.113.002740

Vineberg, A. M. (1948). Development of anastomosis between the coronary vessels and a transplanted internal mammary artery. *J. Thorac. Surg.* 18, 839–850. doi: 10.1016/s0096-5588(20)31305-2

Whittemore, A. D., Clowes, A. W., Couch, N. P., and Mannick, J. A. (1981). Secondary femoropopliteal reconstruction. *Ann. Surg.* 193, 35–42. doi: 10.1097/00000658-198101000-00006

Conflict of Interest: The authors declare that the research was conducted in the absence of any commercial or financial relationships that could be construed as a potential conflict of interest.

Advantages of publishing in Frontiers

OPEN ACCESS
Articles are free to read
for greatest visibility
and readership

FAST PUBLICATION
Around 90 days
from submission
to decision

HIGH QUALITY PEER-REVIEW
Rigorous, collaborative,
and constructive
peer-review

TRANSPARENT PEER-REVIEW
Editors and reviewers
acknowledged by name
on published articles

Frontiers
Avenue du Tribunal-Fédéral 34
1005 Lausanne | Switzerland

Visit us: www.frontiersin.org
Contact us: frontiersin.org/about/contact

REPRODUCIBILITY OF RESEARCH
Support open data
and methods to enhance
research reproducibility

DIGITAL PUBLISHING
Articles designed
for optimal readership
across devices

FOLLOW US
@frontiersin

IMPACT METRICS
Advanced article metrics
track visibility across
digital media

EXTENSIVE PROMOTION
Marketing
and promotion
of impactful research

LOOP RESEARCH NETWORK
Our network
increases your
article’s readership